

ERCOFTAC

Bulletin

September 2020

124

European Research Community on Flow, Turbulence and Combustion

ERCOFTAC is a leading European association of research, education and industry groups in the technology of flow, turbulence and combustion. The main objectives of ERCOFTAC are: To promote joint efforts of European research institutes and industries with the aim of **exchanging technical and scientific information**; to promote **Pilot Centres** for collaboration, stimulation and application of

research across Europe; to stimulate, through the creation of **Special Interest Groups**, wellcoordinated European-wide research efforts on specific topics; to stimulate the creation of advanced training activities; and to be influential on funding agencies, governments, the European Commission and the European Parliament.

www.ercoftac.org

Executive Committee

<i>Chairman</i>	Von Terzi, D. Delft University of Technology, Netherlands Tel: +31 15 27 83379 D.A.vonTerzi@tudelft.nl
<i>First Deputy Chairman</i>	Tomboulides, A.
<i>Second Deputy Chairman</i>	Hirsch, C.
<i>Treasurer</i>	Geurts, B.
<i>SPC Chairman</i>	Hickel, S.
<i>SPC Deputy Chairman</i>	Salvetti, M. V.
<i>KNC Chairman</i>	Standingford, D.
<i>KNC Deputy Chairman</i>	Hillewaert, K.
<i>Knowledge Base Editor</i>	Rodi, W.
<i>Bulletin Editor</i>	Elsner, W.

ERCOFTAC Seat of the Organisation

<i>Director</i>	Hirsch, C. Chaussée de la Hulpe 189 Terhulpesteenweg B-1170 Brussels, Belgium Tel: +32 2 643 3572 Fax: +32 2 647 9398 ado@ercoftac.be
-----------------	---

Scientific Programme Committee

<i>Chairman</i>	Hickel, S. Delft University of Technology Faculty of Aerospace Engineering Kluyverweg 1 2629 HS Delft The Netherlands Tel: +31 152 789 570 S.Hickel@tudelft.nl
<i>Deputy Chairman</i>	Salvetti, M. V.

Knowledge Network Committee

<i>Chairman</i>	Standingford, D. Zenotech Ltd. 1 Laarkfield Grove Chepstow, NP16 5UF United Kingdom Tel: +44 7870 628 916 david.standingford@zenotech.com
<i>Deputy Chairman</i>	Hillewaert, K.

ERCOFTAC Central Administration and Development Office (CADO)

<i>Admin. Manager</i>	Jakubczak, M. PO Box 1212 Bushey, WD23 9HT United Kingdom Tel: +44 208 117 6170 admin@cado-ercoftac.org Skype: ERCOFTAC-CADO
-----------------------	--

TABLE OF CONTENTS

Non-Ideal Compressible Fluid Dynamics: Preface	4
<i>A. Guardone and M. Pini</i>	
Oblique Shock Waves in Non-ideal Compressible Flows	5
<i>D. Vimercati, G. Gori, A. Kluwick and A. Guardone</i>	
Boundary Layer Stability, Scaling Methods and Modelling of Turbulence in Supercritical Fluids	11
<i>R. Pecnik, J. Ren and G.J. Otero-R.</i>	
Contributions to the Numerical Modeling of Turbulent Dense Gas Flows	17
<i>P. Cinnella, X. Gloerfelt, F. Grasso and L. Sciacovelli</i>	
Direct Numerical Simulation of a BZT Dense Gas Compressible Shear Layer	23
<i>A. Vadrot, A. Giauque and C. Corre</i>	
Large Eddy Simulation of Transcritical and Supercritical Flows	29
<i>B. Cuenot and T. Schmitt</i>	
On the Simulation of Multicomponent and Multiphase Compressible Flows	35
<i>R. Abgrall, P. Bacigaluppi and B. Re</i>	
Numerical Fluxes for Cryogenic Multi-phase Flow Computations	41
<i>H. Kim and C. Kim</i>	
Enhancing the Predictive Capabilities for High P/T Fuel Sprays; Non-Ideal Thermodynamic Modelling Using PC-SAFT	47
<i>P. Koukouvinis, A. Vidal-Roncero, C. Rodriguez, M. Gavaises and L. Pickett</i>	
High-order Multi-component Lattice Boltzmann Method and its Capabilities for Non-Ideal Fluid Mixtures	53
<i>C. S. From, M. Deligant, M. Specklin, S. Khelladi and E. Sauret</i>	
Experimental Facilities for Non-ideal Compressible Vapour Flows	59
<i>A. Spinelli, A. Guardone, C. De Servi, P. Colonna, F. Reinker, S. aus der Wiesche, M. Robertson and R.F. Martinez-Botas</i>	
Optical Diagnostics For Non-Ideal Compressible Fluid Dynamics	67
<i>F. Cozzi, A. Spinelli, S. Gallarini and A. Guardone</i>	
Professor José Manuel Redondo Apraiz Obituary	73
<i>J. Pons-Prats</i>	

EDITOR	Marek, M.
TECHNICAL EDITOR	Kuban, Ł.
CHAIRMAN	Elsner, W.
EDITORIAL BOARD	Armenio, V. Dick, E. Geurts, B.J.
DESIGN & LAYOUT	Borhani, N. Nichita, B.A.
COVER DESIGN	Aniszewski, W.

SUBMISSIONS

ERCOFTAC Bulletin
 Institute of Thermal Machinery
 Częstochowa University of Technology
 Al. Armii Krajowej 21
 42-201 Częstochowa
 Poland
 Tel: +48 343 250 507
 Fax: +48 343 250 507
 Email:ercoftac@imc.pcz.czyst.pl

HOSTED, PRINTED & DISTRIBUTED BY



CZĘSTOCHOWA UNIVERSITY OF TECHNOLOGY

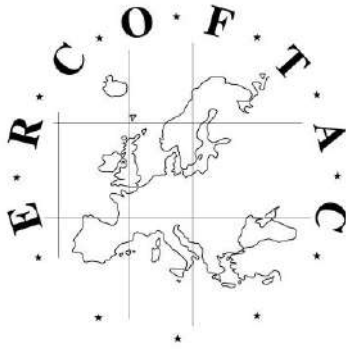
ISSN: 2518-0991

The reader should note that the Editorial Board cannot accept responsibility for the accuracy of statements made by any contributing authors

NEXT ERCOFTAC EVENTS

ERCOFTAC Autumn Festival
 8th of October, 2020
 Rome, Italy

ERCOFTAC Committee Meetings
 9th of October, 2020
 Rome, Italy



The ERCOFTAC Best Practice Guidelines for Industrial Computational Fluid Dynamics

The Best Practice Guidelines (BPG) were commissioned by ERCOFTAC following an extensive consultation with European industry which revealed an urgent demand for such a document. The first edition was completed in January 2000 and constitutes generic advice on how to carry out quality CFD calculations. The BPG therefore address mesh design; construction of numerical boundary conditions where problem data is uncertain; mesh and model sensitivity checks; distinction between numerical and turbulence model inadequacy; preliminary information regarding the limitations of turbulence models etc. The aim is to encourage a common best practice by virtue of which separate analyses of the same problem, using the same model physics, should produce consistent results. Input and advice was sought from a wide cross-section of CFD specialists, eminent academics, end-users and, (particularly important) the leading commercial code vendors established in Europe. Thus, the final document can be considered to represent the consensus view of the European CFD community.

Inevitably, the Guidelines cannot cover every aspect of CFD in detail. They are intended to offer roughly those 20% of the most important general rules of advice that cover roughly 80% of the problems likely to be encountered. As such, they constitute essential information for the novice user and provide a basis for quality management and regulation of safety submissions which rely on CFD. Experience has also shown that they can often provide useful advice for the more experienced user. The technical content is limited to single-phase, compressible and incompressible, steady and unsteady, turbulent and laminar flow with and without heat transfer. Versions which are customised to other aspects of CFD (the remaining 20% of problems) are planned for the future.

The seven principle chapters of the document address numerical, convergence and round-off errors; turbulence modelling; application uncertainties; user errors; code errors; validation and sensitivity tests for CFD models and finally examples of the BPG applied in practice. In the first six of these, each of the different sources of error and uncertainty are examined and discussed, including references to important books, articles and reviews. Following the discussion sections, short simple bullet-point statements of advice are listed which provide clear guidance and are easily understandable without elaborate mathematics. As an illustrative example, an extract dealing with the use of turbulent wall functions is given below:

- Check that the correct form of the wall function is being used to take into account the wall roughness. An equivalent roughness height and a modified multiplier in the law of the wall must be used.
- Check the upper limit on y^+ . In the case of moderate Reynolds number, where the boundary layer only extends to y^+ of 300 to 500, there is no chance of accurately resolving the boundary layer if the first integration point is placed at a location with the value of y^+ of 100.

- Check the lower limit of y^+ . In the commonly used applications of wall functions, the meshing should be arranged so that the values of y^+ at all the wall-adjacent integration points is only slightly above the recommended lower limit given by the code developers, typically between 20 and 30 (the form usually assumed for the wall functions is not valid much below these values). This procedure offers the best chances to resolve the turbulent portion of the boundary layer. It should be noted that this criterion is impossible to satisfy close to separation or reattachment zones unless y^+ is based upon y^* .
- Exercise care when calculating the flow using different schemes or different codes with wall functions on the same mesh. Cell centred schemes have their integration points at different locations in a mesh cell than cell vertex schemes. Thus the y^+ value associated with a wall-adjacent cell differs according to which scheme is being used on the mesh.
- Check the resolution of the boundary layer. If boundary layer effects are important, it is recommended that the resolution of the boundary layer is checked after the computation. This can be achieved by a plot of the ratio between the turbulent to the molecular viscosity, which is high inside the boundary layer. Adequate boundary layer resolution requires at least 8-10 points in the layer.

All such statements of advice are gathered together at the end of the document to provide a 'Best Practice Checklist'. The examples chapter provides detailed expositions of eight test cases each one calculated by a code vendor (viz FLUENT, AEA Technology, Computational Dynamics, NUMECA) or code developer (viz Electricité de France, CEA, British Energy) and each of which highlights one or more specific points of advice arising in the BPG. These test cases range from natural convection in a cavity through to flow in a low speed centrifugal compressor and in an internal combustion engine valve.

Copies of the Best Practice Guidelines can be acquired from:

ERCOFTAC (CADO)
PO Box 1212
Bushey, WD23 9HT
United Kingdom
Tel: +44 208 117 6170
Email: admin@cado-ercoftac.org

The price per copy (not including postage) is:

ERCOFTAC members		
First copy		<i>Free</i>
Subsequent copies		75 Euros
Students		75 Euros
Non-ERCOFTAC academics		
Non-ERCOFTAC industrial		140 Euros
EU/Non EU postage fee		230 Euros
		10/17 Euros

BPG for CFD in Turbulent Combustion

ERCOFTAC

Best Practice Guidelines for CFD of Turbulent Combustion

Editors: Profs. Luc Vervisch, & Dirk Roekaerts

The aim of this Best Practice Guide (BPG) is to provide guidelines to CFD users in a wide range of application areas where combustion is an essential process. Since the first edition published in 2015, the interest in numerical modeling of the emission of particulate material formed in flames is continuously growing. For this reason, this second edition includes an new Chapter on the modeling of sooting flames.

The overall structure of the BPG is as follows:

Chapters 1-3 summarize key issues in turbulent combustion model formulation. Chapter 4 is addressing the validation of modelling using available experimental databases. In the new Chapter 5 the fundamentals driving the formation and the evolution (nucleation, growth, agglomeration, oxidation) of flowing non-inertial particles are discussed, before presenting best practices for major soot modeling approaches in CFD of turbulent flames. Then, two application areas are elaborated in separate chapters: Chapter 6 on Internal Combustion Engines, and Chapter 7 on Gas Turbines. Best practice guidelines by the nature of technology development are always temporary. New insights and approaches will take over after some time. Therefore this BPG ends with a Chapter 8 on Emerging Methods, providing a preview of approaches so far only useful for simulating canonical configurations or requiring further developments.

A comprehensive CFD approach to turbulent combustion modelling relies on appropriate submodels for flow turbulence, chemistry and radiation, and their interactions. In the framework of this BPG, knowledge of turbulent flow modeling is a pre-requisite and only briefly explained. Instead the discussion on models is divided in three parts: turbulence-chemistry interaction (Chapter 1), chemistry (Chapter 2) and radiative heat transfer (Chapter 3). Many of the models introduced in the first three chapters will reappear in the discussion in Chapters 4 to 6 and comments on challenges, advantages and disadvantages are formulated in all chapters. Those looking for immediate advices to tackle a specific application may want to proceed immediately to the application chapters (IC engines in Chapter 5 and Gas Turbines in Chapter 6) and return to the basic chapters when necessary. But everyone not finding in these chapters an immediate answer to the basic question: What is the best model for my specific application? should certainly spend some time on Chapter 4, because it addresses the mandatory preliminary steps that have to be considered to validate a simulation involving any sort of turbulent flames.



ERCOFTAC
Best Practice Guidelines



*Computational Fluid Dynamics of
Turbulent Combustion*



Second Edition

Luc Vervisch & Dirk Roekaerts

Editors

Table of Content

- 1-Introduction to turbulent combustion modelling
- 2-Combustion Chemistry
- 3-Thermal Radiation
- 4-RANS and LES validation
- 5-Sooting flames
- 6-Internal Combustion Engine
- 7-Gas-Turbines
- 8-Emerging Methods

To order please visit:

https://www.ercoftac.org/publications/ercoftac_best_practice_guidelines/cfd_of_turbulent_combustion/

Or from:

ERCOFTAC (CADO)
PO Box 1212
Bushey, WD23 9HT
United Kingdom
Tel: +44 208 117 6170

Email: admin@cado-ercoftac.org

The price per copy (not including postage) is:

ERCOFTAC members

First copy Free

Subsequent copies 75 Euros

Students 75 Euros

Non-ERCOFTAC academics, 140 Euros

Non-ERCOFTAC industrial, 230 Euros

EU / Non EU postage fee 10/ 17 Euros

NON-IDEAL COMPRESSIBLE FLUID DYNAMICS: PREFACE

A. Guardone¹ and M. Pini²

¹Coordinator of ERCOFTAC SIG 49, Department of Aerospace Science and Technology, Politecnico di Milano, Italy

²Deputy Coordinator of ERCOFTAC SIG 49, Propulsion and Power, Delft University of Technology, The Netherlands

Non-ideal compressible fluid dynamics (NICFD) is the branch of fluid-mechanics concerning the study of non-reacting flows of fluids in non-ideal thermodynamic states. It therefore deals with dense vapor flows, vapor-liquid flows, supercritical and near-critical fluid flows, and compressible liquid flows.

Fluid ideality here refers to the thermodynamics of perfect gases, namely dilute gases with constant isochoric specific heat. In NICFD flows, the well-understood non-ideal thermodynamics of vapours and supercritical fluids, phase transition, and the liquid-vapour critical point result in significant departure from the the well-known gas dynamic behaviour of dilute, constant-specific-heat gases, under both a quantitative and a qualitative point of view. Non-ideal compressible flows may exhibit non-monotone Mach variation along isentropic expansions, Mach-increasing oblique shock waves, condensation and liquefaction shocks. If the so-called fundamental derivative of gasdynamics Γ —a dimensionless measure of the speed-of-sound variation along isentropes—is negative, non-classical phenomena such as rarefaction shock waves or double-sonic shocks are physically admissible. Fluids exhibiting a negative- Γ region in the single-phase vapour are called Bethe-Zel'dovich-Thompson (BZT) fluids. Their actual existence is still to be verified experimentally, after over a century from the first theoretical results.

Since the 2000's, the interest in NICFD flows has steadily grown, arguably driven by engineering applications related to the conversion of renewable and waste energy sources, like, e.g., organic Rankine cycles, supercritical CO₂ cycle power plants, combustors operating with supercritical fluids, and heat-pumps. The importance of non-ideality in classical gasdynamics was recognized and the theory and physical aspects systematically investigated. To complement and to assess the accuracy of theoretical and simulation studies, the community felt the need for experimental validation and a number of set-ups were established to measure the thermo-physical

properties of NICFD flows. A special interest group on NICFD was established within the ERCOFTAC as SIG 49, to provide a reference point for the NICFD community. ERCOFTAC recently supported the organisation of the International Seminar on NICFD in October 2020, the third edition of a successful series of bi-annual meetings of the NICFD community.

The present ERCOFTAC thematic issue on NICFD provides an overview of current research activities carried out worldwide. Due to the intrinsic multi-disciplinary nature of NICFD, current research encompasses fundamental theoretical aspects of gasdynamics, including shock-wave properties and the characterisation of turbulence; modelling of thermodynamic properties of pure fluids and mixtures; numerical methods accounting for complex thermodynamics models of single-phase and of two-phase flows of pure fluids and mixtures; experimental techniques and facilities to investigate NICFD flows, assess the accuracy of numerical models, and support the development of the next-generation of components operating in the NICFD regime like, e.g., turbines, compressors and heat exchangers.

The review on non-ideal oblique shock-waves by Vimercati *et al.* opens the thematic issue and it is followed by the review of Pecnik *et al.* on turbulence in supercritical flows. Turbulence in NICFD flows is then addressed in the contributions by Cinnella *et al.* and by Vadrot *et al.* for non-classical fluid flows and by Cuenot & Schmitt for transcritical and supercritical fluid flows. Numerical methods for two-phase non-ideal compressible flows are reviewed by Abgrall *et al.*; the application to cryogenic two-phase flow is then presented by Kim & Kim. Modelling and numerical methods for mixtures are described by Koukouvinis *et al.* and From *et al.*, respectively. Spinelli *et al.* reviews current experimental activities and facilities operating in the NICFD regime; Cozzi *et al.* presents optical measurements techniques tailored to NICFD flows.

OBLIQUE SHOCK WAVES IN NON-IDEAL COMPRESSIBLE FLOWS

D. Vimercati¹, G. Gori², A. Kluwick³ and A. Guardone⁴

¹Universität der Bundeswehr München, 85577 Neubiberg, Germany

²Centre Inria Saclay – Île-de-France, 91120 Palaiseau, France

³Technische Universität Wien, 1060 Vienna, Austria

⁴Politecnico di Milano, 20156 Milan, Italy

Abstract

The nature of shock waves is dictated by the values of the thermodynamic parameter Γ , known as the fundamental derivative of gasdynamics, which expresses the variation of the speed of sound with the density at constant entropy. Flows evolving in a region where $\Gamma < 0$ allow for expansion shock waves only (i.e. the fluid particles experience a decrease in pressure as the shock front is crossed) to be formed, in contrast to the conventional, compressive shocks if $\Gamma > 0$. In the mixed regime where Γ can change its sign, so-called sonic shocks, having unitary normal Mach number relative to the front, can also be formed. Within the context of single-phase steady flows, the present work provides an overview of the non-ideal effects that characterise shock waves occurring in fluids having $\Gamma < 1$. Three main topics are covered: the increase of the Mach number across the shock, the formation of expansion and sonic shocks and finally anomalies in the interaction of shock waves.

1 Introduction

The states far upstream and downstream of an isolated shock wave, i.e. the states immediately upstream and downstream of the shock front in the inviscid limit of the equation of fluid dynamics, are related via the well-known Rankine-Hugoniot relations (see, e.g. [1]). In the case of ideal gases with constant specific heats (i.e. for gases at sufficiently high temperatures and low pressures) closed-form expressions for the fluid states on each side of the shock can be obtained. From the qualitative point of view, from these formula it follows that the pressure, density, temperature and entropy increase, while the Mach number decreases, in passing through the shock. A number of discrepancies from this ideal picture of shock waves can be traced back to anomalies, i.e. a *non-ideal* behaviour, in the speed of sound.

To fix ideas, let us focus our attention on a steady supersonic stream having given values of pressure P_A , specific volume v_A and Mach number $M_A \geq 1$, together with the flow direction. An oblique shock brings the flow from the given (pre-shock) state to another state characterised by P_B , v_B , M_B (post-shock state). Assuming that the pressure jump $[P] = P_B - P_A$ is small and $\Gamma = \mathcal{O}(1)$, the Taylor series expansion for the post-shock entropy and Mach number can be written as [2, 3]

$$s_B = s_A + \frac{\Gamma_A}{6T_A} \frac{[P]^3}{\rho_A^3 c_A^4} + \mathcal{O}([P]^4) \quad (1)$$

and

$$\frac{M_B}{M_A} = 1 + \left(1 - \Gamma_A - \frac{1}{M_A^2}\right) \frac{[P]}{\rho_A c_A^2} + \mathcal{O}([P]^2), \quad (2)$$

respectively, where $\rho = 1/v$ is the density, s the specific entropy, T the temperature and $M = \|\mathbf{u}\|/c$, in which \mathbf{u} is the velocity and $c = \sqrt{(\partial P/\partial \rho)_s}$ the speed of sound. The thermodynamic parameter Γ is defined as

$$\Gamma = 1 + \frac{\rho}{c} \left(\frac{\partial c}{\partial \rho} \right)_s \quad (3)$$

and is known as the fundamental derivative of gasdynamics for the special role it plays in many areas of compressible fluid dynamics [4]. If $\Gamma > 1$, which is true for example for ideal gases with constant specific heats ($\Gamma = (\gamma + 1)/2$, where $\gamma > 1$ is the ratio of the specific heats), the speed of sound increases if the substance is compressed isentropically.

By substituting the definition of the speed of sound into the expression for Γ , it is easily seen that if $\Gamma > 0$, the isentropes are convex in the pressure-specific volume plane. For weak shocks ($[P]$ sufficiently small), Eq. (1) shows that, if $\Gamma > 0$, only compression shocks satisfy $s_B \geq s_A$, as required by the second law of thermodynamics. Conversely, if $\Gamma < 0$, expansion shocks are admissible rather than compression shocks. Expansion shocks are an example of *non-classical* shock waves; here the term non-classical indicates the reversed, unconventional character of the shock wave (more in general, the gasdynamics in the regime $\Gamma < 0$ is referred to as non-classical gasdynamics).

Eq. (2) shows that the Mach number does not necessarily decrease across the shock as in perfect gases. Note that the normal Mach number, u_n/c , formed using the velocity component perpendicular to the shock front, instead always decreases across admissible shocks (in accordance with speed ordering stability criterion, see [5]). If $\Gamma < 1$, the speed of sound can decrease across a compression shock and in a sufficient amount to compensate the decrease of the velocity magnitude, resulting in an overall increase of the Mach number. For a weak shock, $M_B > M_A$ is realized if the upstream state is such that $1 - \Gamma - 1/M^2$ is positive. Following the nomenclature introduced by Vimercati et al. [3], we refer to Mach number-increasing shocks as *non-ideal* oblique shocks.

In the present work, the conditions for the formation of non-ideal and non-classical shock waves are reviewed. Finite-amplitude shocks will be considered, i.e. the assumption of weak shocks, used in this section for introduction purposes and useful to delineate existence conditions, is dropped in the following. As a result, specific domains are reported in which the state upstream of the shock must be located in order that any of the aforementioned non-ideal phenomena can be observed. Moreover, selected mechanisms of non-classical shock interaction are discussed.

Thermodynamic states featuring $\Gamma < 1$ can be found in the vapour-liquid equilibrium region in the neighbourhood of the critical point [7] or in the single-phase vapour

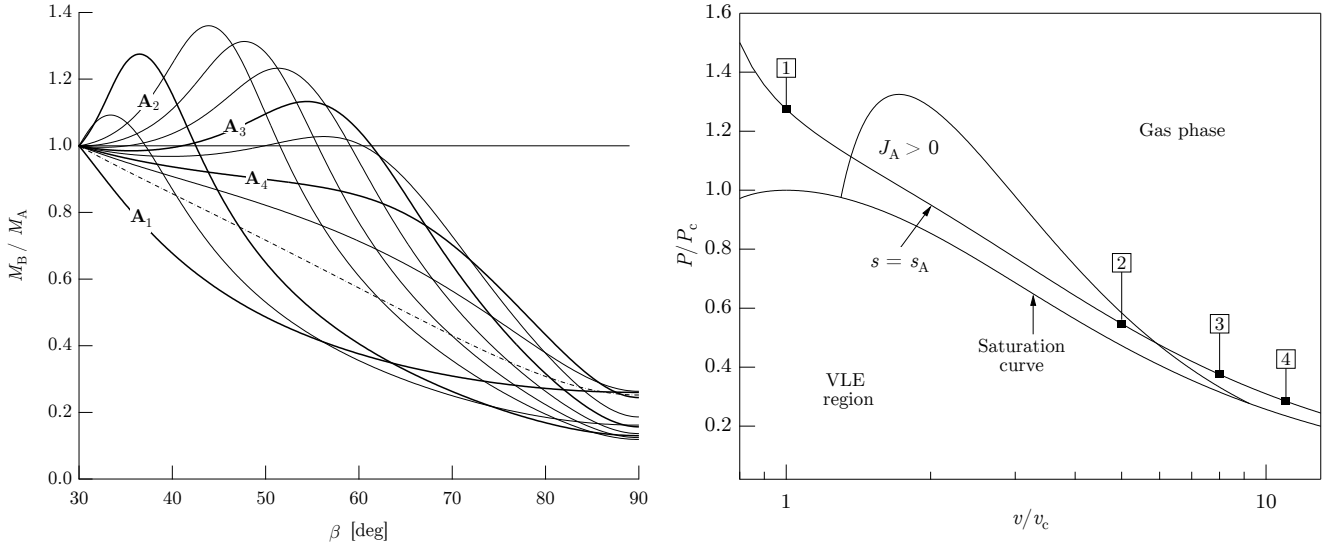


Figure 1: Shock curves for MDM in the post-shock Mach number–shock angle plane (thermodynamic properties from REFPROP [6]). The pre-shock Mach number is fixed to $M_A = 2$. The pre-shock thermodynamic states are selected along the same isentrope $s_A = s(1.2743P_c, v_c)$ crossing the region $J_A > 0$ (subscript c for critical-point quantities). Marked configurations: $v_1 = v_c$, $v_2 = 5v_c$, $v_3 = 8v_c$, $v_4 = 11v_c$. Also shown is the ideal gas limit (dash-dotted curve)

region of molecularly complex fluids, near to the saturation curve and critical point [8]. In this study, the focus is on the latter class of fluids; in particular, when discussing non-classical shock waves, so-called Bethel-Zel’dovich-Thompson fluids or briefly BZT fluids (from the names of the pioneers of this field) are considered.

The structure of this work is as follows. In §2, non-ideal oblique shocks featuring an increase of the Mach number are examined in the classical gasdynamic context. Section §3 presents the non-classical theory of oblique shock waves, within a generalised framework of oblique wave curves (shock polars in the classical context). Possible ways in which non-classical oblique shocks interact producing further non-classical waves are discussed in §4. Section 5 outlines the concluding remarks.

2 Non-ideal oblique shock waves

As the Mach number is a parameter of primary interest in many applications, the potential increase of the Mach number across oblique shock waves is among the most significant shock-related non-ideal effects. Analysis of the isentropic limit of weak compression shock waves (Eq. (2)) demonstrates that oblique shock waves in which the post-shock Mach number is larger than the pre-shock Mach number are indeed admissible if $\Gamma < 1$. In the following we show how non-ideal oblique shocks of finite amplitude arise. For simplicity, the analysis is restricted to fluids exhibiting $\Gamma > 0$ in the gaseous phase. To this end, selected shock parameters are varied, clarifying in particular the role of the pre-shock thermodynamic state at a given pre-shock Mach number. The fluid used in this section for illustrative purposes is MDM (ocatmethyl-trisiloxane, $C_8H_{24}O_2Si_3$), modelled via the REFPROP library [6].

Figure (1) shows the variation of the post-shock Mach number with the shock angle β (i.e. the angle formed by the shock front and the pre-shock flow direction) for a fixed pre-shock Mach number $M_A = 2$ and different pre-shock thermodynamic states selected along the same

isentrope s_A crossing the region $J_A > 0$, where $J = 1 - \Gamma - 1/M^2$ using the notation of Cramer & Best [9]. With the pre-shock Mach number fixed, the locus $J_A = 0$ shown in figure Figure (1) coincides with the isoline $\Gamma = 1 - 1/M_A^2$. Four pre-shock thermodynamic states are now considered, as representative of the possible qualitative evolution of the post-shock Mach number along the shock curve

State A_1 is located at higher densities than those characterising the region $J_A > 0$. In this case, the post-shock Mach number monotonically decreases with increasing shock angle. Exemplary non-monotonic Mach number distributions are those corresponding to pre-shock states A_2 and A_3 in Figure (1). State A_2 is taken as representative of the Mach number evolution for pre-shock states featuring $J_A > 0$. For increasing shock angles starting from $\beta = \sin^{-1}(1/M_A)$, the post-shock Mach number increases. As the magnitude of the tangential velocity decreases (i.e. with increasing shock angle), the post-shock Mach number reaches a local maximum and subsequently decreases towards the subsonic values characterizing strong oblique shocks.

If the pre-shock state exhibits $J_A < 0$, yet the thermodynamic state is selected in the close proximity of the region $J_A > 0$, such as case A_3 shows, the post-shock Mach number features a non-monotonic profile comprising two stationary points. The Mach number initially decreases as required by Eq. (2), but subsequently increases as the post-shock speed of sound decreases enough to compensate the change in the velocity magnitude.

By increasing the pre-shock specific volume along the reference isentrope, the two stationary points found in A_3 -like configurations occur at $M_B < M_A$ and ultimately become coincident. Therefore, any further increase in v_A is such that the post-shock Mach number monotonically decreases with increasing shock angle (despite a somewhat anomalous, non-ideal curvature of the Mach number distribution can be observed close to the region $J_A > 0$).

If the flow conditions resulting in the non-ideal Mach number increase across oblique shocks are collectively

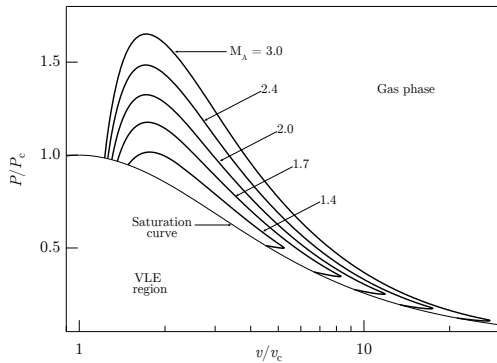


Figure 2: Existence domains of non-ideal oblique shocks in MDM (thermodynamic properties from REFPROP [6]). For a given pre-shock Mach number, the region enclosed between the corresponding locus in the gaseous phase and the saturation curve embeds all the pre-shock thermodynamic states from which non-ideal oblique shocks can occur

considered, a domain of existence of non-ideal oblique shocks in the parameter space of pre-shock thermodynamic states and Mach number can be defined. If the pre-shock state lies in this domain, there exists at least one value of the shock angle leading to $M_B > M_A$. For a given pre-shock Mach number and for each value of the pre-shock entropy, the limit values of the pre-shock pressure or density, that bound the range where the shock curve possibly exhibits $M_B > M_A$ for some values of the shock angle, are computed. These limiting thermodynamic states define a locus embedding the region in which the pre-shock thermodynamic state must be selected (together with the given M_A) in order to observe a non-ideal oblique shock. As the pre-shock Mach number is varied, this procedure determines a one-parameter family of thermodynamic regions embedding all the pre-shock states from which non-ideal oblique shock can possibly occur [3].

Figure (2) reports the existence domain of non-ideal oblique shocks in the pressure-specific volume diagram, for selected pre-shock Mach numbers. Each domain is represented by the region between the saturation curve and the limit curve corresponding to a given Mach number. For the most part, the domain associated with a given value of M_A coincides with the isoline $\Gamma = 1 - 1/M_A^2$ [3]. As a result, the domains are similar in shape to each other and their extension decreases as the pre-shock Mach number decreases. The existence domain of non-ideal oblique shocks shrinks as the pre-shock Mach number approaches the limit value $M_{A,min} = (1 - \Gamma_{min})^{-1/2}$, where Γ_{min} denotes the minimum values of the fundamental derivative in the gaseous phase. For $M_A < M_{A,min}$, non-ideal oblique shocks are not possible.

3 Non-classical oblique shock waves

The most prominent example of non-classical oblique shock waves is undoubtedly the expansion oblique shock as predicted in the weak limit by Eq. (1) if $\Gamma_A < 0$. If finite-amplitude shocks are considered, the possibility that Γ changes sign has interesting consequences not only on expansion shocks, but also on compression shocks, due to the appearance of so-called sonic shocks, i.e. shocks

having normal Mach number $M_n = u_n/c$ equal to 1 in either the pre-shock state (pre-sonic shock) or the post-shock state (post-sonic shock) or both states (double sonic shock) [10].

In contrast to the classical shock theory, in the non-classical context the presence of sonic shocks implies that the shock curves, i.e. the locus of post-shock state that can be connected to a given pre-shock state, may be discontinuous. It is instructive to examine this problem in the framework of the ramp/wedge problem, where a uniform supersonic stream with known properties is suddenly deflected by a ramp/wedge. The problem consists in finding the wave providing the turning of the uniform stream together with its downstream state, for a given ramp angle Θ . The solution set of the ramp problem is known as a wave curve, namely the locus of downstream states that can be connected to the given upstream state by means of wave originating in the corner of the ramp (scale invariance). In the classical gasdynamic context, the compression branch of the wave curve is the well-known shock polar [1]. If BZT fluids are considered, the structure of the wave curves becomes more complicated and exhibit a multitude of configurations.

Figure (3) illustrates the possible structure of non-classical wave curves in the downstream pressure-deflection diagram associated with a ramp/wedge, according to the classification of Vimercati et al. [11] The van der Waals gas model with $c_v/R = 57.69$, where c_v is the isochoric specific heat and R the gas constant, is used in this section. Non-classical shock waves can be found either in the compression or the expansion side of the wave curve. The wave-curve branches comprising non-classical shocks are described in the following.

Case \mathcal{N}_1 features classical oblique shocks for sufficiently small deflections (which implies $\Gamma_A > 0$). Increasing Θ causes the downstream normal Mach number to decrease until a post-sonic oblique shock is formed. To continue the compression, a post-sonic shock followed by an adjacent compression fan centred on the corner of the ramp/wedge is required. The fan is indeed the type of wave that makes the compression of a uniform sonic or supersonic stream possible in the $\Gamma < 0$ regime. As the ramp angle increases, the amplitude of the compression fan increases, until $\Gamma = 0$ at the end of the fan. Compression beyond this point requires the inclusion of another sonic shock, this time with pre-shock sonic state; the overall configuration is denoted as a shock-fan-shock compression wave. With increasing ramp angles, the compression fan becomes weaker and ultimately disappears, thereby recovering the configuration with a single non-sonic oblique shock. Type- \mathcal{N}_2 and type- \mathcal{N}_3 curves are generated if the upstream thermodynamic state is inside the negative- Γ region. As a result, for small deflection angles, an inverted behaviour is observed. For increasing downstream pressures, the compression is first realised by a centred fan, until $\Gamma = 0$ at the downstream state and a pre-sonic oblique shock must be inserted to continue the compression (fan-shock compression wave). The largest compressions are accomplished by conventional oblique shocks; the boundary between these two branches is a pre-sonic shock solution. Given that $\Gamma_A < 0$, non-classical oblique shocks are of course found also in the expansion branch. Here, expansion oblique shocks are observed for the entire range of deflection angles (case \mathcal{N}_2) or for a range of deflection angles only (case \mathcal{N}_3) until $M_n = 1$ on the post-shock state and a fan is required to continue the expansion (shock-fan expansion wave).

Curves \mathcal{N}_4 and \mathcal{N}_5 , for which $\Gamma_A > 0$, include non-

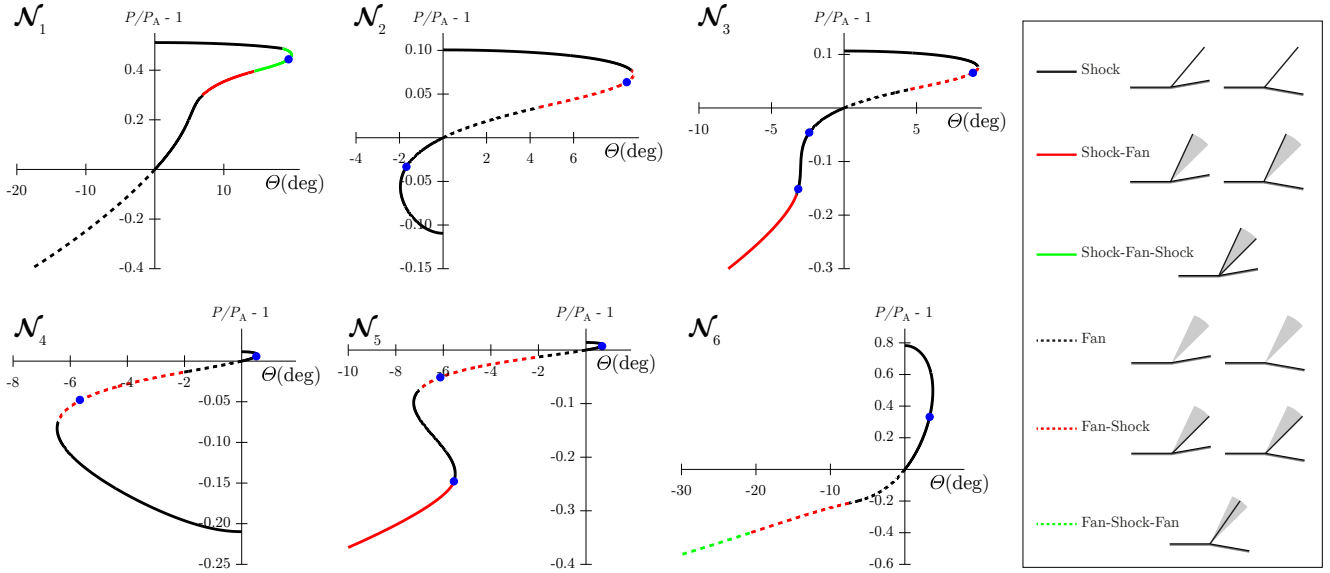


Figure 3: Pressure-deflection diagrams for centred oblique waves in the ramp problem for a van der Waals gas ($c_v/R = 57.69$). The upstream states are all selected along the same isentrope $s_A = s(0.74P_c, 2.5v_c)$; the upstream specific volume and Mach number are (\mathcal{N}_1) $v_A = 2.5v_c$, $M_A = 1.09$; (\mathcal{N}_2) $v_A = 1.3v_c$, $M_A = 1.08$; (\mathcal{N}_3) $v_A = 1.3v_c$, $M_A = 1.1$; (\mathcal{N}_4) $v_A = v_c$, $M_A = 1.08$; (\mathcal{N}_5) $v_A = v_c$, $M_A = 1.1$; (\mathcal{N}_6) $v_A = 0.7v_c$, $M_A = 1.6$. Symbol \bullet for downstream sonic states

classical waves in the expansion branch only. Non-classical shocks are observed after the initial fan reaches the condition $\Gamma = 0$; the expansion is continued by inserting a pre-sonic oblique shock (fan-shock expansion wave). The fan becomes weaker with decreasing ramp angles until it disappears and a single expansion oblique shock provides the deflection. For type- \mathcal{N}_5 curves, the expansion shock ultimately features $M_n = 1$ in the post-shock state and an additional shock-fan expansion wave provides the strongest expansions. Finally, curves of type \mathcal{N}_6 ($\Gamma_A > 0$) are distinguished by the following sequence of oblique waves along the expansion branch, in the order of decreasing downstream pressure: fan, fan-shock, fan-shock-fan. Here the fan-shock-fan waves are characterised by the presence of a double-sonic shock between the two centred fans.

As the choice of the upstream states in Figure (3) demonstrates, for certain upstream thermodynamic states, two different types of wave curves are possible depending on the value of the upstream Mach number. Based instead on the upstream thermodynamic state only, the non-classical wave curves can be grouped as follows: \mathcal{N}_1 , $\mathcal{N}_2/\mathcal{N}_3$, $\mathcal{N}_4/\mathcal{N}_5$, \mathcal{N}_6 . A procedure for determining the transition between each of this groups is detailed by Vimercati et al [11]. It is based on detecting, for any given value of the upstream entropy, limiting values of the pressure or density (for example, the $\Gamma = 0$ locus for the group $\mathcal{N}_2/\mathcal{N}_3$ or the so-called double sonic locus [12] for the transition between the $\mathcal{N}_4/\mathcal{N}_5$ and the \mathcal{N}_6 groups). The result of the procedure is a map, shown in Figure (4) in the $P-v$ plane, of upstream states associated with each type of wave curve. It is seen that the region of upstream thermodynamic states leading to non-classical wave curves is significantly larger than the $\Gamma < 0$ region and covers a wide range of states for which $s_{vle} < s_A < s_\tau$, where s_{vle} and s_τ denote the isentrope tangent to the saturation curve and $\Gamma = 0$ locus, respectively. Outside the non-classical region, only type- \mathcal{C} curves (i.e. the classical wave curves composed of oblique shocks/centred fans in the compression/expansion branch) are generated. For the regions of

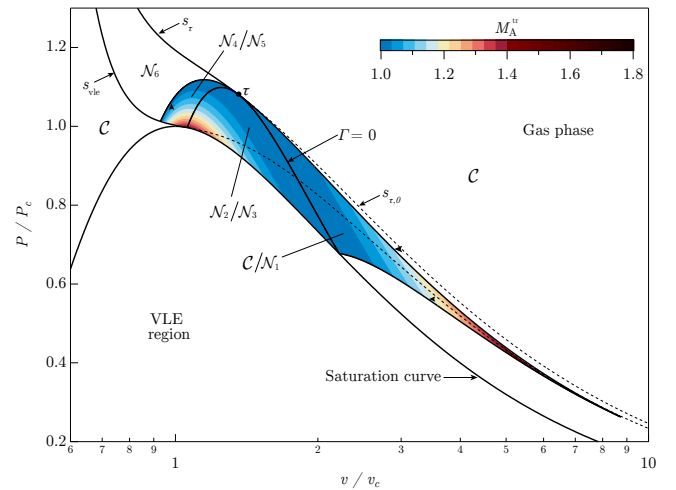


Figure 4: Upstream-state map of the wave curves in the $P-v$ for a van der Waals gas with $c_v/R = 57.69$. Superposed is the value of transitional upstream Mach number for the regions where two different configurations are possible

upstream thermodynamic states where two different configurations are possible, the following holds: type- \mathcal{C} , \mathcal{N}_2 and \mathcal{N}_4 curves occur if $M_A < M_A^{tr}$; \mathcal{N}_1 , \mathcal{N}_3 and \mathcal{N}_5 curves are observed if $M_A > M_A^{tr}$, where M_A^{tr} is the transitional Mach number which depends on the upstream thermodynamic state.

4 Non-classical interactions of oblique shock waves

The existence of non-classical waves for supersonic flow over a ramp/wedge implies that non-classical waves can also be generated by the crossing, overtaking and splitting of compression and expansion oblique shocks. Re-

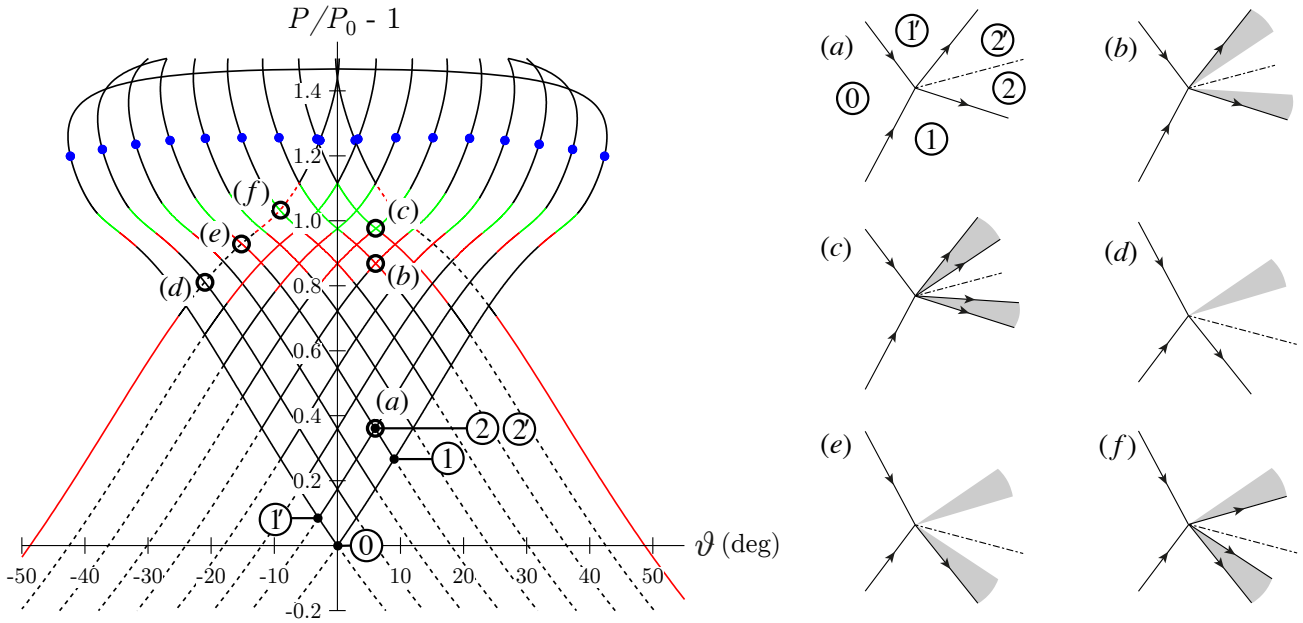


Figure 5: Pressure–deflection diagram for the crossing of compression shocks in a polytropic van der Waals gas ($c_v/R = 57.69$) and schematic illustrations of the cross-node patterns (upstream flow from left to right). Only oblique compression waves are generated in this type of interaction. Upstream state: $P_0 = 0.527P_c$, $v_0 = 4v_c$, $M_0 = 1.5$. Same conventions for the wave curves as in Figure (3)

restricting the analysis to node patterns, i.e. to the immediate neighbourhood of the interaction point in a scale-invariant flow, makes it possible to directly use the wave curves computed for the ramp/wedge problem to predict the outgoing waves of the interaction, for a given couple of incoming shock waves. This is the classical method of the wave curves [13], which we apply here to non-classical flow solutions. A detailed analysis of shock interactions in BZT fluids can be found in [14]; in this section some of the most relevant configurations are discussed.

Figure (5) shows a pressure–deflection diagram for a cross-node (two shocks travelling in opposite directions collide) in the same van der Waals gas used in the previous section. Two incident wave curves (one for each propagation direction of the incoming shocks) and a number of reflected wave curves (i.e. computed from the state immediately downstream of an incident wave) are reported. As an example, two shocks travelling in a uniform supersonic stream (state 0) result in state 1 and 1' of the flow. In order to turn the flow to a final common direction, two additional shocks are generated, which cause a further jump to states 2 and 2' separated by a contact discontinuity. The outgoing wave are determined by the intersection of the reflected wave curves, as the pressure and flow direction must match across the contact discontinuity emanating from the node.

In Figure (5), both incident shocks are compression shocks; as the graphical analysis shows, only compression waves can be generated in this type of interaction. Case *a* depicts the typical configuration of a cross node in classical gasdynamics. Two incident compression shocks produce two outgoing shocks with a slip line in between. By increasing the strength of the incident shocks, the intersection of the reflected wave curves occurs along the non-classical branches, implying that non-classical outgoing waves can be observed. Cases *b* and *c* are two such examples, which involve outgoing shock-fan and shock-fan-shock waves, respectively. Qualitative changes in the wave-structure across the incoming shocks are also possible, see cases *d-f*, further confirming that a wide variety

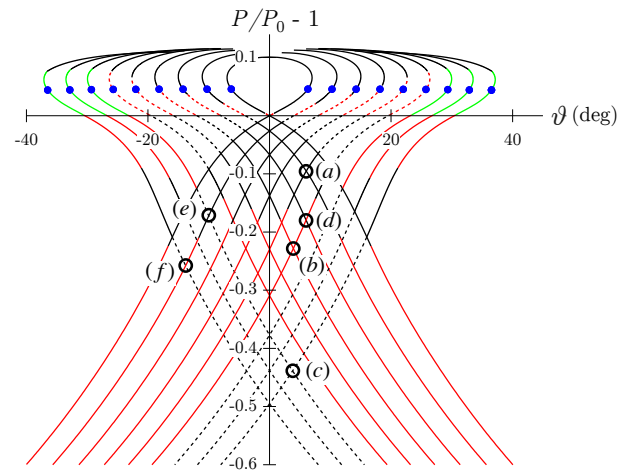


Figure 6: Pressure–deflection diagram for the crossing of expansion shocks in a polytropic van der Waals gas ($c_v/R = 57.69$) and schematic illustrations of the cross-node patterns (upstream flow from left to right). Only oblique expansion waves are generated in this type of interaction. Upstream state: $P_0 = 1.032P_c$, $v_0 = 1.1v_c$, $M_0 = 1.5$. Same conventions for the wave curves as in Figure (3)

of interaction patterns is to be expected in BZT fluid flows.

The crossing of expansion shocks is illustrated in Figure (6). Here, only expansion waves can be generated at the node. For relatively small pressure jumps across the incident shocks, it is seen that the interaction produces outgoing expansion shocks (case *a*). However, for larger pressure jumps more complicated configurations are necessary, such as a couple of expansion shock-fan waves (*b*) or pure fans (*c*). As for the case of compression shocks, transitions in the wave-curve structure play an important role and allow for the combination of expansion shock and shock-fan wave (*d*), shock and pure fan (*e*), fan and shock-fan wave (*f*) to be generated at the cross-node.

It should also be noticed that for a perfectly symmetric incident shock configuration, the outgoing wave pattern is also symmetric and the velocity and entropy jumps across the slip line vanish. Therefore, the flow configuration in each of the half planes about the symmetry axis is identical to that of a regular reflection.

5 Conclusions

Oblique shocks in the regime $\Gamma < 1$ may exhibit significant differences compared to oblique shocks in the ideal-gas regime, due to the peculiar variation of the speed of sound along the shock adiabat. Two classes of oblique shocks in single-phase gases were reviewed in this work.

Firstly, non-ideal oblique shocks, for which the Mach number increases from the pre-shock to the post-shock state, were investigated for thermodynamic states in the range $0 < \Gamma < 1$. In order to observe non-ideal oblique shocks, it is necessary that $1 - \Gamma - 1/M^2 > 0$ either in the pre-shock state or along the shock curve.

Next, non-classical oblique shock occurring the mixed regime where Γ can be either positive or negative were studied. The prototypical problem of a supersonic flow over a ramp/wedge served as a framework for the generalisation of the classical theory of the wave curves to the non-classical context. Non-classical oblique shocks, which include expansion shocks and sonic shocks (these can be both compression and expansion shocks), characterise the branches of the wave curves crossing the $\Gamma < 0$ region. Non-classical wave curves can be classified into six configurations and are expected to occur for a wide range of state located along isentropes crossing the negative- Γ region.

Finally, on the basis of the wave-curve analysis, interactions of oblique shocks in the cross-node configuration were analysed. It was shown that the collision of oblique compression shocks travelling in the opposite directions can easily generate non-classical sonic shocks and that the collision of oblique expansion shocks in most situations produces other expansion shocks.

Acknowledgment

This research is supported by ERC Consolidator Grant N. 617603, Project NSHOCK, funded under the FP7-IDEAS-ERC scheme.

References

- [1] P. A. Thompson, *Compressible Fluid Dynamics*. McGraw-Hill, 1988.
- [2] H. A. Bethe, “The theory of shock waves for an arbitrary equation of state,” Technical paper 545, Office Sci. Res. & Dev., 1942.
- [3] D. Vimercati, G. Gori, and A. Guardone, “Non-ideal oblique shock waves,” *J. Fluid Mech.*, vol. 847, pp. 266–285, 2018.
- [4] P. A. Thompson, “A fundamental derivative in gas-dynamics,” *Phys. Fluids*, vol. 14, no. 9, pp. 1843–1849, 1971.
- [5] P. D. Lax, “Hyperbolic systems of conservation laws II,” *Commun. Pur. Appl. Math.*, vol. 10, no. 4, pp. 537–566, 1957.
- [6] E. W. Lemmon, M. L. Huber, and M. O. McLinden, “NIST reference database 23: reference fluid thermodynamic and transport properties—REFPROP, version 9.1,” *Standard Reference Data Program*, 2013.
- [7] N. R. Nannan, C. Sirianni, T. Mathijssen, A. Guardone, and P. Colonna, “The admissibility domain of rarefaction shock waves in the near-critical vapour-liquid equilibrium region of pure typical fluids,” *J. Fluid Mech.*, vol. 795, pp. 241–261, 5 2016.
- [8] P. Colonna and A. Guardone, “Molecular interpretation of nonclassical gasdynamics of dense vapors under the van der Waals model,” *Phys. Fluids*, vol. 18, no. 5, pp. 056101–1–14, 2006.
- [9] M. S. Cramer and L. M. Best, “Steady, isentropic flows of dense gases,” *Phys. Fluids A*, vol. 3, no. 4, pp. 219–226, 1991.
- [10] A. Kluwick, “Rarefaction shocks,” in *Handbook of Shock Waves* (G. Ben-Dor, O. Igra, and T. Elperin, eds.), pp. 339–411, Academic Press, 2001.
- [11] D. Vimercati, A. Kluwick, and A. Guardone, “Oblique waves in steady supersonic flows of Bethe-Zeldovich-Thompson fluids,” *J. Fluid Mech.*, vol. 855, pp. 445–468, 2018.
- [12] C. Zamfirescu, A. Guardone, and P. Colonna, “Admissibility region for rarefaction shock waves in dense gases,” *J. Fluid Mech.*, vol. 599, pp. 363–381, March 2008.
- [13] J. Glimm, C. Klingenberg, O. McBryan, B. Plohr, D. Sharp, and S. Yaniv, “Front tracking and two-dimensional Riemann problems,” *Advances in Applied Mathematics*, vol. 6, no. 3, pp. 259–290, 1985.
- [14] D. Vimercati, A. Kluwick, and A. Guardone, “Shock interactions in two-dimensional steady flows of Bethe-Zeldovich-Thompson fluids,” *J. Fluid Mech.*, vol. 887, 2020.

BOUNDARY LAYER STABILITY, SCALING METHODS AND MODELLING OF TURBULENCE IN SUPERCRITICAL FLUIDS

R. Pecnik¹, J. Ren² and G.J. Otero-R.¹

¹*Delft University of Technology, Leeghwaterstraat 39, 2628 CB Delft, The Netherlands*

²*University of Nottingham, University Park, Nottingham, NG7 2RD, UK*

Abstract

From concentrated solar power plants to rocket engines, energy conversion systems are continually re-engineered to perform ever better. Often this involves fluids being pushed into the supercritical region, where highly non-ideal thermodynamic effects are at play. Yet, our fundamental understanding of flow physics at such conditions lags behind to successfully realise these exciting engineering applications. In this work we summarise our latest work on boundary layer stability and on scaling and modelling turbulent flows with non-ideal fluids. We highlight how complex thermophysical properties in the vicinity of the critical point affect the stability of an adiabatic flow over a flat plate and how fully turbulent flows can be characterised and modeled using the semi-local scaling framework we recently developed. At the end of the paper we will provide an outlook to future research directions.

1 Introduction

The continuous demand to increase the efficiency of energy conversion systems and the productivity of process plants forces engineers and scientists to use fluids at increasingly higher pressures and temperatures. For instance, to increase the thermal efficiency of power plants, engineers are currently developing a thermodynamic power cycle that operates with carbon dioxide in the supercritical region, at pressures and temperatures high enough to exceed the critical point where fluids behave in a highly non-ideal way. Such a power cycle has the potential to enable a break-through of cost-competitive, utility-scale solar thermal power plants. Another example where pressures and temperatures of fluids continuously increase is in the development of more powerful rocket engines. The idea of engineers is to use rocket fuels at supercritical conditions not only to increase fuel mixing with the oxidizer but also to cool the rocket engine using the fuel before it is injected into the combustion chamber. While cooling the rocket nozzle, the fuel is heated from initially cryogenic conditions into the supercritical region. The net result is a rocket engine that provides higher specific thrust, enabling space access with increasingly higher payloads.

One of the major obstacles in successfully realizing these technologies is the limited knowledge of turbulence in the supercritical fluid region, especially when flows are heated or cooled across the Widom line (see black dotted line in Figure (1)) in the supercritical region. The sharp variations in all thermophysical properties in the vicinity of the Widom line lead to significantly richer flow physics and even more intricate phenomena in turbulence.

In this paper we will discuss three topics related to flows in the supercritical fluid region. In the first topic we

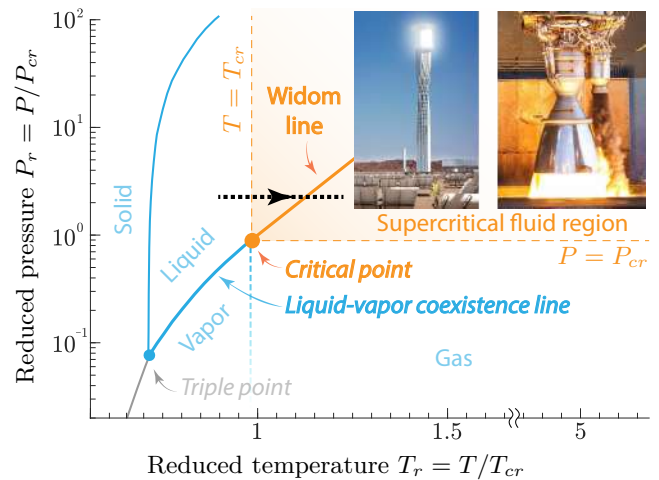


Figure 1: Pressure – temperature phase diagram of an arbitrary substance indicating the thermodynamic critical point and the supercritical fluid region. P_{cr} and T_{cr} are critical pressure and temperature, respectively. Two applications are shown which will operate in the supercritical regime

will discuss boundary layer instability with fluids in the vicinity of the critical point, where we will identify the range of disturbances to which a given laminar base flow is unstable and how these instabilities can trigger the development of turbulence. In the second topic we will discuss how fully developed turbulent flows with highly non-ideal fluids can distinctively be characterized by the semi-local Reynolds number and a scaling approach we proposed recently in Ref. [1]. In the third topic we will show how this scaling approach can be used to properly sensitize common turbulence models to account for the “leading-order effect” of variable properties on wall bounded turbulence.

Boundary layer stability In general, hydrodynamic stability analysis aims at identifying the range of disturbances to which a given laminar base flow is unstable and how these instabilities can trigger the development of turbulence. The current view is that a decreasing viscosity towards a wall stabilizes the flow [2], while fluid compressibility significantly enriches the physics of hydrodynamic stability [3]. For example, Mack [4] showed that transition in compressible high-speed boundary layers with ideal gases can be triggered by trapped acoustic waves, which exceed the growth rate of the viscous mode around a free stream Mach number of 4. How non-ideal gas effects modify the hydrodynamic stability of a boundary layer is yet unknown.

Fully developed turbulent flows In this regard, we recently achieved a major breakthrough, which nicely exemplifies how simple ideas can lead to significant discov-

eries. Generally, if an ideal gas is heated, the viscosity increases and the density decreases. How these changes affect turbulent heat transfer has captivated fluid dynamicists for decades, especially when they have to predict heat transfer to prevent devices from catastrophic failure. In contrast to past research, we asked a seemingly simple question: “how is turbulent heat transfer affected if only the density of a fluid changes with temperature and viscosity remains constant?” Such a fluid does not exist in reality, but using large-scale computer simulations of several *hypothetical* fluids, enabled us to develop a scaling law that now allows to predict heat transfer to liquids and ideal gases, irrespectively if they are heated or cooled. Pecnik & Patel [1] derived an alternative formulation of the turbulent kinetic energy equation using semi-local quantities. Using this approach, it is then possible to quantify turbulence modulation related to density and viscosity stratifications using the semi-local Reynolds number. Recently, Kawai [5] performed DNSs on supercritical turbulent boundary-layer flow with transcritical temperature, and showed that the turbulent mass flux terms in the turbulent kinetic energy equation largely exceed values as observed for ideal gas at the same free-stream Mach numbers. Hence, in turbulence with large density fluctuations this terms has to be accounted for when modelling wall bounded turbulent flows.

Turbulence modelling Turbulence plays a vital role in heat transfer and skin friction across the boundary layer in wall bounded flows. For engineers, it is therefore of paramount importance to accurately model turbulence during the design process of any flow guiding devices, such as heat exchangers with strongly cooled or heated flows, rocket propulsion systems, combustion chambers with chemically reacting flows, or turbomachinery flows with unconventional working fluids. In all these applications, strong heat transfer causes large temperature gradients and consequently large variations in density, viscosity, thermal conductivity, heat capacity, etc., which alter the conventional behavior of turbulence. Despite decades of research, turbulent flows with variable thermophysical properties are still far from being understood. Accordingly, turbulence models for engineering applications with large heat transfer rates are not able to provide accurate results for Nusselt numbers, pressure losses, or any other quantities of interest.

2 Transition to turbulence

Most of the present knowledge on stability and laminar-turbulent transition is limited to ideal gases [3] or incompressible flows, where thermodynamic properties are constant. On the other hand, numerical simulations of real gas effects (high-temperature chemical effects) in hypersonic flows has just gone through an initial stage [6, 7, 8]. These effects, often referred to as real-gas effects, include vibrational excitation, dissociation and recombination of gas species, ionization, radiation and surface ablation. Apart from the high-temperature chemical effects, stratifications in thermodynamic or/and transport properties can substantially influence the stability (see review by Govindarajan & Sahu [9], and references therein). These stratifications exist both naturally (e.g. in the Earth’s outer core) and artificially (e.g. exert wall heating/cooling), revealing some of the non-ideal-gas effects.

We recently investigated the stability of boundary layer flows with fluids close to the critical point [10], through linear stability theory [11], direct numerical simulation and inviscid analysis. To account for the full non-

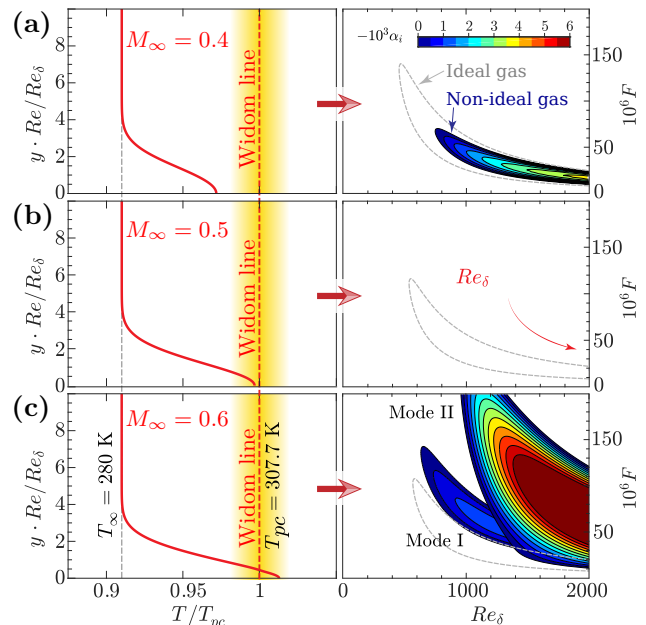


Figure 2: Boundary layer temperature profiles (left column) and corresponding neutral stability curves as function of Reynolds number, Re_δ , and perturbation frequency, F , (right column) for cases with increasing free stream Mach number ($M_\infty = [0.4, 0.5, 0.6]$). The equivalent ideal gas solution is shown in gray to highlight differences. The wall is adiabatic and the free stream temperature is at 280 K

ideal gas effects, one must take the non-ideal equation-of-state into consideration as well as the complicated functions of thermodynamic/transport properties in terms of its thermodynamic state, which can be determined by two independent thermodynamic quantities (such as density and internal energy). We study boundary layer flows with carbon dioxide (CO_2) at a constant pressure of 80 bar, which is above the critical pressure (73.9 bar). The flow conditions are such chosen that different thermodynamic regimes of interests shall be well revealed.

If a fluid at constant supercritical pressure is heated, such that the Widom line is crossed (see black dotted line in Figure (1)), highly non-ideal effects are at play. In the vicinity of the Widom line, which is an extension of the liquid-vapor coexistence line into the supercritical fluid regime (see solid orange line in Figure (1)), a seemingly continuous phase transition from a compressible liquid to a dense vapor occurs with large changes in all thermophysical properties [12, 13, 14]. As the temperature at the wall increases towards the Widom line (due to viscous heating), the stability of the flow increases significantly (see neutral stability curves in the right column of Figure (2) (a,b) for two different Mach numbers). By crossing the Widom line, Figure (2)(c), a novel and peculiar second mode (Mode II) appears which overlaps with Mode I. Until now, such a phenomenon has not been observed and further research is required to unveil this intriguing mechanisms using advanced theory, comprehensive simulations and novel experiments.

To characterise the boundary layer flow we use the Reynolds number, Re_∞ , Prandtl number, Pr_∞ , Eckert number, Ec_∞ and the Mach number, Ma_∞ (all based on freestream parameters) which are given as:

$$Re_\infty = \frac{\rho_\infty^* u_\infty^* l_0^*}{\mu_\infty^*}, \quad Pr_\infty = \frac{\mu_\infty^* C_{p\infty}^*}{\kappa_\infty^*},$$

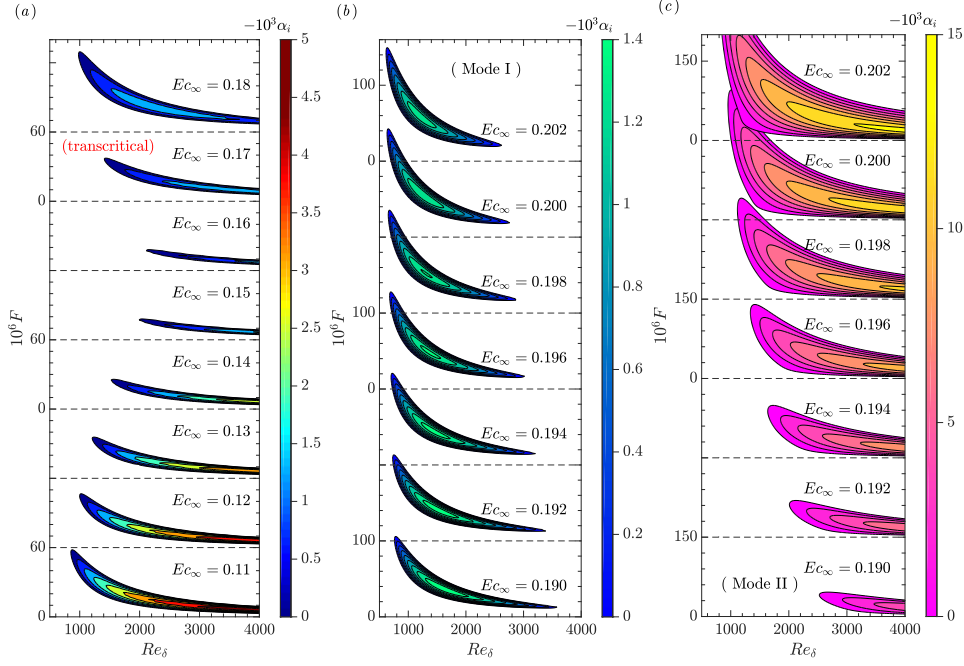


Figure 3: Growth rates of perturbations in the $F - Re_\delta$ stability diagram with $T_\infty^* = 280$ K. (a) $Ec_\infty = 0.11, 0.12, \dots, 0.19$, (b) $Ec_\infty = 0.194, 0.196, \dots, 0.202$ (Mode I), (c) $Ec_\infty = 0.190, 0.192, \dots, 0.202$ (Mode II)

$$Ec_\infty = \frac{u_\infty^{*2}}{C_{p\infty}^* T_\infty^*}, \quad Ma_\infty = \frac{u_\infty^*}{a_\infty^*}. \quad (1)$$

The subscript ∞ denotes freestream values, superscript $*$ stands for dimensional variables, l_0^* is a chosen length scale, a_∞^* is the speed of sound in the freestream. Note that for an ideal gas $Ec_\infty = (\gamma - 1)Ma_\infty^2$, where γ is the heat capacity ratio. In linear stability theory, l_0^* is chosen to be the local boundary layer thickness scale δ^* , which results in the definition of Re_δ :

$$\delta^* = \left(\frac{\mu_\infty^* x^*}{\rho_\infty^* u_\infty^*} \right)^{1/2},$$

$$Re_\delta = \frac{\rho_\infty^* u_\infty^* \delta^*}{\mu_\infty^*} = \left(\frac{\rho_\infty^* u_\infty^* x^*}{\mu_\infty^*} \right)^{1/2}. \quad (2)$$

Besides the known stabilization of compressibility effects (increase Ec_∞), the boundary layer flow is further stabilized by non-ideal gas effects in the subcritical or supercritical regime. In either regime, the temperature profile remains below or above T_{pc}^* , the stabilization is more prominent when T_∞^* is closer to T_{pc}^* and/or Ec_∞ is increased.

The most interesting results lie in the transcritical regime, where the temperature profile crosses the pseudo-critical point ($T_{pc} = 307.7$ K). We show in Figure (3) a detailed evolution of the growth rate with $T_\infty = 280$ K by gradually increasing the Eckert number afrom $Ec_\infty = 0.11$ to $Ec_\infty = 0.202$, such that the insulated wall temperature increases. Figure (3)(a,b) shows the neutral curve of Mode I, while in Figure (3)(c) we show Mode II that becomes unstable at $Ec_\infty \geq 0.19$. It appears that the maximum critical Reynolds number Re_δ occurs at $Ec_\infty = 0.16$. The flow enters the transcritical regime (the temperature crosses the pseudo-critical point) at $Ec_\infty \geq 0.17$, and the growth rate and the extent of the neutral curve of Mode I again increases. Figure (3)(b) shows the evolution of Mode I in the transcritical regime. With an increase in Ec_∞ , the range of

unstable Re_δ decreases, while the range for unstable F increases. Most noteworthy is the growth rate of Mode II, which increases much faster with Ec_∞ and becomes much larger than Mode I. This indicates that the flow in the transcritical regime is significantly destabilized by non-ideal gas effects through Mode II.

The inviscid analysis shows that in the transcritical regime, Mode II is not caused by the trapped acoustic waves which is deemed to give rise to higher modes in hypersonic flows. We show that the generalized inflection point criterion, derived in [15], expressed in density $D(\rho_0 D U_0)$ is also valid for non-ideal gases. As result, an inviscid mechanism is present in the trans- and supercritical regimes in contrast to the subcritical regime which contains the viscous instability only.

3 Fully turbulent flows

Figure (4) shows three turbulent channel flow simulations using DNS. The fluid is volumetrically heated, while the temperature at the wall is kept at a constant value. Different constitutive relations for density, ρ , and viscosity, μ , as a function of temperature, T , were used. The case Re_τ^* (figure (a)) corresponds to a flow for which density and viscosity are decreasing away from the wall, such that the semi-local Reynolds number Re_τ^* is constant across the whole channel height. The semi-local Reynolds number is defined as

$$Re_\tau^* \equiv \frac{\sqrt{\langle \rho \rangle} / \rho_w}{\langle \mu \rangle / \mu_w} Re_\tau, \quad (3)$$

where $\langle \cdot \rangle$ denotes Reynolds averaging, the subscript w indicates quantities at the isothermal wall (no averaging at the wall is required), $Re_\tau = \rho_w u_{\tau w} h / \mu_w$ is the friction Reynolds number based on friction velocity, $u_{\tau w}$, and a characteristic length, h . Although this case has arbitrary thermophysical properties, it is worthwhile to mention that it bears similarities to supercritical fluids, for which both density and viscosity decrease when heated across

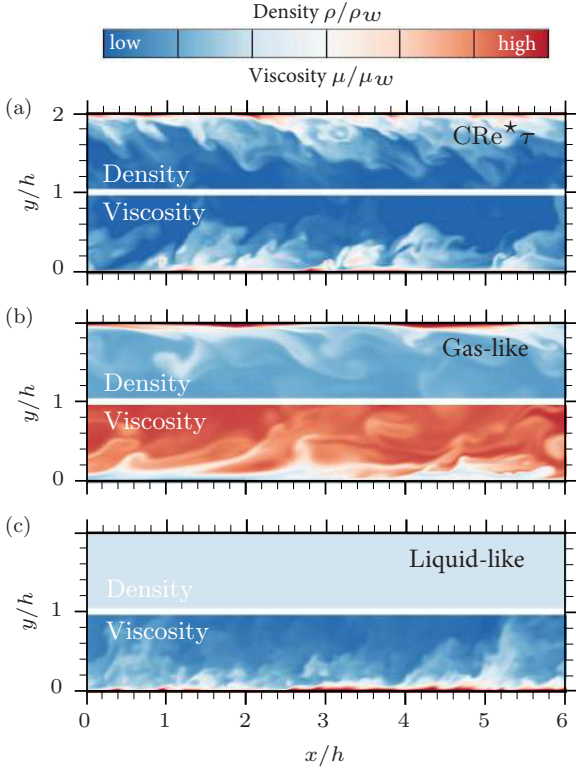


Figure 4: Contour plots of instantaneous density ρ (top half) and dynamic viscosity μ (lower half) for cases CRe_τ^* (a), Gas-like (b), and Liquid-like (c)

the pseudo-critical temperature [16, 17]. The cases GL and LL (figure (b) and (c)) are flows with gas-like and liquid-like property variations that both have large gradients in Re_τ^* . More details on the governing equations, the numerical scheme and the DNS cases can be found in [1].

The streamwise velocity profiles are shown in Figure (5). Note, the van Driest velocity transformation (left figure), which is defined as $u^{vD} = \int \sqrt{\langle \rho \rangle / \rho_w} d(\langle u \rangle / u_{\tau_w})$, is not capable to provide a collapse for the velocity profiles of these three DNS cases. On the other hand, the velocity scaling as proposed by [18], and later independently derived by [19], provides a good collapse for all cases (right figure). The u^* -velocity scaling based on the semi-local Reynolds number is ex-

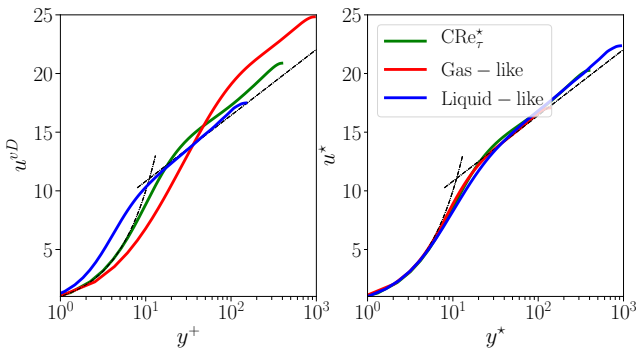


Figure 5: Contour plots of instantaneous density ρ (top half) and dynamic viscosity μ (lower half) for cases CRe_τ^* (a), Gas-like (b), and Liquid-like (c)

pressed as,

$$u^* = \int_0^{\bar{u}^{vD}} \left(1 + \frac{y}{Re_\tau^*} \frac{dRe_\tau^*}{dy} \right) d\langle u^{vD} \rangle. \quad (4)$$

This transformation has been obtained by scaling the Navier-Stokes equation using semi-local scales, which is the key to account for the leading-order effect of variation in thermophysical properties on turbulence. This semi-local scaling approach provides a framework to collapse other turbulence properties as well and consequently provides insight to properly models turbulence as discussed in the next section.

4 Turbulence Modeling

Common turbulence models for solving the Reynolds-averaged Navier-Stokes (RANS) equations do not correctly account for variations in thermodynamic/transport properties, such as density and viscosity, which can cause substantial inaccuracies in predicting important quantities of interest, for example, heat transfer and drag. RANS equations with simple extensions of eddy viscosity models (EVM) are currently used to predict turbulence in supercritical fluids. For example, if the turbulent kinetic energy (TKE) equation is derived on the basis of the compressible Navier-Stokes equations, additional terms appear, i.e. pressure-work and -dilatation, dilatational dissipation, and additional terms related to fluctuations of density, velocity, pressure, etc. The modification of the TKE in flows with strong heat transfer has been attributed to these terms and according models have been proposed in the past [20, 21, 22]. A different approach to sensitize turbulence models for compressible flows with large density variations, was proposed by Catris and Aupoix [23]. They used the formulation developed by Huang *et al.* [24] for the closure coefficients, to modify the diffusion term of the turbulent dissipation transport equation. Additionally, they argued that the diffusion of TKE acts upon the energy per unit volume [$(kg \ m^2/s^2)/m^3$] of turbulent fluctuations, which can be expressed as ρk . The diffusion of TKE is therefore based on ρk , while the diffusion coefficient is divided by the density on the basis of dimensional consistency.

Based on the semi-locally scaled turbulent kinetic energy equation, introduced in [1], we analytically derive a modification of the diffusion term of turbulent scalar equations to improve the prediction of eddy viscosity models for wall-bounded turbulent flows with strong gradients in the thermo-physical properties. The modifications are based on the fact that the “leading-order effect” of variable properties on wall bounded turbulence can be characterized by the semi-local Reynolds number only [19]. For instance, the modified TKE equation reads (averaging operators omitted),

$$\frac{\partial \rho k}{\partial t} + \frac{\partial \rho k u_j}{\partial x_j} = P_k - \rho \varepsilon + \frac{1}{\sqrt{\rho}} \frac{\partial}{\partial x_j} \left[\frac{1}{\sqrt{\rho}} \left(\mu + \frac{\mu_t}{\sigma_k} \right) \frac{\partial \rho k}{\partial x_j} \right]. \quad (5)$$

If compared to the conventional model for the TKE, the newly derived equation shows only one major difference that lies in the diffusion term. The diffusion term that emerges from the semi-local scaling methodology is a function of ρk (instead of k), while the diffusion coefficient and the overall diffusion term are divided by

$\sqrt{\rho}$. This is similar to the density corrections proposed by [23], except that in [23], only the diffusion coefficient is divided by ρ .

The developed methodology is generic and applicable to a wide range of eddy viscosity models. We have applied the same methodology to several turbulent scalars (ε , ω , among others) of common eddy viscosity models: the eddy viscosity correlation of Cess [25], the one-equation model of Spalart Allmaras (SA) [26], the low Reynolds number $k - \varepsilon$ model of Myong and Kasagi (MK) [27], Menter's shear stress transport model (SST) [28], and the four-equations $v^2 - f$ model (V2F) [29]. An additional modification we have introduced is to replace y^+ and Re_τ , e.g. within the eddy viscosity correlation of Cess and for the damping function of the MK turbulence model, by their semi-local counterparts, namely y^* and Re_τ^* [1].

We have tested the EVM to available direct numerical simulations (DNS) of volumetrically heated fully developed turbulent channel flows with varying thermo-physical properties which have been introduced earlier. The density and the viscosity are a function of temperature and different constitutive relations are used, that resemble behaviours of liquids (LL), gases (GL), supersonic fluids (SS), and fluids close to the vapour-critical point (CRe_τ^*).

The results are reported in Figure (6) in terms of u^* (see equation (4)) and u^{vD} , which is the van Driest velocity transformation. The modifications clearly improve the EVM for flows with strong variations on the thermo-physical properties. A substantial improvement is seen in Cess and the MK model; the damping function of these modified models is able to correctly account for variations of transport properties. Interestingly, the original SA model, originally developed for external flow, gives the most reliable results, with respect to other conventional EVM, for the cases studied. For the modified SST model, the performance with respect to the universal law of the wall is not satisfactory. The modified V2F formulation improves the collapse with the DNS data if compared to the conventional form for all the cases. For the profile of u^* , a good collapse is seen with the DNS data for most of the modified EVM, outperforming the original models.

5 Conclusion

Several conclusions can be drawn on the topics discussed in this paper, which are separately discussed hereafter.

Boundary layer stability The compressibility effects close to the critical point strongly stabilise the boundary layer. Using modal stability analysis we showed that for conditions where the free-stream temperature is below the pseudo-critical point, the maximum boundary layer stabilisation is achieved when the temperature at the wall increase towards the Widom line. Once the temperature at the wall crosses the Widom line, due to an increase in Mach number, a novel instability mode appears. The growth rate of this mode increases much faster with Ec_∞ and becomes much larger than Mode I. This indicates that the flow in the transcritical regime is significantly destabilised by non-ideal gas effects.

Fully developed turbulent flows We have recently derived a simple scaling transformation of the Navier-Stokes equations using semi-local quantities, which allows to account for the "leading order effect" of variable properties on turbulence. One outcome of this approach

is a velocity transformation that allows to collapse velocity profiles for channel flows with arbitrary variations in density and viscosity.

Turbulence modelling Based on the semi-local scaling framework we have also derived a novel methodology to improve eddy viscosity models for predicting wall-bounded turbulent flows with strong variations in thermo-physical properties. The major difference of the new methodology is the formulation of the diffusion term in the turbulence scalar equations. The conclusion is that the diffusion of turbulent kinetic energy acts upon the energy per unit volume and not per unit mass. In general, the modified EVMs result in a much better agreement with the DNS data in terms of velocity profiles and heat transfer of fully developed turbulent channel flows with variable property fluids. The next step in modelling turbulence should focus on effects related to very large density fluctuations (larger than the ones considered herein) and to turbulence deterioration emerging from flow acceleration and buoyancy forces.

References

- [1] R. Pecnik and A. Patel, "Scaling and modelling of turbulence in variable property channel flows," *Journal of Fluid Mechanics*, vol. 823, no. R1, 2017.
- [2] A. Sameen and R. Govindarajan, "The effect of wall heating on instability of channel flow," *Journal of Fluid Mechanics*, vol. 577, pp. 417–442, 2007.
- [3] A. Fedorov, "Transition and stability of high-speed boundary layers," *Annual Review of Fluid Mechanics*, vol. 43, no. 1, pp. 79–95, 2011.
- [4] L. M. Mack, "Boundary-layer linear stability theory," in *AGARD Report No. 709 Special Course on Stability and Transition of Laminar Flow*, 1984.
- [5] S. Kawai, "Direct numerical simulation of transcritical turbulent boundary layers at supercritical pressures with strong real fluid effects," in *54th AIAA Aerospace Sciences Meeting*, p. 1934, 2016.
- [6] X. Zhong and X. Wang, "Direct numerical simulation on the receptivity, instability, and transition of hypersonic boundary layers," *Annual Review of Fluid Mechanics*, vol. 44, no. 1, pp. 527–561, 2012.
- [7] O. Marxen, T. E. Magin, E. S. Shaqfeh, and G. Iaccarino, "A method for the direct numerical simulation of hypersonic boundary-layer instability with finite-rate chemistry," *Journal of Computational Physics*, vol. 255, pp. 572–589, 2013.
- [8] O. Marxen, G. Iaccarino, and T. E. Magin, "Direct numerical simulations of hypersonic boundary-layer transition with finite-rate chemistry," *Journal of Fluid Mechanics*, vol. 755, pp. 35–49, 2014.
- [9] R. Govindarajan and K. C. Sahu, "Instabilities in viscosity-stratified flow," *Annual Review of Fluid Mechanics*, vol. 46, pp. 331–353, 2014.
- [10] J. Ren, O. Marxen, and R. Pecnik, "Boundary-layer stability of supercritical fluids in the vicinity of the widom line," *Journal of Fluid Mechanics*, vol. 871, pp. 831–864, 2019.
- [11] J. Ren, S. Fu, and R. Pecnik, "Linear instability of poiseuille flows with highly non-ideal fluids," *Journal of Fluid Mechanics*, vol. 859, pp. 89–125, 2019.

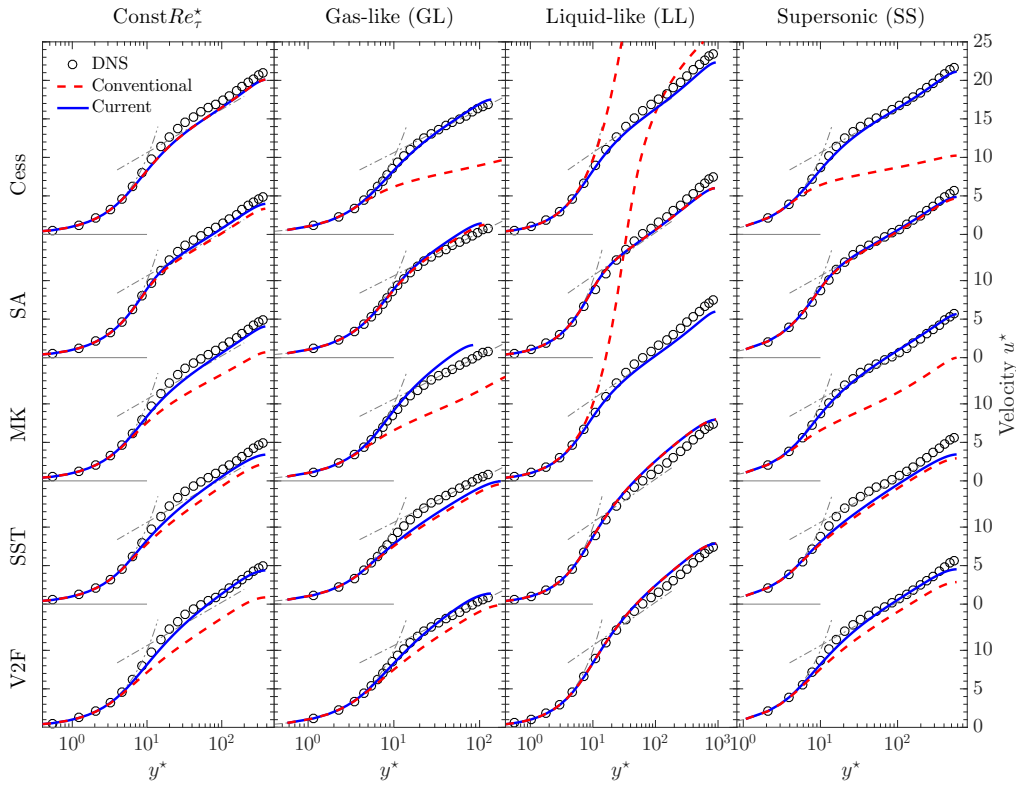


Figure 6: Universal velocity transformation u^* with respect to the semi-locally scaled wall normal distance y^* for a fully developed turbulent channel. The grey dashed lines represent $u^* = y^*$ and $u^* = 1/\kappa \ln(y^*) + C$, the viscous sublayer and log-law region, respectively, where $C = 5.5$

- [12] G. G. Simeoni, T. Bryk, F. A. Gorelli, M. Krisch, G. Ruocco, M. Santoro, and T. Scopigno, “The Widom line as the crossover between liquid-like and gas-like behaviour in supercritical fluids,” *Nature Physics*, vol. 6, pp. 503–507, 2010.
- [13] D. Bolmatov, V. V. Brazhkin, and K. Trachenko, “Thermodynamic behaviour of supercritical matter,” *Nature Communications*, vol. 4, pp. 1–7, 2013.
- [14] D. Banuti, “Crossing the widom-line – supercritical pseudo-boiling,” *The Journal of Supercritical Fluids*, vol. 98, pp. 12 – 16, 2015.
- [15] L. Lees and C. C. Lin, “Investigation of the stability of the laminar boundary layer in a compressible fluid,” *NACA Technical note*, 1946.
- [16] J. W. Peeters, R. Pecnik, M. Rohde, T. van der Hagen, and B. Boersma, “Turbulence attenuation in simultaneously heated and cooled annular flows at supercritical pressure,” *Journal of Fluid Mechanics*, vol. 799, pp. 505–540, 2016.
- [17] H. Nemati, A. Patel, B. J. Boersma, and R. Pecnik, “The effect of thermal boundary conditions on forced convection heat transfer to fluids at supercritical pressure,” *Journal of Fluid Mechanics*, vol. 800, pp. 531–556, 2016.
- [18] A. Trettel and J. Larsson, “Mean velocity scaling for compressible wall turbulence with heat transfer,” *Physics of Fluids*, vol. 28, no. 2, p. 026102, 2016.
- [19] A. Patel, B. Boersma, and R. Pecnik, “The influence of near-wall density and viscosity gradients on turbulence in channel flows,” *Journal of Fluid Mechanics*, vol. 809, pp. 793–820, 2016.
- [20] P. G. Huang, P. Bradshaw, and T. J. Coakely, “Turbulence models for compressible boundary layers,” *AIAA Journal*, vol. 32, no. 4, pp. 735–740, 1994.
- [21] S. Sarkar, G. Erlebacher, M. Hussaini, and H. Kreiss, “The analysis and modelling of dilatational terms in compressible turbulence,” *Journal of Fluid Mechanics*, vol. 227, pp. 473–493, 1991.
- [22] O. Zeman, “A new model for super/hypersonic turbulent boundary layers,” in *31st Aerospace Sciences Meeting*, p. 897, 1993.
- [23] S. Catris and B. Aupoix, “Density corrections for turbulence models,” *Aerospace Science and Technology*, vol. 4, no. 1, pp. 1–11, 2000.
- [24] P. Huang, P. G., Coleman, G. N., Bradshaw, “Compressible Turbulent channel flows, DNS results and modelling,” *JFM*, no. 1995, pp. 185–218, 1995.
- [25] R. Cess, “A survey of the literature on heat transfer in turbulent tube flow,” *Res. Rep*, pp. 8–0529, 1958.
- [26] P. R. Spalart, S. R. Allmaras, *et al.*, “A one equation turbulence model for aerodynamic flows,” *RECHERCHE AEROSPATIALE-FRENCH EDITION-*, pp. 5–5, 1994.
- [27] N. Myong, H.K. and Kasagi, “A New Approach to the Improvement of k-e turbulence model for wall-bounded shear flows,” *JSME*, vol. 33, no. 2, 1990.
- [28] F. R. Menter, “Zonal Two Equation k-w, Turbulence Models for Aerodynamic Flows,” *AIAA paper*, p. 2906, 1993.
- [29] P. A. Durbin, “Separated Flow Computations with the k-e-v2 Model,” *AIAA Journal*, vol. 33, no. 4, pp. 659–664, 1995.

CONTRIBUTIONS TO THE NUMERICAL MODELING OF TURBULENT DENSE GAS FLOWS

P. Cinnella¹, X. Gloerfelt¹, F. Grasso² and L. Sciacovelli¹

¹*Laboratoire DynFluid, Arts et Métiers Institute of Technology*

²*Laboratoire DynFluid, Cnam*

Abstract

The present article reviews some recent contributions to the study of dense gas effects in turbulent flows by using high-performance computing models, namely, direct and large eddy simulations. Significant deviations from perfect-gas compressible turbulence are observed, driven by the large heat capacity and the peculiar behavior of transport properties. The most striking differences are encountered for gas flows characterized by values of the fundamental derivative of gas dynamics close to zero, or possibly negative, and/or for high Mach number flows. The high-fidelity databases open the way to the development of improved turbulence and transition models, specific to complex non-ideal gases.

1 Introduction

The dynamics of dense gases, of importance for a number of engineering applications and more particularly for energy-conversion devices, is still featuring a number of ill or partially understood physical mechanisms. The scarcity of comprehensive and reliable experimental data, due to the difficulty of designing and building suitable test benches, has led to an extensive use of theoretical and numerical models for unraveling the flow physics and for designing components in engineering applications. In the past, our group has made considerable research efforts for developing appropriate numerical methods [1, 2], applying them to non classical flow phenomena [1, 3, 4], developing suitable strategies for aerodynamic design and optimization [5, 6, 7], quantifying the effect of uncertainties in the input parameters and closure models [8, 9, 10] and incorporating them in the design process by means of robust optimization techniques [11, 12, 13]. The modeling tools have evolved during the years from the inviscid flow simulations to high-resolution turbulent flow computations requiring advanced high-performance computing (HPC).

In recent years our group has investigated, for the first time in the literature to the best of our knowledge, the role of dense-gas effects in compressible turbulent flows by means of direct numerical simulations (DNS) or highly resolved large eddy simulations (LES) [14, 15, 16, 17, 18, 19]. The physical understanding of the turbulence dynamics of dense gas flows is relevant, e.g., for high-Reynolds wind tunnels [20, 21], energy conversion cycles [22] and refrigeration [23]. The study is motivated by the well-known deficiencies of Reynolds-Averaged Navier–Stokes (RANS) turbulence models, especially for turbomachinery flows, and by need of high-fidelity data for their assessment and improvement. In the following of this paper, we describe the main contributions and findings and we provide some perspectives for future research.

2 Governing equations and numerical methods

We consider flows of gases governed by the compressible Navier-Stokes equations for a single-phase Newtonian fluid. The second viscosity is set according to Stokes' hypothesis, assuming a zero bulk viscosity. This approximation is well verified for a dense gas (see Appendix B of [15]). The heat flux is modeled by the classical Fourier law. The system is supplemented by suitable thermal and caloric equations of state (EoS) and transport-property laws. Most of the results presented in the following are obtained for PP11 (commercial name of the perfluoro-perhydrophenanthrene), which was used in our previous studies since it exhibits a relatively large inversion zone, a thermodynamic region above the liquid/vapor coexistence curve such that the fundamental derivative of gas dynamics Γ [24] is negative. PP11 then belongs to the family of Bethe–Zel'dovich–Thompson (BZT) fluids, and it was chosen to emphasize the role of dense gas effects. However, preliminary studies with different working fluids and EoS indicate the most important trends are also observed in other dense gases.

For PP11, we use the thermal EoS of Martin and Hou [25], often used for fluorocarbons [24, 26, 27]. For other fluids, we use the reference EoS available through the NIST REFPROP library [28]. For the fluid viscosity and thermal conductivity we use the generalized laws of Chung *et al.* [29], which account for the strong density dependence of the transport properties in the dense gas region, or the transport property laws of REFPROP, whose accuracy and complexity may vary greatly from one fluid to another.

For DNS and well-resolved LES in simple geometries, an in-house high-accurate finite-difference code is used to solve the governing equations. The inviscid fluxes are discretized by means of tenth-order standard centered differences or 11-point optimized finite differences. The scheme is supplemented with a high-order selective dissipation, along with a Jameson-type shock capturing term. The viscous fluxes are discretized with standard fourth-order centered derivatives, and a low-storage Runge–Kutta algorithm is used for time integration. For more details, the reader is referred to [14, 15]. For LES in more complex geometries we used our in-house finite-volume solver DynHOLab and selected a central third-order scheme with nonlinear artificial viscosity for the inviscid fluxes and a standard second-order approximation for the viscous fluxes. The time stepping still relies on Runge–Kutta schemes, supplemented with a high-order implicit residual smoothing operator to enlarge the stability domain for high-Reynolds flows (see [30] for more details).

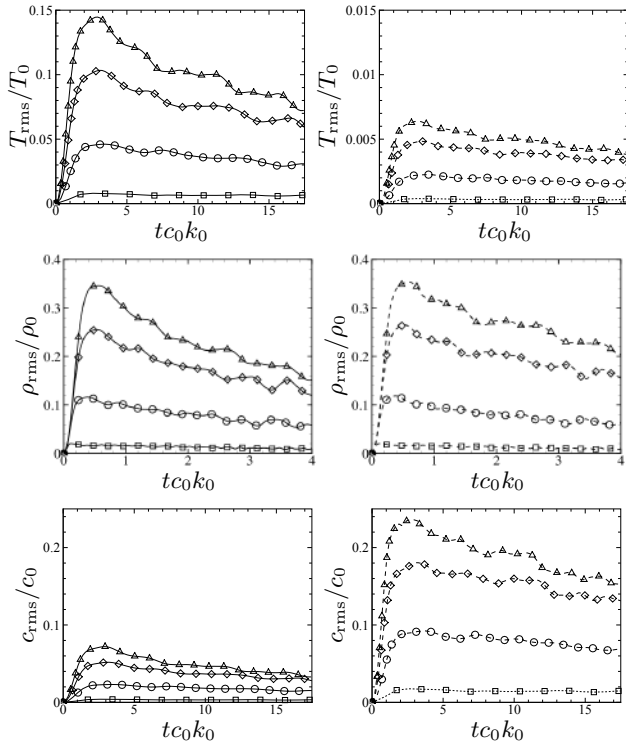


Figure 1: Time histories of the rms temperature (first row), density (second row), and sound speed (third row), for air (left) and PP11-IC1 (right) at various Mach numbers, $M_{t_0} = 0.2$ (\square), 0.5 (\circ), 0.8 (\diamond), 1 (\triangle)

3 HPC simulations of turbulent dense gas flows

Turbulent dense gas flows have been simulated at various fidelity degrees for a variety of configurations. These include classical building blocks of turbulent flow studies, such as the freely decaying homogeneous isotropic turbulence, compressible plane channel flows and high-speed boundary layers. We also report recent LES results for a simplified transonic turbine cascade, showing that natural transition is also deeply modified and that standard turbulence models in use in industry fail to reproduce the relevant mechanisms.

3.1 Freely decaying homogeneous and isotropic turbulence

Dense gas effects were first investigated for compressible homogeneous isotropic turbulence (CHIT), with focus on the influence of the complex thermodynamic behavior and transport properties on small scale structures, viscous dissipation and enstrophy generation [14, 16]. Compressible turbulence decay is governed by the initial turbulent Mach number $M_{t_0} = u_{rms_0}/\bar{c}_0$ and the Reynolds number $Re_{\lambda_0} = u_{rms_0}\lambda_0\bar{\rho}_0/\bar{\mu}_0$, based on the initial root-mean-square (*rms*) velocity u_{rms_0} , sound speed \bar{c}_0 , and Taylor microscale λ_0 , where the overlines denote volume averages. We performed direct simulations of dense-gas CHIT at various $M_{t_0} = 0.2, 0.5, 0.8$ and 1 , and at $Re_{\lambda_0} = 200$. We considered two initial thermodynamic states: IC1 lies immediately outside the inversion zone ($\rho_0/\rho_c = 1.618$, $p_0/p_c = 1.02$, $T_0/T_c = 1.01$, $\Gamma_0 = 0.1252$); IC2 is located inside ($\rho_0/\rho_c = 1.618$, $p_0/p_c = 0.98$, $T_0/T_c = 1.001$, $\Gamma_0 = -0.093$), and may lead to BZT effects.

Dense gas effects modify the time evolution of mean turbulence properties, especially for initial turbulent

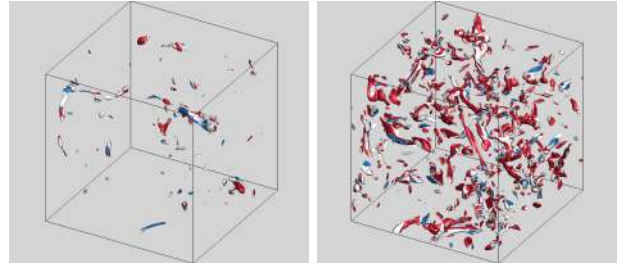


Figure 2: Strong expansions $\theta/\theta_{rms}M_{t_0}^2 = 3$ for air (left) and PP11-IC1 (right) at $M_{t_0} = 1$, colored with the local type of structure. Blue: eddy; white: shear; red: convergence. The reader is referred to [16] for more details

Mach numbers greater than 0.5, although most kinematic properties (velocity spectra, total kinetic energy and total enstrophy) are weakly sensitive to the thermodynamic behavior of the gas. Figure (1) shows that, for a given turbulent Mach number, the *rms* fluctuations of temperature and pressure are much smaller than in a light perfect gas like air. This effect is mostly driven by the specific heat ratio γ of the gas, related in turn to the gas molecular complexity. It has been shown that, for a perfect gas, p_{rms}/\bar{p} and T_{rms}/\bar{T} scale as $\gamma M_{t_0}^2$ and $(\gamma - 1)M_{t_0}^2$, respectively. As a consequence, temperature fluctuations tend to vanish as $\gamma \rightarrow 1$, while pressure fluctuations are greatly reduced. Density fluctuations are little sensitive to γ , since they simply scale as $M_{t_0}^2$. Additional differences with respect to standard air flows are due to the non-ideal thermodynamics. For instance, sound speed fluctuations scale as $(\gamma - 1)/2M_{t_0}^2$ for a perfect gas. However, in the dense gas region these fluctuations are correlated with the density ones, and the fluid compressibility is large. As a consequence, c_{rms}/\bar{c} is greatly enhanced, especially for high M_{t_0} values.

An analysis of the statistical properties of turbulent structures in the plane of the second and third invariant of the deviatoric strain-rate tensor [16] shows a weakening of compression regions and an enhancement of expanding ones for dense gas turbulence. These regions are classified according to the local level of normalized velocity divergence $\theta/\theta_{rms}M_{t_0}^2$ [14] and regions with $|\theta/\theta_{rms}M_{t_0}^2| > 2$ are categorized as strong expansions/compressions. Additionally, strong expansion regions are mostly populated by non-focal convergence structures typical of strong compression regions, in contrast with the perfect gas that is dominated by eddy-like structures. Figure (2) reports the iso-surface $\theta/\theta_{rms}M_{t_0}^2 = 3$, colored with the local type of structure. The expanding structures contribute to the dilatational dissipation in a similar way as compression ones. Interestingly, these effects are observed for both IC1 and IC2, although they are stronger in the BZT conditions.

3.2 Turbulent channel flows

In order to investigate dense gas effects in sheared, confined turbulent flows, DNS of compressible turbulent channel flows were carried out at three bulk Reynolds numbers $Re_B = \bar{\rho}_B \tilde{u}_B h / \bar{\mu}_w$ (3000, 7000 and 12000) and three bulk Mach numbers $M_B = \tilde{u}_B / \bar{c}_w$ (1.5, 2.25 and 3) [15], where the subscripts $(\cdot)_B$ and $(\cdot)_w$ denote time and space averaged values over the channel cross-section and at the wall, respectively. Reynolds averaging is indicated as $\overline{(\cdot)}$, with $(\cdot)'$ the Reynolds fluctuations; similarly, $\widetilde{(\cdot)}$ and $(\cdot)''$ denote Favre averages and fluctuations.

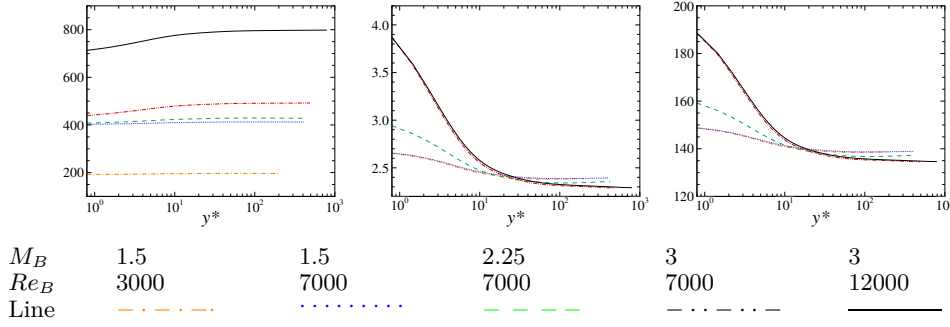


Figure 3: Left to right: local friction Reynolds number (Re_τ^*), average Prandtl number (\overline{Pr}), and average isobaric specific heat normalized with the gas constant ($\overline{c_p}/R$) versus y^* for channel flows of PP11 at various M_B and Re_B

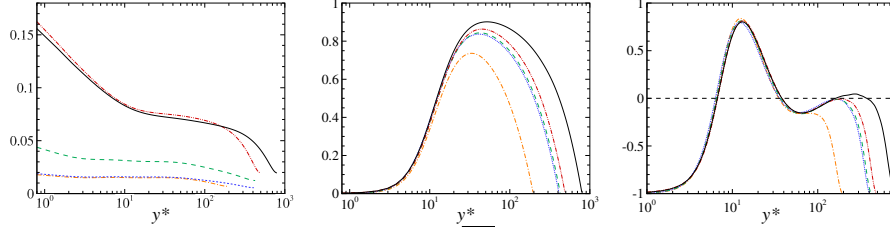


Figure 4: Left to right: normalized density fluctuations ($\sqrt{\overline{\rho''^2}/\overline{\rho}}$), Reynolds shear stresses ($\overline{\rho''v''^+}$), and production-to-dissipation ratio of turbulent kinetic energy ($P_k/\epsilon_k - 1$) versus y^* for channel flows of PP11 at various M_B and Re_B . Lines as in Figure (3)

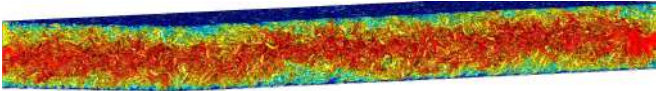


Figure 5: Isosurface of $Q(h/u_B)^2 = 1$ coloured with streamwise velocity ($M_B=3$, $Re_B=7000$)

For PP11, due to the large specific heat of the fluid, the average temperature is almost constant across the channel for any choice of the Mach and Reynolds numbers, variations being less than 1%. Decoupling of dynamic and thermal effects in the dense gas also leads to smaller mean density variations across the channel than for an air flow: the wall density is up to 60% higher than the centerline one for air at $M_B = 3$, whereas variations below 20% are observed for PP11. The viscosity, which follows the temperature variation for air, varies instead like the density for PP11 and tends to decrease toward the channel center. As a consequence the local friction Reynolds number $Re_\tau^* = Re_\tau \sqrt{\overline{\rho(y)}/\overline{\rho_w}} (\overline{\mu_w}/\overline{\mu(y)})$ (with $Re_\tau = \overline{\rho_w} u_\tau h / \overline{\mu_w}$) increases toward the channel centerline in PP11. Specifically, near the wall Re_τ^* is lower than in air at the same conditions, whereas it is much higher at the centerline, where the values are closer to incompressible channel flow at the same Re_B . The average Prandtl number \overline{Pr} , of approximately 2 near the centerline, increases up to about 5 at the wall at high Mach numbers, following specific heat variations across the channel. As a consequence, the thermal boundary layer is about twice thinner than the dynamic one. Figure (3) displays the profiles of the above-mentioned quantities as a function of the semi-local wall coordinate, $y^* = \overline{\rho(y)} u_\tau^* y / \overline{\mu(y)}$, with $u_\tau^* = \sqrt{\overline{\tau_w}/\overline{\rho(y)}}$ the semi-local friction velocity. Despite the liquid-like viscosity behavior, compressibility effects are present, and the turbulent Mach number is comparable (slightly higher) to air flows. In all cases, the maximum turbulent Mach number is well below the limit where strong compressibility effects, like eddy shocklets, are visible. Figure (4) displays selected profiles of the second-order statistics, namely, the rms of the density fluctuations, the semi-locally scaled

Reynolds shear stress $\overline{\rho''v''^+} = \tau_w^{-1} \overline{\rho''v''}$, and the ratio of the turbulent kinetic energy production to dissipation. The relative density (and pressure) fluctuations are of the same order of those observed for air flows, whereas temperature fluctuations (not reported) are nearly two orders of magnitude lower. Remarkably, $\overline{\rho'_{rms}}$ decreases monotonically from wall to centerline, contrary to light gases. This effect is a consequence of the thermodynamic behavior of PP11 at the considered conditions, as discussed in [15]. In all cases, density fluctuations remain small compared to the mean value, and Morkovin's hypothesis is satisfied even at the highest Mach number. Despite the striking differences in the thermodynamic behavior, Reynolds stress profiles are similar to those observed for low-Mach channel flows with temperature-dependent transport properties. The liquid-like behavior of viscosity leads to an increase of the spanwise, wall-normal and Reynolds shear stresses with respect to the corresponding incompressible evolution, whereas the streamwise one decreases. Finally, energy budgets match well the typical distribution for incompressible flow using semi-local scaling. The production peak is located at $y^* \approx 12$ as usual. For the higher Reynolds number, a second peak is observed in the outer region, like in high- Re incompressible flow, due to the reduced dissipation close to centerline. A visualization of flow structures for $M_B = 3$, $Re_B = 12000$ is provided in Figure (5).

The DNS data for turbulent channel flows were used to conduct a priori analyses of the validity of some common modeling assumptions for the eddy viscosity and turbulent Prandtl number. They showed that, for a dense gas, turbulence models for eddy viscosity follow the trend of the DNS reference more closely than in perfect gas (at the present high Mach numbers), due to the higher local Reynolds number, but eddy viscosity is overestimated. Recalibration of the model constants from DNS data could improve model accuracy and will be investigated in the future. A peculiar behavior was observed for the turbulent Prandtl number close to the wall, which peaks more or less abruptly in the viscous sublayer, instead of tending to a constant value of approximately 1. The reader is referred to [31] for more details.

3.3 High-speed boundary layers

The dynamics of transitional and turbulent high-speed boundary layers of dense gases has been investigated by means of the linear stability theory (LST) and quasi-DNS (qDNS) over an extended computational domain encompassing the laminar, transitional and turbulent regimes. Both the LST and qDNS calculations make use of the similarity solution for a zero-pressure-gradient laminar boundary layer (Blasius solution), extended to fluids governed by arbitrary equations of state and transport-property models. This is used as the base flow for LST, and as an initial/inlet condition for qDNS.

Similarly to the preceding cases, the high heat capacity of the dense gas leads to weaker variations of wall thermodynamic quantities (e.g., wall temperature is only 2.5% higher than the freestream one at $M_\infty=6$ for the dense gas, whereas a factor greater than 7 is obtained for the perfect gas) and of the fluid viscosity. As a result, the laminar velocity profiles are almost indistinguishable from the incompressible counterpart. Additionally, the dense-gas viscosity, closely correlated with the density, exhibits an opposite evolution compared to the perfect one, and decreases when approaching the wall.

The linear stability theory (LST) for parallel flows, extended to gases with arbitrary equations of state and transport model has been used to investigate how dense-gas boundary layers react to modal excitations and to select an unstable mode susceptible to trigger transition to turbulence [18]. For PP11, boundary layer stability is first investigated at thermodynamic conditions corresponding to a point inside the inversion zone and free-stream Mach numbers in the range [0.5, 6]. The results depend on a local Reynolds number $Re = (\rho_\infty^* u_\infty^* L^*) / \mu_\infty^*$ based on the freestream velocity u_∞^* and the Blasius length $L^* = (\mu_\infty^* x^* / \rho_\infty^* u_\infty^*)^{1/2}$, with x^* the dimensional wall coordinate, and on the non-dimensional perturbation frequency $\omega = (2\pi f^* L^*) / u_\infty^*$ (or $F = (2\pi f^* \mu_\infty^*) / (\rho_\infty^* u_\infty^{*2})$), with f^* the dimensional frequency. For low Mach numbers, a single unstable 2D viscous mode is found in a low-frequency band (next to $\omega \approx 0.03$), which corresponds to the Tollmien-Schlichting (TS) mode in the incompressible regime. As the Mach number becomes supersonic, the most unstable wave is oblique and its growth rate is rapidly reduced by compressibility. For a light perfect gas like air, the stabilizing effect is progressively counterbalanced, at Mach numbers of 3 or higher, by the appearance of a generalized inflection point, so that the nature of the mode becomes more and more inviscid. For a dense gas, the generalized inflection point is either not present or located very close to the wall. The inviscid mechanisms do not take over at high Mach numbers (between 2 and 3), and the TS mode is continuously damped. For PP11, this mode is stable in 2D at $M_\infty = 2.25$, and even oblique waves are stable at $M_\infty = 3$. At higher speeds ($M_\infty > 4$), the so-called second mode or Mack mode (sometimes qualified as an "acoustic" mode, due to the presence of acoustic waves trapped between the wall and the relative sonic line) becomes dominant in air. For dense gases, the acoustic mode is characterized by a much higher frequency ($\omega \approx 0.5$) due to the large heat capacity that inhibits boundary layer thickening, and it is called a supersonic mode, since its phase speed reaches supersonic values. The isocontours of the growth rate α_i (made non-dimensional with L^*) in the $F-Re$ map, at $M_\infty=4.5$, are reported in Figure (6)a for PP11. Results for air at the same Mach number are also reported for reference. The figure gives an overview of the differences in frequency

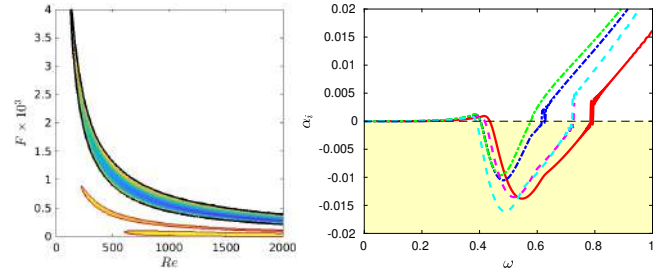


Figure 6: Maps of 2D amplification rate α_i at $M_\infty=4.5$ in the $F-Re$ plane (a): the black line indicates the neutral curve for dense gas; thin red lines are the neutral curves of the first and second mode for air. Color scale for α_i between -0.015 and 0. Influence of the fluid on the growth rate of the supersonic mode at $M_\infty=4.5$ and $Re=2000$ (b): — PP11; - - - R134a; ··· R245fa; - · - MDM; - - - D₆ ($v_\infty/v_c=1.8$, $T_\infty/T_c=0.995$)

and amplitude of the unstable modes. Figure (6)b displays the growth rate of perturbations as a function of ω for various dense gases, namely, PP11, the refrigerants R134a and R245fa and the siloxanes MDM and D₆. The results were obtained for Mach 4.5 and $Re = 2000$. All the considered dense gases exhibit the supersonic mode within a similar frequency range.

Due to the absence of the Tollmien-Schlichting mode and to the high-frequency of the supersonic mode, triggering transition in dense gases through modal excitation is more difficult than in air flows at similar conditions. LES and qDNS at $M_\infty = 2.25$ and 6 [19] show the appearance of very persistent streaks, which eventually break down into turbulence. Additionally, in the simulated air flow cases transition is due to oblique breakdown occurring approximately at the same streamwise location over the whole span, causing an overshoot in the skin friction coefficient (Figure (7)). Transition in dense gas boundary layers is characterized by streak breakdown leading to an irregular turbulent front, and no overshoot is observed. A detailed study of the transitional region extracted from our DNS simulations is underway and will make the object of a forthcoming paper. The simulations were used to investigate dense gas effects in the fully-developed turbulent portion of the boundary layer. As expected, the high heat capacity leads to nearly negligible temperature variations across the boundary layer even at hypersonic conditions, and the thickening rate of the boundary layer in the dense gas is close to that of an incompressible flow. Wall-normal profiles of mean thermodynamic and transport properties change with the Mach number, but their variations across the boundary layer are much smaller than in air flow. Accordingly, variations of the fluid viscosity across the boundary layer are greatly reduced, and they follow an opposite trend than in a perfect gas, as in the laminar case. The above-mentioned effects lead to higher local Reynolds numbers, and to the appearance of an outer peak in the velocity spectra, similar to high-Reynolds incompressible boundary layers. The velocity profiles and turbulent intensities are almost insensitive to the Mach number (Figure (8)). The most significant deviations from standard behavior are observed for the density (and viscosity) fluctuations, which reach a maximum near the wall in DG instead of vanishing as in PG. Such behavior, already observed for turbulent channel flows, is shown in Figure (8) for density.

The reduced thickening of DG boundary layer leads to a more extended supersonic region than in perfect gases

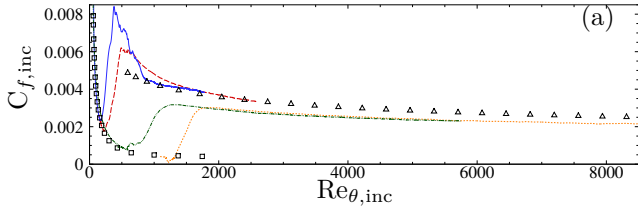


Figure 7: Skin friction distribution versus local Reynolds number (based on incompressible momentum thickness) for various turbulent boundary layers. --- Air $M=2.25$, — Air $M=6$, PP11 $M=2.25$, -.-.- PP11 $M=6$; \square : Blasius laminar solution, \triangle : turbulent correlation $C_{f,inc}=0.024Re_{\theta,inc}^{-1/4}$

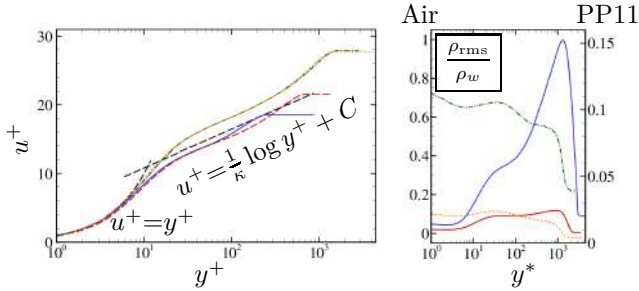


Figure 8: Velocity profiles for Air and PP11 in the classical wall scaling (a) and profiles of the scaled density fluctuations versus the semi-local wall coordinate (b). Black dashed lines denote the linear and logarithmic laws, with $\kappa=0.41$ and $C=5.2$. --- Air $M=2.25$, — Air $M=6$, PP11 $M=2.25$, -.-.- PP11 $M=6$

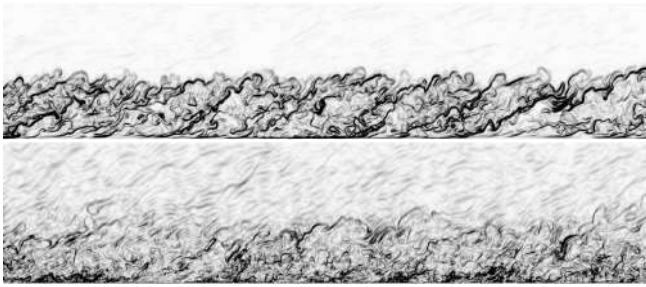


Figure 9: Snapshots of normalized numerical Schlieren for Air (top) and PP11 (bottom) at $M=6$

and to higher turbulent and fluctuating Mach numbers. As previously observed for homogeneous isotropic turbulence, expansion and compression events are rather balanced. Snapshots of numerical Schlieren contours for PP11 and air are reported in Figure (9). Density variations are considerably attenuated in the outer region of the DG boundary layer, while a strong dilatational activity is located in the near-wall region. In the future, the present high-fidelity databases may be used for investigating transition and turbulence models specifically tuned for dense gas flows.

3.4 Transonic flow through a turbine stator cascade

In an attempt to make progress toward high-fidelity simulations of more realistic flow configurations, wall-resolved LES were carried out for PP11 flow through a transonic turbine nozzle vane, for two inlet thermodynamic conditions, corresponding to subcritical and supercritical pressure, and two pressure ratios [17]. The geometry corresponds to the VKI LS-89 configuration,

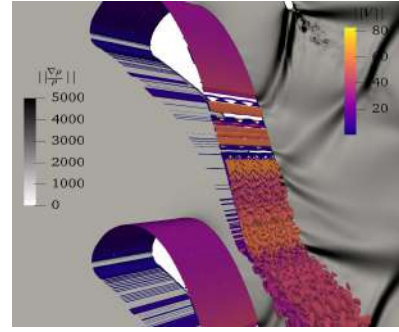


Figure 10: PP11 flow through the VKI LS-89 cascade at supercritical inlet conditions: instantaneous iso-surface of the Q-criterion ($Q = 1000$), and snapshot of the relative density gradient in the background

widely investigated in the literature for air flows. The subcritical conditions lead to mild non-ideal gas dynamic effects in the flow field. On the contrary, dramatic deviations from the ideal-gas behavior are observed for the supercritical operating conditions, including non-classical expansion and compression waves interacting with the surrounding boundary layers and wakes. The LES allows to capture boundary layer transition, which plays a crucial role on flow performance, at least at the moderate Reynolds number investigated up to now. For some operating conditions, transition may lead to abrupt changes in boundary layer thickness resulting in the formation of additional shock waves. Such waves cannot be captured neither by inviscid flow simulations, nor by RANS simulations, for which the boundary layers are fully turbulent. Contrary to theoretical predictions based on inviscid flow, the supercritical inlet operating conditions (characterized by significant BZT effects) do not lead to an improvement of cascade losses. A possible explanation lies in the different state of the boundary layer, characterized by a more extended turbulent portion, and hence by higher viscous losses. In the next future we plan to investigate higher Reynolds number flows, closer to conditions met in practical ORC applications, and other working fluids, with specific focus on the role of laminar-turbulent transition.

4 Conclusions

The recent use of massive numerical simulations of turbulent flows has contributed to shedding light onto the role of dense gas thermodynamic effects and thermo-physical properties on compressible turbulence. The simulations provide useful databases for the assessment and improvement of turbulence models (an essential ingredient for flow design). Additionally, they open the way to the study of laminar-to-turbulent transition and its impact on component performance, totally missed in the Reynolds-Averaged simulations currently employed for the design of engineering systems using dense gases as working fluids. Further research effort is required to extend the use of high-fidelity simulations to turbulent dense gas flows of engineering interest, to better understand the role of dense gas effects in flow transition and to develop suitable turbulence and transition models.

Acknowledgment

This work was granted access to the HPC resources of IDRIS and TGCC under the allocations 7332 and 1736

made by GENCI (Grand Equipement National de Calcul Intensif). We also acknowledge TGCC for awarding access to the Joliot-Curie supercomputer under the allocation "Grands Challenges" gch032.

References

- [1] P. Cinnella and P. Congedo, "Numerical solver for dense gas flows," *AIAA J*, vol. 43, pp. 2458–61, 2005.
- [2] P. Cinnella, "Roe-type schemes for dense gas flow computations," *Comp Fluids*, vol. 35, pp. 1264–81, 2006.
- [3] P. Cinnella and P. Congedo, "Inviscid and viscous aerodynamics of dense gases," *J Fluid Mech*, vol. 580, pp. 179–217, 2007.
- [4] P. Congedo, C. Corre, and P. Cinnella, "Numerical investigation of dense-gas effects in turbomachinery," *Comp Fluids*, vol. 49, pp. 290–301, 2011.
- [5] P. Cinnella and P. Congedo, "Optimal airfoil shapes for viscous transonic flows of Bethe-Zel'dovich-Thompson fluids," *Comp Fluids*, vol. 37, pp. 250–264, 2008.
- [6] P. Congedo, C. Corre, and P. Cinnella, "Shape optimization for dense gas flows in turbine cascades," in *Computational Fluid Dynamics 2006*, pp. 555–560, Springer Verlag, 2006.
- [7] E. Bufi and P. Cinnella, "Preliminary design method for dense-gas supersonic axial turbine stages," *J Eng Gas Turb Power*, vol. 140, p. 112605, 2018.
- [8] P. Cinnella, P. Congedo, L. Parussini, and V. Pediroda, "Sensitivity analysis of dense gas flow simulations to thermodynamic uncertainties," *Phys Fluids*, vol. 23, p. 116101, 2011.
- [9] X. Merle and P. Cinnella, "Bayesian quantification of thermodynamic uncertainties in dense gas flows," *Rel Eng Sys Safety*, vol. 134, pp. 305–23, 2015.
- [10] X. Merle and P. Cinnella, "Robust prediction of dense gas flows under uncertain thermodynamic models," *Rel Eng Sys Safety*, vol. 183, pp. 400–21, 2019.
- [11] P. Cinnella and S. Hercus, "Robust optimization of dense gas flows under uncertain operating conditions," *Comp Fluids*, vol. 39, pp. 1893–1908, 2010.
- [12] S. Hercus and P. Cinnella, "Robust shape optimization of uncertain dense gas flows through a plane turbine cascade," Paper ASME AJK2011-05007.
- [13] E. Bufi and P. Cinnella, "Robust optimization of supersonic ORC nozzle guide vanes," *IOP J Phys, CS*, vol. 821, p. 01100117, 2016.
- [14] L. Sciacovelli, P. Cinnella, C. Content, and F. Grasso, "Dense gas effects in inviscid homogeneous isotropic turbulence," *J Fluid Mech*, vol. 800, pp. 140–179, 2016.
- [15] L. Sciacovelli, P. Cinnella, and X. Gloerfelt, "Direct numerical simulations of supersonic turbulent channel flows of dense gases," *J Fluid Mech*, vol. 821, pp. 153–199, 2017.
- [16] L. Sciacovelli, P. Cinnella, and F. Grasso, "Small-scale dynamics of dense gas compressible homogeneous isotropic turbulence," *J Fluid Mech*, vol. 825, pp. 515–549, 2017.
- [17] J.-C. Hoarau, P. Cinnella, and X. Gloerfelt, "Large eddy simulation of dense gas flow around a turbine cascade," AIAA Paper 2019-2843.
- [18] X. Gloerfelt, J.-C. Robinet, L. Sciacovelli, P. Cinnella, and F. Grasso, "Dense gas effects on compressible boundary layer stability," *J Fluid Mech*, vol. 893, p. A19, 2020.
- [19] L. Sciacovelli, X. Gloerfelt, D. Passiatore, P. Cinnella, and F. Grasso, "Numerical investigation of high-speed turbulent boundary layers of dense gases," *Flow Turbul Combust*, 2020. DOI:10.1007/s10494-020-00133-1.
- [20] E. Bodenschatz, G. P. Bewley, H. Nobach, M. Sinhuber, and H. Xu, "Variable density turbulence tunnel facility," *Rev Sci Instrum*, vol. 85, p. 093908, 2014.
- [21] J. Corliss and S. Cole, "Heavy gas conversion of the NASA Langley Transonic Dynamics Tunnel," AIAA Paper 98-2710.
- [22] P. Colonna, E. Casati, C. Trapp, T. Mathijssen, J. Larjola, T. Turunen-Saaresti, and A. Uusitalo, "Organic Rankine cycle power systems: from the concept to current technology, applications, and an outlook to the future," *J Eng Gas Turb Power*, vol. 137, no. 10, p. 100801, 2015.
- [23] C. Zamfirescu and I. Dincer, "Performance investigation of high-temperature heat pumps with various BZT working fluids," *Thermochimica Acta*, vol. 488, pp. 66–77, 2009.
- [24] P. Thompson, "A fundamental derivative in gas dynamics," *Phys Fluids*, vol. 14, pp. 1843–1849, 1971.
- [25] J. Martin and Y.-C. Hou, "Development of an equation of state for gases," *AIChE Journal*, vol. 1, no. 2, pp. 142–151, 1955.
- [26] M. Cramer, "Negative nonlinearity in selected fluorocarbons," *Phys Fluids A*, vol. 1, pp. 1894–97, 1989.
- [27] A. Guardone, L. Vigevano, and B. Argrow, "Assessment of thermodynamic models for dense gas dynamics," *Phys Fluids*, vol. 16, pp. 3878–87, 2004.
- [28] E. Lemmon, M. Huber, and M. McLinden, "NIST – REFPROP, Version 9.1." <http://www.nist.gov/srd/nist23.cfm>, 2013.
- [29] T. Chung, M. Ajlan, L. Lee, and K. Starling, "Generalized multiparameter correlation for nonpolar and polar fluid transport properties," *Ind Eng Chem Res*, vol. 27, no. 4, pp. 671–679, 1988.
- [30] J.-C. Hoarau, P. Cinnella, and X. Gloerfelt, "Large eddy simulation of turbomachinery flows using a high-order implicit residual smoothing scheme," *Comp Fluids*, vol. 198, p. 104395, 2020.
- [31] L. Sciacovelli, P. Cinnella, and X. Gloerfelt, "A priori tests of RANS models for turbulent channel flows of a dense gas," *Flow Turbul Combust*, vol. 101, pp. 295–315, 2018.

DIRECT NUMERICAL SIMULATION OF A BZT DENSE GAS COMPRESSIBLE SHEAR LAYER

A. Vadrot¹, A. Giauque¹ and C. Corre¹

¹*Laboratoire de Mécanique des Fluides et d'Acoustique - UMR 5509, Ecole centrale de Lyon, Ecully, France*

Abstract

This study extends a previous analysis conducted at $M_c = 1.1$ [1] to higher compressible regime at $M_c = 2.2$. Direct numerical simulations of a compressible temporal shear layer are performed with a BZT dense gas (FC-70) described using the Martin-Hou Equation of State (EoS) and air described using the Perfect Gas EoS as point of comparison. The initial thermodynamic operating point is chosen for the dense gas inside the inversion region where the fundamental derivative of gas dynamics Γ is negative. After having carefully defined the self-similar period, results averaged over this period are compared between dense and perfect gas. The well-known compressibility-related reduction of the shear layer growth rate seems to be influenced by dense gas effects at $M_c = 2.2$ unlike previous analysis at $M_c = 1.1$ [1]. A detailed comparison of the turbulent kinetic energy equation contributing terms is provided for both dense and perfect gases.

1 Introduction

Dense gases (DG) are single-phase vapours characterized by long chains of carbon atoms and by medium to large molecular weights. Over the past forty years, they have known a growing interest particularly in Organic Rankine Cycles (ORCs) industry. Their large heat capacity and their low boiling point temperature make them suitable working fluids for low-temperature heat sources (waste heat recovery, solar thermal power, geothermal plants,...). Coupling with a turbine enables power generation and the reduction of losses in such ORC turbines is naturally desirable. Shocks created in the transonic and supersonic regimes are major loss sources. However, in dense gas flows, entropy jumps through shocks are significantly reduced in specific thermodynamic regions near the critical point, where the sound speed drops significantly leading to strong compressibility effects even in flows at moderate velocity. This feature is yet difficult to exploit because of the lack of knowledge in these particular thermodynamic zones.

Up to now, although dense gases display non-classical phenomena, Reynolds-Averaged Navier Stokes (RANS) and Large Eddy Simulation (LES) closure models developed in the context of Perfect Gas (PG) flows have been assumed relevant for DG flows and applied to the simulation of such turbulent DG flows [2, 3]. This assumption is actually debatable and its confirmation or disproof constitutes an active research field. Direct Numerical Simulation (DNS) is the favoured tool in this study to better understand the development of turbulence in DG flows and provides both guidelines and validation databases for the aforementioned closure models development. DNS of dense gases has been used in few previous works for various flow configurations such as freely decaying and forced homogeneous isotropic turbulence [4, 5, 6] and turbulent channel flow [7, 8]. In the present study, the compressible

shear layer, which is representative of the blade wake region in ORC turbines, is investigated. This configuration has been largely used to develop and validate compressibility corrections for turbulence models [9, 10, 11]. Since DG flows influence compressibility effects, the choice to study the compressible shear layer is relevant to assess the validity of PG turbulence closure models. The temporal mixing layer is chosen instead of the spatial mixing layer because it makes DNS less computationally expensive. The recently performed DNS of a DG temporal compressible shear layer [1] reveals a much faster growth for the DG flow w.r.t. the PG flow during the initial unstable growth phase but only slight differences during the self-similar period, where turbulence is in statistically stable state and which is the regime of interest when studying shear layers. The convective Mach number M_c characterizing the shear layer is defined as:

$$M_c = \frac{U_1 - U_2}{c_1 + c_2} = \frac{\Delta u}{c_1 + c_2} \quad (1)$$

where U_i and c_i denote respectively the flow speed and the sound speed of stream i (upper or lower) of the shear layer (see Figure (1)). Results obtained in [1] with $M_c = 1.1$ show that the turbulent Mach number (defined as $M_t = \sqrt{u'_i u'_i}/c$, where u'_i represents the fluctuating velocity in direction i) was actually in the low-limit to yield shocklets. These observations call therefore for an extension of the study to larger convective Mach numbers in order to reach a highly compressible regime allowing in particular to observe a more significant effect of shocklets. The present work extends the previous analysis of a DG compressible shear layer to $M_c = 2.2$.

Section 2 describes the flow configuration and reviews key physical and numerical parameters. In section 3, simulations results are validated and the self-similar period is carefully selected. Finally, both DG and PG shear layers are compared in section 4 so as to highlight and explain observed differences between DG and PG turbulent flows.

2 Problem Formulation

2.1 Thermodynamic modelling and initialisation

The DNS of a 3D shear layer at a convective Mach number $M_c = 2.2$ is performed for air modelled as a perfect gas and for the perfluorotripropylamine (FC-70) dense gas. FC-70 belongs to the Bethe-Zel'dovich-Thompson (BZT) sub-family of dense gas. The fundamental derivative of gas dynamics being defined as:

$$\Gamma = \frac{v^3}{2c^2} \frac{\partial^2 p}{\partial v^2} \Big|_s = \frac{c^4}{2v^3} \frac{\partial^2 v}{\partial p^2} \Big|_s = 1 + \frac{\rho}{c} \frac{\partial c}{\partial \rho} \Big|_s \quad (2)$$

with v the specific volume, ρ the density, $c = \sqrt{\partial p / \partial \rho}|_s$ the speed of sound, p the pressure and s the

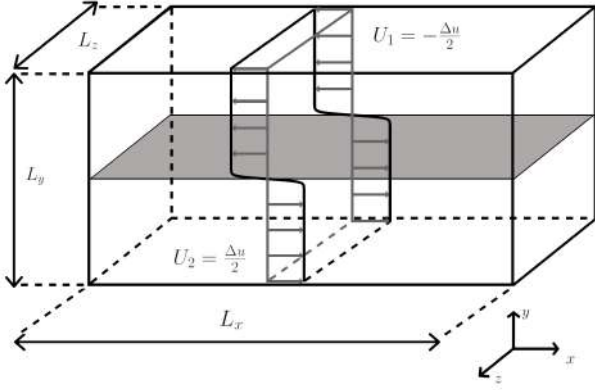


Figure 1: Temporal shear layer configuration

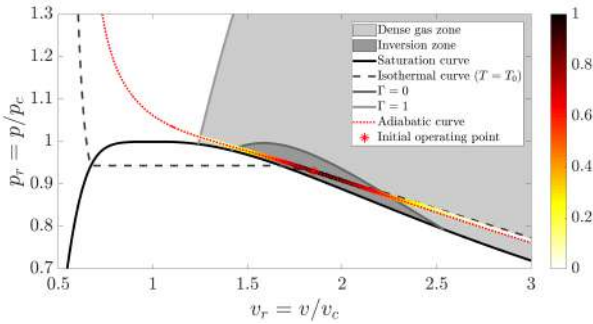


Figure 2: The initial thermodynamic state and its statistical distribution at $\tau = 4000$ are represented in the non-dimensional $p-v$ diagram for the FC-70 BZT dense gas. The DG zone ($\Gamma < 1$) and the inversion zone ($\Gamma < 0$) are plotted for the Martin-Hou equation of state

entropy, BZT dense gases do not only display a $\Gamma < 1$ region as other dense gases but have the particularity to yield $\Gamma < 0$ in a so-called inversion zone located in the vicinity of the critical point (as illustrated in Figure (2)). Physical parameters associated to FC-70 and used in the Martin-Hou EoS accurately describing the DG thermodynamic behaviour are given in Table (1).

Table 1: Physical parameters of FC-70 [12]. The critical pressure p_c , the critical temperature T_c , the boiling temperature T_b and the compressibility factor $Z_c = p_c v_c / (RT_c)$ are the input data for the Martin-Hou equation. The critical specific volume v_c is deduced from the aforementioned parameters. The acentric factor n and the $m = c_{v\infty}(T_c)/R$ ratio are used to compute the heat capacity $c_v(T)$ ($R = \mathcal{R}/M$ being the specific gas constant computed from the universal gas constant \mathcal{R} and M , the gas molar mass). p_c is given in atm and temperatures T_c, T_b in K

	T_c	p_c	Z_c	T_b	m	n
FC-70	608.2	10.2	0.270	488.2	118.7	0.493

The initial thermodynamic state is chosen inside the inversion region in order to maximise compressibility effects and to favour expansion shocklets, which are physically allowed in BZT dense gas. Figure (1) shows the initial state in the $p-v$ diagram for DG flow and its statistical distribution at reduced time $\tau = 4000$, which corresponds to the beginning of the self-similar regime. The initial value of the fundamental derivative for FC-70

is $\Gamma_{initial} = -0.28$. For air, the same values of reduced specific volume and reduced pressure are selected to define the initial thermodynamic state.

Key non-dimensional parameters for the shear layer flow under study are the convective Mach number defined by Eq. (1) and the Reynolds number based on the initial momentum thickness $\delta_{\theta,0}$:

$$Re_{\delta_{\theta,0}} = \Delta u \delta_{\theta,0} / \nu \quad (3)$$

where ν denotes the initial kinematic viscosity. For the Reynolds numbers computed from $\delta_{\theta}(t)$ and the centreline value of λ_x in Table (3), the kinematic viscosity is chosen equal to respectively the mean value over the whole domain and the mean value over the centreplane. The momentum thickness at time t is defined as:

$$\delta_{\theta}(t) = \frac{1}{\rho_0 \Delta u^2} \int_{-\infty}^{+\infty} \bar{\rho} \left(\frac{\Delta u^2}{4} - \tilde{u}_x^2 \right) dy \quad (4)$$

with $\rho_0 = (\rho_1 + \rho_2)/2$ the averaged density and \tilde{u}_x the Favre-averaged streamwise velocity (defined for a flow variable ϕ as $\tilde{\phi} = \overline{\rho\phi}/\bar{\rho}$, with $\bar{\cdot}$ the Reynolds-average operator). The initial momentum thickness Reynolds number is set equal to 160 for PG and DG flows.

Table (2) summarizes the computational parameters retained in the simulations performed for both PG and DG gases (domain size, number of grid elements, differential speed and initial momentum thickness). Note the domain size is twice larger in the y -direction for PG w.r.t. DG because of the longer time required for the PG shear layer to achieve self-similarity as illustrated in Figure (3). Enlarging the computational domain ensures the developing shear layer does not interfere with the lower and upper boundaries.

Table 2: Simulation parameters. L_x, L_y and L_z denote computational domain lengths measured in terms of initial momentum thickness. N_x, N_y and N_z denote the number of grid points. All grids are uniform. Δu and $\delta_{\theta,0}$ are respectively given in $m.s^{-1}$ and nm

	$L_x:L_y:L_z$	$N_x:N_y:N_z$	Δu	$\delta_{\theta,0}$
Air	688:688:172	1024:1024:256	753.0	6.153
FC-70	688:344:172	1024:512:256	125.1	93.77

The temporal shear layer comprises two streams flowing in opposite directions. Velocity is initially equal to $-\Delta u/2$ and $\Delta u/2$ respectively in the upper and lower stream (see also Figure (1)). In addition, periodic boundary conditions are imposed in the x and z directions and non-reflective conditions are set in the y direction. The NSCBC model proposed by Poinot & Lele (1992) [13] is used. The streamwise velocity field is initialised using an hyperbolic tangent profile:

$$\tilde{u}_x(y) = \frac{\Delta u}{2} \tanh\left(-\frac{y}{2\delta_{\theta,0}}\right) \quad (5)$$

The mean initial velocity field is set equal to zero in the y and z directions. A Passot-Pouquet spectrum is used to compute the initial velocity fluctuations:

$$E(k) = (k/k_0)^4 \exp(-2(k/k_0)^2) \quad (6)$$

where k denotes the wavenumber. The peak wavenumber k_0 controls the size of the initial turbulent structures. For both PG and DG shear layers, k_0 is set equal to $2\pi/(L_x/8)$. The velocity field is then spatially filtered to initialize turbulence only inside the initial momentum thickness. Initial structures are larger compared to the previous analysis for $M_c = 1.1$ [1]. It has been indeed noticed that larger initial turbulent structures accelerate the transition to self-similarity.

2.2 Governing equations

In order to describe the temporally evolving shear layer, the unsteady, three-dimensional, compressible Navier-Stokes equations are solved (see details in Vadrot et al., 2020[1]). Transport coefficients are modelled using respectively the Chung et al. model [14] for DG flows and the Sutherland's law completed with a constant Prandtl number equal to 0.71 for PG flows.

In this study, comparison between PG and DG shear layers is mainly conducted through the analysis of the turbulent kinetic energy (TKE) equation, which highlights terms at stake in the development of turbulence in shear layers. Density, pressure and velocity are decomposed into mean and fluctuating components as follows:

$$\begin{cases} \rho = \bar{\rho} + \rho' \\ p = \bar{p} + p' \\ u_i = \bar{u}_i + u_i'' \end{cases} \quad (7)$$

where $\bar{\phi}$ denotes the Reynolds average for a flow variable ϕ and $\tilde{\phi}$ the Favre average. Reynolds averaging is equivalent here to plane averaging along x and z directions because of the periodic boundary conditions. With Reynolds and Favre fluctuations respectively noted ϕ' and ϕ'' , the specific turbulent kinetic energy is defined as $\tilde{k} = \frac{1}{2} \overline{u_i'' u_i''}$. The TKE equation describing the evolution of k is obtained from an averaging process of the Navier-Stokes equation and reads:

$$\begin{aligned} \frac{\partial \tilde{\rho} \tilde{k}}{\partial t} + \frac{\partial \tilde{\rho} \tilde{k} \tilde{u}_j}{\partial x_j} = & \underbrace{-\overline{\rho u_i'' u_j''} \frac{\partial \tilde{u}_i}{\partial x_j}}_{\text{Production}} - \underbrace{\overline{\tau'_{ij} \frac{\partial u_i''}{\partial x_j}}}_{\text{Dissipation}} \\ & \underbrace{-\frac{1}{2} \frac{\partial \overline{\rho u_i'' u_i'' u_j''}}{\partial x_j}}_{\text{Turbulent transport}} - \underbrace{\frac{\partial \overline{p' u_i''}}{\partial x_i}}_{\text{Pressure transport}} + \underbrace{\frac{\partial \overline{u_i'' \tau'_{ij}}}{\partial x_j}}_{\text{Viscous transport}} \\ & \underbrace{+ \overline{p' \frac{\partial u_i''}{\partial x_i}}}_{\text{Pressure dilatation}} - \underbrace{\overline{u_i'' \left(\frac{\partial \bar{p}}{\partial x_i} - \frac{\partial \bar{\tau}_{ij}}{\partial x_j} \right)}}_{\text{Mass-flux term}} \end{aligned} \quad (8)$$

where $\tau_{ij} = \mu \left(\frac{\partial u_i}{\partial x_j} + \frac{\partial u_j}{\partial x_i} - \frac{2}{3} \frac{\partial u_k}{\partial x_k} \delta_{ij} \right)$ denotes the viscous stress tensor (with μ the dynamic viscosity). The main terms in Eq. (8) are production, dissipation and transport terms. Pressure dilatation and mass-flux term are equal to zero in the incompressible case. In addition to compressible Navier-Stokes equations, thermal and calorific PG Equation of State (EoS) are used to describe the air flow:

$$\begin{cases} p = \rho RT \\ e = e_{ref} + \int_{T_{ref}}^T c_v(T') dT' \end{cases} \quad (9)$$

where R is the specific gas constant, c_v the specific heat capacity, T the temperature.

The Martin-Hou EoS is retained to model FC-70 since it has been previously established [15] that it provides an accurate representation of the dense gas thermodynamic

behaviour:

$$\begin{cases} p = \frac{RT}{v-b} + \sum_{i=2}^5 \frac{A_i + B_i T + C_i e^{-kT/T_c}}{(v-b)^i} \\ e = e_{ref} + \int_{T_{ref}}^T c_v(T') dT' \\ + \sum_{i=2}^5 \frac{A_i + C_i (1 + kT/T_c) e^{-kT/T_c}}{(i-1)(v-b)^{i-1}} \end{cases} \quad (10)$$

where $(\cdot)_{ref}$ denotes a reference state, $b = v_c(1 - (-31, 883Z_c + 20.533)/15)$, $k = 5.475$ and the coefficients A_i , B_i and C_i are numerical constants determined in [16].

2.3 Numerical Setup

The present DNS are performed using the explicit unstructured numerical solver AVBP. AVBP is designed for massively parallel computation and is used to perform LES as well as DNS simulations (Refs. [17], [18]). The 3D unsteady compressible Navier-Stokes equations coupled with the perfect gas EoS (Eq. (9)) for Air and the MH EoS for FC-70 (Eq. (10)) are solved using a two-step time-explicit Taylor Galerkin scheme (TTGC) for the hyperbolic terms based on a cell vertex formulation [19]. The scheme provides high spectral resolution and low numerical dissipation, ensuring a third-order accuracy in space and time. The scheme is completed with a shock capturing method. In regions where strong gradients exist, an additional dissipation term is added following the approach of Cook and Cabot [20].

3 Verification & Validation of the shear layer DNS

Shear layers development can be decomposed into three main stages. The first stage is a kind of delay, where turbulent production evolves very slowly and which is likely to be a transition of modes. In the next stage, some unstable modes are amplified leading to an unstable growth phase, where the production term increases abruptly, reaching a peak. Finally, turbulent production relaxes until it reaches a plateau, the so-called self-similar period. During this regime, turbulence is in a statistically stationary state: momentum thickness evolves linearly with time and mean velocity and Reynolds stress profiles collapse into a single curve.

Since production, dissipation and transport terms con-

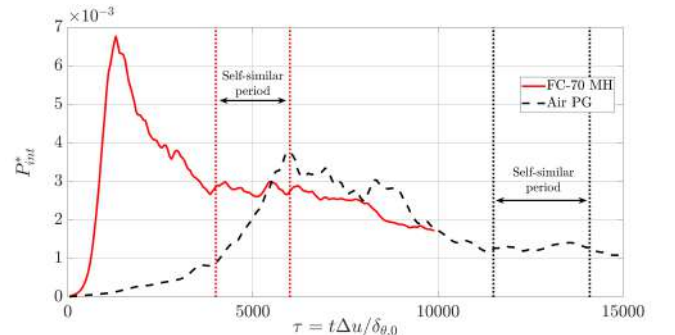


Figure 3: Temporal evolution of the non-dimensional streamwise production term integrated over the whole domain $P_{int}^* = (1/(\rho_0 \Delta u^3)) \int_{L_y} \bar{\rho} P_{xx} dy$ (with $\bar{\rho} P_{xx}(y) = -\overline{\rho u_x'' u_y'' \frac{\partial \tilde{u}_x}{\partial y}}$) at $M_c = 2.2$. Comparison is made between air and FC-70

tribution to the TKE equation is studied over the self-similar stage, this stage must be rigorously identified.

The following relationship between shear layer growth rate and production power ($\bar{\rho}P_{xx} = -\overline{\rho u_x'' u_y'' \frac{\partial \bar{u}_x}{\partial y}}$) has been established by Vreman *et al.* [21]:

$$\delta_\theta' = \frac{d\delta_\theta}{dt} = \frac{2}{\rho_0 \Delta u^2} \int \bar{\rho} P_{xx} dy \quad (11)$$

One can deduce from Eq. (11) that a constant integrated production term leads to a linear evolution of the momentum thickness. Figure (3) displays the temporal evolution of the non-dimensional streamwise production integrated over the whole domain. The above-mentioned successive stages of shear layer development can be identified and the self-similar period properly selected. Note that the same process was used in [1] for the $M_c = 1.1$ shear layer.

One can note that a much longer time (about two times longer) is required to achieve a plateau for PG when compared to DG. Selected self-similar periods are indicated in Figure (3): $\tau = t\Delta u/\delta_{\theta,0} \in [4000; 6000]$ and $\tau \in [11500; 14100]$ respectively for DG and PG shear layers. One can also note that levels of production for the DG flow during the self-similar period is about two times larger than the one for the PG flow. This ratio is also found in Figure (6), providing momentum thickness growth rates for both types of flow, which is found consistent with Eq. (11).

Table 3: Non-dimensional parameters computed at the beginning (τ_i) and at the end (τ_f) of the self-similar period for $M_c = 2.2$ simulations. Re_{λ_x} denotes the Reynolds number based on the longitudinal Taylor microscale $\lambda_x = \sqrt{2u_x'^2/(\partial u_x'/\partial x)^2}$ computed at the centreline. L_η denotes the Kolmogorov length scale computed at the centreline

	Re_{δ_θ}	Re_{λ_x}	$L_\eta/\Delta x$	l_x/L_x	l_z/L_z
Air (τ_i)	3487	146	1.44	0.12	0.07
Air (τ_f)	3700	191	1.64	0.11	0.10
FC-70 (τ_i)	4663	263	0.52	0.10	0.06
FC-70 (τ_f)	6259	390	0.57	0.16	0.05

Table (3) provides computed values of key physical parameters which allow to confirm the validation of the present DNS. The integral lengths l_x and l_z are defined using the streamwise velocity field:

$$l_x = \frac{1}{2u_x^2} \int_{-L_x/2}^{L_x/2} \overline{u_x(\mathbf{x})u_x(\mathbf{x} + r\mathbf{e}_x)} dr \quad (12)$$

$$l_z = \frac{1}{2u_x^2} \int_{-L_z/2}^{L_z/2} \overline{u_x(\mathbf{x})u_x(\mathbf{x} + r\mathbf{e}_z)} dr \quad (13)$$

The computed integral length scales show that the domain size is sufficiently large to ensure the size of the largest turbulent structures are not constrained by the streamwise and spanwise domain lengths. The highest value ($l_x/L_x = 0.16$) is obtained for DG flow in the streamwise direction at the end of the self-similar period. As a comparison, the reference PG DNS of Pantano & Sarkar [22] displays normalized integral length scale reaching 0.18 for a $M_c = 0.7$ shear layer in air and other computed values remain close to the ones obtained in this study. The ratio $L_\eta/\Delta x$ characterizes the resolution of the simulations, with a larger ratio indicating a better resolution. The minimum value $L_\eta/\Delta x = 0.52$ is obtained for DG flow. For PG flow, the ratio is three times larger because of low-dissipation in high compressible regimes. As a comparison, Pantano & Sarkar's ratio

is about 0.38 for their most resolved (PG) simulation [22]. One can consider that turbulent scales are adequately resolved since the turbulent kinetic energy is very low close to the Kolmogorov scale [23].

Additional simulations have nonetheless been per-

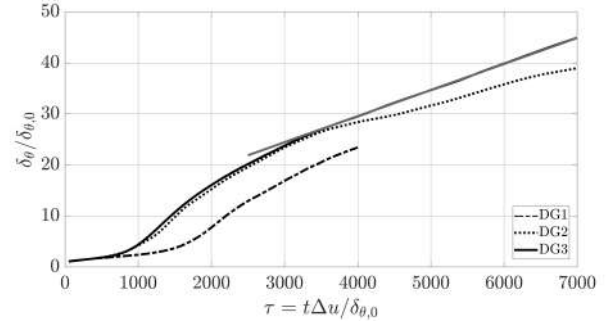


Figure 4: Temporal evolution of the shear layer momentum thickness for DG shear layer simulations which features are given in Table (4).

formed for DG shear layer in order to confirm proper resolution and domain size. Table (4) reviews these simulations (all performed at $M_c = 2.2$ and $Re_{\delta_{\theta,0}} = 160$) with their corresponding computational parameters.

Table 4: Simulation parameters for DG shear layer. L_x, L_y, L_z : computational domain lengths normalized by $\delta_{\theta,0}$. N_x, N_y, N_z : number of grid points per direction. L_0 : initial turbulent structures size normalized by $\delta_{\theta,0}$

	$L_x:L_y:L_z$	$N_x:N_y:N_z$	L_0
DG1	344:172:86	1024:512:256	$L_x/48$
DG2	344:344:86	1024:1024:256	$L_x/4 = 86$
DG3	648:344:172	1024:512:256	$L_x/8 = 86$

Figure (4) displays the temporal evolution of the momentum thickness for the simulations listed in Table (4). DG1 is performed with the same domain lengths and size of initial turbulent structures (relatively to the initial momentum thickness) as in the previous study at $M_c = 1.1$ [1]. At $\tau = 4000$, self-similarity is not yet achieved but flow field inspection indicates the y boundaries of the domain have been reached. DG2 is thus conducted with a double size domain in the y direction and smaller initial turbulent structures corresponding to $L_x/4 = 86\delta_{\theta,0}$, in order to accelerate transition to turbulence. Simulations show that the size change for the initial structures only impacts the time required to reach the unstable growth phase but not the growth rate itself.

However, one can notice next for DG2 a significant drop in the growth rate at around $\tau = 4000$, which prevents from reaching self-similarity. Figure (5) reports integral length scales in the z direction for DG2 and DG3 simulations. At around $\tau = 4000$, the integral length scales l_z/L_z suddenly decreases for DG2 after having reached a value of 0.2: the DG2 domain is thus not large enough to account for spanwise turbulent structures. The domain is therefore doubled in size in the x and z directions, which corresponds to DG3 simulation, used to compare results between DG and PG flows. Even though the grid refinement in the y direction is divided by a factor 2 when moving from DG2 to DG3, the resolution remains large enough for DG3 to capture shear layer growth. The momentum thickness evolution reaches a perfectly linear stage for DG3 (see Figure (4)) with achievement of self-similarity as confirmed by Figure (3).

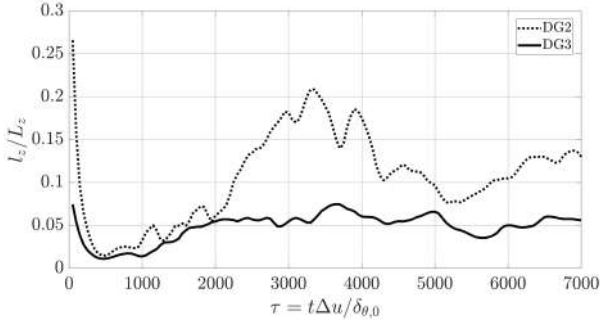


Figure 5: Temporal evolution of the normalized integral length scale l_z/L_z for DG shear layer simulations given in Table (4)

4 Comparison between DG and PG shear layer flows

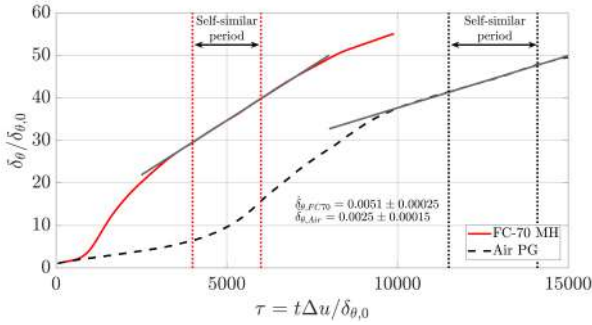


Figure 6: Temporal evolution of the shear layer momentum thickness for DG and PG flows

Figure (6) displays the evolution of the momentum thickness normalized by its initial value with the non-dimensional time $\tau = t\Delta u/\delta_{\theta,0}$. The three main phases discussed in section 3 can be clearly identified. Interestingly, PG and DG shear layers evolve very differently for this highly compressible $M_c = 2.2$ regime, in contrast with the previous analysis at $M_c = 1.1$ reported in [1]. The initial delay corresponding to a transition of modes is found much smaller for the DG flow; similarly, the unstable growth is also shorter for DG when compared to PG. The most noticeable difference is the growth rate value computed during the self-similar period: as reported in Figure (6) the DG growth rate is about twice the PG one, consistently with the levels of integrated turbulent production displayed in Figure (3) and previously discussed in section 3. The DG shear layer develops two times faster when compared to a classical PG shear layer in the high compressible regime ($M_c = 2.2$).

Following the methodology used in [22] to study the impact of M_c on the shear layer growth rate, TKE equation terms are investigated. Once selected a relevant self-similar time period, flow solutions are averaged over this period and over the two periodic directions (x and z). Figure (7) displays these quantities drawn versus the non-dimensional cross-stream direction $y/\delta_{\theta}(t)$. Consistently with momentum thickness growth (Figure (6)) and integrated turbulent production (Figure (3)), much larger production, dissipation and transport terms are observed for DG flows. A feature previously observed for $M_c = 1.1$ [1] is found amplified for $M_c = 2.2$: the propagation of the TKE terms at the boundaries of the mixing layer is slower for dense gas flows; curves are in-

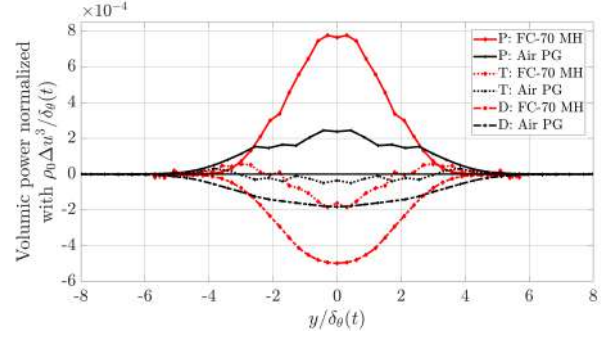


Figure 7: Distribution of the volumetric normalized powers over the non-dimensional cross-stream direction $y/\delta_{\theta}(t)$. P: Production, D: Dissipation and T: Transport are normalized by $\rho_0\Delta u^3/\delta_{\theta}(t)$. Distributions are averaged between the upper and the lower stream to get perfectly symmetrical distributions

deed widened for PG with respect to DG. Strong turbulence is localized at the center of the DG shear layer unlike the PG shear layer, where turbulence is spread over the whole shear layer including its upper and lower boundaries.

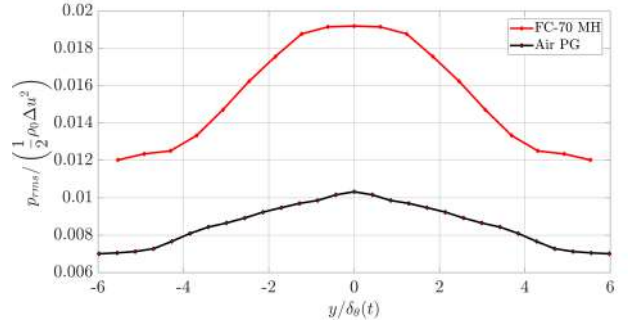


Figure 8: Root mean square values of pressure, averaged over the self-similar period and plotted along the normalized y direction. Comparison between FC-70 and air

For PG flows, the well-known compressibility-related reduction of the momentum thickness growth rate is explained by a reduction of pressure-strain terms. These terms only explicitly appear in the turbulent stress tensor equations. Their abatement is itself caused by a reduction of normalized pressure fluctuations, which causes a communication breakdown across large structures. Further explanations are given by the sonic-eddy model [24]. Figure (8) reports the root mean square values of pressure averaged over the self-similar period. In PG flows, normalized pressure fluctuations are significantly reduced at $M_c = 2.2$, leading to a reduced growth rate consistently with the well-known effect. Meanwhile in DG flows, normalized pressure fluctuations are doubled. This thermodynamic effect induces much larger pressure-strain terms and thus larger turbulent intensity, leading to a faster growth. Note that such effect was not observed in the previous analysis at $M_c = 1.1$. Increasing the convective Mach number appears to intensify discrepancies between DG and PG flows and reveal a different behavior for DG shear layers, less influenced by compressibility effects.

5 Conclusion

DNS of a temporal compressible mixing layer at convective Mach number $M_c = 2.2$ are achieved for air de-

scribed as a perfect gas and for FC-70, a BZT dense gas, described using the Martin-Hou EoS. Results are validated for both types of gases and a self-similar period carefully identified. The well-known compressibility-related reduction of the momentum thickness growth rate, caused by a reduction of normalized pressure fluctuations, does not seem to apply to DG flows in the high compressible regime studied. It remains to fully explain the physical mechanisms yielding these DG/PG differences. The influence of initial thermodynamic operating conditions, impacting both the fundamental derivative Γ and the transport coefficients, is also currently investigated.

Acknowledgment

This work is supported by the JCJC ANR EDGES project, grant #ANR-17-CE06-0014-01 of the French Agence Nationale de la Recherche. Simulation have been carried out using HPC resources at CINES under the project grant #A0062A07564.

References

- [1] A. Vadrot, A. Giauque, and C. Corre, "Analysis of turbulence characteristics in a temporal dense gas compressible mixing layer using direct numerical simulation," *Journal of Fluid Mechanics*, vol. 893, 2020.
- [2] P. Cinnella and P. M. Congedo, "Numerical solver for dense gas flows," *AIAA Journal*, vol. 43, no. 11, pp. 2458–2461, 2005.
- [3] F. J. Durá Galiana, A. P. Wheeler, and J. Ong, "A study of trailing-edge losses in ORC turbines," *Journal of Turbomachinery*, vol. 138, no. 12, 2016.
- [4] L. Sciacovelli, P. Cinnella, and F. Grasso, "Small-scale dynamics of dense gas compressible homogeneous isotropic turbulence," *Journal of Fluid Mechanics*, vol. 825, pp. 515–549, 2017.
- [5] A. Giauque, C. Corre, and M. Menghetti, "Direct numerical simulations of homogeneous isotropic turbulence in a dense gas," *Journal of Physics: Conference Series*, vol. 821, no. 1, p. 012017, 2017.
- [6] A. Giauque, C. Corre, and A. Vadrot, "Direct numerical simulations of forced homogeneous isotropic turbulence in a dense gas," *Journal of Turbulence*, pp. 1–23, 2020.
- [7] L. Sciacovelli, P. Cinnella, and X. Gloerfelt, "Direct numerical simulations of supersonic turbulent channel flows of dense gases," *Journal of Fluid Mechanics*, vol. 821, pp. 153–199, 2017.
- [8] L. Sciacovelli, P. Cinnella, and X. Gloerfelt, "Analysis of dense gas effects in compressible turbulent channel flows," in *Direct and Large-Eddy Simulation XI*, pp. 341–347, Springer, 2019.
- [9] O. Zeman, "Dilatation dissipation: the concept and application in modeling compressible mixing layers," *Physics of Fluids A: Fluid Dynamics*, vol. 2, no. 2, pp. 178–188, 1990.
- [10] S. Sarkar, G. Erlebacher, M. Hussaini, and H. Kreiss, "The analysis and modeling of dilatational terms in compressible turbulence," *Journal of Fluid Mechanics*, vol. 227, pp. 473–493, 1991.
- [11] D. C. Wilcox, "Dilatation-dissipation corrections for advanced turbulence models," *AIAA journal*, vol. 30, no. 11, pp. 2639–2646, 1992.
- [12] M. S. Cramer, "Negative nonlinearity in selected fluorocarbons," *Physics of Fluids A: Fluid Dynamics*, vol. 1, no. 11, pp. 1894–1897, 1989.
- [13] T. J. Poinso and S. K. Lele, "Boundary conditions for direct simulations of compressible viscous flows," *Journal of computational physics*, vol. 101, no. 1, pp. 104–129, 1992.
- [14] T. H. Chung, M. Ajlan, L. L. Lee, and K. E. Starling, "Generalized multiparameter correlation for nonpolar and polar fluid transport properties," *Industrial & engineering chemistry research*, vol. 27, no. 4, pp. 671–679, 1988.
- [15] A. Guardone, L. Vigeveno, and B. Argrow, "Assessment of thermodynamic models for dense gas dynamics," *Physics of Fluids*, vol. 16, no. 11, pp. 3878–3887, 2004.
- [16] J. J. Martin and Y. Hou, "Development of an Equation of State for Gases," *AIChE journal*, vol. 2, no. 4, pp. 142–151, 1955.
- [17] G. Desoutter, C. Habchi, B. Cuenot, and T. Poinso, "DNS and modeling of the turbulent boundary layer over an evaporating liquid film," *International Journal of Heat and Mass Transfer*, vol. 52, no. 25-26, pp. 6028–6041, 2009.
- [18] F. Cadieux, J. A. Domaradzki, T. Sayadi, T. Bose, and F. Duchaine, "DNS and LES of separated flows at moderate Reynolds numbers," *Proceedings of the 2012 Summer Program, CTR, Stanford, CA, June*, pp. 77–86, 2012.
- [19] O. Colin and M. Rudgyard, "Development of high-order Taylor–Galerkin schemes for LES," *Journal of Computational Physics*, vol. 162, no. 2, pp. 338–371, 2000.
- [20] A. W. Cook and W. H. Cabot, "A high-wavenumber viscosity for high-resolution numerical methods," *Journal of Computational Physics*, vol. 195, no. 2, pp. 594–601, 2004.
- [21] A. W. Vreman, N. D. Sandham, and K. H. Luo, "Compressible mixing layer growth rate and turbulence characteristics," *Journal of Fluid Mechanics*, vol. 320, pp. 235–258, 1996.
- [22] C. Pantano and S. Sarkar, "A study of compressibility effects in the high-speed turbulent shear layer using direct simulation," *Journal of Fluid Mechanics*, vol. 451, pp. 329–371, 2002.
- [23] P. Moin and K. Mahesh, "Direct numerical simulation: a tool in turbulence research," *Annual review of fluid mechanics*, vol. 30, no. 1, pp. 539–578, 1998.
- [24] R. E. Breidenthal, "Sonic eddy - a model for compressible turbulence," *AIAA Journal*, vol. 30, no. 1, pp. 101–104, 1992.

LARGE EDDY SIMULATION OF TRANSCRITICAL AND SUPERCRITICAL FLOWS

B. Cuenot¹ and T. Schmitt²

¹*CERFACS, 42 A. G. Coriolis 31057 Toulouse, France*

²*Laboratoire EM2C, CNRS, CentraleSupélec, Université Paris-Saclay, 3 rue Joliot Curie, 91192 Gif-sur-Yvette cedex, France*

Abstract

Transcritical and supercritical flows are encountered in cryogenic rocket engines, where reactants are stored and injected at high pressure and low temperature. This implies specific thermodynamic and diffusive behaviors, which have direct impacts on the combustion and flow dynamics. To predict such systems, the Large Eddy Simulation approach is today commonly used as it allows a good description of the turbulence and other transient phenomena. The formulation involves the fully compressible flow equations, associated to a cubic equation of state and modified transport properties to properly describe the dense fluid. In the paper, the complete formulation is recalled and specific numerical treatments implemented in the code AVBP to ensure accuracy and robustness are described. Validation test cases as well as rocket engine applications are then presented to demonstrate the capacities of the numerical approach and the reliability of the models for such complex systems. Ongoing developments and future works are finally given.

1 Introduction

The combustion chamber in Liquid Rocket Engines (LRE) reaches extremely high pressure levels, exceeding the critical pressure (P_c) of most propellants. Depending on their injection temperature respectively to their critical one (T_c), reactants are injected in different thermodynamic conditions. With low P_c and T_c (12.8 bars and 33 K respectively), hydrogen, commonly used in LREs, is most of the time supercritical (i.e. gaseous) before burning. Liquid oxygen, having $P_c = 50.5$ bars is often injected at supercritical pressure and subcritical temperature ($T_{c,O_2} = 155$ K), a regime generally referred to as transcritical. Today seen as a promising alternative fuel, methane has a P_c of 46.5 bars, i.e., much higher than hydrogen but still lower than usual chamber pressures, meaning also a supercritical regime. However in the context of LRE manufacturing and operating costs reduction, which introduces additional constraints linked to operational flexibility and engine reusability, methane may be either at subcritical or supercritical pressure and may even change state during a launch.

In the transcritical regime, the fluid thermodynamic behavior changes drastically and the ideal gas Equation of State (EoS) does not hold anymore [1]. Transport properties are also impacted and the surface tension vanishes. This supercritical fluid state has therefore direct consequences on the fuel injection, atomization and combustion processes occurring in the LRE. Instead of forming droplets as in subcritical conditions, the supercritical, dense fluid diffuses in the surrounding lighter fluid without forming a thin interface [2, 3]. This leads to modified mixing processes and, in turn, modified chem-

ical activity. These phenomena have been observed in lab-scale experiments, for both LO_2/H_2 and LO_2/CH_4 [4, 5]. Measurements are however very difficult in such extreme conditions, and it is essential to have numerical tools for the understanding and prediction of flames, heat transfer and acoustics in LRE combustion chambers. If sufficiently reliable and accurate, such tools may be extremely useful for the design of LRE at a reduced cost in comparison with real tests.

2 Equations and models

Stable combustion in a LRE occurs in the turbulent, thin flame non-premixed regime. The very fast chemistry of H_2/O_2 leads to a flame anchored at the injector lips, i.e., a purely diffusion flame controlled by turbulent mixing [4]. As CH_4/O_2 chemistry is slower, the flame may detach and lead to a partially premixed combustion mode [5]. It is then important to include chemical kinetics in the model equations. Turbulence is treated with the Large-Eddy-Simulation (LES) approach for a good description of the intermittent flow structures and their interaction with the flame.

The governing equations therefore are based on the spatially filtered (in the sense of LES), fully compressible Navier-Stokes equations, added with species conservation equations and closed with a real-gas EoS. They write:

$$\frac{\partial \bar{\rho} \tilde{u}_i}{\partial t} + \frac{\partial}{\partial x_j} (\bar{\rho} \tilde{u}_i \tilde{u}_j) = - \frac{\partial}{\partial x_j} [\bar{P} \delta_{ij} - \bar{\tau}_{ij} + \tau_{ij}^t] \quad (1)$$

$$\frac{\partial \bar{\rho} \tilde{E}}{\partial t} + \frac{\partial}{\partial x_j} (\bar{\rho} \tilde{E} \tilde{u}_j) = - \frac{\partial}{\partial x_j} [\tilde{u}_i (\bar{P} \delta_{ij} - \bar{\tau}_{ij}) + \bar{q}_j + q_j^t] + \bar{\omega}_T \quad (2)$$

$$\frac{\partial \bar{\rho}_k}{\partial t} + \frac{\partial}{\partial x_j} (\bar{\rho}_k \tilde{u}_j) = - \frac{\partial}{\partial x_j} [\bar{J}_{j,k} + J_{j,k}^t] + \bar{\omega}_k \quad (3)$$

where $\bar{\mathcal{Q}}$ and $\tilde{\mathcal{Q}}$ denote spatial and mass-weighted (Favre) spatial filter of any quantity \mathcal{Q} . In Eq. (1) to Eq. (3), which respectively correspond to the conservation laws for momentum, total energy and species, the following symbols (ρ , u_i , E , ρ_k) denote the density, the velocity components, the total energy per unit mass ($E = e_c + e$, with e the sensible energy) and the density of the chemical species k : $\rho_k = \rho Y_k$ for $k = 1$ to N (where N is the total number of species) with Y_k the mass fraction. P denotes the pressure, τ_{ij} the stress tensor, q_j the heat flux vector and $J_{j,k}$ the vector of the diffusive flux of species k . The source term in the species transport equations ($\bar{\omega}_k$ in Eq. (3)) comes from the consumption or production of species by chemical reactions. The source term in the total energy equation ($\bar{\omega}_T$ in Eq. (2)) is the heat release rate, which is the variation of sensible

enthalpy associated to species variation:

$$\dot{\omega}_T = - \sum_{k=1}^N \dot{\omega}_k h_k^0 \quad (4)$$

with h_k^0 , the mass enthalpy of formation of species k . The stress tensor τ_{ij} is calculated from the filtered velocity, using a viscosity calculated with the Chung et al. method [6]. The species and heat fluxes (J_k and q) use classical gradient approaches, with a constant Schmidt (Sc_k) number while heat diffusion coefficient is also computed with the Chung et al. method. The subgrid scale quantities (stress tensor τ_{ij}^t , heat flux q^t , species flux J_k^t) are computed with a turbulent viscosity ν_t using the WALE model [7]. The above conservation equations are closed with a cubic EoS, either Peng-Robinson (PR) [8] or Soave-Redlich-Kwong (SRK) [9], which are very similar and can be written in the following generic form:

$$P = \frac{RT}{v-b} - \frac{\theta(T)}{v^2 + d_1bv + d_2b^2} \quad (5)$$

$$\text{PR} : (d_1, d_2) = (2, -1) \quad (6)$$

$$\text{SRK} : (d_1, d_2) = (1, 0) \quad (7)$$

where P is the pressure, T the temperature, v the molar volume ($v = W/\rho$ with W the mean molar mass of the mixture), $\theta(T)$ and b are parameters computed with respect to the critical points of the species contained in the mixture and their acentric factor.

Turbulent combustion modeling for diffusion flames is usually based on the flamelet concept. The flame structure is described as laminar strained flames, which are pre-tabulated in look-up tables as functions of the mixture fraction Z , for given boundary conditions and strain rates [10]. In the case of very fast chemistry as for H_2/O_2 combustion, the infinitely fast chemistry solution is a good approximation for the flame structure. In this case, only the equilibrium is tabulated with Z , and the source term $\dot{\omega}_k$ is calculated as a relaxation to equilibrium [11, 12]. The interaction with turbulence is then introduced using an β -function shape parameterized with the mixture fraction mean and variance. Flamelet approaches have demonstrated their capacity to accurately describe stable turbulent diffusion flames in rocket engines [12, 13, 14, 15]. However as they force a stable laminar flame structure, these methods are less performant in transient cases or in the occurrence of heat losses. These effects can be taken into account with the flamelet concept, but at the cost of extended look-up tables which may be difficult to build and costly to handle in CFD codes [16]. Other approaches may be used, with various levels of complexity and performance [17]. In particular, the direct integration of chemistry is very attractive as it is able to explicitly describe transient processes as well as the interaction of the flame with any flow feature [18].

3 Applications

The above set of equations and models have been implemented in the code AVBP [19, 12], a third-order finite element solver on unstructured meshes [20]. Because of the non-linear nature of the thermodynamics, simulations of high-pressure flows are subject to stability issues [21]. The numerical stabilization method used in AVBP relies on artificial viscosity. Details are given in [22, 12]. For sufficiently refined meshes, the simulation naturally tends to Direct Numerical Simulation (DNS),

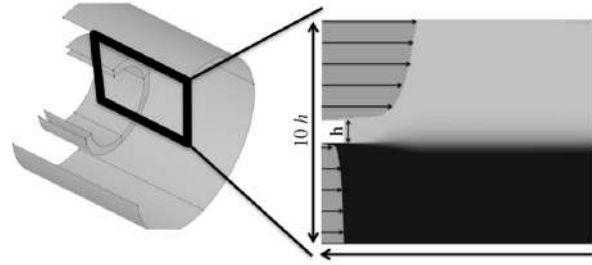


Figure 1: Configuration and 2D computational domain used in DNS of flame stabilization [23]

which means the direct resolution of the full turbulence spectrum, i.e., without any model. As illustrated below this approach is useful to understand the details of physical processes.

In the following, the model is applied to various configurations of increasing complexity, to show the capacities of numerical study of transcritical and supercritical reacting flows.

3.1 DNS of flame stabilization behind a splitter plate

The mechanism of flame anchoring at the coaxial injector is critical as it ensures the flame stability. It is the result of the flow dynamics behind the splitter that separates the ergols, the combustion chemistry and the heat transfer in the splitter. To have a detailed description of these phenomena, DNS is performed in a simplified configuration, illustrated in Figure (1). In all cases below, chemistry is described with reduced chemical schemes accounting for about 10 species.

Ruiz et al. [23] performed the DNS of a H_2/O_2 transcritical flame at 10 MPa. In this benchmark case, light gaseous H_2 is injected at high speed and 150 K, while O_2 is transcritical at injection, at a temperature of 100 K and with a low velocity. The resulting density ratio is about 80, which is a very difficult challenge for numerics. The turbulence that develops behind the splitter requires typically a grid cell of $h/100$ where h is the splitter height. The obtained non-reacting flow is illustrated in Figure (2) (top) with an instantaneous snapshot of the density field. As expected for supercritical fluids, no atomization of the dense O_2 is observed, replaced by the formation of elongated ligaments and diffusive mixing between the two ergols. After ignition a diffusion flame stabilizes at the splitter plate surface Figure (2) (bottom), where a small recirculation zone develops and allows the flame anchoring. The flame is highly wrinkled by the strong turbulence induced by the shear flow, but never quenches. The temperature increase in the burnt gas bring them back to perfect gas thermodynamics.

In [23] the splitter plate surface is considered adiabatic. The impact of heat losses on the flame anchoring mechanism was studied by Mari et al. [25], with coupled combustion - heat conduction simulations. Although the heat flux at the splitter tip reaches about 14 MW/m^2 , the flame stays attached to the solid (Figure (3)). The heat loss is partially compensated by the pre-heating of the ergols along the splitter during injection, and by the near-wall chemistry, where the lower temperature favors the exothermic formation of radicals such as HO_2 and H_2O_2 as found for example in ignition. This explains the peak of heat release rate at the splitter tip, visible in Figure (3).

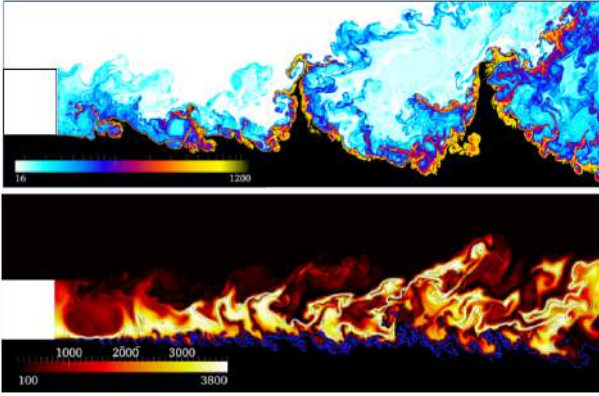


Figure 2: DNS of H_2/O_2 transcritical flow and flame: density [kg/m^3] in the non-reacting flow (top) and temperature [K] of the flame (bottom) [24].

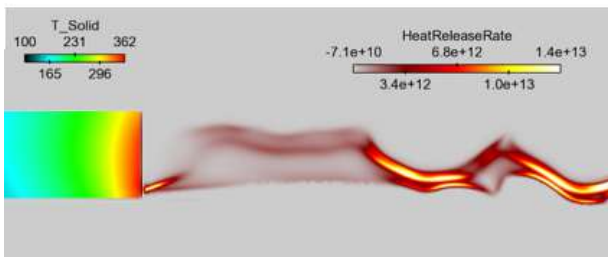


Figure 3: DNS of H_2/O_2 transcritical flame coupled with heat conduction in the splitter: heat release rate [$J/m^3/s$] and solid temperature [K] [25].

Recent DNS studies focused on CH_4/O_2 combustion, in doubly transcritical conditions [26]. Despite the 2D mesh and some uncertainty linked to chemical kinetics of high pressure methane oxy-combustion, the simulation revealed the underlying mechanisms of flame stabilization. Compared to H_2/O_2 flames, here the weaker flame leads to a more intermittent stabilization, allowing reactant leakage and partial premixing close to the wall. The impact of heat loss in coupled combustion - heat conduction simulations, in comparison with adiabatic surfaces, is found similar to the H_2/O_2 case described above, with a peak of heat release at the splitter tip (Figure (4)).

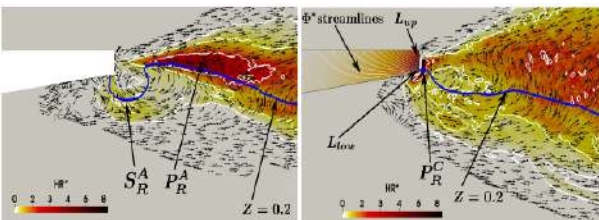


Figure 4: DNS of CH_4/O_2 doubly transcritical flame: adiabatic splitter plate (left) and coupled heat conduction in the splitter (right) [26]. Heat release rate (non-dimensionalized) and velocity vectors. The blue line is the isocontour of mixture fraction at 0.2, and Φ is the thermal flux. In the adiabatic case P_R^A and S_R^A are primary and secondary reaction zones, while only a primary zone P_R^C is observed in the coupled case. The flame intermittently anchors between locations L_{up} and L_{low} .

3.2 Validation : LES of a single injector configuration

The Mascotte test bench, operated at ONERA [3], has been specifically designed to study H_2/O_2 and CH_4/O_2 combustion in LRE conditions [3, 4]. It can reach chamber pressures up to 100 bars and has the capacity to apply transverse acoustic perturbations [27]. Although measurements are very difficult in these conditions, optical access and advanced laser techniques such as CARS or PLIF, as well as direct imaging give some information about the flame shape and stability. The configuration consists in a square combustion chamber of 50 mm side length, with lateral windows, fed with a coaxial injector and closed by a choked nozzle.

For the purpose of validation, three test cases have been investigated in [12], named A60, C60 and G2 reproducing transcritical flames [28, 5]. Dense oxygen (i.e. liquid-like oxygen) is injected at low velocity (less than 10 m/s), surrounded by gaseous hydrogen cases A60 and C60 or methane (case G2) flowing at high velocity (more than 100 m/s), in a chamber at supercritical pressure for both reactants (60 bar for case A60 and C60, 56 bar for case G2). Cases A60 and C60 only differ by the mass flow rate and injection velocity of H_2 , 50 % larger for case A60 than C60.

The flow and flame structures are well illustrated with instantaneous views as shown in Figure (5) for case C60. A fully turbulent flame develops around the low velocity cold inner jet. High density oxygen pockets are produced downstream.

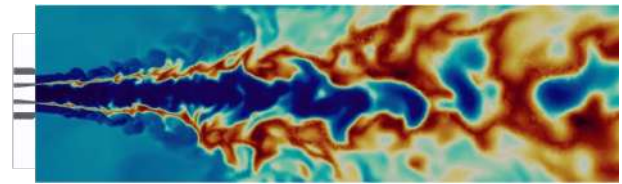


Figure 5: LES of MASCOTTE case C60. Longitudinal instantaneous field of temperature between 80 K and 3 600K [12].

A qualitative comparison with experiment is shown in Figure (6) for all three cases, where Abel transforms of OH^* emission [28, 5] are compared with isocontours of the average OH mass fraction from the simulation (see [12] for OH^* fields). Although the two quantities are not exactly equivalent, it can be seen that the topology of the flame is qualitatively recovered in all the cases, with a correct axial position of the opening and a proper flame length for cases A60 and G2. As in the experiment, the flame is found longer in case C60 compared with case A60, by near 100% in the LES, due to the smaller H_2 mass flow rate. In both cases the flame is attached to the injector lips, consistently with the DNS results of the above section. The absence of reactant leakage leads to purely diffusion flames, highly strained by the strong turbulence.

3.3 LES of a realistic rocket engine configuration

The numerical approach and modeling described above, and the computational power now available, allow today the simulation of multi-injectors, lab-scale engines. First steps were taken with simulations of combustion chambers with a limited number of injectors, in order to study possible interactions between flames and their impact

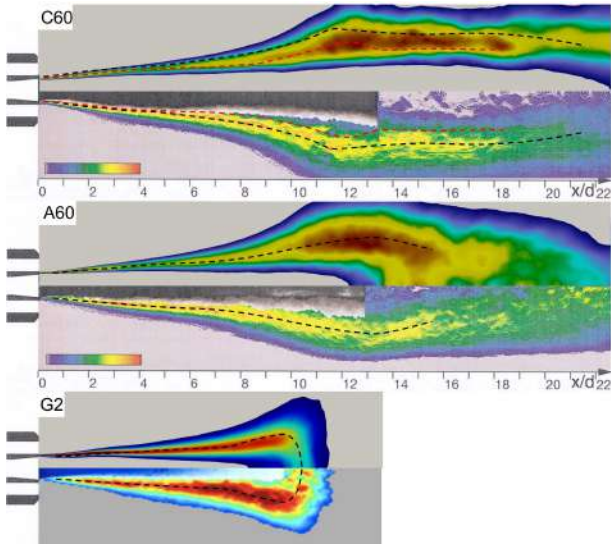


Figure 6: LES of MASCOTTE cases C60 (top), A60 (middle) and G2 (bottom). Comparison between the Abel transform of the average field of OH* emission [28, 5] and the average OH mass fraction from the simulation. Dashed lines show the top (in red) and bottom (in black) experimental flame position corresponding to the position of maximum emission [12].

on turbulent mixing, combustion efficiency and thermo-acoustic instabilities. With this objective, a five injectors combustor has been investigated experimentally at ONERA [27, 29]. The experimental facility allowed to apply transverse acoustic waves to the flames attached to the linearly arranged injectors. To gain better knowledge of the turbulent flames and their interaction, the experiment was computed using LES [29], for the operating conditions summarized in Table (1).

P_{ch} [MPa]	MR	J
6.7	1.1	3.7

Table 1: Chamber pressure, Mixture ratio MR , and momentum flux ratio J for the methane-oxygen five-injector case.

The simulations were able to reproduce both the non-modulated and the modulated cases, as illustrated in Figure (7), showing a good agreement with experiment. It can be seen that even in the non-modulated case, the flames interact as they widen under the effect of the developing turbulence. The transverse acoustic waves significantly reduce the flame length, and the dense core is notably shortened. This goes with an expansion in the transverse direction, leading to flattened flame shapes. The simulations allowed to analyze in detail the flow dynamics induced by transverse acoustics, as well as the flame response. In particular, the Rayleigh criterion showed a different behavior of the central and lateral flames, which produce larger heat release fluctuations. A complementary detailed study of the dynamics of a transcritical coaxial flame under a high-frequency transverse acoustic forcing is given in [30].

Today, LES of real rocket engine configurations with tens of injectors is feasible, although requiring important computational resources. Recently, the LES of a 42-injector rocket engine has been performed to study thermo-acoustic instabilities [31, 32]. The simulated BKD configuration operated at DLR Lampoldshausen

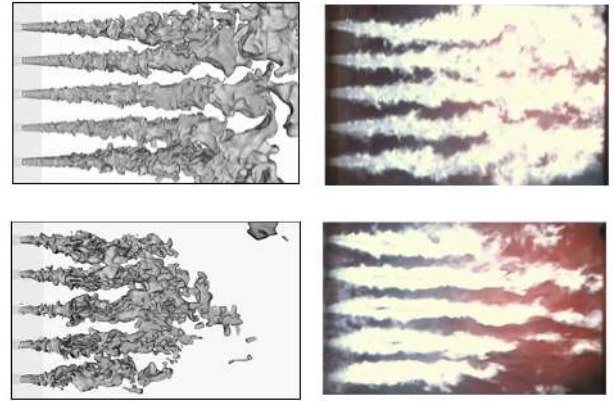


Figure 7: Instantaneous images of the five flames in the five-injector case [30]: numerical iso-surfaces of temperature (left) and experimental instantaneous light emission (right). Top: without modulation, bottom: with modulation.)

[33] consists of a cylindrical combustion chamber of diameter 8 cm, closed by a choked nozzle (Figure (8)). The 42 coaxial injectors, arranged on the injection plate in three concentric rings, feed the combustor with hydrogen and oxygen in transcritical conditions. Both stable and unstable cases were observed experimentally. A stable case (LP1) and an unstable case (LP4) were simulated operating respectively at 70 bar and 80 bar. Note that in that case, a much coarser mesh than in previous single injector calculations was used. The impact of mesh resolution in single injector simulations was studied in [12], showing that the accuracy of stable flame prediction was kept on a coarse mesh similar to the one used for the BKD configuration. The impact of the mesh on combustion instability is however not yet fully assessed, and is the subject of current work.



Figure 8: Overview of the BKD configuration: temperature isosurface colored with axial velocity [34].

In order to investigate the stability of the combustor, an external perturbation was applied in the LES in the form of a pressure perturbation corresponding to the first transverse mode of the chamber. In case LP1, the imposed perturbation is rapidly damped whatever its amplitude, confirming a stable operating point. On the contrary, case LP4 leads to a limit cycle for sufficiently high perturbation amplitudes, above 11 % of the chamber pressure. This means that for LP4 the LES is nonlinearly unstable. This is in agreement with the experimental observations, where case LP4 is unstable and case LP1 is stable. Pressure signals may be analyzed with spectral density plots as shown in Figure (9), also showing the experimental power spectral densities for comparison. Peak frequencies are observed at the same values in both LES and experiment, a first peak at 10700 Hz in the LES and 10260 Hz in the experiment, and a second peak at 21400 Hz in the LES and 20520 Hz in the experiment.

To characterize the stability of a combustor, the

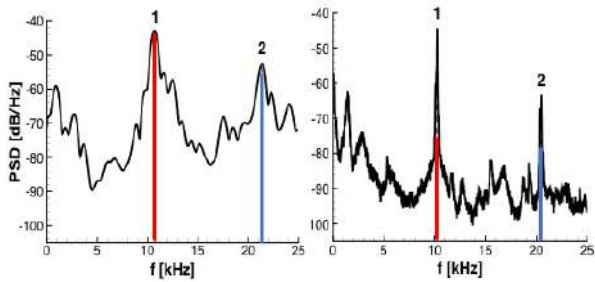


Figure 9: PSD of the pressure signal for LP4: comparison with experiment (raw experimental data courtesy of DLR, processed with the same tools as the LES results) [31, 32]

Rayleigh index R is used to measure the correlation between the flame power fluctuations q' and the pressure fluctuations p' . Positive R indicates a growing instability. The Rayleigh index obtained for both cases LP1 and LP4 and different pressure perturbation levels are reported in Table (2). First, R is always positive, meaning that pressure and combustion fluctuations always feed each other. As a consequence, stable cases can only be the result of energy losses through boundaries or dissipation. Second, R increases with the initial perturbation amplitude and reaches a maximum for LP4 with the largest perturbation. In this latter case, energy losses do not anymore counteract the fast instability growing and the combustor becomes unstable.

The objective of current studies is the prediction of the natural stability of the system and the transition between stable and unstable situations in order to identify the mechanisms leading to instability [34].

	LP1 [MPa]			LP4		
ΔP [bar]	2.5	5	8	2.5	5	10
R [kW]	32.5	39.9	65.9	23.9	29.1	143

Table 2: Rayleigh source term for different pressure amplitude ΔP [31, 32]

4 Conclusions

Although it remains challenging to compute transcritical and supercritical reacting flows, a numerical methodology is today available and validated. It allows to study complex phenomena such as ignition, combustion efficiency, flame stability or thermo-acoustic instabilities in real rocket engines. It can also be coupled to heat transfer simulation (conduction in solids and thermal radiation) to describe the combustion chamber thermal state and design efficient cooling systems [35]. The complexity of the physics involved, in particular the strong density gradients at injection, necessitate locally very fine meshes which induces extremely CPU cost: typically the simulation of the 42 injectors configuration required 100 000 CPU hours per ms of physical time on a BlueGene Q [31]. This demands a high parallel efficiency of the solver and the access to powerful computers.

Today a lot of efforts are devoted to the study of CH₄/LO_x thermo-kinetics effects on the engine behavior, in order to help the design of the new generation of rocket engines in the context of cost reduction and commercial competitiveness. In particular the modeling and simulation of the transition between supercritical and

subcritical conditions has emerged as a key problem and is the subject of current research.

Acknowledgment

Support provided by ArianeGroup, the prime contractor of the Ariane launcher cryogenic propulsion system and CNES, the French National Space Agency, is gratefully acknowledged.

References

- [1] J. C. Oefelein and V. Yang, "Modeling high-pressure mixing and combustion processes in liquid rocket engines," *Journal of Propulsion and Power*, vol. 14, no. 5, pp. 843–857, 1998.
- [2] M. Oswald, J. J. Smith, R. Branam, J. Hussong, A. Shick, B. Chehroudi, and D. Talley, "Injection of fluids into supercritical environments," *Combustion Science and Technology*, vol. 178, pp. 49–100, 2006.
- [3] M. Habiballah, M. Orain, F. Grisch, L. Vingert, and P. Gicquel, "Experimental studies of high-pressure cryogenic flames on the Mascotte facility," *Combustion Science and Technology*, vol. 178, no. 1, pp. 101–128, 2006.
- [4] S. Candel, M. Juniper, G. Single, P. Scouffaire, and C. Rolon, "Structure and dynamics of cryogenic flames at supercritical pressure," *Combustion Science and Technology*, vol. 178, pp. 161–192, 2006.
- [5] G. Singla, P. Scouffaire, C. Rolon, and S. Candel, "Transcritical oxygen/transcritical or supercritical methane combustion," *Proceedings of the Combustion Institute*, vol. 30, no. 2, pp. 2921–2928, 2005.
- [6] L. L. Lee, K. E. Starling, T. H. Chung, and M. Ajlan, "Generalized multiparameters corresponding state correlation for polyatomic, polar fluid transport properties.," *Industrial and Chemical Engineering Research*, vol. 27, pp. 671–679, 1988.
- [7] F. Nicoud and F. Ducros, "Subgrid-scale stress modelling based on the square of the velocity gradient," *Flow, Turbulence and Combustion*, vol. 62, no. 3, pp. 183–200, 1999.
- [8] D. Peng and D. B. Robinson, "A new two-constant equation of state," *Ind. Eng. Chem. Fundam.*, vol. 15, pp. 59–64, 1976.
- [9] G. Soave, "Equilibrium constants from a modified redlich-kwong equation of state," *Chemical Engineering Science*, vol. 27, pp. 1197–1203, 1977.
- [10] N. Peters, "Laminar diffusion flamelet models in non-premixed turbulent combustion," *Progress in energy and combustion science*, vol. 10, pp. 319–339, 1984.
- [11] T. Schmitt, Y. Méry, M. Boileau, and S. Candel, "Large-eddy simulation of oxygen/methane flames under transcritical conditions," *Proceedings of the Combustion Institute*, vol. 33, no. 1, pp. 1383–1390, 2011.
- [12] T. Schmitt, "Large-eddy simulations of the mascotte test cases operating at supercritical pressure," *Flow, Turbulence and Combustion*, 2020.

- [13] P. C. Ma, D. Banuti, J.-P. Hickey, and M. Ihme, "Numerical framework for transcritical real-fluid reacting flow simulations using the flamelet progress variable approach," in *55th AIAA Aerospace Sciences Meeting*, p. 0143, 2017.
- [14] H. Huo and V. Yang, "Large-eddy simulation of supercritical combustion: Model validation against gaseous h₂-o₂ injector," *Journal of Propulsion and Power*, vol. 33, no. 5, pp. 1272–1284, 2017.
- [15] J. Zips, H. Müller, and M. Pfitzner, "Efficient thermo-chemistry tabulation for non-premixed combustion at high-pressure conditions," *Flow, Turbulence and Combustion*, vol. 101, no. 3, pp. 821–850, 2018.
- [16] B. Fiorina, R. Baron, O. Gicquel, D. Thevenin, S. Carpentier, and N. Darabiha, "Modelling non-adiabatic partially premixed flames using flame-prolongation of ildm," *Combustion Theory and Modelling*, vol. 7, pp. 449–470, 2003.
- [17] M. Ma and C. Devaud, "A conditional moment closure (cmc) formulation including differential diffusion applied to a non-premixed hydrogen-air flame," *Combustion and Flame*, vol. 162, pp. 144–158, 2015.
- [18] G. Lacaze, B. Cuenot, T. Poinso, and M. Oschwald, "Large eddy simulation of laser ignition and compressible reacting flow in a rocket-like configuration," *Combustion and Flame*, vol. 156, pp. 1166–1180, 2009.
- [19] V. Moureau, G. Lartigue, Y. Sommerer, C. Angelberger, O. Colin, and T. Poinso, "High-order methods for DNS and LES of compressible multi-component reacting flows on fixed and moving grids," *Journal of Computational Physics*, vol. 202, no. 2, pp. 710–736, 2005.
- [20] O. Colin and M. Rudgyard, "Development of high-order taylor-galerkin schemes for unsteady calculations," *Journal of Computational Physics*, vol. 162, no. 2, pp. 338–371, 2000.
- [21] G. Lacaze, T. Schmitt, A. Ruiz, and J. Oefelein, "Comparison of energy-, pressure-and enthalpy-based approaches for modeling supercritical flows," *Computers and Fluids*, vol. 181, pp. 35–56, march 2019.
- [22] T. Schmitt, L. Selle, A. Ruiz, and B. Cuenot, "Large-Eddy Simulation of Supercritical-Pressure Round Jets," *AIAA Journal*, vol. 48, no. 9, 2010.
- [23] A. Ruiz, B. Cuenot, L. Selle, and T. Poinso, "The flame structure of a turbulent supercritical hydrogen/oxygen flow behind a splitter plate," in *47th AIAA/ASME/SAE/ASEE Joint Propulsion Conference & Exhibit*, p. 6121, 2011.
- [24] A. Ruiz, *Unsteady Numerical Simulations of Transcritical Turbulent Combustion in Liquid Rocket Engines*. Phd thesis, Univ. Toulouse, 2012.
- [25] R. Mari, B. Cuenot, J. Rocchi, L. Selle, and F. Duchaine, "Effect of pressure on hydrogen / oxygen coupled flame-wall interaction," *Combustion and Flame*, vol. 168, pp. 409–419, 2016.
- [26] C. Laurent, L. Esclapez, D. Maestro, G. Staffelbach, B. Cuenot, L. Selle, T. Schmitt, F. Duchaine, and T. Poinso, "Flame-wall interaction effects on the flame root stabilization mechanisms of a doubly-transcritical lo₂/lch₄ cryogenic flame," *Proceedings of the Combustion Institute*, vol. 37, no. 4, pp. 5147–5154, 2018.
- [27] Y. Méry, L. Hakim, P. Scoufflaire, L. Vingert, S. Ducruix, and S. Candel, "Experimental investigation of cryogenic flame dynamics under transverse acoustic modulations," *Compt. Rend. Mécan.*, vol. 341, pp. 100–109, 2013. Special issue "Combustion for Aerospace Propulsion".
- [28] M. Juniper, A. Tripathi, P. Scoufflaire, J. Rolon, and S. Candel, "Structure of cryogenic flames at elevated pressures," *Proceedings of the Combustion Institute*, vol. 28, no. 1, pp. 1103–1110, 2000.
- [29] L. Hakim, A. Ruiz, T. Schmitt, M. Boileau, G. Staffelbach, S. Ducruix, B. Cuenot, and S. Candel, "Large eddy simulations of multiple transcritical coaxial flames submitted to a high-frequency transverse acoustic modulation," *Proceedings of the Combustion Institute*, vol. 35, no. 2, pp. 1461–1468, 2015.
- [30] L. Hakim, T. Schmitt, S. Ducruix, and S. Candel, "Dynamics of a transcritical coaxial flame under a high-frequency transverse acoustic forcing: Influence of the modulation frequency on the flame response," *Combustion and Flame*, vol. 162, no. 10, pp. 3482–3502, 2015.
- [31] A. Urbano, L. Selle, G. Staffelbach, B. Cuenot, T. Schmitt, S. Ducruix, and S. Candel, "Exploration of combustion instability triggering using large eddy simulation of a multiple injector liquid rocket engine," *Combustion and Flame*, vol. 169, pp. 129–140, 2016.
- [32] A. Urbano, Q. Douasbin, L. Selle, G. Staffelbach, B. Cuenot, T. Schmitt, S. Ducruix, and S. Candel, "Study of flame response to transverse acoustic modes from the les of a 42-injector rocket engine," *Proceedings of the Combustion Institute*, vol. 36, no. 2, pp. 2633–2639, 2017.
- [33] S. Gröning, D. Suslov, J. S. Hardi, and M. Oschwald, "Influence of hydrogen temperature on the stability of a rocket engine combustor operated with hydrogen and oxygen," *CEAS Space Journal*, pp. 1–18, 2016.
- [34] T. Schmitt, G. Staffelbach, S. Ducruix, S. Gröning, J. Hardi, and M. Oschwald, "Large-eddy simulations of a sub-scale liquid rocket combustor: influence of fuel injection temperature on thermo-acoustic stability," in *7TH European Conference for Aeronautics and Aerospace Sciences (EUCASS)*, 2017.
- [35] D. Maestro, B. Cuenot, and L. Selle, "Large eddy simulation of combustion and heat transfer in a single element gch₄/gox rocket combustor," *Flow, Turbulence and Combustion*, vol. 103, pp. 699–730, 2019.

ON THE SIMULATION OF MULTICOMPONENT AND MULTIPHASE COMPRESSIBLE FLOWS

R. Abgrall¹, P. Bacigaluppi² and B. Re^{1*}

¹*Institute of Mathematics, University of Zürich*

²*Laboratory of Hydraulics, Hydrology and Glaciology, ETH Zürich*

Abstract

The following paper presents two simulation strategies for compressible two-phase or multicomponent flows. One is a full non-equilibrium model in which the pressure and velocity are driven towards the equilibrium at interfaces by numerical relaxation processes, the second is a four-equation model that assumes stiff mechanical and thermal equilibrium between phases or components. In both approaches, the thermodynamic behaviour of each fluid is modelled independently according to the stiffened-gas equations of state. The presented methods are used to simulate the de-pressurization of a pipe containing pure CO₂ liquid and vapour under the one-dimensional approximation.

1 Introduction

Multiphase and multicomponent flows are ubiquitously encountered in nature as well as in industrial applications. Hence, their numerical simulation has been an active research field for a long time producing a large variety of models as well as numerical methods relying on the most different assumptions. Among the possible distinctive aspects of such a modelling, is the thermodynamic description. In this work, we assume that each (pure) fluid has its own, known, equations of state (EOS), independently from the actual phase—liquid or gaseous—that composes the flow. How the phases or materials interact among each other represents another important feature. Specifically, we focus on the so-called diffuse interface methods (DIMs), which consider in each cell the presence of all phases or materials, be it an arbitrarily small amount for the “pure” fluids, and do not explicitly track the interfaces separating different components [1, 2].

To allow an effective description of the considered numerical methods, it is important to remark the difference between multicomponent and multiphase flows. In *multicomponent flows*, the different species (typically gases, but also liquid mixtures) are intimately mixed and, whatever the size of a volume of fluid, the different components appear all. An example is given by air, where O₂ and N₂, as well as the other gases, are simultaneously present, but the mixture composition varies. In such cases, the Dalton law applies, and the pressure is the sum of the partial pressures. This kind of flows are mostly considered to simulate gas combustion, hypersonic flows, or real gas networks, where several gases are injected from different origins. In *multiphase flows*, different phase are separated by multi-material interfaces, so there exists a limit size for which one can say in which

pure fluid we are. In *multiphase flows*, each phase occupies a well-determined volume fraction, i.e., there exists a limit in the spatial scale for which one can say in which pure fluid we are. Take the example of a fog, where droplets can appear in a gaseous environment: if we are looking below the characteristic size of a droplet of water, then we know if we are in, say, gas or in water. Such types of flows are generally assumed while investigating combustion processes, break-up of liquid jets, but also in the oil industry, the nuclear industry, and during the transport of CO₂, etc.. According to the flow topology, we can have, for instance, stratified, bubbly, or droplet two-phase flows.

From a numerical point of view, these two descriptions have many similar common features, but also many differences. If we neglect viscous effects, a multicomponent model always leads to a hyperbolic system, and the main difference with the single component case (e.g., with the standard Euler equations), is that the number of linearly degenerate fields increases. The main difficulty occurs at the contact discontinuities where the pressure may not have the right continuous behaviour that is expected. This artefact becomes more important if the slip line is aligned with the mesh, and may lead, in some cases, to the blow up of the code. The case of multiphase flows is way more complicated. First, there is a very difficult modelling issue: it is not possible, in general, to have a very fine description of the flow, but we have to introduce averages, a situation somehow similar to turbulence modelling. Hence, we need closure relations, and they are case dependent. This averaging procedure is a translation, from the physical to the numerical level, of the flow topology; hence, it depends on the shape of interfaces, distinguishing e.g. between small, large or elongated bubbles, or on the behaviour, e.g. how a bubble breaks. The averaging procedure might impact also the mathematical properties of the model.

Here, we intend to describe two possible ways of proceeding that are suitable to simulate both compressible multiphase and multicomponent flows. The proposed strategies are based on primitive formulations. It means that the set of partial differential equations describing the flows is not written in conservative form, and the solution variables comprise, instead of the total energy, the pressure or the internal energy, which are, in general, more relevant in engineering applications. One aspect linked with this choice, which requires some attention and it is non-trivial, is the involved numerical method to guarantee conservation among the variables for the four-equation model [3, 4].

In this contribution, we narrow our interests to two-phase flows (or two components, as, in the following, we will not distinguish any more between them). First, in Sec. 2, we introduce diffuse interface methods for the

*Corresponding author: barbara.re@math.uzh.ch

simulation of compressible two-phase flows. In Sec. 2.1, we describe a pressure-based finite-volume solver for the seven-equation model, in which the equilibrium between pressure and velocity at multi-material interfaces is enforced through numerical relaxation processes. In Sec. 2.2, we briefly resume the finite-volume-type solver adopted for the four-equation model. The results of a CO₂ pipe de-pressurization test are presented in Sec. 3, while the conclusions drawn in Sec. 4.

2 Diffuse interface methods for two-phase flows

A distinguishing feature of compressible two-phase flows is the presence of dynamic interfaces separating different fluids, which represents a main challenge in their numerical simulation. The size, shape, and the number of interfaces present in the domain depend on the topology of the flows, and the thermodynamic and/or chemical properties of the flow may undergo abrupt variations across them. DIMs is possibly an easy and efficient way to cope with moving interfaces, as it artificially (i.e., numerically) lets the fluids mix in a thin region surrounding them [2]. In other words, the dynamics of the fluids is coupled in thin interfacial regions, while it tends to their respective pure behaviour away from them. The modelling of the thermodynamic behaviour of the mixture near interfaces, which may significantly depart from the bulk fluids, is a rather delicate matter and it can be controlled by different modelling assumptions.

The archetype of the DIMs is the full non-equilibrium model by Baer and Nunziato (BN) [5], which comprises seven equations: the evolution equation for the volume fraction of one phase and a set of balance equations for mass, momentum and total energy for each phase. Each phase evolves with its own pressure, velocity, and temperature. The original BN model has been equipped with instantaneous pressure and velocity relaxation, to enforce mechanical equilibrium across interfaces [1]. Despite the great flexibility and some favourable numerical features such as the hyperbolic character, the extensive use of BN-like models is hindered by the large number of waves, that need to be taken into consideration [6]. This aspect prompts the diffusion of reduced models, which are derived by means of asymptotic expansions, assuming pressure, velocity, and/or thermal equilibrium between phases [7]. Among others, we mention the six-equation single-velocity two-phase flow model [8], and the five-equation model derived by Kapila et al. [9] in the limit of stiff mechanical relaxation, and the 4-equation homogeneous equilibrium model with mechanical and thermal equilibrium [10, 11]. The choice of the most suitable model depends on the features of the flow field, the desired simulation outputs, and the available computational resources.

A difficulty that we need to face while developing numerical methods for compressible multiphase flows concerns the non-conservative terms. In the seven- and six-equation models, these terms result from the averaging procedure and involve the gradient of the volume fraction. In the five-equation model, it involves the velocity divergence. The impossibility to write the governing equation in conservative form precludes the definition of weak solutions in the standard distribution sense and calls for ad-hoc numerical techniques, which provide an unambiguous discretization of non-conservative terms. A possible one is provided

by the discrete equation method, which applies the principle of the Godunov method in a probabilistic framework [12]. Alternatively, we can derive a numerical discretization that explicitly enforces the pressure and velocity non-disturbance condition across multi-material interfaces [13]. More specifically, it can be noticed that if the two fluids are in mechanical equilibrium, the pressure and the velocity are and should remain constant across the interface. Enforcing the mechanical equilibrium at multi-material interfaces is mandatory to avoid spurious velocity and pressure oscillations. Primitive formulations offer a natural way to enforce the interface mechanical equilibrium [14], so we focus on them in this paper.

In the next sections, we describe a finite-volume method that solves the pressure-based formulation of the seven-equation non-equilibrium model, with finite pressure and velocity relaxations, where the pressure and velocity non-disturbance constrain is inherently enforced in the finite volume discretization; along this model, we also present a finite-volume-type solver for the non-conservative four-equation model written in terms of internal energy. This system in particular considers pressure and velocity, along with temperature relaxations.

2.1 A pressure-based non-equilibrium BN-type model

The non-equilibrium model is based on the symmetric variant of the BN model with pressure and velocity relaxation proposed by Saurel and Abgrall [1]. With the aim to derive a model well suited to simulate multiphase flows at low Mach numbers, we derived the corresponding pressure-based formulation [15], which is made dimensionless according to the special pressure scaling

$$P_k = \frac{\tilde{P}_k - \tilde{P}_r}{\tilde{\rho}_r \tilde{u}_r^2} \quad \text{with} \quad M_r^2 = \frac{\tilde{\rho}_r \tilde{u}_r^2}{\tilde{P}_r},$$

where \tilde{P}_k is the dimensional pressure of the phase k , while \tilde{P}_r , $\tilde{\rho}_r$, and \tilde{u}_r are, respectively, the reference (dimensional) pressure, density, and velocity. M_r is the resulting reference Mach number, which expresses the global level of compressibility of the flow field, as explained later. This special scaling filters out the acoustics and recovers the correct order of pressure fluctuations in the zero Mach limit [16]. The resulting model reads [17]:

$$\frac{\partial \alpha_k}{\partial t} + u_I \frac{\partial \alpha_k}{\partial x} = \mu \Delta_k P \quad (1)$$

$$\frac{\partial \alpha_k \rho_k}{\partial t} + \frac{\partial (\alpha_k \rho_k u_k)}{\partial x} = 0 \quad (2)$$

$$\frac{\partial \alpha_k m_k}{\partial t} + \frac{\partial (\alpha_k m_k u_k + \alpha_k P_k)}{\partial x} = P_1 \frac{\partial \alpha_k}{\partial x} - \lambda \Delta_k u \quad (3)$$

$$\begin{aligned} M_r^2 \alpha_k \left[\frac{\partial P_k}{\partial t} + u_k \frac{\partial P_k}{\partial x} \right] + \left[M_r^2 \rho_k c_k^2 + \kappa_k \right] \alpha_k \frac{\partial u_k}{\partial x} \\ - \left[M_r^2 \rho_k c_{1,k}^2 + \kappa_k \right] (u_I - u_k) \frac{\partial \alpha_k}{\partial x} \\ = -M_r^2 \left[\rho_k c_{1,k}^2 \mu \Delta_k P + \kappa_k (u_I - u_k) \lambda \Delta_k u \right] - \kappa_\mu \Delta_k P \end{aligned} \quad (4)$$

where α is the volume fraction, m the momentum, and the subscript $k = \{1, 2\}$ indicates the phase. The operator Δ_k takes the difference between the phase k and the opposite one, e.g., $\Delta_1 u = u_1 - u_2$, and λ and μ are

the relaxation parameters for the velocity and the pressure, respectively. Since the phases occupy all volume, $\alpha_1 + \alpha_2 = 1$, so Eq. (1) is solved only for one phase, while Eq. (2)–Eq. (4) are solved for both phases. The system is closed by two thermodynamic models, one for each phase, which are assumed to be given in the general form $P = P(\rho, e)$, with e the internal energy. Accordingly, the speed of sound c is defined for each phase as:

$$c^2 = \chi + \kappa \frac{P + e}{\rho}, \quad \text{with } \chi = \left(\frac{\partial P}{\partial \rho} \right)_e, \quad \kappa = \left(\frac{\partial P}{\partial e} \right)_\rho. \quad (5)$$

Finally, the subscript I denotes interfacial variables, which are modelled as

$$u_I = \frac{\sum_k \alpha_k m_k}{\sum_k \alpha_k \rho_k}, \quad P_I = \sum_k \alpha_k P_k, \\ c_{I,k}^2 = \chi_k + \kappa_k \frac{P_I + e_k}{\rho_k}.$$

The definition of the *interfacial* speed of sound $c_{I,k}$ is not related to a specific EOS, and it does not have a formal thermodynamic meaning, but it simply mimics Eq. (5), for the pressure P_I instead of P_k . The usage of two EOSs circumvents the possible occurrence of negative values of squared speed of sound in the two-phase region [1].

In Eq. (4), we highlight the role of the parameter M_r^2 , in front of some terms. It is representative of the global compressibility of the flow and it allows to recover the correct incompressible solution at low Mach [18]. Indeed, for $M_r^2 \rightarrow 0$, Eq. (4) reduces to $\frac{\partial \alpha_k}{\partial t} + \frac{\partial \alpha_k u_k}{\partial x} = 0$, which can be considered the multiphase counterpart of the incompressible kinetic constraint on the velocity divergence for single phase flows.

The solution strategy of the pressure-based seven-equation model given above is based on the Strang splitting, namely, the solution at the end of time step $\Delta t = t^{n+1} - t^n$ is achieved by applying two subsequent operators: the hyperbolic operator, which solves the system without source terms, and the relaxation operator, which solves two ordinary differential equation (ODE) systems associated with the velocity and the pressure relaxation, starting from the solution of the hyperbolic operator.

The numerical discretization of the hyperbolic operator is described in [15]. We recall here only some core features. The governing equations are spatially discretized over staggered grids to avoid spurious pressure oscillations at low Mach number, and we use a first-order finite volume scheme based on the Rusanov fluxes. The staggering of the variables facilitates the solution of the system of equations in a segregated approach, so first the densities and the volume fraction and the predicted momentums are computed, by treating explicitly the convective terms and the pressure gradients. Then, the pressure equations are solved by integrating implicitly the acoustic terms, in order to circumvent the most stringent limitation on the time step imposed by the acoustic CFL constraint. Finally, the momentums and velocities are updated according to the pressure correction. As mentioned in the first part of Sec. 2, the conservative terms involving the gradient of the volume fraction are integrated starting from the consideration that a two-phase flow uniform in pressure and velocity should preserve this uniformity [1]. By analytically imposing this condition in the discrete version of the equations, we achieve an unambiguous discretization of the non-conservative terms, which, however, depends on the adopted numerical fluxes [17, 1].

For what concerns the relaxation operator, we solve two systems of ODEs, which include only the time derivatives of the variables and the relaxation terms (we refer the reader to [1] for a description of the systems of ODEs, but here λ and μ are finite parameters). The first system accounts for velocity relaxation only, and it consists of the two momentum equations. Using a backward Euler time integration scheme and considering the solution of the hyperbolic operator as initial state, we obtain an easy system which is solved analytically. The second ODEs problem applies the pressure relaxation and it consists of three equations: one for the volume fraction and two for the pressure. The implicit Euler integration of this initial value problem leads to a highly non-linear problem, which is solved by using standard numerical techniques provided by the library PETSc [19].

Finally, we recall that the standard BN-type models, as the one here described, consider immiscible phases, that is, unless the components are not premixed, the only mixing that may occur is due to numerical diffusion. However, mass transfer may be added to the model by means of additional source terms modelling the Gibbs free energy relaxation [20].

2.2 An internal energy-based four-equation model

The four-equation model is a simplified version of the Baer-Nunziato two-phase model [5], with the assumption of both mechanical and thermal relaxation. In particular, to retrieve the four equations starting from the Baer-Nunziato model we have assumed pressure and velocity, as well as temperature equality between the two phases (cf. Sec. 2.3 for further details). This leads to the following set of equations, where we have one equation for the conservation of mass for each phase k and an equation for the mixture momentum Eq. (8) and the mixture internal energy Eq. (9).

$$\frac{\partial(\alpha_1 \rho_1)}{\partial t} + \frac{\partial(\alpha_1 \rho_1 u)}{\partial x} = 0 \quad (6)$$

$$\frac{\partial(\alpha_2 \rho_2)}{\partial t} + \frac{\partial(\alpha_2 \rho_2 u)}{\partial x} = 0 \quad (7)$$

$$\frac{\partial(\rho u)}{\partial t} + \frac{\partial(\rho u^2 + P)}{\partial x} = 0 \quad (8)$$

$$\frac{\partial e}{\partial t} + u \cdot \frac{\partial e}{\partial x} + (e + P) \frac{\partial u}{\partial x} = 0 \quad (9)$$

Note that system Eq. (6)-Eq. (9) is written for the one-dimensional case and, more specifically, the last equation is featuring the non-conservative formulation, and requires a careful numerical method, in order to provide the conserved quantities. Further, the thermodynamic assumptions behind this model are different from the original Homogeneous Relaxation Model (HRM) model of Downar [10], which does not assume a temperature equilibrium.

Let us denote the two phases identified for a liquid phase by subscript 1 and a gaseous one by 2. Here u represents the velocity, ρ the mixture density, P the pressure and c the mixture speed of sound. The Wood velocity $\frac{1}{\rho c^2} = \sum_k \frac{\alpha_k}{\rho_k c_k^2}$ describes the total sound speed, where c_k^2 is the squared speed of sound for phase k , as defined in Eq. (5).

The volume fractions α_k fulfil the requirement $\sum_k \alpha_k = 1$. We define the total energy as $E = e + \frac{1}{2}\rho u^2$, with the total internal energy $e = \sum_k \alpha_k e_k$, where e_k is the internal energy of phase k .

The numerical discretization of the four-equation system is described in [4, 21]. We recall hereafter some of its main features. The governing equations are spatially discretized via a finite volume-based technique, called the Residual Distributions Finite Volume (RD), which has been duly presented in some recent work [22, 23]. This method is used in combination with a second-order explicit (Runge-Kutta) method, which has been inspired by the work of [24] and [22]. This temporal discretization is based on a prediction-correction approach, where the prediction step is first-order accurate and given by a flux difference. The second-order in time is then achieved via a correction step, which takes the obtained prediction approximation as the previous sub-timestep solution.

Overall, for what concerns the numerical spatial approximation, diverse methodologies, ranging from Lax-Friedrichs to Godunov approximations, could be adopted. Nevertheless, to guarantee overall a good accuracy of the solution, providing at same time a robust scheme, has led to the choice of adopting a so-called a posteriori limiting, as presented in [23]. This strategy allows us to combine a second-order accurate scheme in smooth regions and reverting locally to first-order in case the second-order does not fulfil a series of criteria, such as the absence of numerical oscillations or physically inadmissible solutions, as, e.g., negative densities. In this work, the second-order approximation is retrieved by a stabilized, blended Rusanov scheme, while the first-order is provided by the Rusanov scheme. The interested reader may refer to [4, 21]. While the feature of accuracy can be well preserved, some remarks on the conservation among the variables need to be provided.

In particular, the feature behind the choice of a non-conservative formulation, as seen in [3], is due to the many advantages, especially for engineering applications, which are represented by the possibility to work directly with quantities, such as pressures or internal energies instead of having them computed from the total energy. Indeed, for example, across contact discontinuities, the velocity and the pressure do not change, while the density does. Deriving the internal energy or pressures from the total energy, may, therefore, not be completely accurate from a numerical point of view, possibly resulting in oscillations. The interested reader may refer to [4] for a comparisons between conservative and non-conservative formulations. Further, another relevant advantage is represented by the possibility of dealing easily with non-linear equations of state, as for example the family of Mie-Grüneisen equations of state. These reasons mainly motivate the interest behind the adoption of Eq. (9) and the conservation can be retrieved in the specific RD scenario via a correction term (cf. [3]). Mass transfer may be added to Eq. (6)-Eq. (7), on the right-hand side, by means of the term $\Gamma = \theta(\nu_1 - \nu_2)$ with ν the chemical potentials (Gibbs function) of the phases and θ the relaxation time of the process at which the thermodynamic equilibrium is reached (which enables the fulfilment of the entropy inequality). The solution would then be obtained by first computing the hyperbolic part and then proceeding by adding the mass transfer as shown in [25, 4, 21].

Table 1: Parameters of the stiffened gas EOS for the CO₂ phases, used in the numerical test

		Liquid	Vapour
γ	[-]	1.23	1.06
P_∞	[Pa]	1.32 10 ⁸	8.86 10 ⁵
q	[J/kg]	-6.23 10 ⁵	-3.01 10 ⁵
c_v	[J/kg K]	2440	2410

2.3 Thermodynamic modelling

In this work, we consider a stiffened gas EOS for each phase. Considering dimensional variables, the pressure and the temperature are given by

$$P(\rho, e) = (\gamma - 1)e - \gamma P_\infty - (\gamma - 1)\rho q,$$

$$T(\rho, e) = \frac{P(\rho, e) + P_\infty}{(\gamma - 1)c_v \rho},$$

where the parameters γ , c_v , and q are, respectively, the ratio of specific heats, the isochoric specific heat capacity, and the zero point energy. Finally, the parameter P_∞ models the attractive effects in condensed materials. All these parameters are fluid-specific and are computed by fitting experimental data, e.g. the saturation curve [26].

Despite its simple analytical formulation, the stiffened EOS permits to model the essential physics at molecular level, that is attractive and repulsive effects. Hence, it is often used for shock dynamics in condensed materials and to simulate phase transfer.

For completeness, we briefly mention how the temperature, pressure and velocity equality among phases is reached for the four-equations, having possibly different states, as e.g. densities. For the temperature we will have

$$T = \sum_k \frac{P + P_{\infty,k}}{\alpha_k \rho_k C_{v,k} (\gamma_k - 1)},$$

whereas for the internal energy

$$e = \sum_k \alpha_k \rho_k \left(C_{v,k} T \frac{P + \gamma_k P_{\infty,k}}{P + P_{\infty,k}} + q_k \right).$$

and, finally, for the pressure

$$P = \frac{1}{2} \sum_k (A_k - P_{\infty,k}) + \sqrt{\frac{1}{4} (A_2 - A_1 - (P_{\infty,2} - P_{\infty,1}))^2 + A_1 A_2},$$

with

$$A_k = \frac{\rho_k \alpha_k (\gamma_k - 1) C_{v,k}}{\sum_k \rho_k \alpha_k C_{v,k}} \left(e - \sum_k (\alpha_k \rho_k q_k) - P_{\infty,k} \right).$$

3 Numerical results

In this section, we show the results obtained by both the pressure-based non-equilibrium BN-type model, presented in Sec. 2.1, and the internal energy-based four-equation model, described in Sec. 2.2, on the two-phase CO₂ de-pressurization test proposed in [11].

The experiment considers pure CO₂, initially at rest in a pipe of length $L = 80$ m. The pipeline is split in two

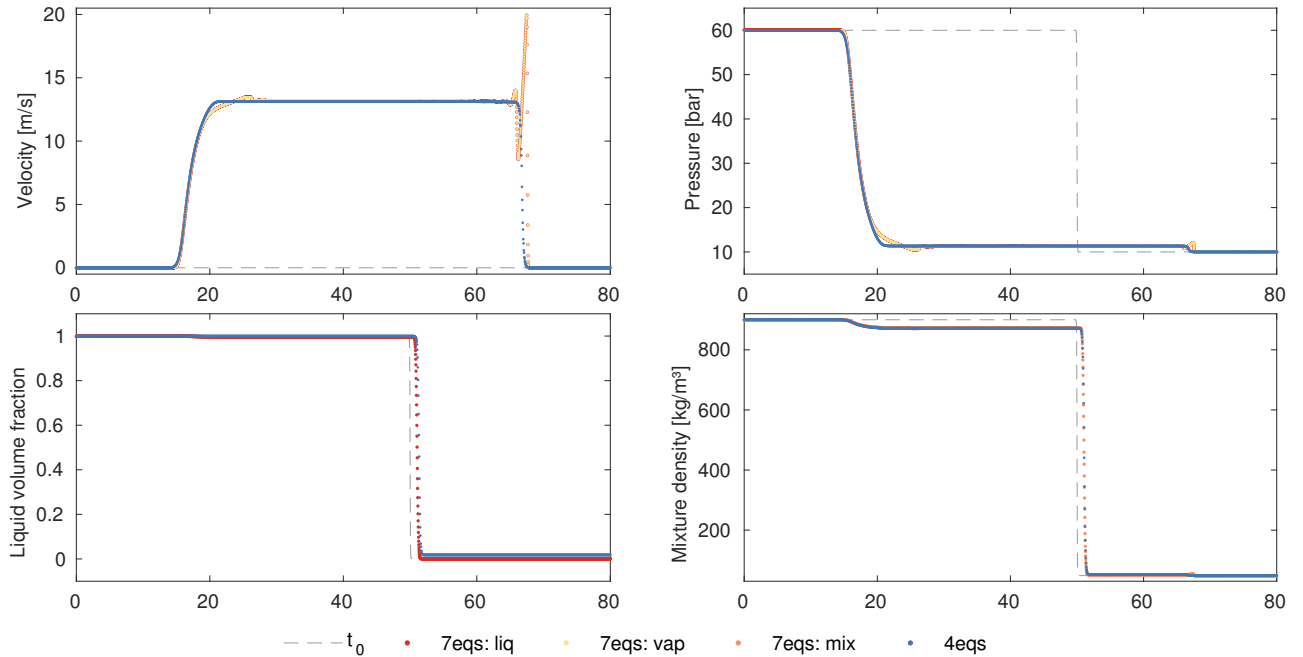


Figure 1: CO₂ de-pressurization test: numerical results obtained with the seven-equation model of Sec. 2.1, referred to as **7eqs**, and the four-equation model of Sec. 2.2, referred to as **4eqs**, at the final time $t_F = 0.08$ s. In the first row, velocity and pressure are displayed. For the seven-equation model, cell values for both liquid and vapour are shown. In the second row, the volume fraction of the liquid and the mixture density, defined as $\rho = \alpha_1 \rho_1 + \alpha_2 \rho_2$, are shown. In all pictures, the initial solution is displayed as a dashed line. In the simulation with the **7eqs** model, since the numerical discretization is only first-order accurate, the domain is split into 4000 cells; while in the simulation with the **4eqs** model, which is second-order accurate, 2000 cells are used

chambers, the left one ($x < 50$ m) contains liquid CO₂ at $P_L = 60$ bar; the right one ($x > 50$ m) is filled with vapour at $P_R = 10$ bar. The temperature is $T = 273$ K everywhere. The parameters of the stiffened gas EOS for liquid and vapour CO₂ are given in Table (1).

The diffuse interface methods assume that a small amount of all phases is present in every computational cells, so we impose a liquid volume fraction $\alpha_{1,L} = 0.999$ in the left part, and $\alpha_{1,R} = 0.001$ in the right part. The results of the simulation at $t_F = 0.08$ s are shown in Figure (1).

As the time evolves, the initial discontinuity generates a rarefaction wave propagating towards the left, within the liquid, and a shock propagating towards the right, across the vapour. The interface separating the fluids propagates as a contact discontinuity across which a jump in the (numerical) mixture density (defined as $\rho = \alpha_1 \rho_1 + \alpha_2 \rho_2$) takes place, but the pressure and velocity are continuous. Indeed, no spurious oscillations occur in these variables (first row of Figure (1)) at $x \approx 51$ m, which is the location of the interfaces at the final time. Unfortunately, the seven-equation model does generate velocity oscillations across the shock wave. As a possible explanation, we remind that this numerical method has been developed especially for low-Mach phase flows, i.e., in a regime where strong shocks are not expected. However, we will further investigate this issue.

We observe a good agreement between our numerical results and the ones in [11]. The relaxation processes in the seven-equation model described in 2.1 drive correctly the velocity and the pressure towards the equilibrium: as the pictures in the first row of Figure (1) show, the cell values of these variables are the same for liquid and vapour CO₂. These values, as well as the volume fraction and the mixture density, agree very well with the results achieved by the four-equation model, despite the profound differences in the modelling assumptions.

4 Conclusions

In this work, we have presented two different methods for the simulation of unsteady compressible two-phase or two-component flows. In particular, we have focused on diffuse interface methods, which permit to describe each fluid according to its own equation of state. We have shown how spurious oscillations across the interfaces that separate different fluids can be avoided by adopting primitive formulations, i.e., by solving the governing equations for the pressure or the internal energy, instead of the corresponding conservative variable, i.e. the total energy.

In the presented de-pressurization test of pure two-phase CO₂, the two simulation strategies described here give similar results, although they rely on different modelling hypotheses, first of all, the mechanical and thermal equilibrium or dis-equilibrium between phases. In particular, the physical constraint of continuous pressure and velocity across interfaces is correctly recovered in both simulations.

With this work, we wanted to stress the simple—and probably not new—observation that the simulation of compressible multiphase or multicomponent flows can be addressed in several ways but some similar conclusions can often be drawn, and used to implement new numerical methods. Hence, a simulation strategy developed for a reduced model can serve as an important building block for more complex models, which sometimes are required to simulate unsteady multiphase flows, for which no equilibrium assumption can be made a priori.

Acknowledgement

This publication has been produced with support from the *NCCS Centre*, performed under the Norwegian re-

search program Centres for Environment-friendly Energy Research (FME). B. Re and R. Abgrall acknowledge the following partners for their contributions: Aker Solutions, Ansaldo Energia, CoorsTek Membrane Sciences, Emgs, Equinor, Gassco, Krohne, Larvik Shipping, Norcem, Norwegian Oil and Gas, Quad Geometrics, Shell, Total, Vår Energi, and the Research Council of Norway (257579/E20). We would also like to acknowledge Julien Carlier and Pietro Congedo for their support in developing the four-equation model, and Svend Tollak Munkejord (SINTEF, Norway) for the helpful discussions about multiphase CO₂ flows.

References

- [1] R. Saurel and R. Abgrall, “A Multiphase Godunov Method for Compressible Multifluid and Multiphase Flows,” *J. Comput. Phys.*, vol. 150, no. 2, pp. 425–467, 1999.
- [2] R. Saurel and C. Pantano, “Diffuse-Interface Capturing Methods for Compressible Two-Phase Flows,” *Annu. Rev. Fluid Mech.*, vol. 50, no. 1, pp. 105–130, 2018.
- [3] R. Abgrall, P. Bacigaluppi, and S. Tokareva, “A high-order nonconservative approach for hyperbolic equations in fluid dynamics,” *Computers & Fluids*, vol. 169, pp. 10–22, 2018.
- [4] P. Bacigaluppi, *High order fully explicit residual distribution approximation for conservative and non-conservative systems in fluid dynamics*. PhD thesis, University of Zurich, 2019.
- [5] M. Baer and J. Nunziato, “A two-phase mixture theory for the deflagration-to-detonation transition (DDT) in reactive granular materials,” *Int. J. Multiph. Flow*, vol. 12, pp. 861–889, nov 1986.
- [6] S. Tokareva and E. Toro, “HLLC-type Riemann solver for the Baer–Nunziato equations of compressible two-phase flow,” *J. Comput. Phys.*, vol. 229, no. 10, pp. 3573–3604, 2010.
- [7] H. Lund, “A Hierarchy of Relaxation Models for Two-Phase Flow,” *SIAM J. Appl. Math.*, vol. 72, pp. 1713–1741, jan 2012.
- [8] R. Saurel, F. Petitpas, and R. A. Berry, “Simple and efficient relaxation methods for interfaces separating compressible fluids, cavitating flows and shocks in multiphase mixtures,” *J. Comput. Phys.*, vol. 228, no. 5, pp. 1678–1712, 2009.
- [9] A. K. Kapila, R. Menikoff, J. B. Bdzil, S. F. Son, and D. S. Stewart, “Two-phase modeling of deflagration-to-detonation transition in granular materials: Reduced equations,” *Phys. Fluids*, vol. 13, pp. 3002–3024, oct 2001.
- [10] P. Downar-Zapolski, Z. Bilicki, L. Bolle, and J. Franco, “The Non-equilibrium Relaxation Model for One-dimensional Flashing Liquid Flow,” *International journal of multiphase flow*, vol. 22, no. 3, pp. 473–483, 1996.
- [11] H. Lund and P. Aursand, “Two-Phase Flow of CO₂ with Phase Transfer,” *Energy Procedia*, vol. 23, pp. 246–255, 2012.
- [12] R. Abgrall and R. Saurel, “Discrete equations for physical and numerical compressible multiphase mixtures,” *J. Comput. Phys.*, vol. 186, no. 2, pp. 361–396, 2003.
- [13] R. Abgrall, “How to Prevent Pressure Oscillations in Multicomponent Flow Calculations: A Quasi Conservative Approach,” *J. Comput. Phys.*, vol. 125, no. 1, pp. 150–160, 1996.
- [14] S. Karni, “Hybrid Multifluid Algorithms,” *SIAM J. Sci. Comput.*, vol. 17, no. 5, pp. 1019–1039, 1996.
- [15] B. Re and R. Abgrall, “Non-equilibrium Model for Weakly Compressible Multi-component Flows: the Hyperbolic Operator,” in *Non-Ideal Compressible-Fluid Dyn. Propuls. Power* (F. Di Mare, A. Spinelli, and M. Pini, eds.), Springer, 2019.
- [16] I. Wenneker, A. Segal, and P. Wesseling, “A Mach-uniform unstructured staggered grid method,” *Int. J. Numer. Methods Fluids*, vol. 40, pp. 1209–1235, nov 2002.
- [17] B. Re and R. Abgrall, “Pressure-based non-equilibrium model for the simulation of weakly compressible multiphase flows,” *In preparation*, 2020.
- [18] C.-D. Munz, S. Roller, R. Klein, and K. J. Geratz, “The extension of incompressible flow solvers to the weakly compressible regime,” *Comput. Fluids*, vol. 32, no. 2, pp. 173–196, 2003.
- [19] “PETSc Web page.” <http://www.mcs.anl.gov/petsc>, 2018.
- [20] A. Zein, M. Hantke, and G. Warnecke, “Modeling phase transition for compressible two-phase flows applied to metastable liquids,” *J. Comput. Phys.*, vol. 229, no. 8, pp. 2964–2998, 2010.
- [21] P. Bacigaluppi, J. Carlier, R. Abgrall, M. Pelanti, and P. Congedo, “Assessment of a non-conservative residual distribution scheme for solving a four-equation two-phase system with phase transition.” *In preparation*.
- [22] R. Abgrall and P. Bacigaluppi, “Design of a second-order fully explicit residual distribution scheme for compressible multiphase flows,” in *International Conference on Finite Volumes for Complex Applications*, pp. 257–264, Springer, 2017.
- [23] P. Bacigaluppi, R. Abgrall, and S. Tokareva, ““A Posteriori Limited” High Order and Robust Residual Distribution Schemes for Transient Simulations of Fluid Flows in Gasdynamics.” in (minor) revision.
- [24] M. Ricchiuto and R. Abgrall, “Explicit Runge-Kutta Residual Distribution Schemes for Time Dependent Problems: Second Order Case,” *J. Comput. Phys.*, vol. 229, no. 16, pp. 5653–5691, 2010.
- [25] M. Pelanti and K. Shyue, “A Mixture-energy-consistent Six-equation Two-phase Numerical Model for Fluids with Interfaces, Cavitation and Evaporation Waves,” *Journal of Computational Physics*, vol. 259, pp. 331–357, 2014.
- [26] O. Le Métayer, J. Massoni, and R. Saurel, “Élaboration Des Lois D’État D’Un Liquide Et De Sa Vapeur Pour Les Modèles D’Écoulements Diphasiques,” *Int. J. Therm. Sci.*, vol. 43, no. 3, pp. 265–276, 2004.

NUMERICAL FLUXES FOR CRYOGENIC MULTI-PHASE FLOW COMPUTATIONS

H. Kim¹ and C. Kim^{1,*}

¹*Seoul National University, Department of Aerospace Engineering, Seoul, Republic of Korea*

*Corresponding author: chongam@snu.ac.kr

Abstract

This work presents the extension of flux schemes for ideal gas to enable multi-phase flow computations with general equation of state (EOS). Based on the homogeneous flow model, several modifications were made to obtain AUSMPW+_N and RoeM_N numerical flux schemes that are compatible with general EOS. Extended flux schemes with tabular EOS were applied to simulate multi-phase flows in liquid rocket engines such as cryogenic cavitating flow around a turbo-pump inducer and phase change flow inside a cryogenic tank.

1 Introduction

Most current liquid rocket engines utilise cryogenic fluids as propellants, oxidisers, purging gases, etc. Detailed flow analysis from the tank to the combustion chamber is essential to ensure accuracy and efficiency in engine designs and safety. Though numerical analyses have long been conducted, studies in the past have mainly focused on water, and corrections for real fluids have usually been obtained via experiments. One of the reasons why researchers adopted water simulations is that numerical methods available were only for a simple EOS, such as the ideal gas law or stiffened-gas model. With the advances of computational studies on numerical methods for non-ideal gas flows, however, real-fluid computations have begun to be performed. Typical examples include the definition of numerical speed of sound at a cell interface in the AUSM+ flux scheme [1] and the shock-discontinuity-sensing term (SDST) in more elaborated fluxes [2, 3]. These flux schemes target compressible aerodynamics, and thus, the ideal gas assumption can be adopted. As known well, such simple EOS has a limited range of validity and shows difficulties in describing real-fluid properties, especially near the critical point where non-linear thermodynamic behaviours are ubiquitous. Since cryogenic fluids are generally working near their critical points, numerical methods for simple EOS are not compatible with cryogenic flows.

This work summarises several features that must be undertaken in extending flux schemes developed for ideal gas into multi-phase flow with general EOS. Section 2 briefly introduces the adopted multi-phase model, and Section 3 describes the extension of flux schemes. In Section 4, two examples of cryogenic flows computed with the extended schemes are included.

2 Numerical Modelling

2.1 Homogeneous Mixture Model

The homogeneous mixture model with mass fraction [4] was adopted to describe multi-phase flows in this study. This model assumes the mechanical and thermal equilibrium between phases in a computational cell; thus, all phases in a computational cell are described by the same pressure, velocity and temperature. Although the detailed non-equilibrium effects at the phase interface could be reflected with more sophisticated non-equilibrium models [5, 6, 7], the homogeneous mixture approach is an attractive trade-off between computational efficiency and numerical accuracy. Above all, the extension of two-phase flow model to multi-phase situations is readily accomplished without incurring a significant increase in complexity.

The compressible Reynolds-averaged Navier–Stokes equations are cast in an integral, Cartesian tensor form within an arbitrary control volume Ω with control surface $\partial\Omega$ as follows:

$$\frac{\partial}{\partial t} \int_{\Omega} \mathbf{W} d\Omega + \oint_{\partial\Omega} [\mathbf{F} - \mathbf{F}_{\text{vis}}] dS = \int_{\Omega} \mathbf{S} d\Omega, \quad (1)$$

$$\mathbf{W} = [\rho \quad \rho u \quad \rho v \quad \rho w \quad \rho E \quad \rho y_{\ell} \quad \rho y_{\nu}]^T, \quad (2)$$

$$\mathbf{F} = [\rho U \quad \rho u U + n_x p \quad \rho v U + n_y p \quad \rho w U + n_z p \quad \rho H U \quad \rho y_{\ell} U]^T, \quad (3)$$

where $U (\equiv n_x u + n_y v + n_z w)$ is the contravariant velocity component normal to the surface element dS . In Eq. (1), \mathbf{F}_{vis} is the viscous flux vector and \mathbf{S} is the source term vector. The mass fractions satisfy the constitutive relation, $y_{\ell} + y_{\nu} = 1$. The subscripts (ℓ, ν) signify the liquid and vapour phases, respectively. The speed of sound of a mixture was evaluated from the following definition:

$$c^2 \equiv \left. \frac{\partial p}{\partial \rho} \right|_s = \frac{\rho \frac{\partial h}{\partial T}}{\rho \frac{\partial \rho}{\partial p} \frac{\partial h}{\partial T} + \frac{\partial \rho}{\partial T} \left(1 - \rho \frac{\partial h}{\partial p} \right)}. \quad (4)$$

The density and partial derivative values of the mixture were determined from the definitions of mixture density and enthalpy (Eq. (5) and Eq. (6)). Figure (1) shows that the mixture speed of sound obtained by Eq. (4) is lower than the Wood's speed of sound (speed of sound of the mixture in the mechanical equilibrium), indicating that the current model satisfies the sub-characteristic condition with respect to the mechanical equilibrium model [8].

2.2 Equation of State (EOS)

The mixture density was defined by Amagat's law:

$$\frac{1}{\rho} = \frac{(1 - y_{\nu})}{\rho_{\ell}} + \frac{y_{\nu}}{\rho_{\nu}}. \quad (5)$$

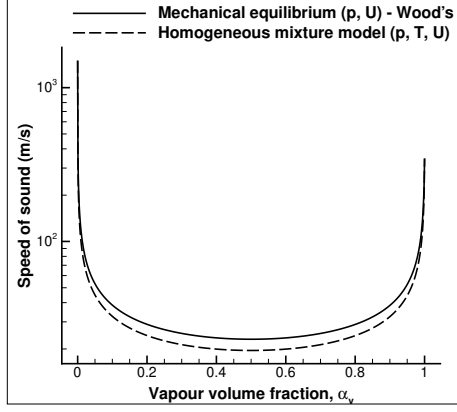


Figure 1: Comparison of speed of sound (log scale)

The mixture enthalpy was calculated as

$$h = h_\ell(1 - y_v) + h_v y_v. \quad (6)$$

The system was then closed by including an EOS for the constituent phases. All thermodynamic properties of each phase were generated by the Standard Reference Database 23, available from the National Institute of Standard and Technology (NIST) [9]. To obtain thermodynamic properties efficiently during computations, we constructed a table for each phase by the spline-based table look-up method (SBTL) [10] which is accessed by local pressure and temperature. This method creates bi-quadratic spline functions to describe the intermediate regions between the data points that were generated from the NIST database. Each spline function is C^1 continuous across every data point.

2.3 Low-Mach Preconditioning

To handle compressible multi-phase flows, which commonly accompany both subsonic and supersonic regions, the governing equations Eq. (1) were preconditioned as follows:

$$\mathbf{\Gamma} \frac{\partial}{\partial \tau} \int_{\Omega} \mathbf{Q} d\Omega + \oint_{\partial\Omega} [\mathbf{F} - \mathbf{F}_{\text{vis}}] dS = \int_{\Omega} \mathbf{S} d\Omega. \quad (7)$$

The time variable t was changed into τ , indicating that Eq. (7) should be applied to steady computations. The primitive variable vector \mathbf{Q} is given by

$$\mathbf{Q} = [p \quad u \quad v \quad w \quad T \quad y_v]^T. \quad (8)$$

The preconditioning method by Weiss and Smith [11] was adopted, and the preconditioning matrix $\mathbf{\Gamma}$ can be referred to [4]. The eigenvalues of the preconditioned system are then given by

$$\lambda \left(\mathbf{\Gamma}^{-1} \frac{\partial \mathbf{F}}{\partial \mathbf{Q}} \right) = U' - D, U' + D, U, U, U, U. \quad (9)$$

Here,

$$U' = \frac{1}{2} \left(1 + \frac{c'^2}{c^2} \right) U, \quad (10)$$

$$D = \frac{1}{2} \sqrt{\left(1 - \frac{c'^2}{c^2} \right)^2 U^2 + 4c'^2}. \quad (11)$$

The preconditioned speed of sound c' was defined by

$$c' = \min \left(c, \max \left(\sqrt{u^2 + v^2 + w^2}, V_{\text{co}} \right) \right). \quad (12)$$

In Eq. (12), V_{co} is a cut-off value that prevents c' from becoming zero in the vicinity of the stagnation region, and generally set as $V_{\text{co}} = kV_{\infty}$. In supersonic flows, the preconditioned speed of sound becomes the local speed of sound, meaning that the preconditioning is turned off.

For unsteady low Mach number computations, the dual time-stepping method was employed. When the physical time step Δt becomes large, the preconditioned speed of sound for steady flows Eq. (12) still works, but it causes unsatisfactory convergence behaviour for intermediate and small time steps. To overcome this, the unsteady preconditioning parameter V_{un} was proposed [12] based on the von Neumann stability analysis for the dual time-stepping method. The resulting preconditioned speed of sound for unsteady flows is given by

$$c'_{\text{un}} = \min \left(c, \max \left(\sqrt{u^2 + v^2 + w^2}, V_{\text{co}}, V_{\text{un}} \right) \right), \quad (13)$$

with $V_{\text{un}} = L_{\text{ch}}/(\pi\Delta t) = L_{\text{ch}}/(\pi\Delta tV) \times V = \text{St} \times V$. The domain size, a representative length scale of the lowest wave number, is typically taken as L_{ch} . Though V_{un} was derived for single-phase gas flows, it is applicable in multi-phase flows because multi-phase effects induced by the homogeneous mixture model simply change the magnitude of the speed of sound.

3 Extension of Flux Schemes

Shock-capturing flux schemes have been traditionally developed and improved for ideal gas flows. Among numerous schemes available, AUSMPW+ [2] and RoeM [3] are well known for their robustness and accuracy. Taking advantage of the mathematical simplicity of the homogeneous mixture model, such flux schemes can be extended to compute compressible multi-phase flows. To ensure the compatibility with the most general EOS for cryogenic multi-phase flow computations, the following modifications have been made, which yields the AUSMPW+_N and RoeM_N schemes [13].

3.1 Interfacial Speed of Sound

In AUSM-type fluxes, the notion of the common speed of sound at a cell interface, $c_{1/2}$, is crucial in capturing contact or shock discontinuity. The AUSMPW+ defines $c_{1/2}$ based on the Prandtl relation for gas dynamics and local flow directions:

$$c_{1/2} = \begin{cases} c_s^2 / \max(c_s, |U_L|) & \text{for } (U_L + U_R) > 0 \\ c_s^2 / \max(c_s, |U_R|) & \text{for } (U_L + U_R) < 0, \end{cases} \quad (14)$$

where the speed of sound normal to a cell interface, c_s , is given by $\sqrt{2(\gamma - 1)H_{\text{normal}}/(\gamma + 1)}$ for a calorically perfect gas. This enables an exact capture of a single stationary oblique shock and the elimination of an unphysical expansion shock.

However, the Prandtl relation for gas dynamics is not applicable across a phase interface. The interfacial numerical speed of sound in multi-phase flow computations cannot be determined by Eq. (14), and it should be approximated based on multi-phase flow physics. The homogeneous mixture model gives a lower sound speed in the mixture than that of either phase; any interfacial speed of sound defined from an averaged mass fraction on both sides satisfies this property [14]. For example, $c_{1/2}$ can be obtained from the Roe-averaged mass fraction of $\hat{y}_v = \frac{\sqrt{\rho_L} y_{v,L} + \sqrt{\rho_R} y_{v,R}}{\sqrt{\rho_L} + \sqrt{\rho_R}}$:

$$c_{1/2} = c_{1/2}(p_{1/2}, T_{1/2}, \hat{y}_v), \quad (15)$$

where $p_{1/2}$ and $T_{1/2}$ are simple arithmetic averages of left and right values. Note that $c_{1/2}$ obtained from the direct combination of the left and right sound speeds, such as $c_{1/2} = \min(c_L, c_R)$ or $c_{1/2} = (c_L + c_R)/2$, cannot reflect the physical property of mixture sound speed, and numerical instability can occur.

3.2 Shock-discontinuity-sensing Term

Various shock instabilities, such as carbuncles or numerical oscillations, have caused troubles in numerical flux schemes. The AUSMPW+ and RoeM schemes for gas dynamics contain a shock-discontinuity-sensing term (SDST), which detects shock and controls the amount of numerical diffusion to improve the shock stability and numerical accuracy compared to preceding AUSM-type or Roe-type schemes. This sensing term is designed by checking pressure distribution around a cell interface:

$$\Pi_{1/2}^o = \min\left(\frac{p_L}{p_R}, \frac{p_R}{p_L}\right). \quad (16)$$

However, in two-phase flows, even in a subsonic condition, the pressure field can vary drastically due to the large density and high speed of sound in the liquid phase. The original SDST Eq. (16) can misinterpret a physically non-shock region as a shock region. A two-phase SDST is thus derived from the ideal gas law (for gas phase) and stiffened-gas model (for liquid phase) [14]:

$$\Pi_{1/2} = \min\left(\frac{\bar{p}_L}{\bar{p}_R}, \frac{\bar{p}_R}{\bar{p}_L}\right), \quad \bar{p}_{L,R} = \frac{1}{\frac{\alpha_{v,1/2}}{p_{L,R}} + \frac{1-\alpha_{v,1/2}}{p_{L,R}+p_c}}, \quad (17)$$

where p_c comes from the stiffened-gas EOS. In case of general EOS, such as the one used in this study, the p_c term is indeterminate. By analysing the steady one-dimensional shock relations, an SDST for general EOS is designed [13] as follows:

$$\Pi_{1/2}^* = \min\left(\frac{\bar{p}_L^*}{\bar{p}_R^*}, \frac{\bar{p}_R^*}{\bar{p}_L^*}\right), \quad \bar{p}_{L,R}^* = p_{L,R} + 0.1 \times \min(\rho_L c_L^2, \rho_R c_R^2). \quad (18)$$

3.3 Scaling for All-speed Flux Schemes

In accordance with the all-speed preconditioning technique (Section 2.3), the AUSMPW+ and RoeM flux schemes need to be scaled for unsteady all-speed flow computations. Unlike the traditional preconditioning technique for steady computations, treating the velocity and pressure difference dissipation terms separately with different scaling functions is important in securing both accuracy and computational efficiency at low-Mach high-Strouhal number limits. The scaling functions for the velocity and pressure difference terms are given respectively by

$$\phi_u = \theta_u(2 - \theta_u), \quad \phi_p = \theta_p(2 - \theta_p) \quad (19)$$

with

$$\theta_u = \min\left(1, \max\left(\frac{\sqrt{u_{1/2}^2 + v_{1/2}^2 + w_{1/2}^2}}{c_{1/2}}, \frac{V_{co}}{c_{1/2}}\right)\right), \quad (20)$$

$$\theta_p = \min\left(1, \max\left(\frac{\sqrt{u_{1/2}^2 + v_{1/2}^2 + w_{1/2}^2}}{c_{1/2}}, \frac{V_{co}}{c_{1/2}}, \frac{V_{un}}{c_{1/2}}\right)\right). \quad (21)$$

These functions were designed in a consistent manner with the preconditioned speed of sound c' Eq. (12) and c'_{un} Eq. (13).

3.4 AUSMPW+_N & RoeM_N

Applying the features in Sections 3.1–3.3 to the original AUSMPW+ and RoeM flux schemes leads to AUSMPW+_N, RoeM_N schemes for multi-phase flow computations with general EOS. Although some attractive properties of the original schemes in gas dynamics, such as one-cell capturing of a stationary shock, may be compromised due to the use of general EOS, other advanced properties such as the enhanced resolution of contact discontinuities and better stability are still retained by the AUSMPW+_N and RoeM_N schemes. Detailed formulations and analyses along with various test results can be found in [13, 4].

4 Numerical Results

4.1 Cryogenic Cavitating Flow around Turbopump Inducer

Cavitation around a high-speed turbopump inducer has been a consistent obstacle in developing liquid rocket engines. This section shows the capability that numerical analyses using general EOS could contribute to uncovering the cavitation mechanism around the inducer, or at least, to predicting the cavity size under various operating conditions. A model inducer was experimented upon with cold water at the Korea Aerospace Research Institute (KARI), and the numerical predictions for the inducer performance agreed well with the experimental data [13]. Using the validated numerical solver, cryogenic cavitating flows have been computed for the same configuration. Since the AUSMPW+_N and RoeM_N give similar results, the RoeM_N scheme with MLP5 limiter [15] was used, and the LU-SGS method [16] was adopted to obtain steady-state RANS solutions. The cavitation model by Merkle [17] and the $k - \omega$ SST turbulence model [18] were employed. The grid consisted of approximately 11.3 million computational cells, and the mass flow rate inlet and pressure outlet boundary conditions were applied. Table (1) summarises the computational conditions. The thermodynamic parameter Σ in Table (1) is a crucial variable to determine the thermal effect in bubble dynamics, which is defined as

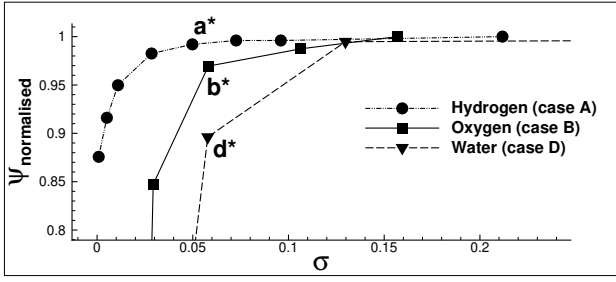
$$\Sigma(T_\infty) = \frac{\rho_v^2 \mathcal{L}^2}{\rho_\ell^2 c_{p\ell} T_\infty \mathcal{D}_\ell^{1/2}}, \quad (22)$$

where \mathcal{L} is the latent heat. The flow coefficient ϕ of all cases was identically set as 0.099.

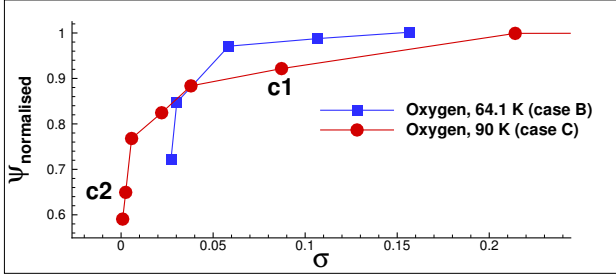
Figure (2) plots the head-rise coefficient Ψ in terms of the cavitation number σ . Here, Ψ is normalised by the value at the non-cavitating condition. Each variable is

Table 1: Flow conditions around inducer

Case	Fluid	RPM	T_{in} (K)	Σ
A	Hydrogen	10,000	20.8	1.12×10^6
B	Oxygen	5,000	64.1	14.42
C			90	1.56×10^4
D	Water		305.4	14.22



(a) Thermal effect according to working fluid (case: A, B, D).



(b) Effect of inlet temperature (case: B, C).

Figure 2: Normalised head-rise coefficient of an inducer according to the tip cavitation number

given by

$$\Psi = \frac{p_{\text{out}} - p_{\text{in}}}{\rho_{\text{in}} g}, \quad \sigma = \frac{p_{\text{in}} - p_{\text{sat}}(T_{\text{in}})}{0.5 \rho_{\text{in}} V_{\text{tip}}^2}. \quad (23)$$

The head-rise coefficient quantifies the inducer performance. As σ decreases by lowering the outlet pressure, cavitation occurs on the blade. The generation and collapse of the vapour volume disturbs the liquid flow and reduces the pumping capability of the inducer.

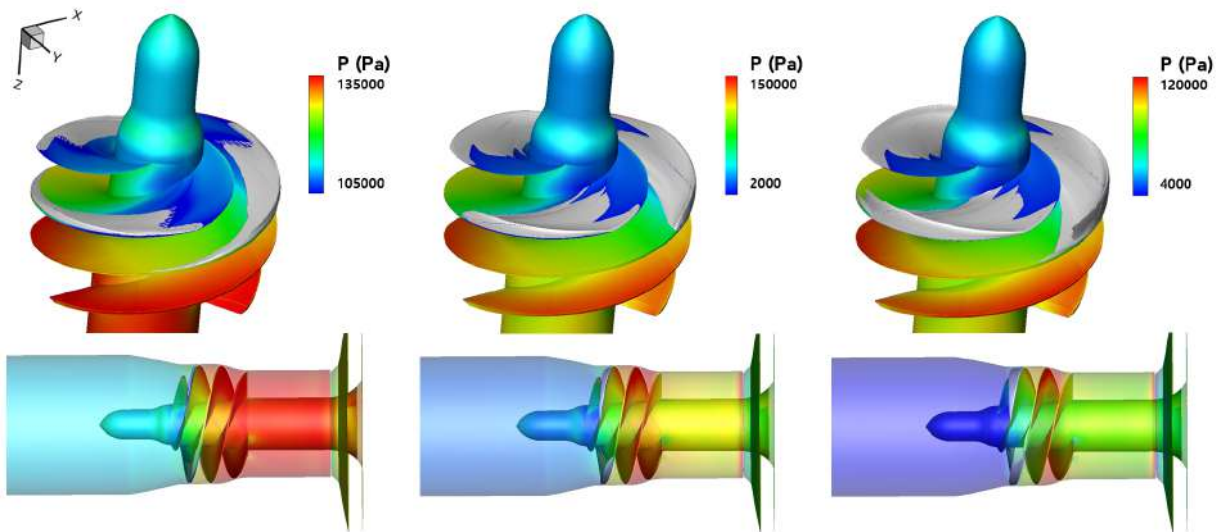
To verify the thermal effect in cryogenic cavitation, the numerical results of hydrogen, oxygen (case B), and water are compared in Figure 2(a). The inlet condition of oxygen was adjusted so that the thermodynamic parameter matches that of water case, although complete scaling between any two cavitating flows is not possible [19]. As expected, hydrogen flow characterized by

high Σ shows a far delayed cavitation breakdown (i.e., total loss of pump capability). When the ratio of liquid density to vapour density (ρ_{ℓ}/ρ_v) is large, only a small amount of liquid mass is required to generate a cavity. Consequently, the heat of vaporisation needed is small, and the bubble temperature does not fall much below the bulk liquid temperature. On the contrary, with a small ρ_{ℓ}/ρ_v , the bubble temperature and thus the saturation pressure inside the bubble are lowered considerably. This thermal effect reduces the bubble growth rate, leading to improved pump performance. As shown in Table (2), the ρ_{ℓ}/ρ_v of case A was very small. This explains the highest value of Σ and the delayed cavitation breakdown of the hydrogen case.

Interestingly, oxygen and water test cases under the same Σ conditions resulted in a noticeable gap. The density ratios of the two cases were different, but the difference was not dramatic as in the case of hydrogen. The gap between the oxygen and water results can be understood by the critical time t_C from the bubble growth theory. According to the theory, the growth rate is almost constant at the early stage of bubble growth. As the bubble grows further, the rate decreases by the thermal effect and becomes proportional to $t^{-1/2}$. The moment at which the thermal effect becomes large enough to take over the bubble growth rate is the critical time. The critical time can be approximated by $t_C \approx (p_{\text{sat}} - p)/(\rho_{\ell} \Sigma^2)$ [20]. A fair assumption of the time during which the bubble passes through the inducer is $t_B \approx 1/(\Omega \phi)$ with the angular frequency of inducer Ω . Table (2) displays t_C and t_B for each case assuming zero local pressure for a conservative estimation of t_C . Only case D corresponds to $t_C > t_B$, which means the thermal effect was not sig-

Table 2: ρ_{ℓ}/ρ_v , t_C , t_B for the cavitating inducer cases

Case	Fluid	ρ_{ℓ}/ρ_v	t_C	t_B
A	Hydrogen	47	1.30×10^{-9}	9.65×10^{-3}
B	Oxygen	10943	0.0073	0.0193
C		262	3.57×10^{-7}	
D	Water	28988	0.024	



(a) Hydrogen, $\sigma=0.050$ (a^* in Fig. 2(a)) (b) Oxygen, $\sigma=0.058$ (b^* in Fig. 2(a)) (c) Water, $\sigma=0.058$ (d^* in Fig. 2(a))

Figure 3: Computed results of different working fluids at similar cavitation numbers, top: surface pressure distribution and iso-surface of $\alpha_v = 0.2$, bottom: pressure change along the z-axis

nificant the whole time while bubble travelled through the inducer blades. In all other cases, it appears $t_C < t_B$. It can be deduced that the thermal effect influences the cavitation in case B, although Σ is similar to that of case D. Figure (3) shows the surface pressure distributions with the iso-surface of $\alpha_v = 0.2$ and the pressure change along the z-axis for three different working fluids at similar cavitation numbers (points a*, b*, d* in Figure 2(a)). Again, the largest cavity was formed in water, despite the equal σ and the similar Σ here, leading to the lowest $\Psi_{\text{normalised}}$.

Figure 2(b) presents the effect of inlet temperature on the same fluid (oxygen). The higher the temperature, the greater the thermal effect becomes because ρ_l/ρ_v decreases as the temperature gets closer to the critical temperature. To contrast the results before and after the breakdown, surface pressure distributions and the iso-surface of the vapour phase for points c1 and c2 are presented in Figure (4). Before the cavitation breakdown, cavities existed only locally near the leading-edge tip. After the breakdown occurred, the cavities not only covered the blade surface but also almost blocked the whole passageway. In both results, local high-pressure regions were observed immediately after the cavity closure, manifesting that structural damage may occur as a result of cavitation.

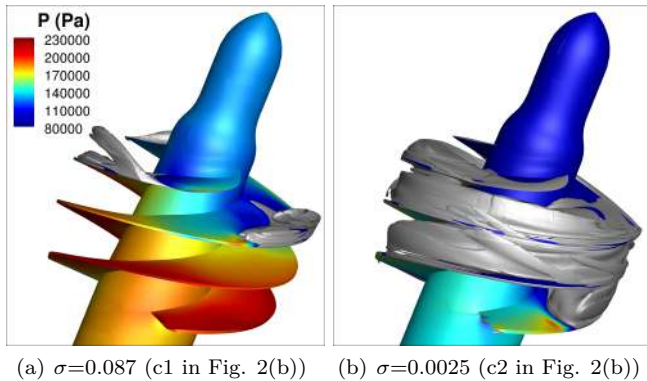


Figure 4: Surface pressure distribution and iso-surface of $\alpha_v = 0.2$ for oxygen, $T_{\text{in}} = 90$ K

4.2 Phase Change Flow Inside a Cryogenic Tank

Cryogenic fuel used in a liquid rocket is highly susceptible to temperature changes, so the cryogenic fluid stored in the tank experiences a continuous phase change during a mission. Since perfect insulation is impossible, the heat flux from the tank wall evaporates liquid fuel. The pressure inside the tank increases accordingly, and the vaporised fuel can no longer be used as fuel. Hence, predicting the pressure change and evaporation rate inside the tank after the rocket launch is essential for the safety and successful completion of a mission.

This section presents the numerical results for the second-stage hydrogen tank of the AS-203 flight test [21]. The grid was generated with 1.75 million hexahedral cells (Figure (5)). The initial condition as well as the time-varying heat fluxes and acceleration ($\mathcal{O}(10^{-4}g)$) were the same as the simulation conducted by Grayson *et al.* [22]. Additionally, the zero acceleration condition was computed to determine the effects of gravity. All numerical methods used were the same as the previous section except that this time AUSMPW+_N flux scheme was adopted. Computations were conducted up to $t = 200$ s

because 5,000 s of the experiment is too costly to compute even with the present compressible flow solver based on the relatively efficient multi-phase model.

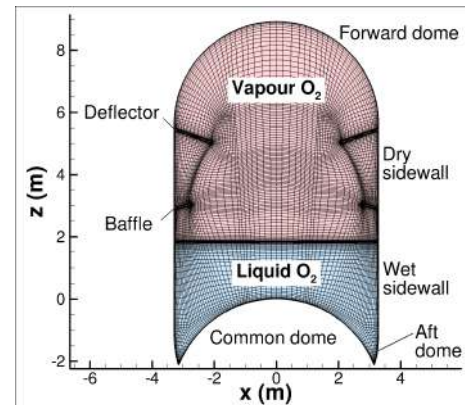


Figure 5: Cross-section of grid for the hydrogen tank

Figure (6) compares the computational results with and without acceleration at $t=200$ s. Because the heat transfer characteristic of each wall section was different, the wall temperature seemed to be patched. Although the acceleration was very low ($\mathcal{O}(10^{-4}g)$), its effects was obvious. With gravity, the heated vapour was lifted upward and accumulated under the deflector. However, without gravity, each wall section showed almost uniform temperature distribution. The iso-surface shows the vapour phase. Since the evaporation occurred from the liquid adjacent to the wall, it looked like the vapour phase wrapped around the liquid bulk. Another distinction between the two results was the shape of this vapour iso-surface (or the shape of liquid bulk). Without buoyancy, the generated vapour could not go upward, so the vapour volume grew between the liquid and the wall, pushing the liquid radially to the centre. Since the surface tension was not modelled, the edge of the liquid sprouted. If the surface tension was included, overall liquid bulk should retain a round shape, and the centre of the bulk, not the edge, will swell. However, with gravity, the shape of the liquid bulk remained almost steady as the evaporated mass rose without pushing the liquid. Figure (7) compares the pressure changes with the experimental data and other numerical results using the ideal gas law. The predictions of the current model with general EOS agree well with the experimental data.

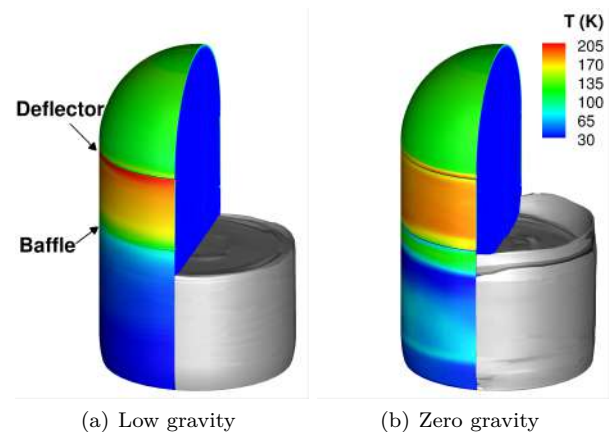


Figure 6: Wall temperature distribution and iso-surface ($\alpha_v=0.25$) of vapour phase enclosing the liquid hydrogen

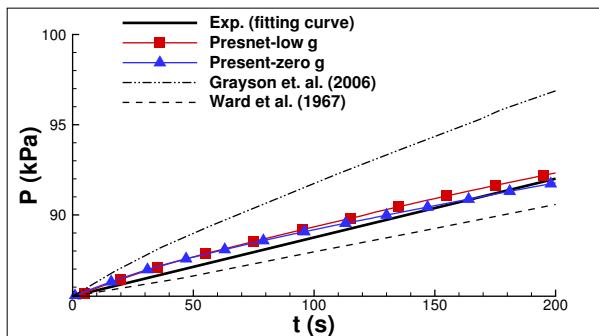


Figure 7: Comparison of pressure change in tank

5 Conclusions

Based on the homogeneous flow assumptions with system preconditioning for all-speed flows, the numerical speed of sound in flux schemes for multi-phase flows was obtained from the most general form of EOS. The SDST in flux schemes was also modified to deal with multi-phase real-fluid flows. Extended flux schemes with tabular EOS successfully simulated cryogenic cavitating flow around a turbo-pump inducer and phase change flow inside a cryogenic tank. Additional work is in progress to improve the phase change model for cryogenic multi-phase flows.

Acknowledgment

This research was supported by the National Research Foundation of Korea (NRF-2013R1A5A1073861).

References

- [1] M.-S. Liou, "A sequel to AUSM: AUSM+," *Journal of Computational Physics*, vol. 129, no. 2, pp. 364–382, 1996.
- [2] K. H. Kim, C. Kim, and O.-H. Rho, "Methods for the Accurate Computations of Hypersonic Flows," *Journal of Computational Physics*, vol. 174, no. 1, pp. 38–80, 2001.
- [3] S.-s. Kim, C. Kim, O.-H. Rho, and S. K. Hong, "Cures for the shock instability: Development of a shock-stable Roe scheme," *Journal of Computational Physics*, vol. 185, no. 2, pp. 342–374, 2003.
- [4] H. Kim, Y. Choe, H. Kim, D. Min, and C. Kim, "Methods for compressible multiphase flows and their applications," *Shock Waves*, vol. 29, pp. 235–261, 2018.
- [5] M. R. Baer and J. W. Nunziato, "A two-phase mixture theory for the deflagration-to-detonation transition (DDT) in reactive granular materials," *International Journal of Multiphase Flow*, vol. 12, no. 6, pp. 861–889, 1986.
- [6] R. Saurel and R. Abgrall, "A Multiphase Godunov Method for Compressible Multifluid and Multiphase Flows," *Journal of Computational Physics*, vol. 150, no. 2, pp. 425–467, 1999.
- [7] A. K. Kapila, R. Menikoff, J. B. Bdzil, S. F. Son, and D. S. Stewart, "Two-phase modeling of deflagration-to-detonation transition in granular materials: Reduced equations," *Physics of Fluids*, vol. 13, no. 10, pp. 3002–3024, 2001.
- [8] T. FLÄTTEN and H. LUND, "Relaxation Two-Phase Flow Models and the Subcharacteristic Condition," *Mathematical Models and Methods in Applied Sciences*, vol. 21, no. 12, pp. 2379–2407, 2011.
- [9] E. W. Lemmon, M. L. Huber, and M. O. McLinden. NIST Standard Reference Database 23: Reference Fluid Thermodynamic and Transport Properties-REFPROP, Version 8.0 [Online] <http://www.nist.gov/srd/nist23.cfm>, 2007.
- [10] International Association for the Properties of Water and Steam, "Guideline on the Fast Calculation of Steam and Water Properties with the Spline-Based Table Look-Up Method (SBTL)," technical report, 2015.
- [11] J. M. Weiss and W. A. Smith, "Preconditioning applied to variable and constant density flows," *AIAA Journal*, vol. 33, no. 11, pp. 2050–2057, 1995.
- [12] S. Venkateswaran and C. L. Merkle, "Dual time-stepping and preconditioning for unsteady computations," in *33rd Aerospace Sciences Meeting and Exhibit, Aerospace Sciences Meetings*, American Institute of Aeronautics and Astronautics, Jan. 1995.
- [13] H. Kim, H. Kim, and C. Kim, "Computations of Homogeneous Multiphase Real Fluid Flows at All Speeds," *AIAA Journal*, vol. 56, no. 7, pp. 2623–2634, 2018.
- [14] S.-W. Ihm and C. Kim, "Computations of Homogeneous-Equilibrium Two-phase Flows with Accurate and Efficient Shock-Stable Schemes," *AIAA Journal*, vol. 46, no. 12, pp. 3012–3037, 2008.
- [15] S.-H. Yoon, C. Kim, and K.-H. Kim, "Multi-dimensional limiting process for three-dimensional flow physics analyses," *Journal of Computational Physics*, vol. 227, pp. 6001–6043, 2008.
- [16] S. Yoon and A. Jameson, "Lower-Upper Symmetric-Gauss-Seidel Method for the Euler and Navier-Stokes Equations," *AIAA Journal*, vol. 26, no. 9, pp. 1025–1026, 1988.
- [17] C. L. Merkle, J. Z. Feng, and P. E. O. Buelow, "Computational modeling of the dynamics of sheet cavitation," in *3rd International Symposium on Cavitation*, (Grenoble, France), 1998.
- [18] F. R. Menter, M. Kuntz, and R. Langtry, "Ten Years of Industrial Experience with the SST Turbulence Model," in *4th International Symposium on Turbulence, Heat and Mass Transfer*, 2003.
- [19] J.-P. Franc, C. Rebattet, and A. Coulon, "An Experimental Investigation of Thermal Effects in a Cavitating Inducer," *Journal of Fluids Engineering*, vol. 126, pp. 716–723, 12 2004.
- [20] C. Brennen, *Hydrodynamics of Pumps*. A Concepts ETI Book Series, Concepts ETI, 1994.
- [21] W. D. Ward *et al.*, "Evaluation of AS-203 low gravity orbital experiment," Technical Report NASA CR 94045, 1967.
- [22] G. Grayson, A. Lopez, F. Chandler, L. Hastings, and S. Tucker, "Cryogenic Tank Modeling for the Saturn AS-203 Experiment," in *42nd AIAA/ASME/SAE/ASEE Joint Propulsion Conference & Exhibit*, American Institute of Aeronautics and Astronautics, 2006.

ENHANCING THE PREDICTIVE CAPABILITIES FOR HIGH P/T FUEL SPRAYS; NON-IDEAL THERMODYNAMIC MODELLING USING PC-SAFT

P. Koukouvinis^{1,2}, A. Vidal-Roncero¹, C. Rodriguez¹, M. Gavaises¹ and L. Pickett²

¹*SMCSE, City University London, Northampton Square EC1V 0HB, United Kingdom*

²*Combustion Research Facility, Sandia National Laboratory, 7011 East Ave, Livermore, CA 94550, US*

Abstract

The present work aims to investigate the complex phenomena occurring during high-pressure/high-temperature fuel injection of the Engine Combustion Network (ECN) Spray-A case. While commonly in the literature transcritical mixing cases are approached using traditional cubic equation-of-state models, such models can prove insufficient in the accurate prediction of liquid density and speed of sound. The purpose of the present investigation is to employ a general tabulated approach which can be applied to any type of thermodynamic closure. At the same time, a more advanced model based on the Perturbed-Chain Statistical Associating Fluid Theory (PC-SAFT) is employed to create the thermodynamic table, as it is proven superior to the traditional cubic models, while also having the capacity of predicting Vapor-Liquid-Equilibrium. The model has been used for a combination of dodecane and nitrogen mixing, corresponding to the well known Spray-A conditions. Vapor penetration and mixing both in terms of temperature and mass fraction are found in agreement to experiments, within the experimental errors. Also, the thermodynamic states correspond well with the adiabatic isobaric-mixing curve, demonstrating the energy-conservative nature of the approach.

1 Introduction

The operation of modern Internal Combustion Engines (ICEs) involves injection and mixing of fuel with oxidiser and, consequently, combustion, as the core of the engine operation; indeed, the processes of fuel atomisation, evaporation, mixing with the gas and combustion greatly affect engine efficiency and emissions [1], hence are extensively studied both by industry and academic/research institutes. A particular complexity of the operation of modern engines, is the extreme temperature/pressure range that the fuel undergoes from the fuel piping, then through the injector and finally in the combustion chamber/engine cylinder. Indicatively, for modern Diesel engines, a pressure variation from more than 2000bar (at common rail, note that modern systems may even reach 3000bar) to effectively 0bar (cavitation regions in the fuel injector) and a temperature variation from 363K (high pressure side of the fuel pump) to more than 1000K (engine cylinder) are expected. At such pressure/temperature ranges fuel properties cannot be assumed constant. Indicatively, diesel density may change by 14% over a range of 0-2000bar, at 363K; for the same range viscosity can change over 200% [2]. Such variations have severe thermodynamic implications in the behaviour of the fuel. In particular, the expansion

of the fuel as pressure drops induces cooling due to the Joule-Thomson effect. On the other hand, the immense shear stresses the fuel is subjected into, cause strong heating. Previous works have identified the dependence of induced heating or cooling on the fuel injector discharge coefficient, which is a measure of the efficiency of the fuel injector.

Additional complexities that take place along property variation, involve phase change mechanisms, such as cavitation at sharp geometric features inside the injector or evaporation and mixing with the oxidiser. Also, as the downstream conditions of the injector may exceed the critical point of the fuel/gas, departure from classical atomisation may occur, giving its place to transcritical mixing. Indeed, evidence exists that, at elevated pressures and temperatures, surface tension effects diminish and the fuel/gas mixing is dominated by diffusive mixing [3]. It is notable, that the aforementioned effects are not solely related to Diesel engines, as similar transcritical operation is also relevant to gasoline engines [4], high-pressure gas turbines [5] and rocket engines [6]. The previous description of phenomena during fuel injection provides a brief overview of the complexities that necessitate the use of accurate real-fluid modelling, as it is necessary to capture phase transitions, subcritical/transcritical/supercritical mixing and temperature changes due to fuel expansion. Traditionally, models capable of describing such phenomena are cubic Equations of State (EoS); a representative example is the Peng Robinson EoS[7]. Despite their widespread use, cubic EoS are known to suffer from deficiencies, as they commonly underpredict liquid density and overpredict speed of sound (the interested reader is addressed to [8, 9]). Improvements, aiming mainly to address the liquid density exist; e.g. the generalised Redlich-Kwong-Peng-Robinson EoS[10], or volume translated methods[11], however, inaccuracies or inconsistencies are still present.

On this aspect, there are more complex models, which however require extensive calibration based on experimental data (see e.g. [12]). An attractive alternative, is the Perturbed Chain Statistical Associating Fluid Theory (or PC-SAFT) model, which has a higher accuracy comparing to cubic EoS in predicting thermodynamic and transport properties, both for pure components and mixtures, requiring minimal input of just three molecular characteristics of the component to be modelled. In the present work, the PC-SAFT model is used to predict properties of a hydrocarbon and nitrogen mixture, aiming to replicate a well-known benchmark case in the area of high pressure/high temperature fuel injection, the Spray-A case from the Engine Combustion Network (ECN). In the next sections, the mathematical and thermodynamic models are presented, followed by the geometry of the Spray-A case and the case set-up. A detailed

comparison between the numerical simulations and the experimental data is made, examining the mass fraction and temperature distributions in the radial and axial direction of the spray.

2 Mathematical model

The simulations are carried out by assuming a diffuse interface approach, under a homogeneous mixture assumption under mechanical and thermal equilibrium [13]; all fluids involved share the same velocity, pressure and temperature fields. Hence, the model consists of four Partial Differential Equations, plus the thermodynamic closure. It is highlighted that the term mixture is used to denote multicomponent (multiple materials) mixture, rather than multiple phases. The governing equations are provided below:

-Mixture mass conservation equation:

$$\frac{\partial \rho}{\partial t} + \nabla \cdot (\rho \mathbf{u}) = 0 \quad (1)$$

where ρ is the mixture density and \mathbf{u} is the velocity vector field.

- Dodecane mass fraction, y_{C12} , transport equation:

$$\frac{\partial \rho y_{C12}}{\partial t} + \nabla \cdot (\rho \mathbf{u} y_{C12}) = -\nabla \cdot \mathbf{J} \quad (2)$$

where \mathbf{J} is the mass diffusion flux defined as:

$$\mathbf{J} = -\left(\rho D_m + \frac{\mu_t}{Sc_t}\right) \nabla y_{C12} - D_T \frac{\nabla T}{T} \quad (3)$$

D_m and D_T are the mass and temperature diffusion coefficients respectively and Sc_t is the turbulent Schmidt number, which plays an important role, as the simulations are performed with a RANS turbulence model. The value of turbulent Schmidt number used here is 0.5. The diffusion coefficients are calculated using kinetic theory, as:

$$D_m = 0.00188 \frac{\left[T^3 \left(\frac{1}{MW_{C12}} + \frac{1}{MW_{N2}}\right)\right]^{1/2}}{p \sigma^2 \Omega_D} \quad (4)$$

where Ω_D is the diffusion collision integral, which can be found in tabulated form or analytic expressions (see [14]) and is a function of $T^* = \frac{T}{\epsilon/k_B}$. The temperature diffusion coefficient is calculated based on the multicomponent approximation of [15]. Quadratic Upwind Interpolation For Convective Kinematics (QUICK) has been used for the transport equation of dodecane. The parameters needed for calculating the diffusion coefficients are presented in Table (1) (from [16]). The values

Table 1: Kinetic theory parameters for the components examined

	σ (Å)	ϵ/k_B (K)
C_{16}	8.89	764.03
C_{14}	8.3	701.92
C_{12}	7.58	622.51
N_2	3.4	102.12

used for estimating T^* and D_m are arithmetic and geometric averages of the involved components, respectively.

- Mixture Momentum equation:

$$\frac{\partial \rho \mathbf{u}}{\partial t} + \nabla \cdot (\rho \mathbf{u} \otimes \mathbf{u}) = -\nabla p + \nabla \cdot \tau \quad (5)$$

where p stands for the pressure and τ corresponds to the stress tensor $\tau = \mu_{\text{eff}}[\nabla \mathbf{u} + (\nabla \mathbf{u})^T]$, with μ_{eff} the sum of laminar, μ , and turbulent, μ_t , dynamic viscosity. The momentum equation is resolved using a Second Order Upwind [17] scheme, to minimise numerical diffusion, while also maintaining stability.

- The mixture energy equation:

$$\frac{\partial \rho E}{\partial t} + \nabla \cdot (\mathbf{u}(\rho E + p)) = \nabla \cdot (\lambda_{\text{eff}} \nabla T) + \nabla \cdot (\tau \cdot \mathbf{u}) + \nabla \cdot (h \mathbf{J}) \quad (6)$$

where E is the total energy, defined as internal energy plus the kinetic energy, or $E = h - \frac{p}{\rho} + \frac{1}{2} \mathbf{u}^2$ where h is the enthalpy, provided as a function of pressure and temperature (see section of Thermodynamic Properties). The total effective thermal conductivity, λ_{eff} , is equal to the thermal conductivity, λ , being a function of thermodynamic conditions p, T and composition, y_{C12} , plus the turbulent contribution, as follows:

$$\lambda_{\text{eff}} = \lambda + \frac{c_p \mu_t}{Pr_t} \quad (7)$$

where c_p is the heat capacity of the mixture and Pr_t is the turbulent Prandtl number, assumed equal to 0.85, based on the average value obtained from multiple experiments using different materials [18]. The energy equation is discretized using a Second Order Upwind scheme [17]. Turbulence is handled with the standard k- ϵ model, its coefficients, in particular Schmidt number and $C_{\epsilon 1}$, tuned based on previous studies [19], to values of 0.5 and 1.52 respectively.

$$\frac{\partial \rho k}{\partial t} + \nabla \cdot (\rho \mathbf{u} k) = \nabla \cdot \left[\left(\mu + \frac{\mu_t}{\sigma_k} \right) \nabla k \right] + G_k - \rho \epsilon - Y_M \quad (8)$$

$$\frac{\partial \rho \epsilon}{\partial t} + \nabla \cdot (\rho \mathbf{u} \epsilon) = \nabla \cdot \left[\left(\mu + \frac{\mu_t}{\sigma_\epsilon} \right) \nabla \epsilon \right] + C_{\epsilon 1} \frac{\epsilon}{k} G_k - C_{\epsilon 2} \rho \frac{\epsilon^2}{k} \quad (9)$$

where G_k is the turbulence generation term and Y_M is the turbulence dilation term [20].

3 Thermodynamic model

Accurate modelling of fuel/gas properties is done using the Perturbed Chain Statistical Associating Fluid Theory (PC-SAFT) EoS, which is a theoretically derived model, based on perturbation theory, that splits the intermolecular potential energy of the fluid into a reference term accounting for repulsive interactions and a perturbation term accounting for attractive interactions. The reference fluid is composed of spherical segments comprising a hard sphere fluid that then forms molecular chains to create the hard-chain fluid. The attractive interactions, perturbations to the reference system, are accounted for with the dispersion term. Intermolecular interaction terms accounting for segment self- or cross-associations are ignored. Hence, each component is characterized by three pure component parameters, which are

a temperature-independent segment diameter, σ , a segment interaction energy, ϵ/k , and a number of segments per molecule, m ; detailed databases for these parameters exist for non-associating fluids, such as hydrocarbons or gases, see [21, 22].

The PC-SAFT model aims to construct an expression for the residual Helmholtz energy a_{res} , which is the sum of a hard-chain term and a dispersion term; the detailed expression of these terms is rather lengthy, hence the interested reader is addressed to the original model publication [21]. Once the residual Helmholtz energy is obtained, all thermodynamic properties can be defined as functions of that expression. The transport properties are estimated based on the residual entropy scaling method, following Lötgering-Lin and Gross [23] for dynamic viscosity and Hopp and Gross [24] for thermal conductivity.

Identification of Vapor Liquid Equilibrium (VLE) is done through the the minimisation of the molar Helmholtz Free energy, defined in terms of density, temperature and composition. This optimization problem is solved via a combination of the successive substitution iteration (SSI) and the Newton minimization method with a two-step line-search procedure, and the positive definiteness of the Hessian is guaranteed by a modified Cholesky decomposition. The algorithm consists of two stages: first, the mixture is assumed to be in a single-phase state and its stability is assessed via the minimization of the Tangent Plane Distance (TPD) [25]. The stability is tested by purposely dividing the homogeneous mixture in two phases, one of them in an infinitesimal amount and called 'trial phase'. For any feasible two-phase mixture, if a decrease in the Helmholtz free energy is not achieved, then the mixture is stable. In case the minimum of the TPD is found to be negative, the mixture is considered unstable and a second stage of phase splitting takes place consisting on the search for the global minimum of the Helmholtz Free Energy. As a result, the pressure of the fluid and the compositions of both the liquid and vapor phases are calculated.

All the aforementioned process for calculating properties and identifying VLE is done as a precursor step of the simulation, to construct a structured table, where all properties are expressed in terms of the decimal logarithm of pressure ($\log_{10}p$), temperature and mass fraction. The CFD solver uses this table and performs linear interpolation to identify all thermodynamic properties required during the simulation. In the present work, the thermodynamic table had a resolution of $100 \times 400 \times 101$ corresponding to $\log_{10}p$, T , y intervals, for a range of p : [10Pa - 2500bar] \times T : [280 - 2000K] \times y : [0-1] respectively. The structure of the table enables very fast searching and reasonable accuracy in the property representation; validation of the method is in the previous work of the authors, see [26]. An indicative representation of the tabulated EoS used in terms of density is shown in Figure (1).

4 Simulations

4.1 Case set-up

The Spray-A injector is a single hole, tapered (k-factor=1.5) Bosch solenoid-activated injector, with nominal orifice diameter $d_{\text{out}} \sim 90 \mu\text{m}$ and orifice length of 1mm. The geometry of the Spray-A injector used is based on the published geometry from the ECN website. The simulations to be presented, are treated as 2D axis-symmetric, using the published radial profile over

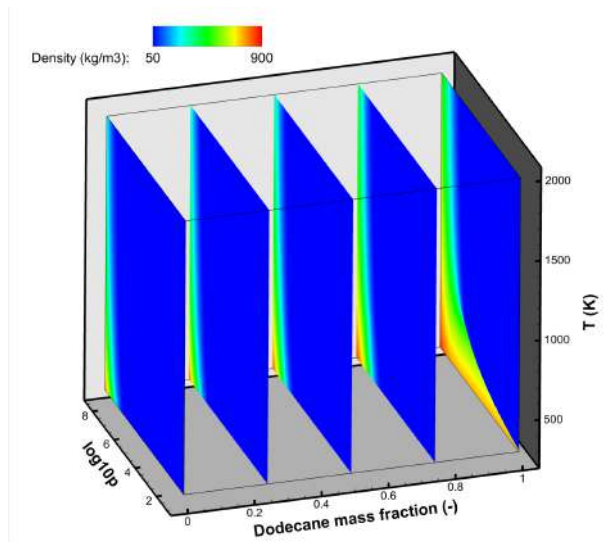


Figure 1: The dodecane(C_{12})- nitrogen phase diagram, used for the CFD solver. Indicative slices are shown for different C_{12} mass fractions: 0 (pure nitrogen), 0.25, 0.5, 0.75, 1.0 (pure dodecane). Coloring is according to the mixture density

the injector axis [27]. Apart from the injector, the computational domain is extended downstream 50mm in the axial and 15mm in the radial directions (or by $\sim 56d_{\text{out}}$ and $\sim 17d_{\text{out}}$ respectively), to include part of the spray chamber over which measurements are available. The computational mesh consists of 100k finite volumes, is purely quadrilateral and is refined in the injector orifice and near the exit of the injector, as shown in Figure (2); the resolution inside the orifice is $2 \mu\text{m}$ (resulting to a maximum y^+ of ~ 50). Boundary conditions correspond to the Spray-A case for injection pressure of 1500bar, 363K to stagnant nitrogen atmosphere at (a) 60bar and 900K and (b) 50bar and 1100K[28]. To emulate the needle motion, a mass flow profile is introduced upstream the injector, based on the online tool from CMT-Motores Térmicos [29]. Apart from the mass flow rate, temperature of the fuel is fixed at 363K and the composition to pure dodecane. At the far-field, fixed pressure is imposed equal to the chamber pressure downstream the injector. Temperature and composition are imposed as zero gradient at farfield, unless backflow is found; in that case fixed composition and temperature are imposed based on the chamber conditions. Nozzle walls are considered as adiabatic, as the injector is kept at the same temperature as the fuel.

4.2 Results

In Figure (3) the temporal evolution of the vapor penetration of the dodecane jet is shown, for the two ambient conditions examined. Vapor penetration was identified by defining the isosurface of mass fraction equal to 0.1%, following ECN guidelines, and calculating its maximum axial coordinate for every time instant. As expected, penetration is faster at 1100K and 50bar, since the ambient density is much lower (by $\sim 50\%$) at this condition. The agreement with experimental results is within the experimental uncertainty, hence is considered satisfactory. Further to instantaneous vapor penetration, the overall distribution of dodecane mass fraction downstream the injector is within good agreement with experiments, as shown in Figure (4) for 900K/60bar and in Figure (5) for 1100K/50bar. Apart from mass frac-

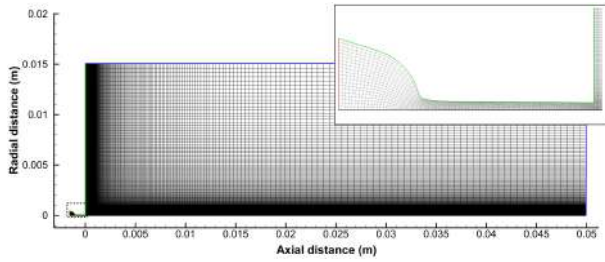


Figure 2: Axis-symmetric geometry of the Spray-A injector used, along with the downstream injection chamber and computational mesh. Boundary conditions are also shown: fixed mass flow, composition and temperature (fuel inlet, red), walls (green), fixed pressure outflow (blue). The magnified insert corresponds to the dashed region, showing the mesh inside the injector. X-axis is the axis of symmetry

tion, a comparison of the axial temperature distribution is shown in Figure (6); the agreement between numerical redictions and the temperature estimations from the experiment are very close. Note that in the region of -2 to 2mm, there is temperature reduction, due to the depressurization of the compressed liquid and mixing with nitrogen.

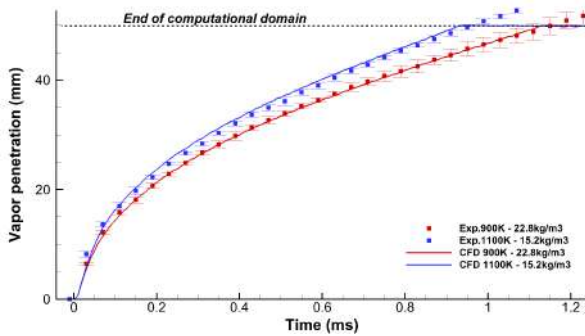


Figure 3: Vapor penetration over time for two downstream conditions; (red) 900K and 60bar (22.8kg/m^3), (blue) 1100K and 50bar (15.2kg/m^3). Symbols correspond to experiments, continuous line to simulations

The predictive capability of the PC-SAFT model, is demonstrated when comparing the vapor penetration of different hydrocarbons. An example here is in Figure (7), for dodecane, tetradecane and hexadecane, all modeled with the same methodology. As shown, the dodecane has slightly higher penetration rate over the other examined hydrocarbons, of which tetradecane is marginally faster than hexadecane. This is expected to happen for two reasons; (1) dodecane density within the injector ranges between $714 - 786\text{kg/m}^3$, whereas for tetradecane $732 - 803\text{kg/m}^3$ and hexadecane $740 - 809\text{kg/m}^3$. Hence, the larger the density, the lower the jet velocity, thus slightly slower penetration. (2) for the three examined hydrocarbons, molecular weight correlates with viscosity. Indeed, at the injector outlet, dodecane viscosity is $0.654\text{mPa}\cdot\text{s}$, tetradecane is $0.795\text{mPa}\cdot\text{s}$ and hexadecane is $1.016\text{mPa}\cdot\text{s}$, hence it is expected that the higher the viscosity, the lower the jet velocity due to viscous losses.

A further validation of the simulations is performed by comparing the CFD solver states with the isobaric, adiabatic mixing curves. For PC-SAFT mixing curves are found directly by using the tabulated EoS, shown in

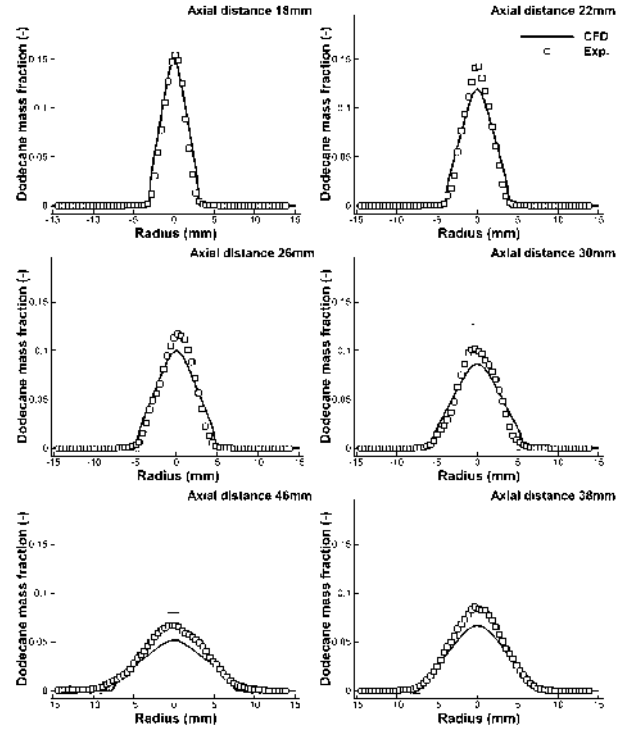


Figure 4: Radial distribution of dodecane mass fraction at different positions from the injector, injection to nitrogen, 900K and 60bar

Figure (1), assuming the initial temperature of the two components at the downstream pressure, calculating enthalpy, then by calculating all the intermediate mixing states assuming isenthalpic mixing at constant pressure (i.e. $h_{\text{mix}} = y_{\text{C}_{12}}h_{\text{C}_{12}} + y_{\text{N}_2}h_{\text{N}_2}$) and finally inverting enthalpy to temperature; it serves as a representation of the cooling due to fuel/gas mixing. Also it serves as a validation of the solver, as roughly the CFD states should follow the of the mixing curve. As shown in Figure (8) the CFD solver states (represented with red dots) follow the trend of the adiabatic, isobaric PC-SAFT mixing curve for both cases. Some scatter is observed, as the injector has been included in the orifice, hence the fuel is not injected at a constant temperature; indeed, fuel near the center of the orifice is colder due to the Joule-Thomson effect, whereas fuel near the orifice walls will be hotter, due to viscous effects. This can be clearly demonstrated from Figure (8), as the temperatures of the pure dodecane component range from $\sim 341\text{K}$ (which corresponds to liquid core temperature; this is the lowest temperature that can be achieved by isentropic expansion of dodecane from 1500bar and 363K) to $\sim 476\text{K}$ near the walls. It is also notable, that the lowest temperature (of $\sim 318\text{K}$) is achieved further downstream the injector orifice outlet, due to dodecane mixing with nitrogen, for a dodecane mass fraction of 99%.

5 Conclusions

In the present work, a numerical model is presented for simulating the complex interaction of fuel mixing with gas, for conditions relevant to modern ICEs. The model is based on accurate thermodynamic modelling using PC-SAFT, to provide properties of pure components and their mixtures, over a wide range of conditions, for which idealised simplifications are grossly insufficient. The model predictions are accurate against

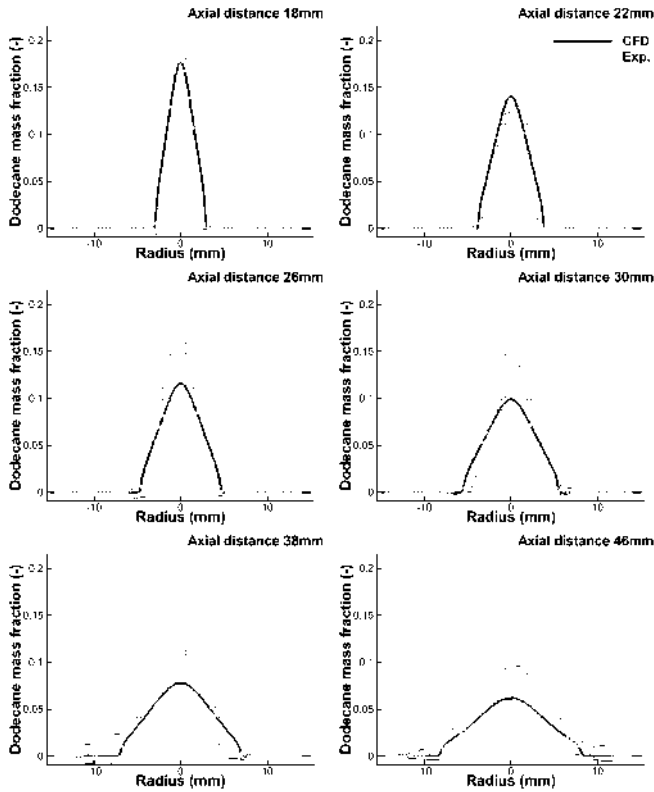


Figure 5: Radial distribution of dodecane mass fraction at different positions from the injector, injection to nitrogen, 1100K and 50bar

experiments, both in terms of instantaneous vapor penetration and the average distributions of mass fractions and temperature. In general, the further from the injector, the agreement becomes worse, though even at the furthest distance examined, at 46mm, is within the experimental uncertainty. Probably this is related to the inherent deficiencies of RANS turbulence models; LES modelling would be expected to provide a much better mass fraction distribution, without the modelling assumptions of the $k-\epsilon$ model. The difference in computational cost between the present approach and an LES study has to be stressed though; indicatively, the results presented in this work are obtained using a regular workstation within 10 hours for a single examined case, making the method attractive for parametric investigations. Furthermore, another attractive feature of the PC-SAFT model is the possibility to investigate the mixing characteristics of different hydrocarbons and even hydrocarbon mixtures (fuel surrogates or real fuels) with relative ease and minimum experimental calibration. This enables to examine what-if scenarios, for different fuels, which will be investigated in the future.

Acknowledgments

This work has received funding from the European Union's Horizon 2020 research and innovation programme under the Marie Skłodowska-Curie grant agreement No 748784. The primary author would also like to thank Sandia National Laboratories, the US Department of Energy (DoE) and the staff at Combustion Research Facility for hosting him. Sandia National Laboratories is a multi-mission laboratory managed and operated by National Technology and Engineering Solutions of Sandia, LLC., a wholly owned subsidiary of Honeywell Inter-

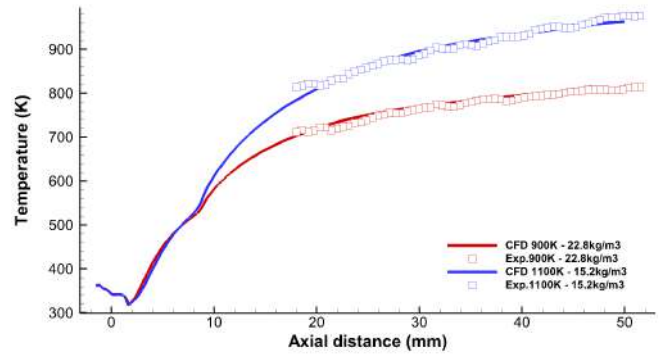


Figure 6: Temperature distribution, along the jet axis, for two downstream conditions; (red) 900K and 60bar ($22.8\text{kg}/\text{m}^3$), (blue) 1100K and 50bar ($15.2\text{kg}/\text{m}^3$)

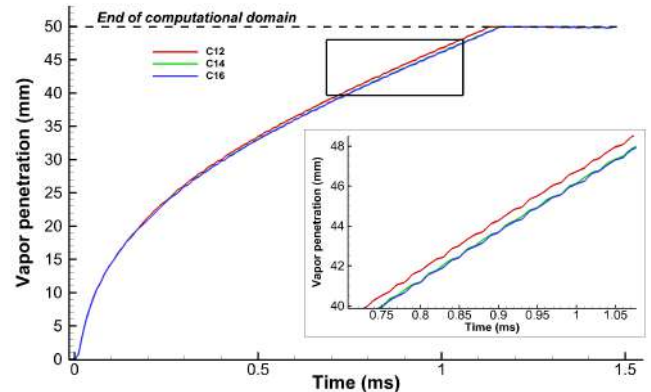


Figure 7: Vapor penetration over time for different fuels, dodecane, tetradecane and hexadecane injected to nitrogen, at 900K and 60bar

national, Inc., for the U.S. Department of Energy's National Nuclear Security Administration under contract DE-NA0003525.

References

- [1] R. D. Reitz, H. Ogawa, R. Payri, T. Fansler, S. Kokjohn, Y. Moriyoshi, ..., and H. Zhao, "IJER editorial: The future of the internal combustion engine," *International Journal of Engine Research*, vol. 21, no. 1, pp. 3–10, 2020.
- [2] N. I. Kolev, *Thermodynamic and transport properties of diesel fuel*, pp. 293–327. Berlin, Heidelberg: Springer Berlin Heidelberg, 2012.
- [3] J. Manin, M. Bardi, L. Pickett, R. Dahms, and J. Oefelein, "Microscopic investigation of the atomization and mixing processes of diesel sprays injected into high pressure and temperature environments," *Fuel*, vol. 134, pp. 531–543, 2014.
- [4] S. Yang, Y. Gao, C. Deng, B. Xu, F. Ji, and Y. He, "Evaporation and dynamic characteristics of a high-speed droplet under transcritical conditions," *Advances in Mechanical Engineering*, vol. 8, no. 4, p. 1687814016642953, 2016.
- [5] R. N. Dahms and J. C. Oefelein, "On the transition between two-phase and single-phase interface dynamics in multicomponent fluids at supercritical pressures," *Physics of Fluids*, vol. 25, no. 9, p. 092103, 2013.

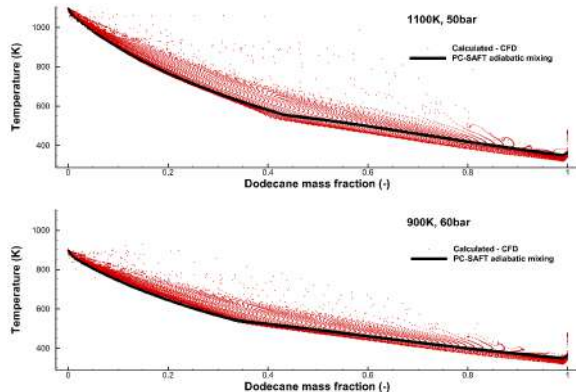


Figure 8: Adiabatic mixing curves, estimated using PC-SAFT, superimposed with the CFD states predicted by the solver, at (up) 1100K/50bar (down) 900K/60bar

- [6] B. Chehroudi, “Recent experimental efforts on high-pressure supercritical injection for liquid rockets and their implications,” *International Journal of Aerospace Engineering*, vol. 121802, p. 31, 2012.
- [7] D.-Y. Peng and D. B. Robinson, “A new two-constant equation of state,” *Industrial & Engineering Chemistry Fundamentals*, vol. 15, no. 1, pp. 59–64, 1976.
- [8] A. G. Perez, C. Coquelet, P. Paricaud, and A. Chapoy, “Comparative study of vapour-liquid equilibrium and density modelling of mixtures related to carbon capture and storage with the SRK, PR, PC-SAFT and SAFT-VR mie equations of state for industrial uses,” *Fluid Phase Equilibria*, vol. 440, pp. 19–35, 2017.
- [9] I. Kikic and T. W. De Loos, *Chapter 2 - Thermodynamic Properties at High Pressure*, vol. 9, pp. 17–63. Elsevier, 2001.
- [10] M. Cismondi and J. Mollerup, “Development and application of a three-parameter RK-PR equation of state,” *Fluid Phase Equilibria*, vol. 232, no. 1, pp. 74–89, 2005.
- [11] M. Nazarzadeh and M. Moshfeghian, “New volume translated pr equation of state for pure compounds and gas condensate systems,” *Fluid Phase Equilibria*, vol. 337, pp. 214–223, 2013.
- [12] E. W. Lemmon and M. L. Huber, “Thermodynamic properties of n-dodecane,” *Energy & Fuels*, vol. 18, no. 4, pp. 960–967, 2004.
- [13] A. Prosperetti and G. Tryggvason, *Computational Methods for Multiphase Flow*. Cambridge University Press, 2009.
- [14] B. E. Poling, J. P. O’Connell, and J. Prausnitz, *The properties of gases and liquids*. McGraw-Hill Education, 5th ed., 2000.
- [15] K. Kuo and R. Acharya, *Applications of Turbulent and Multiphase Combustion*. John Wiley, 2012.
- [16] R. Tahery and H. Modarress, “Lennard-jones energy parameter for pure fluids from scaled particle theory,” *Iranian Journal of Chemistry and Chemical Engineering (IJCCE)*, vol. 26, no. 2, pp. 1–8, 2007.
- [17] H. Versteeg and W. Malalasekera, *An Introduction to Computational Fluid Dynamics: The Finite Volume Method*. Prentice Hall, 2nd ed., 2007.
- [18] W. Kays, M. Crawford, and B. Weigand, *Convective Heat and Mass Transfer*. McGraw-Hill, fourth edition ed., 2005.
- [19] H. Wei, X. Chen, W. Zhao, L. Zhou, and R. Chen, “Effects of the turbulence model and the spray model on predictions of the n-heptane jet fuel-air mixing and the ignition characteristics with a reduced chemistry mechanism,” *Proceedings of the Institution of Mechanical Engineers, Part D: Journal of Automobile Engineering*, vol. 231, no. 14, pp. 1877–1888, 2017.
- [20] S. Sarkar and B. Lakshmanan, “Application of a reynolds stress turbulence model to the compressible shear layer,” *AIAA Journal*, vol. 29, no. 5, pp. 743–749, 1991.
- [21] J. Gross and G. Sadowski, “Perturbed-chain SAFT: An equation of state based on a perturbation theory for chain molecules,” *Industrial & Engineering Chemistry Research*, vol. 40, no. 4, pp. 1244–1260, 2001.
- [22] I. Polishuk, “Standardized critical point-based numerical solution of statistical association fluid theory parameters: The perturbed chain-statistical association fluid theory equation of state revisited,” *Industrial & Engineering Chemistry Research*, vol. 53, no. 36, pp. 14127–14141, 2014.
- [23] O. Lötgering-Lin and J. Gross, “Group contribution method for viscosities based on entropy scaling using the perturbed-chain polar statistical associating fluid theory,” *Industrial & Engineering Chemistry Research*, vol. 54, no. 32, pp. 7942–7952, 2015.
- [24] M. Hopp and J. Gross, “Thermal conductivity of real substances from excess entropy scaling using PCP-SAFT,” *Industrial & Engineering Chemistry Research*, vol. 56, no. 15, pp. 4527–4538, 2017.
- [25] S. Yang, P. Yi, and C. Habchi, “Real-fluid injection modeling and les simulation of the ecn spray A injector using a fully compressible two-phase flow approach,” *International Journal of Multiphase Flow*, vol. 122, p. 103145, 2020.
- [26] P. Koukouvinis, A. Vidal-Roncero, C. Rodriguez, M. Gavaises, and L. Pickett, “High pressure/high temperature multiphase simulations of dodecane injection to nitrogen: application on ecn spray-A,” *Fuel*, vol. 275, p. 117871, 2020.
- [27] Engine Combustion Network, “Spray A geometry, <https://ecn.sandia.gov/diesel-spray-combustion/target-condition/spray-a-nozzle-geometry/>,”
- [28] Engine Combustion Network, “Rayleigh scattering n-dodecane/ambient mixing images for spray A and several other experimental conditions, <https://ecn.sandia.gov/data/bkldaal4mixing/>.”
- [29] CMT, “Virtual injection rate generator, <https://www.cmt.upv.es/ecn03.aspx>,”

HIGH-ORDER MULTI-COMPONENT LATTICE BOLTZMANN METHOD AND ITS CAPABILITIES FOR NON-IDEAL FLUID MIXTURES

C. S. From¹, M. Deligant², M. Specklin², S. Khelladi² and E. Sauret¹

¹*School of Mechanical, Medical and Process Engineering, Science and Engineering Faculty, Queensland University of Technology, QLD 4001, Australia*

²*Arts et Métiers Institute of Technology, CNAM, LIFSE, HESAM University, 75013 Paris, France*

Abstract

High-order lattice Boltzmann (LB) models with pseudopotential interactions set a compelling case as a numerical method for solving the dynamics of non-ideal fluid mixtures. In this paper, purely fundamental study on high-order LB pseudopotential model capability to simulate non-ideal fluid mixtures is presented. The capability of this model for non-ideal fluids is firstly explored by simulating a binary non-ideal fluid mixture undergoing phase-change for both the case of miscible and immiscible components. To further explore the capabilities of this method, the properties of a real refrigerant mixture, namely R245fa and R134a, which exhibits zeotropic behaviour, is considered. It is demonstrated that the numerical model can reproduce the theoretical coexisting densities of each component. Conclusions and perspective on future avenues are provided.

1 Introduction

Multicomponent and multiphase fluid flows are of great interest for a large scientific and industrial community. For instance, waste energy recovery technologies, such as Organic Rankine Cycles (ORC) for low-to-moderate temperature heat sources [1] or supercritical CO₂ for solar-thermal applications [2], offer unique solutions as compared to their conventional fluids (air or water) counterparts by using non-ideal fluid mixtures (typically gas phase) to extract more energy from a given heat source. Using mixtures of real (non-ideal) fluids and tuning their composition [3] will provide a new degree of freedom for the design of adapted ORC systems [4, 5] that will allow to get closer to the Carnot efficiency [6] by reducing the temperature difference in the heat exchangers. However, current waste energy recovery designs and simulations are based mostly on the ideal-gas equations or adapted equation of state, which can introduce inaccuracies in the performance predictions (efficiency and power) of performance. Current available data for both pure and mixtures of non-ideal fluids are quite scarce and usually extrapolated from current equations of state which typically have an error of approximately 10% [7] and may be even more inaccurate for many substances. Advanced look-up table methods [8, 9] can overcome the approximation from the equations of state and speed up the computations, but the table generation still rely on accurate experimental or numerical data. For accurate predictions of non-ideal fluid flow behaviour, accurate thermodynamic models that are able to include non-ideal effects are required [10]. The lack of fundamental knowledge in the dynamics of non-ideal fluid mixtures is a critical aspect of energy-efficient

technologies that underpin their development. Therefore, there is a significant need for more research and analysis of the thermal properties and phase diagram/data of these non-ideal fluids and mixtures. Due to strongly out-of-equilibrium phenomena these flows involve complex dynamics, a challenging case for both numerical and theoretical analysis which motivates numerical tools to be revisited, extended, and/or further developed.

The Lattice Boltzmann (LB) method is one such numerical tool which has far reaching potential to simulate non-ideal fluid mixtures due to its numerical accuracy and easily parallel algorithm allowing for highly efficient computations. The LB method, in general, has already seen tremendous success in a broad range of applications involving computational fluid dynamics [11, 12], including multicomponent and multiphase flows (see, e.g., [13] for a complete review). The flexibility of the source term in the LB method allows for various complex fluids to be simulated efficiently [14]. For instance, in the LB method, multiple components ($\phi = A, B$) can be simulated, each with its own discrete distribution function ($f_\alpha^\phi : \phi = A, B$),

$$f_\alpha^\phi(\mathbf{x} + \boldsymbol{\xi}_\alpha, t + \Delta t) = f_\alpha^\phi(\mathbf{x}, t) - \Omega_\alpha^\phi(\mathbf{x}, t) + \Delta t S_\alpha^\phi(\mathbf{x}, t), \quad (1)$$

where components are then coupled via the source term (S_α^ϕ) and the collision operator (Ω_α^ϕ) to ensure mass and momentum conservation of the entire system. The density and momentum of each ϕ -component is defined from the first two moments of f_α^ϕ , i.e., simple summations, by

$$\rho^\phi = \sum_\alpha f_\alpha^\phi, \quad \text{and} \quad \rho^\phi \mathbf{u}^\phi = \sum_\alpha f_\alpha^\phi \boldsymbol{\xi}_\alpha + \frac{\Delta t}{2} \mathbf{F}^\phi, \quad (2)$$

respectively. It is emphasized that, $\{w_\alpha, \boldsymbol{\xi}_\alpha : \alpha = 0, \dots, Q\}$ is a predefined constant set for a given lattice structure and $(\mathbf{x}, \boldsymbol{\xi}_\alpha) \in \mathbb{Z}^D$. As such, the general algorithm [Eq. (1) and Eq. (2)] allow for highly efficient and scalable computations. In addition, the continuous streaming $f_\alpha^\phi(\mathbf{x} + \boldsymbol{\xi}_\alpha, t + \Delta t)$ ensures that advection is exact (i.e., zero-numerical-diffusion) [15], which is, in particular, important for simulating chaotic mixing of fluids. Non-ideal forces (\mathbf{F}^ϕ) are then introduced via an extension. While there exists various approaches, notably the free energy model [16] and colour-gradient model [17], the pseudopotential model [18] is, arguably, the most popular multi-component/phase model for the LB method [11, 12, 14]. The LB method with the pseudopotential interaction model provides a unique picture of interactions in fluids by mimicking intermolecular force interactions *discretely* on the lattice set $\{\tilde{w}_\alpha, \boldsymbol{\xi}_\alpha\}$, specifically self-interactions ($\mathcal{G}^{\phi\phi}, \psi^\phi : \phi = A, B$) and cross-interactions

(\mathcal{G}^{AB} , Ψ^A , and Ψ^B), i.e.,

$$\begin{aligned} \mathbf{F}^\phi(\mathbf{x}) = & -\psi^\phi(\mathbf{x})\mathcal{G}^{\phi\phi} \sum_{\alpha} \tilde{w}_\alpha \psi^\phi(\mathbf{x} + \boldsymbol{\xi}_\alpha) \boldsymbol{\xi}_\alpha \\ & -\Psi^\phi(\mathbf{x})\mathcal{G}^{\phi\varphi} \sum_{\alpha} \tilde{w}_\alpha \Psi^\varphi(\mathbf{x} + \boldsymbol{\xi}_\alpha) \boldsymbol{\xi}_\alpha, \end{aligned} \quad (3)$$

where superscript ‘ φ ’ denote any other component $\varphi \neq \phi$ and symmetry require $\mathcal{G}^{\phi\varphi} = \mathcal{G}^{\varphi\phi}$. Due to the discrete lattice construction, the spatial accuracy of Eq. (3) conform to the isotropy gradients (rotational invariance) of the lattice set $\{\tilde{w}_\alpha, \boldsymbol{\xi}_\alpha\}$.

Despite the success of the LB method, most studies use the ‘standard’ models, e.g., the popular two-dimensional nine-velocity lattice model known as Q9, which suffer from *non*-Galilean invariance and does *not* recover the momentum dynamics at the Navier-Stokes level [19, 20]. In addition, pseudopotentials [Eq. (3)] directly on the Q9 lattice is plagued by spurious currents due to low-order of isotropy. High-order LB models are available which conform to higher-order-isotropy gradients, are Galilean invariant, and are required to recover the full thermal Navier-Stokes equations [19]. The incentive of high-order LB models is that they do not suffer from the same intrinsic limitations of ‘standard’ models in exchange for increased computational cost due their larger lattice set. However, the increase in computational cost, fortunately, scales linearly with Q-number of velocities in the lattice set, and, on that note, scalable parallel computations remain an inherent feature of the LB method. This is important for current and future computational architectures, in particular graphical processing units (GPU). Since pseudopotential interactions [Eq. (3)] conform to the isotropy gradients of the lattice set, its application on high-order LB models is clearly an advantage. In addition, the extended range can allow for interactions at specific Brillouin zones to be set (e.g., the Q9 only cover the first Brillouin zone), which has seen success in the study of complex fluids, such as soft flowing crystals [21]. These qualities of high-order LB and the pseudopotential interaction extension, collectively, make a compelling case as a numerical tool for studying the dynamics of non-ideal fluid mixtures. Recently, the application of high-order LB with pseudopotential, including both self and cross-interaction, has been addressed [22, 23], making its application for non-ideal fluids mixtures a possibility. While the LB method, in general, has been applied to study non-ideal fluids, to the best of the authors knowledge, the study of non-ideal zeotropic mixtures has not been previously attempted with the LB method.

This paper aims to explore the capabilities of the high-order multi-component LB approach [22, 23] to model non-ideal binary fluid mixtures, including its capability to simulate zeotropic mixtures. While the present research is mostly fundamental, the method proposed can potentially contribute to providing a deeper understanding of the behaviour of non-ideal fluid mixtures for ORC systems and establishing the foundations to advance numerical practices in renewable power systems.

The paper is organised as follows. In section 2, the high-order LB method with all possible interactions and its application to simulating non-ideal fluids is reviewed briefly. In section 3, numerical experiments are conducted to explore the capabilities of the method for non-ideal fluid mixtures. Summary and future perspectives are provided in section 4.

2 The method: high-order LB with non-ideal interactions

The high-order LB pseudopotential model from our previous work [22, 23] is used to simulate, in two-dimensions, a binary zeotropic mixture by considering a binary mixture where the local \mathbf{x} total mixture density is defined as $\rho(\mathbf{x}) = \sum_{\phi} \rho^\phi(\mathbf{x})$, where $\phi = A, B$. In addition to Eq. (1)–Eq. (3), the source term S_α^ϕ is coupled with the Ω_α^ϕ via, e.g.,

$$\begin{aligned} \Omega_\alpha^\phi(\mathbf{x}) = & (\tau^\phi)^{-1} \left\{ f_\alpha^\phi(\mathbf{x}) + \frac{\Delta t}{2} S_\alpha^\phi [f_\alpha^{eq,\phi}(\mathbf{x}), \mathbf{F}^\phi(\mathbf{x})] \right. \\ & \left. - f_\alpha^{eq,\phi} [T_o, w_\alpha, \boldsymbol{\xi}_\alpha, \rho^\phi(\mathbf{x}), \mathbf{u}(\mathbf{x})] \right\}, \end{aligned} \quad (4)$$

where the equilibrium distribution function $f_\alpha^{eq,\phi}$ and S_α^ϕ are evaluated with the common mixture velocity, $\mathbf{u} = [\sum_{\phi} \rho^\phi \mathbf{u}^\phi (\tau^\phi)^{-1}] / [\sum_{\phi} \rho^\phi (\tau^\phi)^{-1}]$. The LB kinematic viscosity of each ϕ -component $\nu^\phi = c_s^2 (\tau^\phi - \frac{1}{2})$, where τ^ϕ is the ϕ -component relaxation and c_s is sound speed, which is equivalently proportional to the reference temperature $T_o = c_s^2$ of the lattice structure, i.e., specific to the lattice $c_s^2 = \sum_{\alpha} w_\alpha (\boldsymbol{\xi}_{\alpha,i})^2$. The lattice structure has to satisfy the constraints, $w_\alpha \in \mathbb{R}_{>0}$ and $\sum_{\alpha} w_\alpha = 1$. In this work, the two-dimensional (2D) 49-discrete velocity lattice structure (Q49) is used, which is constructed on the basis of covering zero-one-two-three (ZOTT) Brillouin zones and recovers up to eight-order-isotropy gradients [22, 24]. This lattice structure with a fourth-order expanded f_α^{eq} yields a high-order LB model that is Galilean invariant and fully compressible. All parameters and variables are dimensionless. More specifically, these are in ‘dimensionless lattice units’, scaled relatively by the real kinematic viscosity, i.e., $\nu_{real} = \nu \times dx^2 dt^{-1}$, where dx and dt are the real physical change in length (e.g., grid spacing $dx = L/n_x$) and change time, respectively.

The consequent bulk static pressure, i.e., equation of state (EOS), due to the discrete interactions [Eq. (3)] using Taylor expansion series up to second-order [22] can be shown to have the continuum approximation (truncated to second-order isotropy gradients), i.e.,

$$\begin{aligned} P_o^\phi(\mathbf{x}) = & T \rho^\phi(\mathbf{x}) + \mathcal{C}_2 \frac{\mathcal{G}^{\phi\phi}}{2} [\psi^\phi(\mathbf{x})]^2 \\ & + \mathcal{C}_2 \frac{\mathcal{G}^{\phi\varphi}}{2} [\Psi^\phi(\mathbf{x}) \times \Psi^\varphi(\mathbf{x})], \end{aligned} \quad (5)$$

where $T \equiv T_o = c_s^2$, the term ‘ $T\rho$ ’ is identified as the ideal pressure contribution and all other terms are the non-ideal contributions. Note that, the exact discrete form of these non-ideal contributions can be obtained from solving $\sum \mathbf{P}^{int} \cdot d\mathbf{A} = -\sum_{\mathbf{x}} \mathbf{F}$ [25] where $d\mathbf{A}$ is some infinitesimal area element in \mathbf{x} (see, [22] for details). The coefficient $\mathcal{C}_{(n)}$, is the n th-order isotropy coefficient of the lattice structure for which the discrete interactions [Eq. (3)] are computed on, e.g., $\mathcal{C}_2 \mathbf{I} = \sum_{\alpha} \tilde{w}_\alpha \boldsymbol{\xi}_\alpha \otimes \boldsymbol{\xi}_\alpha$, where \mathbf{I} is the identity tensor. The cross-interactions terms ($\mathcal{G}^{\phi\varphi}$, Ψ^A and Ψ^B) in Eq. (5) are absent in the bulk liquid phase of any ϕ -component for the case $C > 1$, since $\Psi^A \times \Psi^B \approx 0$.

The self-interactions can be viewed as the intra-particle attractions where the strength $\mathcal{G}^{\phi\phi}$ is understood to represent the normalized inverse temperature [26], i.e., ‘ $\frac{\varepsilon}{k_B T}$ ’, where $k_B T$ is the thermal energy and ε is the energy scale. Hence, sufficiently large ‘energy’ will induce phase change. It is convenient to define this critical point for

phase change by a critical self-interaction strength ($\mathcal{G}_{crit}^{\phi\phi}$), which is obtained for each ϕ -component by solving Eq. (5) for $dP_c^\phi/d\rho^\phi = 0$. Furthermore, the validity of this representation's consistency with thermodynamic theory depends on the form of the self-interaction pseudopotential (ψ) [25, 27, 28, 22]. The theoretical coexisting liquid (ρ_l^ϕ) and gas (ρ_g^ϕ) phase densities are obtained from solving the Maxwell construction (note, in two-dimensions, the specific volume $V^\phi \propto 1/\rho^\phi$)

$$\int_{\rho_g^\phi}^{\rho_l^\phi} P_c^\phi - P_o^\phi(\rho^\phi, \mathcal{G}^{\phi\phi}) dV^\phi = \int_{\rho_g^\phi}^{\rho_l^\phi} [P_c^\phi - P_o^\phi(\rho^\phi, \mathcal{G}^{\phi\phi})] \frac{1}{(\rho^\phi)^2} d\rho^\phi = 0, \quad (6)$$

directly for a given problem; P_c^ϕ (constant), ρ^A , ρ^B , \mathcal{G}^{AA} , and \mathcal{G}^{BB} . To satisfy mechanical equilibrium on the lattice, the integral over the two phases has the constraint (see, [27] for full details)

$$\int_{\rho_g^\phi}^{\rho_l^\phi} [P_c^\phi - P_o^\phi(\rho^\phi, \mathcal{G}^{\phi\phi})] \frac{d\psi^\phi}{d\rho^\phi} \frac{1}{(\psi^\phi)^{1+\epsilon}} d\rho^\phi = 0, \quad (7)$$

where ϵ is the coefficient in the potential ψ and is defined by [22, 27]

$$\epsilon = \frac{6\mathcal{C}_4 - 2\mathcal{C}_2}{6\mathcal{C}_4 + \mathcal{C}_2}, \quad (8)$$

with the interaction pressure tensor truncated to fourth-order-isotropy gradients (fourth-order Taylor expansion series), hence dependencies on \mathcal{C}_4 and \mathcal{C}_2 . For Eq. (7) to conform with the Maxwell construction [Eq. (6)] require $\frac{d\psi^\phi}{d\rho^\phi} \frac{1}{(\psi^\phi)^{1+\epsilon}} = \frac{1}{(\rho^\phi)^2}$ and, hence, thermodynamic consistency depends on the form of ψ . For a standard lattice (accurate up to fourth-order-isotropy), such as the popular Q9 lattice, $\epsilon = 0$ and can satisfy thermodynamic consistency [i.e., Eq. (6)] by $\psi^\phi = e^{-1/\rho^\phi}$ [25]. For any high-order lattice structure (which are generally accurate up to, at least, sixth-order-isotropy) $\epsilon > 0$ and satisfies Eq. (6) with the potential proposed by [27]

$$\psi^\phi = \left(\frac{\rho^\phi}{\epsilon + \gamma\epsilon\rho^\phi} \right)^{1/\epsilon}. \quad (9)$$

In Eq. (9), to avoid mass-collapse in the limit $\rho^\phi \rightarrow \infty$ an asymptotic limit of self-interactions is guaranteed with γ . This limit is commonly set to unity with $\gamma = 1/\epsilon$ for which Eq. (9) then takes the simplified form [27], $\psi^\phi = (\rho^\phi/(\epsilon + \rho^\phi))^{1/\epsilon}$, where it is also interesting to note that as $\epsilon \rightarrow 0$, $\psi^\phi \approx e^{-1/\rho^\phi}$.

The cross-interactions control mutual diffusivity ($\mathcal{D}^{AB} = \mathcal{D}^{BA}$) between components A and B , whose strength can be conveniently set via $\mathcal{G}^{AB} = \mathcal{G}_{crit}^{AB} \times C$, where the constant $C > 1$ ($\mathcal{D}^{AB} > 0$) or $C < 1$ ($\mathcal{D}^{AB} < 0$) allows for components to be immiscible or miscible, respectively. More specifically, \mathcal{D}^{AB} is obtained from the solution in [23], where it can be shown that the critical limit (i.e., when $\mathcal{D}^{AB} = 0$) for the mutual interaction strength (\mathcal{G}_{crit}^{AB}) defined by,

$$\mathcal{G}_{crit}^{AB} = \frac{\left[c_s^2(c^A + c^B) + \mathcal{C}_2(c^A \mathcal{G}^{BB} \psi^B \psi'^B + c^B \mathcal{G}^{AA} \psi^A \psi'^A) \right]}{\mathcal{C}_2(c^A \Psi^B \Psi'^A + c^B \Psi^A \Psi'^B)}, \quad (10)$$

where superscript ' r ' denote derivatives with respect to ρ , i.e., $\psi^r = d\psi/d\rho$ and $\Psi^r = d\Psi/d\rho$, and $c = c^A + c^B$ is the total concentration.

For the binary non-ideal fluid mixtures considered in this work, in the miscible case ($\mathcal{D}^{AB} < 0$) the surface tension between the two-components $\sigma^{AB} \approx 0$, whereas in the immiscible case ($\mathcal{D}^{AB} > 0$) $\sigma^{AB} > 0$. In two-phase flows, in both of these cases, each component will induce phase-change and, as such, each ϕ -component will have a phase-interface tension $\sigma^\phi > 0$. The surface tension is obtained from the Bakker formula, i.e., the integral of mismatch between the normal P_N and tangential P_T components of the total momentum flux tensor across the interface [29] (e.g., with respect to the x -axis) $\sigma^\phi = \int_{\rho_g^\phi, \rho_l^\phi} (P_N^\phi - P_T^\phi) dx$ and $\sigma^{AB} = \int_{\rho^A, \rho^B} (P_N - P_T) dx$, where $\mathbf{P} = \sum_\phi \mathbf{P}^\phi$. To obtain the surface tension for high-order lattices at the discrete level or, at the more practical continuum limit, solutions are available from [22]. It is noted that, in addition to self-interactions and cross-interactions, additional interactions can be included with Eq. (3), such as fluid-structure-interactions to incorporate hydrophobic, hydrophilic, or neutral boundaries [23, 30].

3 Numerical Experiments and Discussion

To demonstrate the capability of high-order LB pseudopotential model to simulate a non-ideal fluid mixtures thermodynamic theory is used directly. More specifically, the theoretical coexisting densities ρ_l^ϕ and ρ_g^ϕ of each ϕ -component are obtained from solving the Maxwell construction Eq. (6) directly for a given problem; P_c^ϕ (constant), ρ^A , ρ^B , \mathcal{G}^{AA} , and \mathcal{G}^{BB} . The coexisting densities (ρ_l^A , ρ_g^A , ρ_l^B , and ρ_g^B) are then compared directly with the equilibrium densities obtained in the numerical simulations. Studies conducted in the present work are in a fully periodic two-dimensional (2D) domain $\mathbf{x} = (1 : L, 1 : L)$ on a symmetric grid ($\Delta x = \Delta y = 1$).

First, a binary non-ideal mixture undergoing phase change is simulated. For the example here, a two-phase binary non-ideal fluid mixture is considered with a basic requirement that at constant $T_o = c_s^2 = 0.3675$, coexisting densities $\rho_l^A \neq \rho_l^B$ and $\rho_g^A \neq \rho_g^B$. This should also hold for both the case where the binary components are miscible and immiscible, which will be tested here. The two components are initially in a *mixed* state, distributed randomly over a $L^2 = 100^2$ grid with approximately equal volume $V^A \approx V^B$, where $\rho^\phi = [\max, \min]$ is set to $\rho^\phi = [3, 0.06]$, $(\rho^A + \rho^B) = [3.75, 0.81]$ and total spatial average $\langle \rho \rangle = 2.28$. It is ensured that the two components are distinctively different fluids by setting $\nu^A/\nu^B = 7/11$ ($\tau^A/\tau^B = 3/4$) and set self-interaction strengths by $\mathcal{G}^{\phi\phi}/\mathcal{G}_{crit}^{\phi\phi} > 1$ where their corresponding theoretical coexisting densities (ρ_l^ϕ, ρ_g^ϕ) are predicted from Eq. (6). For component- A , $\mathcal{G}^{AA}/\mathcal{G}_{crit}^{AA} = 1.075$ is set which results in coexisting densities $\rho_l^A = 1.5847$ and $\rho_g^A = 0.5965$. For component- B , $\mathcal{G}^{BB}/\mathcal{G}_{crit}^{BB} = 1.2375$ is set which results in coexisting densities $\rho_l^B = 2.3$ and $\rho_g^B = 0.4107$. Cross-interactions are set via $\mathcal{G}^{AB} = \mathcal{G}_{crit}^{AB} \times C$ with the critical strength obtained from Eq. (10). For the miscible case $C = 0.5$ and for the immiscible case $C = 1.2$.

The numerical simulations for both cases are presented in Figure (1), where in addition to the total density, the density field of each ρ^A and ρ^B is provided to clearly show the composition of components. The simulated miscible

densities ratios in Fig. 1(a) are $\rho_l^A = 1.6045$, $\rho_g^A = 0.5875$, $\rho_l^B = 2.3069$, and $\rho_g^B = 0.4138$. For the immiscible case in Fig. 1(b), the simulated densities ratios are $\rho_l^A = 1.628$, $\rho_g^A = 0.5492$, $\rho_l^B = 2.3214$, and $\rho_g^B = 0.4058$. Notice that, the upper limit in [1(a)] is equal to $\max[\rho_l^A(\mathbf{x}) + \rho_l^B(\mathbf{x})]$, whereas in [1(b)] its equal to $\max[\rho_g^A(\mathbf{x}) + \rho_l^B(\mathbf{x})]$. To be clear, the gas phase of A (ρ_g^A) and the liquid phase of B (ρ_l^B) can coexist in the same space \mathbf{x} since, in this case for $C = 1.2$, only the liquid phase of A and B are immiscible ($\mathcal{D}^{AB} > 0$). This essentially demonstrates that non-ideal fluid mixture can be simulated, where some of the basic features of a two-phase binary non-ideal fluid mixture is shown.

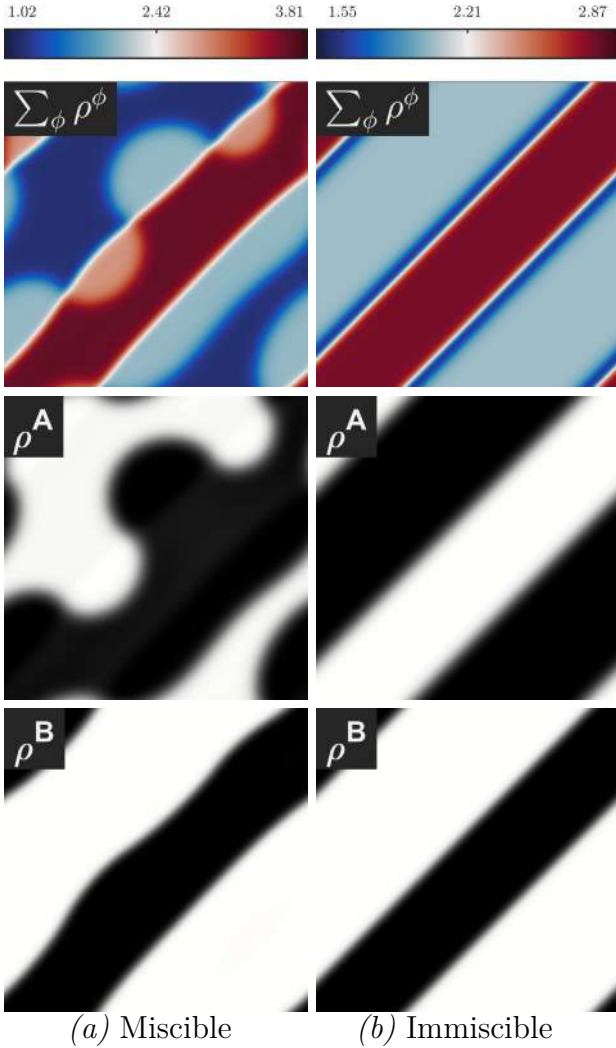


Figure 1: The equilibrium density field of a binary (a) miscible and (b) immiscible non-ideal mixture undergoing phase change. (Top row) The total mixture density $\rho(\mathbf{x}) = \sum_{\phi} \rho^{\phi}(\mathbf{x})$. The normalised gray-scale density contour for (middle row) ρ^A and (bottom row) ρ^B are shown to allow for the composition of components to be distinguished

It turns out that with current conditions in the present numerical model, both components are forced to have the same critical limit $\mathcal{G}_{crit}^{\phi\phi}$ for phase change, despite the present model's ability to control various parameters of each ϕ -component individually, e.g., ν^{ϕ} and interactions strengths $\mathcal{G}^{AA} \neq \mathcal{G}^{BB}$. Thus, the simulations in Figure (1) behave currently like an azeotropic mixture.

The following will discuss the cause of this limitation and potential solutions. Since in the present model $T_o = c_s^2$ has to be fixed in $f_{\alpha}^{eq,\phi}$, the ideal part in the EOS [Eq. (5)] has a fixed $T = T_o$. While it is possible to set a specific T_o with the Q49 lattice, it has to remain the same for both components A and B , due to the lattice construction. The exclusion volume effect is then completely dependent on the self-interaction potential ψ . For this reason, the limitation to azeotropic behaviour is due to fixed asymptotic limit of ψ^{ϕ} [Eq. (9)] for both components A and B . One possible solution to this limitation is to reconstruct the equilibrium collision process [Eq. (4), in particular $f_{\alpha}^{eq,\phi}$] with T as proposed by [31], which allows for exclusion-volume effect to be incorporated into the ideal part of Eq. (5). This approach has already been successfully applied to single component multiphase flows with the standard Q9 LB model [28, 27]. Its application for multicomponent flows with high-order LB models has yet to be demonstrated. Another solution, which is presented here, is to set an asymptotic limit of ψ^{ϕ} [Eq. (9)] specific to each ϕ -component, because in doing so will allow for thermodynamic consistency to be retained. In addition, provided that thermodynamic consistency is indeed retained, such an approach is non-intrusive, which is desirable as it can easily be extended/combined with, for example, the proposed approach by [31] to reconstruct $f_{\alpha}^{eq,\phi}$ with T . To this aim, solving for the limit of Eq. (9) yields

$$\lim_{\rho^{\phi} \rightarrow \infty} \psi^{\phi}(\rho^{\phi}) = \left(\frac{1}{\gamma^{\phi} \epsilon} \right)^{1/\epsilon} := \bar{\psi}^{\phi},$$

and with this can define $\psi^{\phi}[\gamma^{\phi}, \rho^{\phi}(\mathbf{x})]$ to have some arbitrary asymptotic limit $\bar{\psi}^{\phi}$ with

$$\gamma^{\phi} = \frac{(\bar{\psi}^{\phi})^{-\epsilon}}{\epsilon}, \quad (11)$$

where indeed for a saturation limit of one ($\bar{\psi}^{\phi} = 1$), $\gamma^{\phi} = 1/\epsilon$.

We consider a case of a real zeotropic mixture for an ORC cycle and the ratios in its properties. Here, a mixture of refrigerant fluids R245fa and R134a [3] with equal molar concentration is considered (mass fractions 0.568 and 0.432, respectively), which will be referred to as component- A and component- B , respectively. According to the CoolProp database [32], at a pressure of 10^6 Pa this mixture will have the following ratios: viscosity ratio $\nu^A/\nu^B = 1.167$, phase ratios ($\rho_l^A/\rho_g^A = 20.26$ and $\rho_l^B/\rho_g^B = 23.35$), and component density ratio ($\rho_l^A/\rho_l^B = 0.987$ and $\rho_g^A/\rho_g^B = 1.138$). The equivalent phase and component density ratios are set by solving for the Maxwell construction [Eq. (6)] directly for a range of $\mathcal{G}^{\phi\phi}/\mathcal{G}_{crit}^{\phi\phi} > 1$ and varying $\bar{\psi}^{\phi}$ [Eq. (11)], and thus may differ slightly from those in the database. It was found that $\mathcal{G}^{\phi\phi}$ allows for phase density ratios ($\rho_l^{\phi}/\rho_g^{\phi}$) to be controlled while $\bar{\psi}^{\phi}$ allowed for the control of the component density ratios (ρ^A/ρ^B). The predicted theoretical ratios are, for phase ratios ($\rho_l^A/\rho_g^A = 20.214$ and $\rho_l^B/\rho_g^B = 23.349$) and component density ratios ($\rho_l^A/\rho_l^B = 0.987$ and $\rho_g^A/\rho_g^B = 1.14$), where $\mathcal{G}^{AA}/\mathcal{G}^{BB} = 0.9037$ and $\bar{\psi}^A/\bar{\psi}^B = 1.0529$.

Simulations are then conducted to confirm these predicted values. The viscosity ratio and mass fraction are set directly as input parameters in initial conditions. Components are set as miscible ($\mathcal{D}^{AB} \ll 0$) mixture and initially occupy the same space. A small density perturbation is introduced initially to induce phase separation and diffusion process. The results are presented

in Figure (2), where the equilibrium densities of both components from the simulated binary mixture are compared directly against the theoretical [Eq. (6)]. Clearly, the numerical simulation is in agreement with the theoretical. More specifically, the percentage error of the simulated equilibrium densities compared to the theoretical are: For component- A , errors in ρ_l^A and ρ_g^A phase are 0.013% and -0.173% , respectively. For component- B , errors in ρ_l^B and ρ_g^B phase are 0.444% and 0.474%, respectively. The simulated component density ratios are $\rho_l^A/\rho_l^B = 0.983$ (-0.405% error) and $\rho_g^A/\rho_g^B = 1.133$ (-0.5% error). These results collectively confirm that with the present method it is clearly possible to simulate non-ideal fluid mixtures and, with Eq. (11), the basic features of a zeotropic mixture.

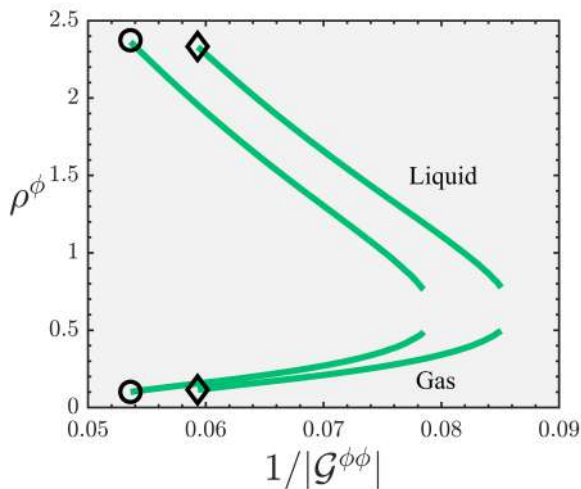


Figure 2: Coexisting densities ρ^ϕ for a binary miscible mixture $\phi = A, B$ as a function of the effective normalized inverse temperature $\mathcal{G}^{\phi\phi}$. Note, system temperature is fixed $T_o = c_s^2$. Equilibrium coexisting densities from the simulations are shown for (\diamond) component- A at $1/|\mathcal{G}^{AA}| = 0.0593$ and (\circ) component- B at $1/|\mathcal{G}^{BB}| = 0.0536$. The theoretical prediction (green solid-line) are obtained directly from the Maxwell construction Eq. (6)

It is noted that there are some limitations of the present model, which the fact the exclusion volume effect is entirely dependent on Eq. (8), which presently does not offer much flexibility, limiting its application. Since the present approach is non-intrusive, there are various avenues to further extended the model, without spoiling thermodynamic consistency. Most notably, extensions include the approach, discussed earlier, by [31] and the other is to utilize the extended interaction range of the high-order lattice structure, known as multi-range pseudopotential [33]. For instance, with the former, by reconstructing f_α^{eq} with T , allows for the exclusion volume effect to not be completely dependent on ψ , which can allow for Eq. (5) to be reformulated to incorporate known EOS, e.g., Van der Waals as demonstrated in [31]. For the latter, multi-range pseudopotential approach allows for interactions at specific Brillouin zones to be set, e.g., can allow for short-range repulsion and long-range attraction to be incorporated discretely on the lattice. This approach, as noted in the introduction, has allowed for various complex fluid systems to be studied [12].

4 Summary and Conclusions

This paper explored the capabilities of a high-order LB pseudopotential approach to model non-ideal fluid mixtures, including its ability to simulate zeotropic behaviour. It was found that the model was initially limited to azeotropic behaviour. By setting the potential of self-interactions for each component to different asymptotic limits allowed for obtaining the basic features of a non-ideal zeotropic mixture while satisfying thermodynamic consistency. The non-intrusiveness of the present model opens possibilities for future extensions. Furthermore, to investigate the accuracy and stability of high-order LB pseudopotential methods for non-ideal fluid mixture flows, the one-dimensional shocktube test of a non-ideal binary mixture should be considered in future work. While the present work is predominantly fundamental, the high-order LB proposed can potentially contribute to providing a deeper understanding of the dynamics of non-ideal fluid mixtures in applications, such as for ORC systems.

References

- [1] K. Braimakis, M. Preifinger, D. Brüggemann, S. Karellas, and K. Panopoulos, “Low grade waste heat recovery with subcritical and supercritical organic rankine cycle based on natural refrigerants and their binary mixtures,” *Energy*, vol. 88, pp. 80–92, aug 2015.
- [2] J. Qi, T. Reddell, K. Qin, K. Hooman, and I. H. J. Jahn, “Supercritical CO2 radial turbine design performance as a function of turbine size parameters,” *Journal of Turbomachinery*, vol. 139, mar 2017.
- [3] P. Collings, Z. Yu, and E. Wang, “A dynamic organic rankine cycle using a zeotropic mixture as the working fluid with composition tuning to match changing ambient conditions,” *Applied Energy*, vol. 171, pp. 581–591, jun 2016.
- [4] K. Satanphol, W. Pridasawas, and B. Suphanit, “A study on optimal composition of zeotropic working fluid in an organic rankine cycle (ORC) for low grade heat recovery,” *Energy*, vol. 123, pp. 326–339, mar 2017.
- [5] Q. Blondel, N. Tauveron, N. Caney, and N. Voeltzel, “Experimental study and optimization of the organic rankine cycle with pure NovecTM649 and zeotropic mixture NovecTM649/HFE7000 as working fluid,” *Applied Sciences*, vol. 9, p. 1865, may 2019.
- [6] W. Xu, S. Deng, W. Su, Y. Zhang, L. Zhao, and Z. Yu, “How to approach carnot cycle via zeotropic working fluid: Research methodology and case study,” *Energy*, vol. 144, pp. 576–586, feb 2018.
- [7] S. Bobbo, G. D. Nicola, C. Zilio, J. S. Brown, and L. Fedele, “Low gwp halocarbon refrigerants: A review of thermophysical properties,” *International Journal of Refrigeration*, vol. 90, pp. 181 – 201, 2018.
- [8] A. Rubino, M. Pini, M. Kosec, S. Vitale, and P. Colonna, “A look-up table method based on unstructured grids and its application to non-ideal compressible fluid dynamic simulations,” *Journal of Computational Science*, vol. 28, pp. 70–77, sep 2018.

- [9] M. Deligant, X. Nogueira, S. Khelladi, E. Sauret, and B. Reding, “Toward a high resolution real gas finite volume solver with multi optimal order detection,” in *5th International Seminar on ORC Power Systems*, pp. 1–9, 2019.
- [10] P. Colonna, N. Nannan, A. Guardone, and T. van der Stelt, “On the computation of the fundamental derivative of gas dynamics using equations of state,” *Fluid Phase Equilibria*, vol. 286, pp. 43–54, nov 2009.
- [11] T. Krüger, H. Kusumaatmaja, A. Kuzmin, O. Shardt, G. Silva, and E. M. Viggien, *The lattice Boltzmann Method: Principles and Practice*. Springer Int. Publishing, 1 ed., 2017.
- [12] S. Succi, *The lattice Boltzmann Equation: For Complex States of Flowing Matter*. Oxford University Press, June 2018.
- [13] Q. Li, K. Luo, Q. Kang, Y. He, Q. Chen, and Q. Liu, “Lattice boltzmann methods for multiphase flow and phase-change heat transfer,” *Progress in Energy and Combustion Science*, vol. 52, pp. 62–105, feb 2016.
- [14] S. Succi, “Lattice Boltzmann 2038,” *EPL (Europhysics Letters)*, vol. 109, p. 50001, mar 2015.
- [15] M. Bernaschi, S. Melchionna, and S. Succi, “Mesoscopic simulations at the physics-chemistry-biology interface,” *Rev. Mod. Phys.*, vol. 91, p. 025004, May 2019.
- [16] M. R. Swift, W. R. Osborn, and J. M. Yeomans, “lattice Boltzmann simulation of nonideal fluids,” *Phys. Rev. Lett.*, vol. 75, pp. 830–833, Jul 1995.
- [17] A. K. Gunstensen, D. H. Rothman, S. Zaleski, and G. Zanetti, “lattice Boltzmann model of immiscible fluids,” *Phys. Rev. A*, vol. 43, pp. 4320–4327, Apr 1991.
- [18] X. Shan and H. Chen, “lattice Boltzmann model for simulating flows with multiple phases and components,” *Phys. Rev. E*, vol. 47, pp. 1815–1819, Mar 1993.
- [19] X. Shan, X.-F. Yuan, and H. Chen, “Kinetic theory representation of hydrodynamics: A way beyond the Navier-Stokes equation,” *J. Fluid Mech.*, vol. 550, pp. 413–441, 2006.
- [20] S. S. Chikatamarla and I. V. Karlin, “Entropy and Galilean invariance of lattice Boltzmann theories,” *Phys. Rev. Lett.*, vol. 97, p. 190601, Nov 2006.
- [21] M. Lulli, R. Benzi, and M. Sbragaglia, “Metastability at the yield-stress transition in soft glasses,” *Phys. Rev. X*, vol. 8, p. 021031, May 2018.
- [22] C. S. From, E. Sauret, S. A. Galindo-Torres, and Y. T. Gu, “Interaction pressure tensor on high-order lattice Boltzmann models for nonideal fluids,” *Phys. Rev. E*, vol. 99, p. 063318, Jun 2019.
- [23] C. S. From, E. Sauret, S. A. Galindo-Torres, and Y. T. Gu, “Application of high-order lattice boltzmann pseudopotential models,” *Phys. Rev. E*, vol. 101, p. 033303, Mar 2020.
- [24] S. S. Chikatamarla and I. V. Karlin, “Lattices for the lattice Boltzmann method,” *Phys. Rev. E*, vol. 79, p. 046701, Apr 2009.
- [25] X. Shan, “Pressure tensor calculation in a class of nonideal gas lattice Boltzmann models,” *Phys. Rev. E*, vol. 77, p. 066702, Jun 2008.
- [26] M. Sbragaglia, R. Benzi, L. Biferale, S. Succi, and F. Toschi, “Surface roughness-hydrophobicity coupling in microchannel and nanochannel flows,” *Phys. Rev. Lett.*, vol. 97, p. 204503, Nov 2006.
- [27] M. Sbragaglia and X. Shan, “Consistent pseudopotential interactions in lattice Boltzmann models,” *Phys. Rev. E*, vol. 84, p. 036703, Sep 2011.
- [28] L. Biferale, P. Perlekar, M. Sbragaglia, and F. Toschi, “Simulations of boiling systems using a lattice Boltzmann method,” *Commun. Comput. Phys.*, vol. 13, no. 3, p. 696–705, 2013.
- [29] M. Sbragaglia, R. Benzi, L. Biferale, S. Succi, K. Sugiyama, and F. Toschi, “Generalized lattice Boltzmann method with multirange pseudopotential,” *Phys. Rev. E*, vol. 75, p. 026702, Feb 2007.
- [30] R. Benzi, L. Biferale, M. Sbragaglia, S. Succi, and F. Toschi, “Mesoscopic modeling of a two-phase flow in the presence of boundaries: The contact angle,” *Phys. Rev. E*, vol. 74, p. 021509, Aug 2006.
- [31] J. Zhang and F. Tian, “A bottom-up approach to non-ideal fluids in the lattice Boltzmann method,” *EPL (Europhysics Letters)*, vol. 81, p. 66005, feb 2008.
- [32] I. H. Bell, J. Wronski, S. Quoilin, and V. Lemort, “Pure and pseudo-pure fluid thermophysical property evaluation and the open-source thermophysical property library CoolProp,” *Industrial & Engineering Chemistry Research*, vol. 53, pp. 2498–2508, jan 2014.
- [33] G. Falcucci, S. Ubertini, and S. Succi, “lattice Boltzmann simulations of phase-separating flows at large density ratios: the case of doubly-attractive pseudopotentials,” *Soft Matter*, vol. 6, pp. 4357–4365, 2010.

EXPERIMENTAL FACILITIES FOR NON-IDEAL COMPRESSIBLE VAPOUR FLOWS

A. Spinelli¹, A. Guardone², C. De Servi³, P. Colonna³,
F. Reinker⁴, S. aus der Wiesche⁴, M. Robertson⁵ and R.F. Martinez-Botas⁵,

¹*Energy Department, Politecnico di Milano, Italy*

²*Department of Aerospace Science and Technology, Politecnico di Milano, Italy*

³*Propulsion and Power, Delft University of Technology, The Netherlands*

⁴*Münster University of Applied Sciences, Germany*

⁵*Turbo Group, Department of Mechanical Engineering, Imperial College, London, United Kingdom*

Abstract

The experimental characterization of non-ideal compressible flows of vapours at thermodynamic conditions close to the saturation curve and the critical point raised considerable interest in the last decade, in both industry and scientific community. The main motivation was the need to validate the tools employed for the design and the analysis of components implementing such flows, which are typically turbomachines, valves, nozzles, diffusers, and pipelines. These tools are based on Computational Fluid Dynamic (CFD) codes specifically conceived for non-ideal flows, whose assessment demands for accurate experimental data, featuring a spatial resolution comparable with the one achievable through numerical simulations. Industrial plants are unsuited to this objective, due to their intrinsic limitation in accessibility for instruments, availability, and operational flexibility, which are typically required by experiments. This brought researchers to design and implement test rigs dedicated to detailed fluid dynamic investigation of non-ideal vapour flows. The facilities existing worldwide for investigation of non-ideal compressible vapour flows are reviewed here. Their configuration and main features are discussed, together with their capabilities in terms of testable flows. Finally, illustrative results obtained up to date are shown for each facility.

1 Introduction

Compressible vapour flows occurring in the vicinity of the vapour saturation curve and of the critical point, thus exhibiting significant deviation from the ideal gas behaviour, are relevant for several applications, for instance in the oil and gas industry, in the chemical sector, and more importantly in the energy field. Such flows are found in valves, nozzles, diffusers, and especially in turbomachines, such as heat pump compressors and expanders of organic Rankine cycles (ORCs) systems.

Since the early 2000s, specific tools were devised for the design and analysis of components implementing non-ideal flows [1, 2, 3]. Based on Computational Fluid Dynamic (CFD) codes and embedding highly accurate equations of states [4, 5, 6], such tools are currently at an advanced state of development and are relatively widespread for both research and manufacturing purposes, but validation against experimental data is still scarce [7]. Indeed, measurement of vapour flow properties at highly non-ideal conditions is often challenged by a hostile working environment, characterized by high

temperature, relatively high pressure and potential fluid condensation.

The accuracy assessment of design tools calls for reliable experimental data typically including the total pressure P_T and temperature T_T , the static pressure P , the velocity vector \mathbf{V} and possibly the Mach number M . Such quantities are related via the fluid thermodynamics. A high spatial resolution of measurements is desirable to resemble the one provided by CFD simulations; therefore, a relatively fine grid of measuring points is to be accessed by instrumentation, possibly through traversing systems. In this respect, optical measurements can be used to deliver a comprehensive view of the flow field [8].

Performing detailed flow measurements within existing industrial plants requires substantial modifications to guarantee accessibility for instrumentation currently available for non-ideal flows. Furthermore, frequent adjustments are usually needed, interfering with plant availability. Also, operating conditions are dictated by the production process, often conflicting with those prescribed by test campaigns. Due to such limitations, experiments cannot be satisfactorily designed to be carried out within actual plants and researchers moved to the implementation of test rigs dedicated to detailed fluid dynamic investigation of non-ideal vapour flows.

Current test rigs consist in closed loop tunnels, where a test section, specifically designed to make the flow domain easily accessible for the instrumentation, is fed with the fluid under scrutiny. The investigated process is included within a thermodynamic cycle implemented by the facility in order to attain the desired test conditions. Working fluids adopted belong to different classes, featuring low and high molecular complexity. If molecularly complex and high molecular mass compounds are employed, non-ideal behaviour can be so strong to involve unconventional flow phenomena such as the increase of speed of sound along isentropic expansions [9].

This paper reviews the facilities currently operating worldwide for investigating non-ideal compressible vapour flows. For each test rig the concept, the main features, the capabilities in terms of feasible tests and illustrative results are presented.

The manuscript is organised as follows. Section 2 discusses the facility concepts, while in section 3 and 4 existing rigs are presented, gathered into batch and continuous-operating ones, respectively. Finally, conclusions are drawn in section 5.

2 Facility concepts

2.1 Fluid selection and test section

The key of the facility conception lies in the choice of the set of fluids to be tested and in the definition of the test section. Flexibility is valuable, therefore rigs are commonly designed to operate with different working fluids and test sections feature adjustable geometry.

Fluid categories of interest include hydrocarbons, halocarbons, siloxanes, ketones, carbon dioxide. The limiting operating pressure P_{max} is generally identified by high critical pressure P_C fluids (halocarbons, CO_2), while high critical temperature T_C compounds (hydrocarbons or siloxanes) dictate the maximum operating temperature T_{max} . Safety issues exclude toxic molecules from laboratory tests; flammable fluids, largely employed in the industrial, are instead considered, providing ATEX regulations are fulfilled.

A major impact of fluid properties on the facility design is given by the high vapour density typical of non-ideal vapour states ($\sim 10^1$ to $\sim 10^2$ kg/m^3). Combined with the transonic to supersonic velocity of highly compressible flows, this entails a considerable mass flow rate, possibly resulting in a power (either thermal or mechanical) requirements even for relatively small cross-sectional area. The test section design is therefore targeted to a compromise among strength of non-ideal effects, achievable Mach number, and cross-sectional area.

The test section is the core of the facility, where the tested flow develops and measurements are performed. A primary distinction can be conveniently made between test sections hosting fixed components or implementing rotating machines. Unconventional turbomachinery flow investigation is of relevance, since they cover a wide range of applications. However, due to the relatively small size of low power rigs, only non-intrusive measurement techniques can be applied.

Channel-type test sections, other than simplicity, present the indubitable advantage of exhibiting limited passage area, but still compatible with intrusive instrumentation and low blockage effects. Moreover, multiple geometrical configurations are of simple implementation. Most importantly, paradigmatic non-ideal flows, lying at the basis of operation of different components, can be attained. For turbomachines, variable area ducts or few-passage blade cascades can be employed to resemble the flow field fundamentals within blade channels. Also, if the passage is used as a wind tunnel, the flow over flat plates, aerodynamic profiles, and bluff bodies can be investigated [10]. As a consequence, most of the existing facilities are channel-fitted ones.

2.2 Thermodynamic cycle

A gas cycle or a phase transition cycle can be adopted to feed the test section with the vapour flow, either at subcritical or supercritical states. Figure (1) compares two exemplifying cycles employed to test an isentropic expansion of siloxane vapour MDM (octamethyltrisiloxane, $\text{C}_8\text{H}_{24}\text{O}_2\text{Si}_3$).

The main advantage of the gas cycle is a reduced input thermal power required, which is only needed to bring the system to the proper temperature level. The rejected thermal power is also limited and benefits from the high temperature difference available for heat exchange. The main disadvantage lies in the compressor operation, which requires a considerable power ($\sim 10^2$ kW) and typically feature poor flexibility, for both working fluids and

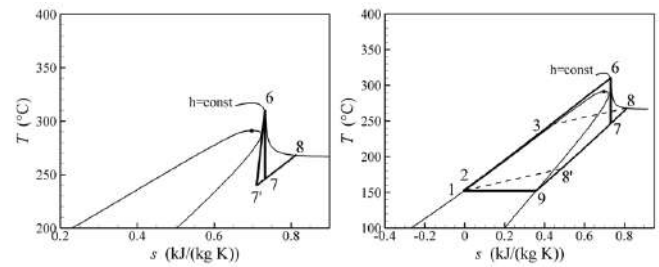


Figure 1: Gas cycle (left) and regenerative phase transition cycle (right) implemented to attain isentropic expansion 6→7 of siloxane vapour MDM. T is the temperature, s and h are the mass specific entropy and enthalpy

operating conditions. Also, bearing operation and sealing can conflict with the need of avoiding fluid contamination. Reducing the maximum Mach number and non-ideality level mitigates the power request, as well as flow diffusion after expansion, while increasing the complexity of operation, especially for supersonic flows.

Phase transition cycles dramatically reduce the power required for compression and increase flexibility due to the easy implementation of variable flow rate machines. Cavitation issues must be managed by providing proper head or liquid cooling. The main drawback of two-phase cycles is the considerable thermal power required to evaporate the fluid ($\sim 10^2$ to 10^3 kW in existing rigs), which suggests the adoption of regeneration, if possible. Rejected thermal power is of the same order of magnitude, but the process is simplified by favourable heat exchange coefficients and temperature differences and by no risk of thermal degradation.

2.3 Operational mode

The operational mode of the test-rig cycle can be either continuous or batch.

Advantages of continuous cycles are flow steadiness, no limits in test duration, and a precise control of the operating conditions. The main disadvantage is the high power requirements, either thermal or mechanical. Also, regulation capabilities can possibly limit the range of thermodynamic conditions that can be tested.

Batch-operating solutions, implemented to limit the installed power, exploit long-lasting storage of the vapour at test conditions. Vapour compression is usually not feasible, since a high temperature storage is required in addition to a volumetric compressor. Thus, batch systems typically implement phase transition cycles. To reduce the power requirements, the heating/cooling processes occurs at a time scale that is orders of magnitude larger than the test one. Other benefits of batch-operating systems are the simplicity of operation and of test set up and, more importantly, the possibility of exploring in a single run, a broad range of thermodynamic states, from highly non-ideal to perfect gas ones, following the emptying of the batch volume. The main drawbacks are the limited test duration and the process unsteadiness, which can be strongly limited by a properly high ratio between stored mass and test mass flow rate. Furthermore, available instruments for fluid dynamic measurements feature frequency response suitable to capture steady pictures of moderately unsteady flows.

3 Batch-operating facilities

3.1 The Test Rig for Organic VApours – TROVA

The Test Rig for Organic VApours (TROVA) is a blow-down facility implementing a discontinuous phase transition cycle and a channel-like test section. The facility was conceived and designed [11, 12, 13] to study non-ideal vapour flows of a large variety of fluids, typically molecularly complex organic compounds. Maximum operating pressure and temperature are 50 bar and of 400 °C. A blowdown rig allows to test geometries with relatively large cross-sectional area, minimizing the blockage effect of instrument insertion and keeping at the same time limited input thermal power. Passage areas up to 10^{-3} m² and flow rate up to 10 kg/s at choked conditions can be obtained, with a heating power installed of 50 kW, which would be of MW-scale in case of continuous operation. Due to batch operation, the time scales of loop processes are different; several hours for heat supply, few seconds to several minutes for tests, approximately one hour for heat rejection. As anticipated in section 2.3, the batch operation mode offers the opportunity of investigating, in a single test run, flows spanning from highly non-ideal to perfect gas states, which is highly valuable to highlight non-ideal flow effects [14].

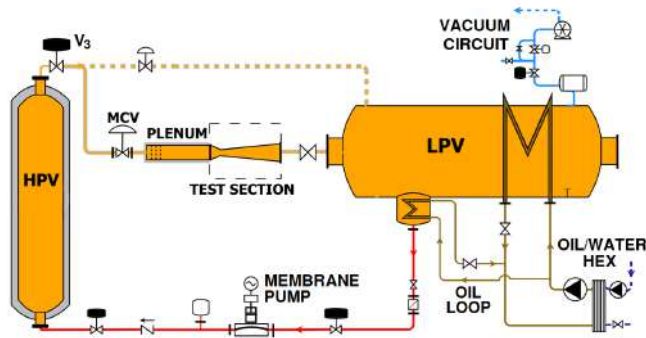


Figure 2: Simplified schematic of the Test Rig for Organic VApours (TROVA) at the CREA Laboratory of Politecnico di Milano

A description of the TROVA and of its operation is given below referring to Figure (2). Complete details can be found in [13, 11]. Within a high pressure vessel (HPV) of 1 m³ volume, the fluid under scrutiny is isochorically brought to saturated, superheated or supercritical vapour state, at the specific pressure P_4 and temperature T_4 required by the test. An accurate mass charge ($\sim 10^2$ kg) guarantees the achievement of the desired thermodynamic state, while low power density electrical heaters are used to prevent local temperature peaks which can possibly lead to fluid decomposition. The opening of the valves V_3 and MCV, trigger the experiment start and the vapour discharge to the test section as HPV empties. Total conditions P_{T6}, T_{T6} at the inlet as well as the whole flow field within the test section are time-dependent, but a sequence of steady flow configurations are captured due to the extremely high ratio between characteristic time of HPV emptying and nozzle flow and the use of instrumentation with appropriately high frequency response. This include pressure probes and taps for total and static pressure, miniaturized thermocouples for total temperature, schlieren imaging for density gradient, Mach number measurements, and shock/fans characterization (see [10]), and Laser Doppler

Velocimetry (LDV) for direct velocity measurements. The test section is a modular planar channel, where nozzles/diffusers, aerodynamic/bluff bodies, flat plates, turbomachine blade cascades can be mounted. The test section dimension is compatible with intrusive instrument insertion, while a frontal quartz windows guarantees a wide optical access. A large volume (5.6 m³) low pressure vessel LPV collects the vapour exiting the nozzle guaranteeing a test duration above ~ 10 s for all fluids and operating conditions. De-superheating and condensation are attained through a shell-mounted oil loop coupled with a cooling tower circuit via a 300 kW oil/water plate heat exchanger. An adjustable flow rate membrane pump closes the loop with condensate compression to HPV.

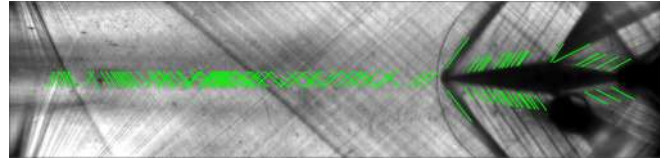


Figure 3: Schlieren visualization of non-ideal flow of siloxane MDM around a supersonic aerodynamic profile mounted on the TROVA test section. Oblique shocks and fan structures are highlighted as well as Mach lines in isentropic regions, from which Mach number measurement can be obtained, see [10, 15]

The TROVA allows to study fundamentals of non-ideal flows. This is for instance the case of non-ideal nozzle expansions documented for the first time in references [14, 16] for a molecularly complex vapour (MDM). Flow regimes range from subsonic to highly supersonic flows and the test section is typically choked, due to the high HPV-to-LPV pressure ratio ($\sim 10^3$ to $\sim 10^4$). In a wind tunnel mode, non-ideal flows around aerodynamic profiles, bluff bodies, and flat plates can be tested, including Mach number measurements and non-ideal shock/fans characterization in case of supersonic flows, see Figure (3) and [15].

Experiments on such paradigmatic flows, allowed to assess the accuracy of CFD models employed for non-ideal flow simulations [7]. The TROVA test section can be also equipped with calibration nozzles for non-ideal pressure probe calibration, an activity currently underway on the facility. Moreover, small turbomachinery blade rows will be implemented in the near future to characterize, up to high supersonic velocities, the aerodynamics of turbine or compressor operating in non-ideal regime.

Finally, as an illustrative result, the outcome of a recent experimental campaign [17] carried out to obtain, for the first time, direct velocity measurements in non-ideal compressible flow is presented. Tests were performed on a two-dimensional nozzle flow of siloxane vapour MM (hexamethyldisiloxane, $C_6H_{18}OSi_2$), in a uniform region at nominal Mach number $M = 0.7$. Here, measurements were taken at three locations on the nozzle axis, labelled from 9 to 11 in the flow direction. At point 9 and 11 static pressure P_9 and P_{11} are acquired, while at point 10 the velocity vector is measured through a two-components LDV system using titanium dioxide seeding particles. As expected, due to nozzle symmetry, a purely axial velocity is obtained. Measurements were completed with acquisition of total temperature T_T and pressure P_T upstream of the nozzle. The velocity V_{10} was also extracted from two-dimensional CFD viscous simulation and, being the flow at the axis adiabatic and isentropic,

calculated from total conditions and static pressure P_9 and P_{11} through a state-of-the-art thermodynamic model for MM [6]. For decreasing levels of non-ideality, marked by decreasing total pressure, figure Figure (4) reports the comparison among flow directly measured, simulated and calculated velocity. A good accordance is found, since deviation is below 3%, thus confirming the accuracy of both CFD and thermodynamic model [6] employed.

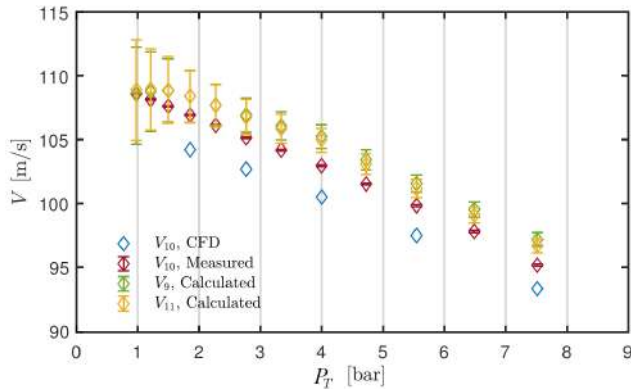


Figure 4: Axial flow velocity measured at variable total pressure P_T at the axis of a subsonic nozzle at nominal Mach number $M = 0.7$. Directly measured velocity $V_{10, Measured}$ is compared with those inferred by pressure and temperature measurements $V_{9, Calculated}$, $V_{11, Calculated}$ and extracted from CFD simulation $V_{10, CFD}$

3.2 The Imperial College Dense Gas Blowdown Facility

The Imperial College Dense Gas Blowdown Facility has been manifested through the requirement to validate Computational Fluid Dynamics (CFD) for highly non-ideal flows, achieved through a set of canonical test cases.

The facility is derived from *MORCEA: Mobile Organic Rankine Cycle Powersystem with Electrified Ancillaries for reduced parasitics*, a 3-year Innovate UK project focusing on the development of a highly efficient diesel-electric powertrain, utilising an organic Rankine cycle to recover exhaust waste heat. To facilitate this, the Imperial blowdown facility is designed for the study of expansions within the 5-30 kW power range [18] [19].

Assuming a 20 kW equivalent expansion power and 10% cycle efficiency, continuous operation would require 200 kW of heat input, considered unsuitable within limited lab space constraints. The choice of batch operation therefore allows the facility to occupy a modest footprint of approximately 4x2 m, standing 2.5 m in height.

A block schematic of the blowdown facility key components is shown in Figure (5). Working fluid is stored in three 60 L reservoir tanks, minimising long-term leakage to atmosphere.

Upon initiating a test, a diaphragm metering pump is activated, capable of delivering flow to the blowdown vessel at up to 69 bar and ensuring no contamination due to lubricant ingress. A 5 kW heater is placed downstream of the pump, consisting of 306L stainless steel piping cast into an aluminium block. Such a design ensures no direct contact with heating elements and reduces the likelihood of working fluid thermal degradation.

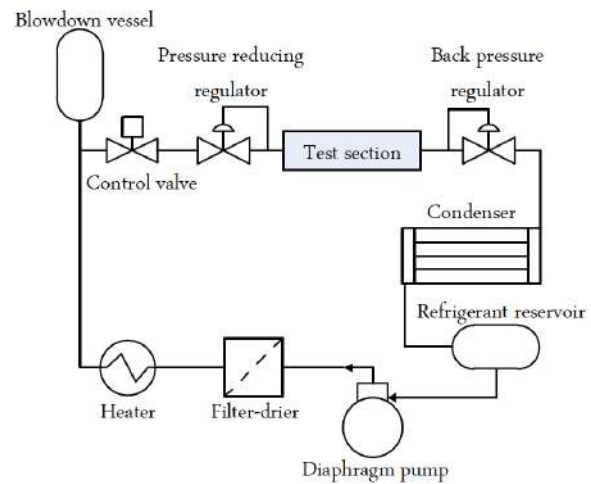


Figure 5: Block schematic of the Imperial College blowdown facility

Once the blowdown vessel (a hemispherically-ended 3.785 L pressure vessel) is filled, the pump is disengaged and the blowdown test is commenced - two ball valves upstream of the test section are activated, opening the high-pressure flow path. Two further pressure-regulating valves are placed either side of the working section, allowing effective pressure ratio to be set.

Downstream of the test section, flow enters a brazed-plate condenser, linked to lab process water - this returns the working fluid to a liquid state, which can then be re-pumped to the reservoir for storage or further blowdown tests.

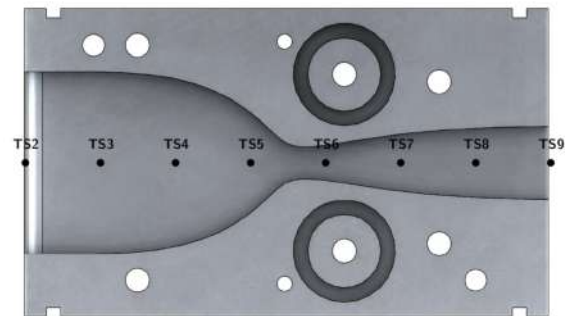


Figure 6: Plan view of the de Laval nozzle section, with centreline pressure tapping (TS) locations marked. The flow is from left to right

Initial validation has been conducted on the de Laval nozzle geometry shown in the 3D model in Figure (6), designed through a Method of Characteristics code modified to incorporate real-gas effects. The nozzle was designed for the next-generation refrigerant R1233zd(E), producing a $M = 2$ flow at the exit plane in the design condition. Measurement was achieved through a series of pressure tappings along the nozzle centreline.

Three nozzle expansions (A,B,C) are shown in Figure (7), across a range of inlet conditions. In each case pressure and temperature were measured up- and downstream of the working section and used directly as boundary conditions for 3D RANS simulations. Alongside R1233zd(E), nitrogen (N_2) was chosen as an ideal-gas baseline. CFD was conducted with multiple equations of state to assess prediction accuracy with increasing model fidelity. Maximum disagreements between simulation and experiment for pressure ratio prediction were

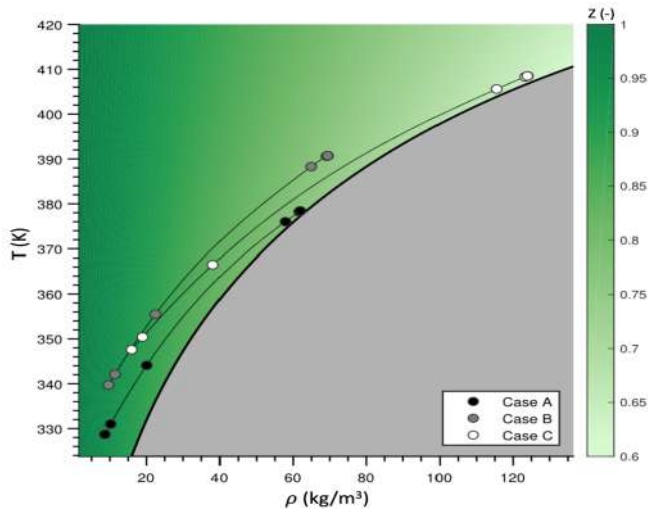


Figure 7: Three R1233zd(E) expansions overlaid onto a map of compressibility factor, $Z = P/\rho RT$, where ρ is the density and R the specific gas constant. Greyed area denotes the two-phase region

found to be 5.65% & 9.59% for N_2 and R1233zd(E), respectively. This indicates an overprediction of real-gas expander power by existing computational methods [18] [19].

Subsequent work now focuses on the construction of a linear blade cascade, incorporating suction/pressure side tappings and Schlieren density gradient imaging [20] - this runs alongside development of a real-gas Direct Numerical Simulation (DNS) code for detailed flow analysis and improvement of real-gas RANS simulations.

4 Continuous-operating facilities

4.1 The Organic Rankine Cycle Hybrid Integrated Device – ORCHID

The ORCHID facility features a single closed loop Balance of Plant (BoP) designed to integrate two different test sections, which can be alternatively fed with working fluid and operated, thus making the setup hybrid. The first test section consists of a De Laval nozzle with optical access to perform fundamental experiments aimed at verifying the Non-Ideal Compressible Fluid Dynamics (NICFD) theoretical fundamentals and at validating the related fluid dynamic and thermodynamic numerical models. The second test section is a test-bench for mini-ORC expanders up to a power output of 80 kW. The closed loop configuration of the setup was chosen to avoid limitations on the testing time of the turbine and nozzle, and to reproduce the operating conditions of a real-world ORC system, while possibly attaining all the thermodynamic conditions of potential interest, i.e., operating the setup in the liquid-vapour, subcritical, and supercritical regimes.

Figure (8) reports an isometric view of the CAD assembly of the ORCHID as-built, where the main components of the facility are itemized and labeled. Only the nozzle test section is shown in the figure, as the turbine test bench is still under design and its construction and commissioning are envisaged for the first quarter of 2022.

The working fluid is extracted from the condensate tank (item 4 in Figure (8)) by a booster pump (item 3) and then is supplied to the evaporator (item 7) by the primary pump (item 2), a positive displacement pump

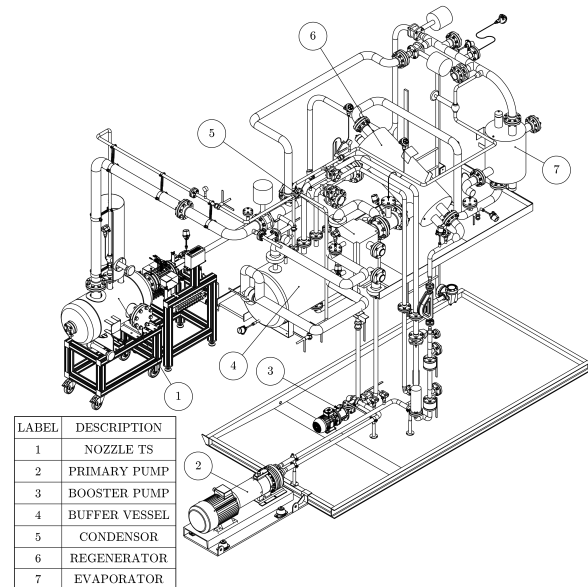


Figure 8: CAD assembly of the ORCHID without the supporting structure

with a rated power of 15 kW. The pump is of the membrane type and can operate with a mass flow rate between 10 to 136 l/min by means of a frequency drive. The adoption of a positive displacement pump allows for a seamless regulation of the flow in the working fluid loop and a larger flow operating range. These features are crucial for the facility at hand, given the different operating conditions envisaged for the nozzle experiments and the turbine test bench, as well as the need to guarantee stable inlet conditions during testing. The booster pump is, instead, of the centrifugal type and it is adopted to ensure enough suction head upstream of the main pump, due to the high NPSH that this requires. Before entering the evaporator, the working fluid is preheated in the regenerator (item 6) by recovering the thermal energy of the superheated vapour discharged by the test sections. This results in a reduction of the thermal input required to achieve the operating conditions requested for the experiments. The vapour leaving the regenerator is then condensed and subcooled by a few degrees in a water-cooled condenser. The regenerator and the evaporator are shell & plate heat exchangers, while the condenser is of the plate type. Shell & plate heat exchangers feature compactness similar to that of plate heat exchangers but are more resistant to thermal stresses, which allows for a swift warm-up of the working fluid loop. For the condenser, a plate heat exchanger was preferred in order to ease the periodic cleaning of the heat transfer surface, as the plates of this kind of heat exchangers, differently from those of the plate & shell type, can be removed and visually inspected.

The thermal power source of the facility is an electric oil heater which can supply up to 400 kW to the working fluid. The adoption of an electric heater allows for an easy modulation of the thermal input to the evaporator, as well as of the vapour temperature at the inlet of the test sections, as the oil temperature can be smoothly varied from 350 K to the maximum allowed operating temperature. This limit is equal to 673 K for Therminol VP1, the synthetic oil chosen for the heating loop of the set-up.

The maximum operating temperature in the test sections is, however, limited by the thermal stability limit of the working fluid under testing. As the compound

currently in use in the ORCHID is the siloxane MM, the maximum temperature in the experiments cannot exceed approximately 573 K [21]. The maximum operating pressure is 25 bar. This value has been determined by the need of limiting the investment costs of the facility. Another constraint on the maximum temperature of the working fluid loop may be imposed by ATEX directive. Given the characteristics of MM, it is not necessary to apply a more stringent operating constraint than that required for the thermal stability of the fluid, provided that any vapour leakage from the test rig is rapidly dispersed to a low and safe concentration. To ensure these conditions, the part of the facility where MM is circulated is surrounded by a cabinet equipped with a dedicated ventilation system that runs at a constant flow rate when the ORCHID is put into operation, thus guaranteeing a continuous provision of fresh air to the cabinet. The limitation on the maximum operating temperature of the set-up may change if another working fluid is used in place of MM. In any case, this cannot exceed the thermal stability limit of the oil of the electric heater.

The first experimental campaigns in the nozzle test section focused on characterizing the expansion process of MM by measuring the pressure evolution along the expansion process through a series of pressure taps, and by reconstructing the Mach field by means of a schlieren setup. Figure (9) shows an exemplary schlieren image, which allows for visualizing the Mach waves or lines associated with the expansion of the working fluid. The angle that the Mach waves form with respect to the nozzle midline is proportional to the flow Mach number. This information can be extracted from the schlieren images and used in combination with the measured values of the pressure distribution along the nozzle to assess the adequacy of the fluid equation of state model adopted in CFD tools for the fluid-dynamic design of ORC turbines.

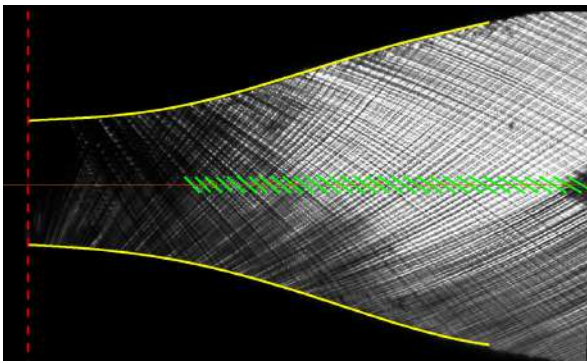


Figure 9: A schlieren photograph highlighting the Mach lines in the dense vapour flow of MM in the diverging portion of the nozzle

4.2 The Closed Loop Organic vapour Wind Tunnel – CLOWT

The closed-loop organic vapour wind tunnel (CLOWT) follows, as it suggests, the concept of a closed loop wind tunnel (Güttlinger-type). In contrast to conventional wind tunnels for air, this facility was primarily designed for operation with organic vapours and equipped with an electrical heating system. The main reasons to select this configuration was to provide high subsonic to transonic organic vapour flows at low levels of turbulence, Tu , and steady state conditions enabling long stable test durations (theoretically unlimited).

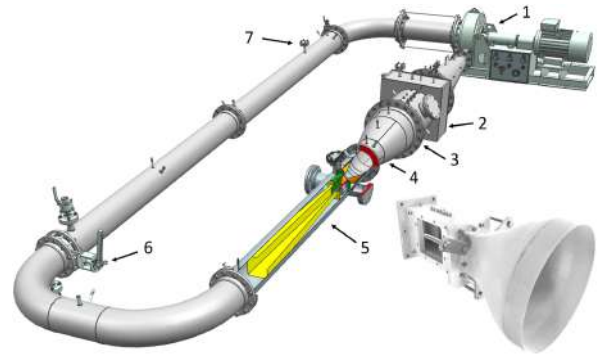


Figure 10: Left: CAD model of CLOWT with its main components (1-7). Right: Photograph of the modular high-speed test section

CLOWT has been designed in accordance with pressure vessel design guidelines in order to work at high pressure and temperature levels. The thermodynamic cycle takes place in the superheated region (gas-cycle), whereby the average density of the wind tunnel flow domain is set by the amount of fluid prior to operation (inventory forward-control approach). Figure (10) illustrates CLOWT with its main components: (1) a radial compressor with a cartridge multiple dynamic lip seal system and rotational speed control, (2) a finned heat exchanger which is necessary to close the thermodynamic cycle and to ensure a stable operation, (3) a settling chamber with flow straighteners and screens, (4) a moderate first contraction zone, (5) a main test section unit, and a return including (6) a throttle valve and (7) an averaging Pitot probe to determine the actual mass flow rate. Individually designed high-speed test sections including a second contraction zone and a diffuser can be placed in the main test section unit, see Figure (10). This includes also a standard test section with a three-dimensional nozzle providing a cross-section change from round to rectangular contraction (DN250 to 50 mm × 100 mm), resulting in an overall contraction ratio of about 38. A detailed description on CLOWT's main components and the first operational experiences can be found in [22, 23, 24, 25].

CLOWT has been primarily planned for operation with Novac™ 649, a harmless perfluorinated ketone, but also air can be investigated for comparing real and ideal gas behavior. The pressure working area ranges from 0 - 0.6 MPa at a maximum temperature level of 423 K (150 °C). Individual test section configurations or even annular cascades can be placed into the relatively large main test section unit (DN250; length 2.5 m) manufactured as pressure vessel. Furthermore, based on the stringent laminar wind tunnel design (low Tu) and the continuous running mode (stable conditions), CLOWT offers a solid base for fundamental testing on dedicated measurement techniques in organic vapour flows, e.g. hot-wire anemometry (HWA) or Pitot and multi-hole probe calibration. CLOWT has been mainly designed for fundamental research and aerodynamic investigations including flow through turbine cascades. Based on the compressor performance, the test rig permits high subsonic up to transonic flow regimes in the actual high-speed test section.

Illustrative results obtained on the CLOWT on turbulence research are presented in the followings. The high-speed test section was equipped with a constant-temperature-anemometry (CTA) system to assess the applicability of HWA in high subsonic organic vapour

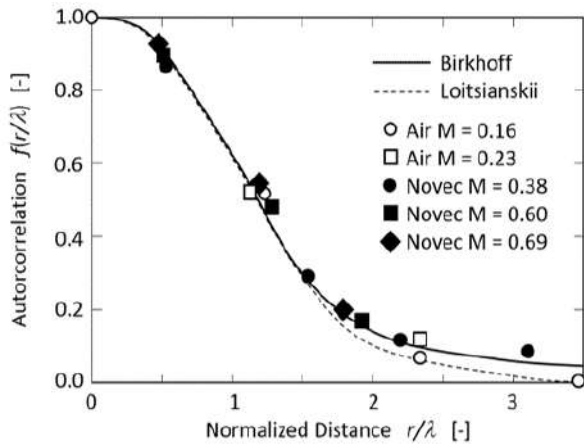


Figure 11: Autocorrelation for NovecTM 649 and air at different Mach numbers

flows. A static calibration procedure with NovecTM 649, based on a laminar heat transfer correlation, led to deviations less than 1%. Turbulent quantities were determined for several Mach number levels. The CTA data was independently checked with a classical turbulence sphere after the first contraction. Without any flow straighteners and screens, the basic value of Tu was 1.5%, and due to the second contraction, it dropped to about 0.5%. A slight increase of Tu with Mach number was observed. A spectral analysis was applied and autocorrelations $f(\frac{r}{\lambda})$, with r as streamwise distance and λ as turbulent micro length scale, were obtained for air and for NovecTM 649 at different Mach numbers (see Figure (11)). A good agreement with theoretical models proposed by Loitsianskii and Birkhoff for (incompressible) isotropic turbulence was found [26]. This result is a strong indication that the well-established turbulence models might be also applicable for modeling high subsonic turbulent real gas flows. Based on $f(\frac{r}{\lambda})$ the turbulent micro length scale λ and the integral length scale Λ were calculated. At very low Mach number the value of $\frac{\lambda}{D_h} \approx 0.07$, with D_h as hydraulic diameter of the high speed test section, agreed well with observations for incompressible pipe and duct flows.

5 Conclusions

Four experimental facilities are currently in operation worldwide aiming at characterizing highly non-ideal compressible vapour flows. Though implementing different thermodynamic cycles, operational modes, working fluids, limiting operating conditions, and test section types, they all share the objective of providing experimental data, still scarcely available, on non-ideal flows. The main purpose is the accuracy assessment of computational tools employed to model such flows. Therefore, experimental activities in these novel rigs focused on paradigmatic compressible flows such as adiabatic nozzle expansions or Mach/shock/expansion wave study. However, test rig capabilities allow to perform test on more complex configurations as, for instance, turbomachine blade cascades. To this aim, the reviewed facilities are also currently in use to calibrate instruments, such as pressure probes and hot wires, which are crucial to investigate challenging flow patterns. The presented rigs feature common ground and complement one another, to address the lack of detailed experimental characterization of non-ideal compressible flows.

References

- [1] P. Colonna and S. Rebay, "Numerical simulation of dense gas flows on unstructured grids with an implicit high resolution upwind Euler solver," *International Journal for Numerical Methods in Fluids*, vol. 46(7), pp. 735–765, 2004.
- [2] P. Cinnella and P. Congedo, "Numerical solver for dense gas flows," *AIAA Journal*, vol. 43, no. 11, pp. 2457–2461, 2005.
- [3] S. Vitale, M. Pini, P. Colonna, G. Gori, A. A. Guardone, T. D. Economon, F. Palacios, and J. J. Alonso, "Extension of the SU2 open source CFD code to the simulation of turbulent flows of fluids modelled with complex thermophysical laws," in *22nd AIAA Computational Fluid Dynamics Conference*, 2015.
- [4] R. Span and W. Wagner, "Equations of state for technical applications. I. Simultaneously optimized functional forms for nonpolar and polar fluids," *Int. J. Thermophys.*, vol. 24, pp. 1–39, January 2003.
- [5] T. van der Stelt, N. Nannan, and P. Colonna, "The iprsv equation of state," *Fluid Phase Equilibria*, vol. 330, pp. 24 – 35, 2012.
- [6] M. Thol, F. Dubberke, G. Rutkai, T. Windmann, A. KÄuster, R. Span, and J. Vrabec, "Fundamental equation of state correlation for hexamethyldisiloxane based on experimental and molecular simulation data," *Fluid Phase Equilibria*, vol. 418, pp. 133–151, 2016.
- [7] G. Gori, M. Zocca, G. Cammi, A. Spinelli, P. Congedo, and A. Guardone, "Accuracy assessment of the Non-Ideal Computational Fluid Dynamics model for siloxane MDM from the open-source SU2 suite," *European Journal of Mechanics - B/Fluids*, vol. 79, pp. 109–120, 2020.
- [8] F. Cozzi, A. Spinelli, and A. Gallarini, S. Guardone, "Optical diagnostics for non-ideal compressible fluid dynamics," in *ERCOFTAC Bulletin*, no. 124, 2020.
- [9] P. A. Thompson, "A fundamental derivative in gas-dynamics," *Physics of Fluids (1958-1988)*, vol. 14, no. 9, pp. 1843–1849, 1971.
- [10] G. Cammi, A. Spinelli, F. Cozzi, and A. Guardone, "Automatic detection of oblique shocks and simple waves in schlieren images of two-dimensional supersonic steady flows," *Measurement*, 2020. In press.
- [11] A. Spinelli, V. Dossena, P. Gaetani, C. Osnaghi, and D. Colombo, "Design of a test rig for organic vapours," in *Proceedings of ASME Turbo Expo, Glasgow, UK*, June 2010.
- [12] M. Pini, A. Spinelli, V. Dossena, P. Gaetani, and F. Casella, "Dynamic simulation of a test rig for organic vapours," *Proceedings of ASME 5th International Conference on Energy Sustainability*, pp. 1977–1988, 2011.
- [13] A. Spinelli, M. Pini, V. Dossena, P. Gaetani, and F. Casella, "Design, simulation, and construction of a test rig for organic vapours," *ASME Journal of Engineering for Gas Turbines and Power*, vol. 135, p. 042303, 2013.

- [14] A. Spinelli, G. Cammi, S. Gallarini, M. Zocca, F. Cozzi, P. Gaetani, V. Dossena, and A. Guardone, “Experimental evidence of non-ideal compressible effects in expanding flow of a high molecular complexity vapor,” *Experiments in Fluids*, vol. 59, p. 126, Jul 2018.
- [15] M. Zocca, A. Guardone, G. Cammi, F. Cozzi, and A. Spinelli, “Experimental observation of oblique shock waves in steady non-ideal flows,” *Experiments in Fluids*, vol. 60, no. 6, 2019.
- [16] A. Spinelli, G. Cammi, C. C. Conti, S. Gallarini, M. Zocca, F. Cozzi, P. Gaetani, V. Dossena, and A. Guardone, “Experimental observation and thermodynamic modeling of non-ideal expanding flows of siloxane mdm vapor for orc applications,” *Energy*, vol. 168, pp. 285 – 294, 2019.
- [17] S. Gallarini, *High temperature non-ideal compressible-fluid flows of siloxanes*. PhD thesis, Politecnico di Milano, 2020.
- [18] M. Robertson, P. Newton, T. Chen, and R. Martinez-Botas, “Development and commissioning of a blowdown facility for dense gas vapours,” *Proceedings of the ASME Turbo Expo*, vol. 3, 2019.
- [19] M. Robertson, P. Newton, T. Chen, A. Costall, and R. Martinez-Botas, “Experimental and numerical study of supersonic non-ideal flows for organic rankine cycle applications,” *ASME Journal of Engineering for Gas Turbines and Power*, 2020. doi: <https://doi.org/10.1115/1.4046758>.
- [20] T. Chen, P. Newton, M. Robertson, and R. Martinez-Botas, “Analysis of transonic nozzle loss generation in organic rankine cycle (orc) turbines,” *Proceedings of ORC 2019 International Seminar on ORC Power Systems*, 2019.
- [21] T. Weith, F. Heberle, P. M., and B. D., “Performance of siloxane mixtures in a high-temperature organic rankine cycle considering the heat transfer characteristics during evaporation,” *Energies*, vol. 7, pp. 5548– 5565, 2014.
- [22] F. Reinker, K. Hasselmann, aus der Wiesche, S., and E. Y. Kenig, “Thermodynamics and fluid mechanics of a closed blade cascade wind tunnel for organic vapors,” *ASME Journal of Engineering for Gas Turbines and Power*, vol. 138, no. 5, p. 052601, 2015.
- [23] M. Passmann, F. Reinker, K. Hasselmann, S. aus der Wiesche, and F. Joos, “Development and design of a two-stage contraction zone and test section of an organic rankine cycle wind tunnel,” in *ASME Turbo Expo 2016: Turbomachinery Technical Conference and Exposition*, p. V003T25A006, 2016.
- [24] F. Reinker, E. Y. Kenig, and S. aus der Wiesche, “Clowt: A multifunctional test facility for the investigation of organic vapor flows,” *ASME 2018 5th Joint US-European Fluids Engineering Division Summer Meeting*, vol. 2018, p. V002T14A004, 2018.
- [25] F. Reinker, E. Y. Kenig, and aus der Wiesche, S., “Closed loop organic vapor wind tunnel clowt: Commissioning and operational experience,” *5. International Seminar on ORC Power Systems, Athens*, p. ID: 47, 2019.
- [26] J. C. Rotta, *Turbulente Strömungen: Eine Einf. in d. Theorie u. ihre Anwendung*, vol. Bd. 15 of *Leitfäden der angewandten Mathematik und Mechanik*. Stuttgart: Teubner, 1972.

OPTICAL DIAGNOSTICS FOR NON-IDEAL COMPRESSIBLE FLUID DYNAMICS

F. Cozzi¹, A. Spinelli¹, S. Gallarini¹ and A. Guardone²,

¹*Dipartimento di Energia, Politecnico di Milano*

²*Dipartimento di Scienze e Tecnologie Aerospaziali, Politecnico di Milano*

Abstract

Optical based techniques are commonly employed in many technical and scientific fields, and those able to give qualitative and/or quantitative results about density and velocity fields are valuable tools to investigate compressible flows. In recent years a strong interest has emerged about non-ideal compressible flows also due to their relevance for variety of applications where such flows are encountered, including for example wind tunnels for aerodynamic testing and turbomachinery. Moreover, such flows theoretically show peculiar behaviour with respect to their ideal counterpart giving rise for example the possibility of rarefaction shocks to occur.

Actually very few examples of application of optical diagnostic techniques along with measured data are reported in the literature about non-ideal compressible flows. This work aims to present a brief summary of available optical techniques that are applied within the TROVA (Test Rig for Organic VApors) facility at the CREA laboratory of Politecnico di Milano. The TROVA test rig is designed to operate with siloxane, a family of silicon oil of particular interest for high temperature Organic Rankine Cycle (ORC) applications. MDM (Octamethyltrisiloxane- $C_8H_{24}O_2Si_3$) or either MM (Hexamethyldisiloxane- $C_6H_{18}OSi_2$) are currently used as a working fluid. To investigate such kind of flows innovative Schlieren and LDV techniques have been developed, tested and applied on the TROVA blow-down wind tunnel. The paper aims to provide a description of the measurement set-up used at CREA laboratory by considering also constraints and issues in their application and design. To support the conclusions, exemplary results achieved so far are reported.

1 Introduction

The interest towards non-ideal fluid dynamics has grown in recent years due to their relevance to industrial applications. Here, the term non-ideal is used to indicate the occurrence of peculiar flow behaviour because of departure from dilute, ideal-gas thermodynamics. It is interesting to observe that such kind of flows can theoretically show unusual phenomena; for example, in the so called non-classical regimes rarefaction shocks are physically admissible [1] [2]. More details about the theoretical analysis of so called non-classical regime can be found for example in [2, 1, 3, 4].

Optical techniques such as Schlieren and Laser Doppler Velocimetry (LDV) are a valuable tools to investigate compressible-fluid flows thanks to their ability to provide information about density gradients and flow velocities. Nevertheless, to the authors knowledge, example of their application to fluid flows featuring non-ideal

behaviour close to liquid-vapour saturation and critical point, or within the supercritical region are still lacking.

The TROVA facility is a blow-down wind tunnel purposely designed to investigate non-ideal compressible-fluid flows by using, but not limited to, Schlieren and Laser Doppler Velocimetry (LDV) techniques. This paper offers a brief description on how those techniques have been successfully implemented, and it briefly analyses some constraints and issues for their application. Results achieved so far are reported.

2 The TROVA Wind Tunnel

The TROVA facility currently uses MDM (Octamethyltrisiloxane, $C_8H_{24}O_2Si_3$) and MM (Hexamethyldisiloxane, $C_6H_{18}OSi_2$) as working fluids. A detailed description of the TROVA test rig can be found in [5, 6, 7, 8, 9, 10, 11].

The TROVA wind tunnel has a 2D test section whose geometry can be easily changed. Straight and convergent-divergent channels are among available geometries. Convergent-divergent supersonic nozzles are designed according to a standard method of characteristics modified for dense gases [12]. A thick quartz window, installed on the channel side-wall, provides easy optical access for Laser Doppler Velocimetry and Schlieren technique, 2.1. It also allows for the Background Oriented Schlieren technique [13] to be implemented. A mirror-polished stainless steel plate is installed on the opposite side of the channel, and it hosts several equally spaced pressure taps for pressure measurements, see 2.1.

With reference to Figure (1), the wind tunnel operates as follows: the fluid stored in the closed high pressure vessel, is heated up to super-heated or supercritical conditions. By opening the Main Control Valve, the fluid is driven by the pressure gradient to flow through the systems down to the test section. Here, the channel geometry and the pressure difference between the inlet and outlet sections rule the flow expansion. The total pressure P_T and total temperature T_T are measured in the still chamber, element 6 in Figure (1), just ahead of the test section. The fluid discharged by the test section is collected into an ambient temperature and low pressure vessel (element 9 in Figure (1)) where it condenses. As the test proceeds the pressure difference between the high pressure and the low pressure vessels decreases until no pressure gradient exists in the system and the flow stops. As discussed in [5, 6] a steady flow within the nozzle can be assumed at any time during the test. The duration of a single run depends on several factors (pressure and temperature of the test, geometry of the test section etc.). In most of the investigated cases, test time is of the order of few minutes.

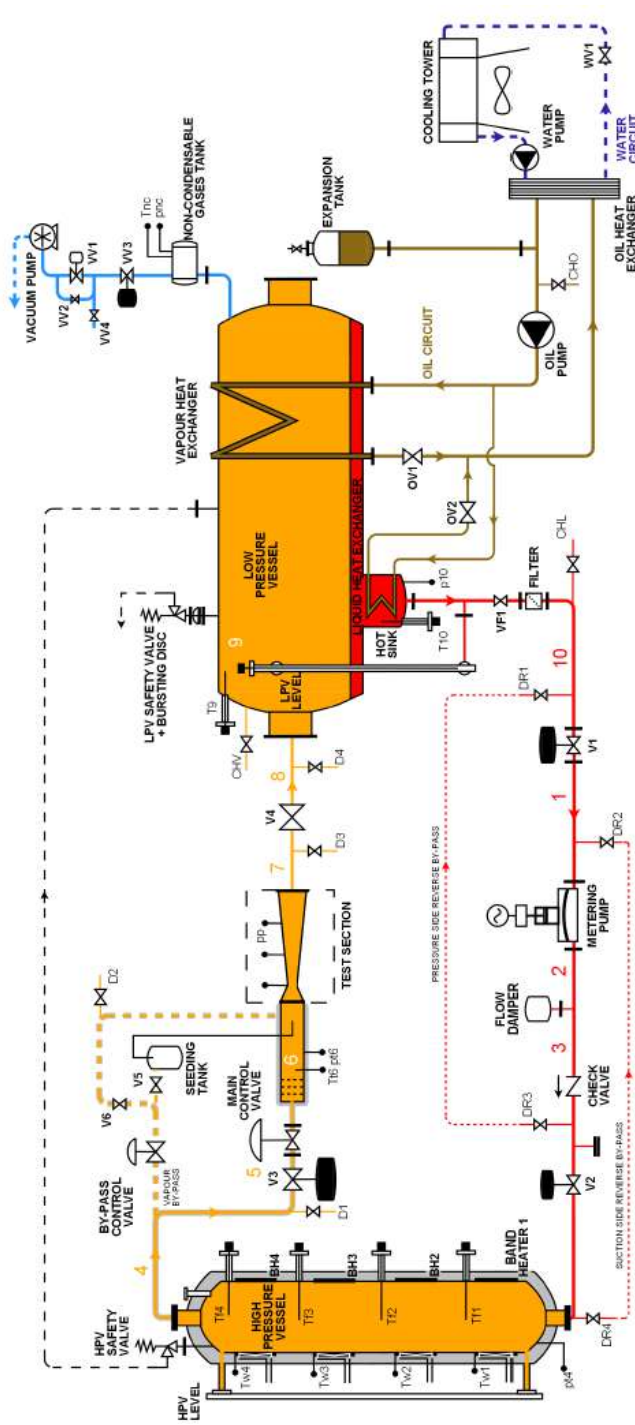


Figure 1: Sketch of the TROVA blow-down wind tunnel

2.1 Schlieren technique

Since the optical access is restricted to one side of the channel, a double-pass Schlieren system is used, Figure (3). The diverging light beam from the light source is collimated by a bi-convex lens ($L1$, focal length $f_1 = 1000$ mm, diameter $d_1 = 150$ mm) and it enters at 90° with respect to the channel axis, Figure (3). Light rays deflected by density gradients in the fluid flow are reflected back by the mirror-polished rear plate 2.1. The reflected rays suffer a further deflection when crossing the fluid flow for the second time, then they focus at the knife edge by means of lens $L1$ (which now acts as the Schlieren head), after a 90° deflection operated by a cube beam splitter, Figure (3). The Schlieren image is formed onto the sensor of a high-speed CMOS camera by

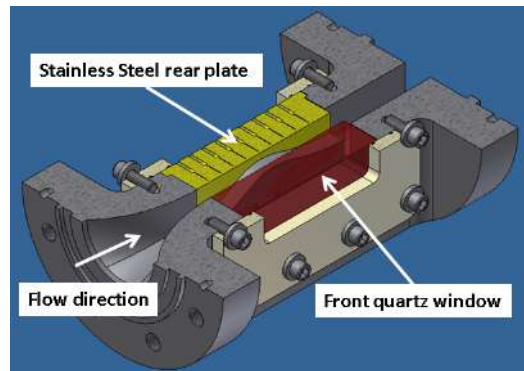


Figure 2: Cut view of the test section, stainless plate and the front quartz window for optical access are highlighted

a second lens ($L2$, $f_2 = 75$ mm, diameter $d_2 = 52$ mm). The knife edge is oriented in the vertical direction so to visualize horizontal density gradients (i.e. those directed along the nozzle axis).

Either a blue led (OSRAM Ostar LEBQ9WN, dominant $\lambda = 460$ nm, emitting surface 0.9×0.9 mm²) or a 100 W Hg arc-lamp have been used as a light sources. The LED light has proven to be a more versatile and stable light source than the Hg arc-lamp. Moreover, the LED can be pulsed and over-driven to improve light output. The mercury lamp also suffers from short terms and long terms light power fluctuations, it needs fans for cooling and it requires a warm up time of at least 1 h, so currently we use the LED as the preferred light source in Schlieren visualization.

To limit the cost of the mirror-polished rear plate, its quality is lower than that of common Schlieren mirrors. Nevertheless it is enough to ensure no significant disturbances in the Schlieren images. The polished surface gets dirty quite quickly, so its has to be cleaned every few tests if good contrast and sharpness in the Schlieren images are sought. Usually some drops of liquid working fluid or isopropyl alcohol are effective cleaning fluids, sometimes more strong solvents (such as acetone for example) are also employed, optical paper or a low lint optical tissue are used to wipe off the liquid. The same procedure is also used to clean the quartz windows.

The reflectivity of the stainless steel plate is somehow affected by the siloxane vapour, after few test the mirror surface assumes a slightly dark aspect, while the amount of light it reflects back to the Schlieren head decreases. This light reduction is compensated by increasing the light output of the lamp or either by increasing the exposure time when a continuous light source is used.

Schlieren images of siloxane flows can evidence measuring range issue as documented in [10, 14]. This problem arise in regions of strong density gradients (for example at the nozzle throat), where the light refraction is enough to deflect light onto some system aperture stop. Consequently, zone that should appear as a bright region can be totally or partially replaced by dark ones. An analysis of this issue was performed in [14] and more details can be found there. It is interesting to note the same issue is also described in [15] for Schlieren images of supersonic air flows.

2.1.1 Schlieren image analysis and results

Schlieren images easily provide qualitative data, nevertheless they can also provide quantitative data about local Mach number, M , and instantaneous slope of shock

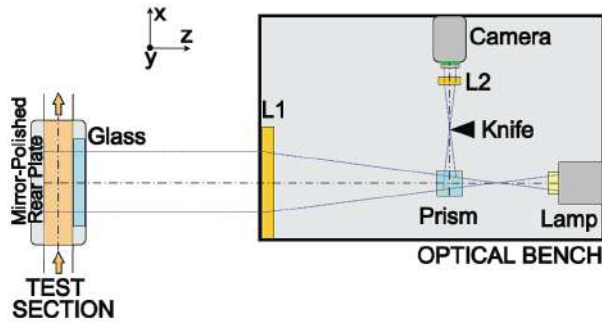


Figure 3: Sketch of the optical bench used for Schlieren visualizations, taken from [14]

waves. To this aim, an image analysis technique has been developed at CREA Laboratory to automatically detect straight flow structures such as oblique shock waves and simple waves in steady two-dimensional supersonic flows. The identification algorithm is based on the Hough transform, and it provides the slope, μ , of the straight flow structure. The Mach line slope with respect to the flow direction is directly linked to the Mach number, namely, $M = 1/\sin\mu$. The detection of Mach lines allows a direct measurement of the local Mach number without involving any thermodynamic model in the calculation, if the direction of the velocity is known. A detailed description of the algorithm is reported in [16] and results can be found in [10, 11, 9, 16, 8].

As an example, a Schlieren image taken from [9] is shown in Figure (4). The Schlieren image refers to MDM vapors flowing in the diverging portion of a convergent-divergent supersonic nozzle. The Mach lines identified by the identification algorithm are superimposed on the same image as green segments. For this case total conditions are $P_T = 9.2$ bar and $T_T = 268$ °C, while the flow is in the non-ideal regime being the compressibility factor $Z_T = 0.63$. The bottom part of Figure (4) shows the evolution of the Mach numbers along the nozzle axis, where green full symbols corresponds to Mach number computed from the Mach lines slope. CFD results (full green line), and Mach numbers (black empty symbols) computed from measured pressure and total conditions, i.e. P_T and T_T , are also reported on the same graph. The coherence of the three data sets is remarkable. Further details and comments can be found in [10, 11, 9, 16, 8].

2.2 Laser Doppler Velocimetry (LDV) technique

Laser Doppler Velocimetry (LDV) is a well established experimental technique used to investigate a wide range of complex flows and fluid-dynamic phenomena in transparent media, i.e. combustion flows, sprays, compressible flows, turbulent flows, coherent structures etc. A comprehensive review on principles, data analysis and practical implementation of the LDV technique can be found in [17]. To the authors knowledge, the present ones are the first LDV velocity measurements in a non-ideal supersonic flow of vapours. The aim of this section is to give an overview of the experimental set-up and of the methodologies used for LDV measurements.

2.2.1 Selection of the seeding material

The LDV technique requires the use of seeding particles dispersed in the flow, a proper choice of the seeding par-

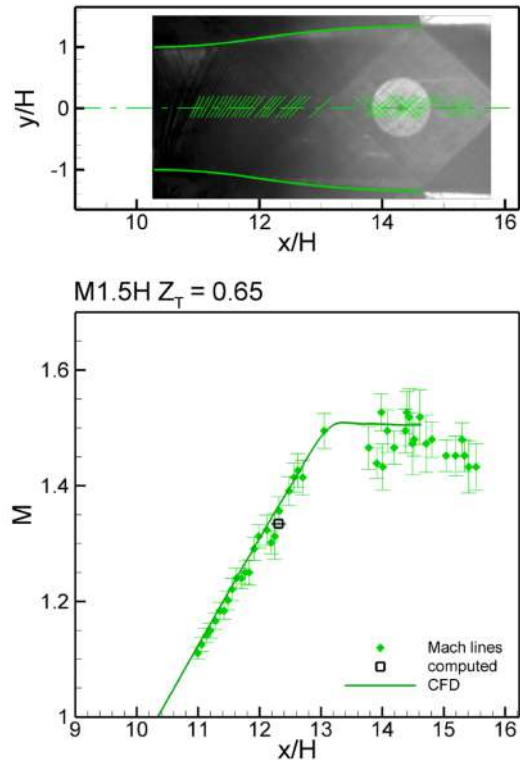


Figure 4: Schlieren image (top) and Mach numbers extracted from Mach lines (bottom), taken from [9]

ticles is of paramount importance to get accurate fluid velocity measurements [17].

First, the seeding material has to be chemically compatible with the fluid under investigation. Chemical modification induced by the seeding particles can alter the thermo-fluid dynamic behaviour of the fluid, jeopardizing the possibility to correctly understand the experimental outcome. Moreover even for chemically compatible seeding materials, a high melting temperature solid seeding has the advantages to be much less prone to evaporate than a liquid one, so it could be a preferred choice at flow temperatures above the ambient one. For example, in our tests, and depending on the operating conditions, the siloxane vapour expands in the TROVA nozzle starting from total pressure and total temperature of the order of about 9 bar and 250 °C, respectively.

The basic requirement of any tracer is to faithfully follow the flow velocity. This requires the response time of the particle, τ_p , to be much smaller than the characteristic time of the flow τ_f , i.e. the particle Stokes number needs to be $St = \tau_p/\tau_f \ll 1$ [17, 18]. For ideal seeding particles the particle to fluid density ratio, $\zeta = \rho_p/\rho_f$, is equal to 1, thus they instantaneously and perfectly adjust their velocity to that of the flow and no velocity slip exists between the particles and the flow [17, 18]. Unfortunately, such ideal situation can hardly be realized, thus a trade-off is required between small particle diameters, for fast response to velocity fluctuations, and large particle diameter, for a high signal-to-noise ratio (SNR) of the scattered light signal. The latter also increases with the ratio of the refractive indexes of the seeding particle n_p to that of the fluid, n_f thus high refractive index materials should be preferred as seeding.

Finally, the flow temperatures in excess of 200 °C restricted our choices to the solid materials shown in Table (1), which are commonly used as seeding in LDV and PIV measurements [19, 17]. By taking all the constrains

Table 1: Physical properties of seeding materials

Material	Refractive index	Density kg/m ³	Melting Point °C
TiO ₂	2.6 – 2.9	3900 – 4200	1840
Al ₂ O ₃	1.79	3960	2015
SiO ₂	1.45	2200	1710
SiC	2.6	3200	2700

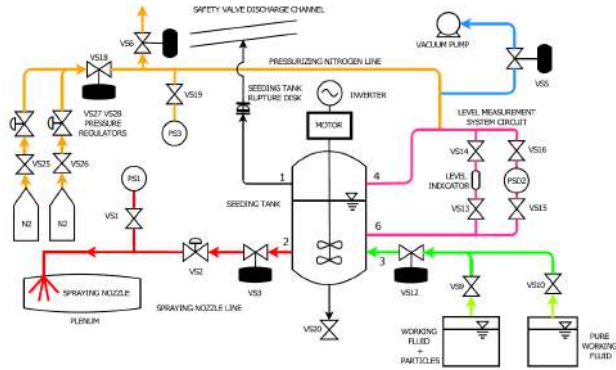


Figure 5: Sketch of the seeding system

into account, TiO₂ resulted to be the most suitable material. The other materials have a much lower refractive index (SiO₂ and Al₂O₃), or being very hard can scratch the quartz windows more easily (SiC). Nanosized TiO₂ powder, with clusters diameter in the range 150 – 250 nm, satisfies the constraint on Stokes number ($St \ll 1$). The analysis on the dynamic response of nanosized TiO₂ particles is reported in [20, 21].

2.2.2 Seeding system

To inject the seeding we resort to the use of a liquid suspension of TiO₂ powder, where the liquid is the same fluid used in the wind tunnel. The TiO₂ powder is dried in an oven at $T > 100$ °C for at least one hour before being dispersed in the liquid, to avoid moisture contamination. The liquid suspension is put in a tank, 2.2.2, and pressurized with nitrogen at about 9 bar above the maximum stagnation pressure of the test. As shown in 2.2.2, two vertical axis blade impellers actuated by an electrical motor are located inside the tank. The impellers rotation creates an intense flow re-circulation preventing the seeding to settle down and keeping the liquid suspension homogeneous. The impeller stirring device performs much better than the mixing nozzle used in our previous design [20]. When the test starts, the valve VS3 in 2.2.2 is opened and the liquid suspension is forced by pressure to the atomizing nozzle located in the section ahead of the nozzle inlet, see Figure (1) and 2.2.2. A full cone nozzle atomizer is used. Since the surrounding fluid is in super-heated vapour (or supercritical) conditions, the spray evaporates leaving the solid particles free to follow the flow. The sketch of the seeding system layout is shown 2.2.2.

The mass of powder required for the liquid suspension is estimated by considering the need to have no more than one particles in the LDV measurement volume. By imposing a probability of 0.5% that two or more particles are in the measurement volume at the same time, the maximum particle concentration, n_p , in the measure-

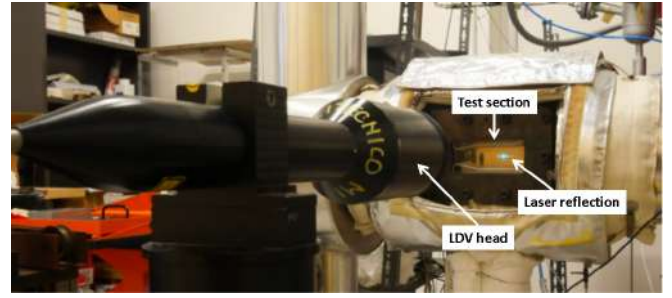


Figure 6: LDV head and tests section

ment volume, V_m , is computed as [17]

$$n_p = \frac{0.1}{V_m}; \quad (1)$$

Using Eq. (1), the local particle flow rate is $N_p = 0.1\dot{V}_f/V_m$, where \dot{V}_f is the volumetric flow rate at the measurement section. Eventually, the required mass of seeding m_p is computed as $m_p = \frac{4}{3}\pi d_p^3 \rho_p \frac{0.1}{V_m} \dot{V}_f \Delta t$ where Δt is the total measurement time. Actually not all the seeding particles reach the measurements location, thus the optimum values of m_p needs to be found from empirical observation of data rate and signal quality. The amount of liquid needed for the suspension depends on the atomizing nozzle and on pressure drop imposed across it, thus it has to be adjusted according to the set-up and the operating conditions. In any case, it is recommended to keep its quantity as small as possible so to minimize any influence the liquid spray can have on flow conditions.

2.2.3 LDV system

To avoid the burden of using a separate receiving optics, which would pose significant alignment issues, the LDV system operates in the back-scatter mode. The LDV uses two Diode Pumped Solid State (DPSS) lasers, each having a maximum output power of 1 W. The lasers wavelength are $\lambda = 513.9$ nm and $\lambda = 489.5$ nm. Both laser beams have a diameter of about $d_{lb} = 1$ mm. The latter are input to a Dantec Fiberflow transmission system, where a Bragg cell acts as a beam splitter and as a 40 MHz frequency shifter. Fiber-optic transmits the two frequency-shifted couples of laser beams from the Fiberflow to the LDV head. The light scattered by the particle is collected by the LDV head and sent to the photo multiplier via a fiber-optic.

The LDV head, Figure (6), is composed by a beam expander (expander ratio of about 1.87) and a frontal lens of focal length $f = 310$ mm and about 80 mm diameter. Each couple of laser beams intersect with a semi-angle of about $\theta/2 = 6.5^\circ$, resulting in a measurement volume of about 0.006 mm³, Table (2). The LDV head is mounted on a XY manual translation stage to allow the accurate positioning of the measurement volume on the channel axis.

Doppler signals are analysed by a Burst Spectrum Analyzer (Dantec Dynamics BSA F800) controlled via a USB connection by a PC. Instantaneous velocities, Doppler burst signals, data rate and burst validation percentage are some of the information provided by the BSA. This allows to promptly identify measurements issues during the test, and if needed to stop the test. A single TTL signal is used to trigger both the BSA system and the pressures and temperatures acquisition system,

Table 2: Computed optical specifications of the LDV probe volume (in air)

Optical Parameters			units
Focal length, f	310	310	mm
Wavelengths, λ	513.9	489.5	nm
Beam intersection angle, θ	0.23	0.23	rad
Measuring volume diameter	0.109	0.104	mm
Measuring volume length	≈ 1	≈ 1	mm
Measuring volume, V_m	0.006	0.005	mm ³
Fringe distance	2.24	2.13	μm
Fringe number	48	48	

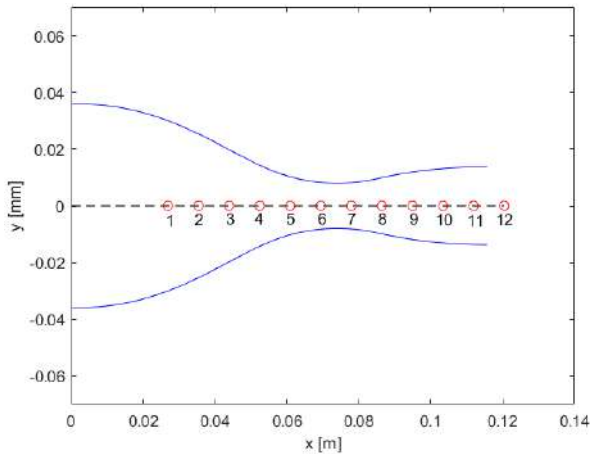


Figure 7: Sketch of the 2D convergent-divergent nozzle, red circles show the locations of pressure taps

to allow all measurements to be easily re-aligned in time and correctly compared.

When dealing with high speed flow, the optical configuration of the LDV head has to ensure a maximum Doppler frequencies below the maximum value accepted by the Burst Spectrum Analyzer, $f_{D,\max}$. The constraint is satisfied if the angle between the two laser beams is below the value θ_{\max} given by Eq. (2), where V is the maximum expected flow velocity.

$$\frac{1}{2}\theta_{\max} = \arcsin\left(\frac{\lambda}{2V}f_{D,\max}\right) \quad (2)$$

In the present case, BSA specifications gives $f_{D,\max} = 200$ MHz (Dantec Dynamics BSA F800), while $V \approx 300$ m/s and $\lambda = 513.9$ nm. Thus, from Eq. (2) we get $\theta_{\max}/2 \approx 9^\circ$, corresponding to a minimum usable focal length $f = 200$ mm. We chose a lens having $f = 310$ mm because besides satisfying the above constraint, it also allows a suitable space between the hot test section and the LDV head.

The probe volume generated by the 310 mm is about 1 mm in length, the short length size greatly reduce the amount of laser light picked up by the LDV head due to beam reflection at the metallic rear plate, Figure (6). More details about the optical specifications of the probe volume are shown in Table (2).

2.2.4 LDV measurements

Velocity measurements have been performed on different channel geometries (2D Convergent-Divergent nozzle and 2D subsonic straight channels) using MM as a working fluid; here just one example of velocity measurements

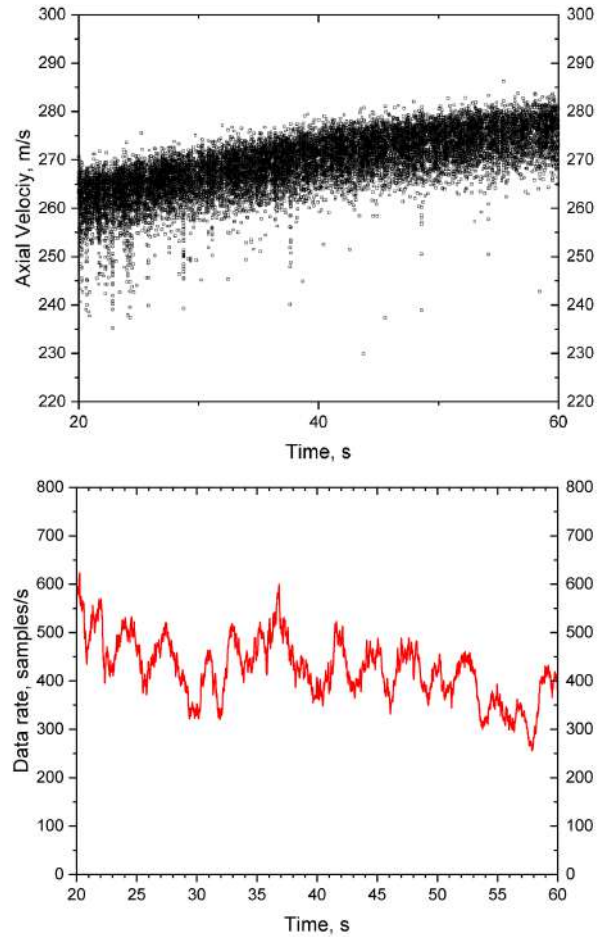


Figure 8: Top: measured axial velocity. Bottom: LDV data rate, moving average ~ 1 s window

taken in the 2D supersonic converging diverging nozzle is reported, Figure (7). The LDV measurement volume was located in the symmetry plane of the 2D channels, and in front of the pressure tap 11 shown in Figure (7), i.e. at axial location close to the nozzle exit.

Using a laser power of about 150 mW, the data rate (mean over 1 s) varied between about 5 kHz and 0.2 kHz decreasing during the tests, see Figure (8)(b), while data validation was always above 95%. At the beginning of the test we measured $P_T \approx 8.4$ bar and $T_T \approx 207$ °C. Being a blow-down wind tunnel, the total pressure decreases significantly during the test. On the other side, due to the high molecular complexity of MM, the total temperature changes only slightly. The total compressibility factor Z_T increases from about 0.75 to a value close to 1 [21]. Thus, the thermodynamic conditions of the flow moves away from the non-ideal region and approaches the ideal gas region as the test proceeds. As an example only velocities measured during the time interval between 20 s to 60 s from the start of the test are shown in Figure (8)(a). The axial velocity clearly increases from about 260 m/s to about 275 m/s, Figure (8). This behaviour can be attributed to the increase of Z_T and it is an indication of the non-ideality of the flow. Moreover, LDV measurements were compared to velocity estimated using the static pressure at pressure tap 11, not reported here, resulting in good agreement between each other [21]. This result further support the validity of the design of the LDV system.

3 Conclusions

Optical techniques such as Schlieren and Laser Doppler Velocimetry (LDV) are valuable tools to investigate compressible flows thanks to their ability to provide information about density gradients, Mach number and flow velocity. Nevertheless, to the authors knowledge, example of their application to fluid flows featuring non-ideal behaviour close to saturation and critical point, or within the supercritical region, are currently not available.

The present paper reported for the first time on the use of Schlieren and Laser Doppler Velocimetry (LDV) techniques to measure non-ideal compressible-fluid flows. All measurements were carried out within the blow-down TROVA facility at Politecnico di Milano. Peculiar aspects of the design and implementation are described. Measurement are reported including Mach number measurements along the nozzle axis and velocity measurements in highly non-ideal conditions.

Acknowledgment

This research is supported by ERC Consolidator Grant N. 617603, Project NSHOCK, funded under the FP7-IDEAS-ERC scheme.

References

- [1] M. Cramer, “Nonclassical dynamics of classical gases,” in *Nonlinear waves in real fluids*, pp. 91–145, Springer, 1991.
- [2] P. A. Thompson, “A fundamental derivative in gas-dynamics,” *The Physics of Fluids*, vol. 14, no. 9, pp. 1843–1849, 1971.
- [3] A. Kluwick, “Rarefaction shocks,” in *Handbook of shock waves*, pp. 339–411, Elsevier, 2001.
- [4] A. Guardone, P. Colonna, E. Casati, and E. Rinaldi, “Non-classical gas dynamics of vapour mixtures,” *Journal of fluid mechanics*, vol. 741, pp. 681–701, 2014.
- [5] A. Spinelli, V. Dossena, P. Gaetani, C. Osnaghi, and D. Colombo, “Design of a test rig for organic vapours,” in *ASME Turbo Expo 2010: Power for Land, Sea, and Air*, pp. 109–120, American Society of Mechanical Engineers Digital Collection, 2010.
- [6] A. Spinelli, M. Pini, V. Dossena, P. Gaetani, and F. Casella, “Design, simulation, and construction of a test rig for organic vapors,” *Journal of engineering for gas turbines and power*, vol. 135, no. 4, 2013.
- [7] A. Spinelli, F. Cozzi, V. Dossena, P. Gaetani, M. Zocca, and A. Guardone, “Experimental investigation of a non-ideal expansion flow of siloxane vapor mdm,” in *ASME Turbo Expo 2016: Turbomachinery Technical Conference and Exposition*, American Society of Mechanical Engineers Digital Collection, 2016.
- [8] A. Spinelli, G. Cammi, M. Zocca, S. Gallarini, F. Cozzi, P. Gaetani, V. Dossena, and A. Guardone, “Experimental observation of non-ideal expanding flows of siloxane mdm vapor for orc applications,” *Energy Procedia*, vol. 129, pp. 1125–1132, 2017.
- [9] A. Spinelli, G. Cammi, S. Gallarini, M. Zocca, F. Cozzi, P. Gaetani, V. Dossena, and A. Guardone, “Experimental evidence of non-ideal compressible effects in expanding flow of a high molecular complexity vapor,” *Experiments in Fluids*, vol. 59, no. 8, p. 126, 2018.
- [10] A. Spinelli, G. Cammi, C. C. Conti, S. Gallarini, M. Zocca, F. Cozzi, P. Gaetani, V. Dossena, and A. Guardone, “Experimental observation and thermodynamic modeling of non-ideal expanding flows of siloxane mdm for orc applications,” *Energy*, vol. 168, pp. 285–294, 2019.
- [11] M. Zocca, A. Guardone, G. Cammi, F. Cozzi, and A. Spinelli, “Experimental observation of oblique shock waves in steady non-ideal flows,” *Experiments in Fluids*, vol. 60, no. 6, p. 101, 2019.
- [12] A. Guardone, A. Spinelli, and V. Dossena, “Influence of molecular complexity on nozzle design for an organic vapor wind tunnel,” *Journal of engineering for gas turbines and power*, vol. 135, no. 4, 2013.
- [13] F. Cozzi, E. Göttlich, L. Angelucci, V. Dossena, and A. Guardone, “Development of a background-oriented schlieren technique with telecentric lenses for supersonic flow,” in *Journal of Physics: Conference Series*, vol. 778, p. 012006, IOP Publishing, 2017.
- [14] C. C. Conti, A. Spinelli, G. Cammi, M. Zocca, F. Cozzi, and A. Guardone, “Schlieren visualizations of non-ideal compressible fluid flows,” in *13th International Conference on Heat Transfer, Fluid Mechanics and Thermodynamics (HEFAT 2017)*, pp. 513–518, EDAS, 2017.
- [15] W. Mair, “The sensitivity and range required in a toepler schlieren apparatus for photography of high-speed air flow,” *The Aeronautical Quarterly*, vol. 4, no. 1, pp. 19–50, 1954.
- [16] G. Cammi, *Measurements techniques for non-ideal compressible fluid flows: applications to organic fluids*. PhD thesis, Politecnico di Milano, 2019.
- [17] H.-E. Albrecht, N. Damaschke, M. Borys, and C. Tropea, *Laser Doppler and phase Doppler measurement techniques*. Springer Science & Business Media, 2013.
- [18] R. Mei, “Velocity fidelity of flow tracer particles,” *Experiments in fluids*, vol. 22, no. 1, pp. 1–13, 1996.
- [19] A. Melling, “Tracer particles and seeding for particle image velocimetry,” *Measurement science and technology*, vol. 8, no. 12, p. 1406, 1997.
- [20] S. Gallarini, A. Spinelli, F. Cozzi, and A. Guardone, “Design and commissioning of a laser doppler velocimetry seeding system for non-ideal fluid flows,” 12th International Conference on Heat Transfer, Fluid Mechanics and Thermodynamics, HEFAT, 2016.
- [21] S. Gallarini, *High Temperature non-ideal compressible-fluid flows of siloxane*. PhD thesis, Politecnico di Milano, 2020.

OBITUARY

Professor José Manuel Redondo Apraiz passed away on July 14, 2020, in Barcelona at the age of 64. He was a full professor at the Universitat Politècnica de Catalunya (UPC) - BarcelonaTech and a faculty member in the Physics department. We at ERCOFTAC are very saddened about this loss as Jose was a very active and much liked member of our research community. He chaired SIG 14 on Stably Stratified and Rotating Turbulence and organized many ERCOFTAC events, including some in Barcelona and Vilanova, his home town, and he participated regularly in our ERCOFTAC committee meetings and enlivened these through his presence and contributions in his very unique way.

Professor Redondo, who obtained a Master degree in Physics and a PhD in Applied Mathematics from Cambridge University, was a prominent and active supporter of the theory of turbulence and is well known for his contributions in the field of "Turbulent Mixing in Geophysical Flows". He has supervised 12 doctoral theses and published 93 journal papers and 9 books as well as 35 book chapters, among many other scientific and technical publications. In the mentioned field he brought together at conferences and later also at summer schools on "Transport Processes in the Atmosphere and Ocean" representatives of various research directions developed in Europe, North and South America, Japan, countries of Eastern Europe, and Russia. His tolerance, friendliness, and enthusiasm have fostered vivid discussions, friendships and the formation of new international research groups, some of which are still active and successful. The ideas and forms of "Turbulent Mixing" conferences continue to develop successfully in a wide range of sciences, including the physics of controlled thermonuclear fusion and infraslow diffusion induced flows. Particularly noteworthy are the efforts of Professor Redondo to support scientific research in Russia with his own participation in conferences there and by inviting researchers to work in Western universities, as well as by giving the assistance in finding and applying to international grants. Further, in the last 10 years, Professor Redondo served our community by being in charge of Turbulence, Transport and Diffusion sessions in the division of Nonlinear Processes in Geosciences at the European Geoscience Union (EGU).

Some of us remember Jose Manuel from his days in DAMTP (Department of Applied Mathematics and Theoretical Physics), Cambridge, from around the mid-1980's to the 1990's, that is about 35 years ago. His PhD supervisor was Paul Linden. He played a fulsome part in the academic and community life at DAMTP; he was very inquisitive, always asking questions especially at the acclaimed Batchelor Departmental Fluid Mechanics seminars on Friday late afternoons. He was friendly and approachable, and conversations with him were punctuated with deep fruity bursts of laughter, which later also enlivened the ERCOFTAC gatherings and which, in fact,



Professor Redondo

became his trademark throughout his life. He loved traveling in Europe; he attended numerous conferences and meetings – London, Cambridge, Vienna, Paris, Lyon, Gdansk, the list is endless – and almost always arrived in his own car. He possessed a strong physique, and was a strong swimmer of professional quality – he missed representing Spain in the Olympics by just 0.1 seconds (perhaps less)! He once mentioned that his ambition was to snatch the world record in the 50's age group and he combined his passion about science with his passion about swimming, doing research about turbulence when swimming. José was much loved and respected by all his friends around the world and, especially, by his numerous friends at DAMTP – we all will miss him sorely. Everyone who met him will never forget his personality and proactivity, his energy which transmits and pushes to keep acting, and his great social abilities.

His loss is a great one for the ERCOFTAC and EGU communities, where he leaves a large number of friends, for the Physics department of UPC, and UPC as a whole, where he leaves a lot of colleagues and co-workers, and specially for his family to which we express our sincere condolences and deepest sympathy.

J. Pons-Prats

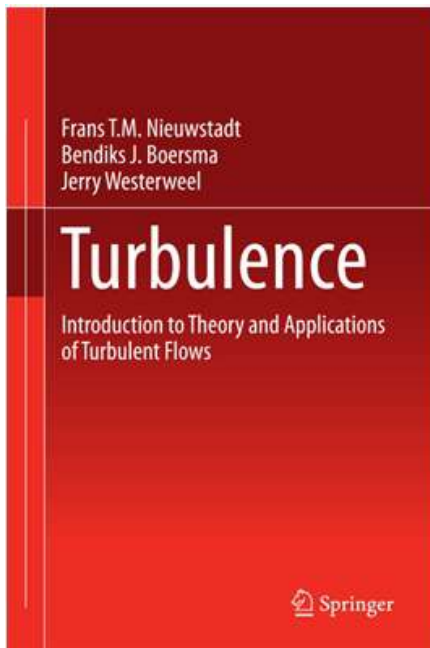
*On behalf of ERCOFTAC's Executive Committee
with contributions from friends and colleagues of
José Redondo.*

Recommended literature

TURBULENCE

Introduction to Theory and Applications of Turbulent Flows

Frans T.M. Nieuwstadt, Bendiks J. Boersma, Jerry Westerweel

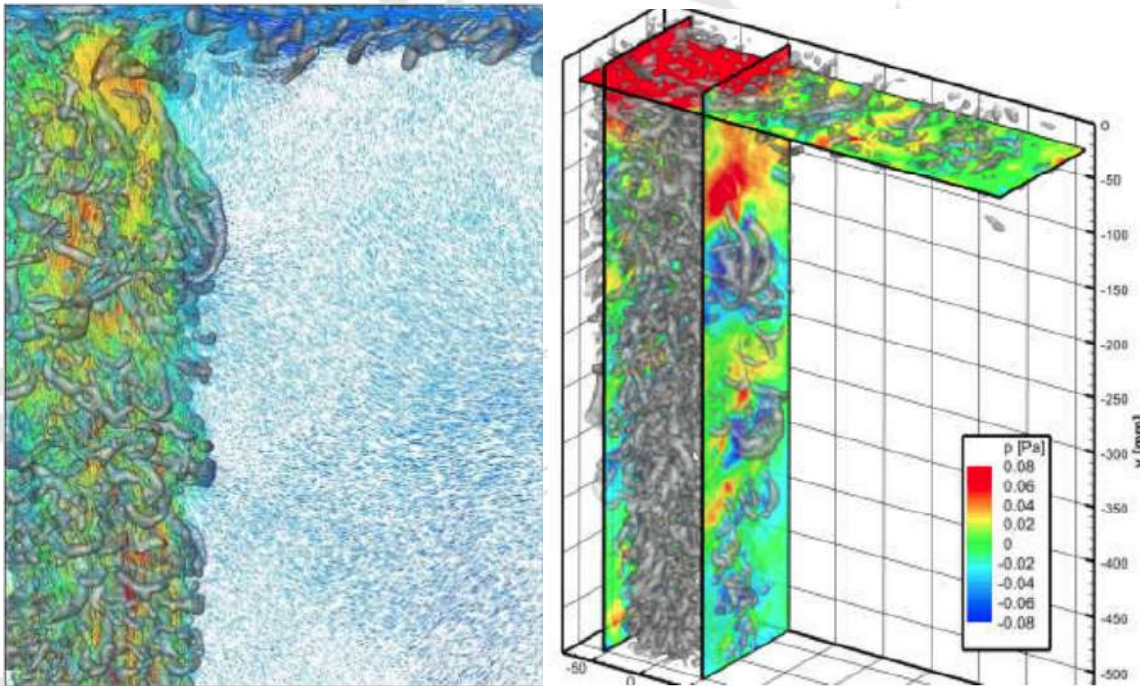


- **Winner of the 2017 Most Promising New Textbook Award from the Textbook & Academic Authors Association**
- Proven to be an excellent course-text over many years
- Combines theory with practical applications
- Avoids lengthy mathematical descriptions

This book provides a general introduction to the topic of turbulent flows. Apart from classical topics in turbulence, attention is also paid to modern topics. After studying this work, the reader will have the basic knowledge to follow current topics on turbulence in scientific literature. The theory is illustrated with a number of examples of applications, such as closure models, numerical simulations and turbulent diffusion, and experimental findings. The work also contains a number of illustrative exercises

3rd Workshop and 1st Challenge on Data Assimilation & CFD Processing for PIV and Lagrangian Particle Tracking

Online workshop on Thursday-Friday
19-20 November 2020



General

We would like to draw your attention to this online workshop that is scheduled for November 19-20, 2020. Recently several data assimilation (DA) methods have been developed at the junction between experimental and numerical fluid mechanics and aerodynamics. DA allows increasing the spatial and temporal resolution of sparse measurement data and calculating and extracting physical meaningful content like pressure fields, coherent structures or periodic flow features for a better insight into the flow dynamics. We assume you might be interested in participating, sharing your views, experience and of course latest research results within a relatively small and focused community.

Scope

Many procedures are nowadays available that increase or enhance the information measured with Particle Image Velocimetry (PIV) or Lagrangian Particle Tracking (LPT) using techniques imported from the CFD and applied mathematics community. The advent of time-resolved and volumetric measurements have multiplied the possibilities with much excitement of PIV and LPT development researchers as well as from the applied fluid mechanics community. The methods range from regularization strategies using the (simplified) Navier-Stokes-equation or the use of the momentum equation to obtain pressure from velocity and acceleration measurements, machine learning, to variational data-assimilation frameworks using adjoint CFD.

Visit: <http://cfdforpiv.dlr.de/>



ANIMATE - Advanced Numerical Modelling and Experimental Research on Turbulent and Transitional Flows with Applications to Chemical, Power, Automotive and Aeroengine Industries October 2019 - September 2021

A. Boguslawski, R. Gnatowska, W. Elsner, A. Tyliczszak, D. Asendrych
Department of Thermal Machinery, Czestochowa University of Technology

The Department of Thermal Machinery, Czestochowa University of Technology initiated in 2019 year an international cooperation within the ANIMATE project. The project is funded by THE POLISH NATIONAL AGENCY FOR ACADEMIC EXCHANGE - NAWA within an International Academic Partnerships Programme. The objective of the Programme is to develop durable solutions in the area of scientific, implementation and teaching process cooperation, pursued within the framework of international academic partnerships. The results of the project should provide a foundation for the development of a long-lasting cooperation of Universities or Research Centers forming a Partnership. Projects implemented under the Programme shall be in line with a long-term development policy of an Applicant and Partners. Turbulent and transitional flows in laboratory and industrial cases have been in a focus of research at Czestochowa University of Technology for more than 50 years. The main goal of the ANIMATE project is to strengthen an international cooperation with partners with whom the project coordinator cooperated already within European or bilateral projects. It is expected that partners' knowledge and experience in the field of turbulent flows will influence the level and scope of the research at Czestochowa University of Technology. The project is aimed also at an intensification of knowledge transfer to industrial partners and preparation of the research project of common academic-industrial institutions in a variety of industrial branches. The partners deliver complementary competences covering advanced modelling of turbulent flows, boundary layers, reactive and multiphase flows, high performance computing and experimental techniques. The goals of the project will be attained through an exchange of academic staff and PhD students concentrated around common research tasks with the use of computer codes, computer resources and experimental facilities of all the research groups involved in the project.

The cooperation is foreseen within the following tasks:

- Task no. 1 - Modelling and High Performance computing for turbulent reactive flows
- Task no. 2 - Development of new methods for multiphase flows investigations
- Task no. 3 Experimental and numerical studies of near wall flows

Six outstanding academic partners accepted the invitation to this project:

1. Institut National des Sciences Appliquées de Rouen Normandie, France, (Prof. Luc Vervish)
2. Centre Europeen de Recherche et de Formation Avance en Calcul Scientifique-CERFACS), France, (Prof. Laurent Gicquel),
3. University of Twente (UT), The Netherlands, (Prof. Bernard Geurts),
4. University of Coimbra (UC), Portugal, (Prof. Maria G. Rasteiro, Prof. Pedro Faia)
5. Royal Institute of Technology (KTH), Sweden, (Prof. Philipp Schlatter)
6. Institute of Thermomechanics, Academy of Science of Czech Republic (IT AS CR), (Prof. Vaclav Uruba).

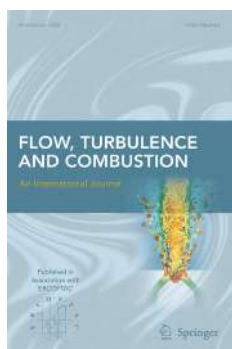
ERCOFTAC Workshops and Summer Schools

ERCOFTAC Workshops, Conferences – 2020, 2021

Title	Location	Date	Coordinators	Organiser
Multiscale and directional approach to single-phase and two-phase flows	France	1/10/2020	Carbon, C. Gorokhovski, M. Casciola, C. M.	SIGs 35, 39, 50, Henry Bénard PC
CFD for Dispersed Multi-Phase Flows 2020 with Problem Shooting Session	Rome, Italy	5-6/10/2020	Sommerfeld, M.	SIG 12
15th International SPHERIC Workshop	Newark, USA	8-10/06/2021	Tafuni, A. Rogers, B.	SIG 40
3rd Workshop and Challenge on Data Assimilation & CFD Processing for PIV and Lagrangian Particle Tracking	Paris, France	19-20/11/2020	Schröder, A. Leclaire, B. Sciacchitano, A.	SIG 32
3rd International Seminar on Non-Ideal Compressible-Fluid Dynamics for Propulsion & Power (NICFD 2020)	Delft, The Netherlands	29-30/10/2020	Pini, M.	SIG 49, 51
Reconstruction methods for complex flows and porous media	Sheffield, UK	?/?/2021	Yi Li	SIG 42, 14

ERCOFTAC Summer Schools, Courses – 2020, 2021

Title	Location	Date	Coordinators	Organiser
2nd International School on Hemophysiscs	Montpellier, France	06-09/10/2020	Nicoud, F. Abkarian, M. Mendez, S.	SIG 37
Course on Particle Image Velocimetry	Delft, Netherlands	12-16/10/2020	Sciacchitano, A.	SIG 32
Fluids under Control	Prague, Czech	23–27/08/2021	Bodnar, T.	PC Czech



RECENT TABLE OF CONTENTS OF FLOW TURBULENCE AND COMBUSTION

AN INTERNATIONAL JOURNAL PUBLISHED BY SPRINGER
IN ASSOCIATION WITH ERCOFTAC

EDITOR-IN-CHIEF: M. A. LESCHZINER, A. M. KEMPF

EDITORS: A. DREIZLER, K. FUKAGATA, E. GUTMARK, S. MENON, W. RODI, R. SANDBERG, T. SCHULLER AND B. VAN WACHEM

VOLUME 105, NUMBER 2, AUGUST 2020

Special Issue: Progress in Direct and Large Eddy Simulation

Guest Editors: Manuel García-Villalba, Hans Kuerten, Maria Vittoria Salvetti

A weakly Compressible, Diffuse-Interface Model for Two-Phase Flows

A. Kajzer, J. Pozorski

A Novel Approach for Direct Numerical Simulation of Hydraulic Fracture Problems

F. Dalla Barba, F. Picano

A-Priori Assessment of Interfacial Sub-grid Scale Closures in the Two-Phase Flow LES Context

J. Hasslberger, S. Ketterl, M. Klein

A Priori Assessment of Subgrid-Scale Models and Numerical Error in Forced Convective Flow at High Prandtl Numbers

L. Sufriá, H. Steiner

On a Proper Tensor-Diffusivity Model for Large-Eddy Simulation of Buoyancy-Drive Turbulence

F.X. Trias, F. Dabbagh, A. Gorobets, C. Oliet

Enabling Adaptive Mesh Refinement for Spectral-Element Simulations of Turbulence Around Wing Sections

Á. Tanarro, F. Mallor, N. Offermans, A. Peplinski, R. Vinuesa, P. Schlatter

A *p*-adaptive Matrix-Free Discontinuous Galerkin Method for the Implicit LES of Incompressible Transitional Flows

F. Bassi, L. Botti, A. Colombo, A. Crivellini, M. Franciolini, A. Ghidoni, G. Noventa

LES of Turbulent Co-current Taylor Bubble Flow

E.M.A. Frederix, E.M.J. Komen, I. Tiselj, B. MikuÅ

Nanoparticle Formation and Behavior in Turbulent Spray Flames Investigated by DNS

A. Abdelsamie, F.E. Kruis, H. Wiggers, D. Thévenin

DNS of an Oblique Jet in a Particle-Laden Crossflow: Study of Solid Phase Preferential Concentration and Particle-Wall Interaction

G. Agati, D. Borello, G. Camerlengo, F. Rispoli, J. Sesterhenn

Influence of Concentration on Sedimentation of a Dense Suspension in a Viscous Fluid

T. Shajahan, W.-P. Breugem

Numerical Investigation of High-Speed Turbulent Boundary Layers of Dense Gases

L. Sciacovelli, X. Gloerfelt, D. Passiatore, P. Cinnella, F. Grasso

Consistent Flow Structure Evolution in Accelerating Flow Through Hexagonal SpherePack

Y. Sakai, M. Manhart

Effects of the Actuation on the Boundary Layer of an Airfoil at Reynolds Number $Re = 60000$

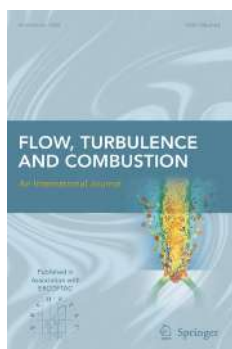
I. Rodriguez, O. Lehmkuhl, R. Borrell

Large Eddy Simulations of Rough Turbulent Channel Flows Bounded by Irregular Roughness: Advances Toward a Universal Roughness Correlation

M. De Marchis, D. Saccone, B. Milici, E. Napoli

Shock-Wave/Boundary-Layer Interactions in Transitional Rectangular Duct Flows

D.J. Lusher, N.D. Sandham



RECENT TABLE OF CONTENTS OF FLOW TURBULENCE AND COMBUSTION

AN INTERNATIONAL JOURNAL PUBLISHED BY SPRINGER
IN ASSOCIATION WITH ERCOFTAC

EDITOR-IN-CHIEF: M. A. LESCHZINER, A. KEMPF

EDITORS: A. DREIZLER, K. FUKAGATA, E. GUTMARK, S. MENON, W. RODI, R. SANDBERG, T. SCHULLER AND B. VAN WACHEM

VOLUME 105, NUMBER 3, SEPTEMBER 2020

Modified Formulation of Laminar Kinetic Energy Transition Models by Means of Elastic-Net of a Big Experimental Database of Separated Flows

S. Daniele, B. Dario, D. Matteo, L. Davide, Y. Vianney

Dynamic Mode Decomposition Analysis of High-Fidelity CFD Simulations of the Sinus Ventilation

H. Calmet, D. Pastrana, O. Lehmkuhl, T. Yamamoto, Y. Kobayashi, K. Tomoda, G. Houzeaux, M. Vázquez

Momentum Diffusion Near Jet Exit in a Round Jet Controlled by Half Delta-Wing Tabs

Y. Ito, K. Naganawa, Y. Sakai, K. Iwano

Aerodynamic Effects of Uniform Blowing and Suction on a NACA4412 Airfoil

M. Atzori, R. Vinuesa, G. Fahland, A. Stroh, D. Gatti, B. Frohnafel, P. Schlatter

Aerodynamic Effects as a Maglev Train Passes Through a Noise Barrier

C. Luo, D. Zhou, G. Chen, S. Krajnovic, J. Sheridan

Effect of Pressure on Hydrogen Enriched Natural Gas Jet Flames in Crossflow

P. Saini, I. Chtere, J. Pareja, M. Aigner, I. Boxx

Study of a Flame Kernel Evolution in a Turbulent Mixing Layer Using LES with a Laminar Chemistry Model

A. Wawrzak, A. Tyliszczak

The Eulerian Stochastic Fields Method Applied to Large Eddy Simulations of a Piloted Flame with Inhomogeneous Inlet

M. Hansinger, T. Zirwes, J. Zips, M. Pfitzner, F. Zhang, P. Habisreuther, H. Bockhorn

Analysis of the Closures of Sub-grid Scale Variance of Reaction Progress Variable for Turbulent Bunsen Burner Flames at Different Pressure Levels

F.B. Keil, N. Chakraborty, M. Klein

Assessment of Droplet Breakup Models for Spray Flow Simulations

C. Sula, H. Grosshans, M.V. Papalexandris

A Computational Investigation of the Effects of Particle Diameter and Particle-Particle Interactions on Jet Penetration Characteristics in a Gas-Solid Fluidized Bed with a Central Jet

J. Handique, S. Kotoky

Further articles can be found at www.springerlink.com

Abstracted/Indexed in Science Citation Index, Science Citation Index Expanded (SciSearch), Journal Citation Reports/Science Edition, SCOPUS, INSPEC, Chemical Abstracts Service (CAS), Google Scholar, EBSCO, CSA, ProQuest, Academic OneFile, ASFA, Current Abstracts, Current Contents/Engineering, Computing and Technology, Earthquake Engineering Abstracts, EI Encompass, Ei Page One, Ei-Compendex, EnCompassLit, Engineered Materials Abstracts, Gale, OCLC, PASCAL, SCImago, STMA-Z, Summon by Serial Solutions, VINITI - Russian Academy of Science.

Instructions for Authors for Flow Turbulence Combust are available at <http://www.springer.com/10494>.

ERCOFTAC Special Interest Groups

1. Large Eddy Simulation

Salvetti, M.V.
University of Pisa, Italy.
Tel: +39 050 221 7262
mv.salvetti@ing.unipi.it

4. Turbulence in Compressible Flows

Dussauge, Jean-Paul
IUSTI, Marseille
jean-paul.dussauge
@polytech.univmrs.fr

5. Environmental Fluid Mechanics

Armenio, V.
Universit di Trieste, Italy
Tel: +39 040 558 3472
armenio@dica.units.it

10. Transition Modelling

Dick, E.
University of Ghent, Belgium
Tel: +32 926 433 01
erik.dick@ugent.be

12. Dispersed Turbulent

Two Phase Flows
Sommerfeld, M.
University of Magdeburg, Germany
Tel: +49 345 552 3680
martin.sommerfeld@ovgu.de

14. Stably Stratified and Rotating Flows

Redondo, J.M.
UPC, Spain
Tel: +34 934 017 984
redondo@fa.upc.edu

15. Turbulence Modelling

Jakirlic, S.
Darmstadt University of Technology,
Germany
Tel: +49 615 116 3554
s.jakirlic@sla.tu-darmstadt.de

20. Drag Reduction and Flow Control

Choi, K-S.
University of Nottingham, England
Tel: +44 115 951 3792
kwing-so.choi@nottingham.ac.uk

28. Reactive Flows

Roekaerts, D.
Delft University of Technology,
The Netherlands.
Tel: +31 152 782 470
D.J.E.M.Roekaerts@tudelft.nl

32. Particle Image Velocimetry

Scarano, F., Sciacchitano, A.
Delft University of Technology,
The Netherlands.
F.Scarano@tudelft.nl
A.Sciacchitano@tudelft.nl

33. Transition Mechanisms, Prediction and Control

Hanifi, A.
FOI, Sweden
Tel: +46 855 503 197
ardeshir.hanifi@foi.se

34. Design Optimisation

Giannakoglou, K.
NTUA, Greece
Tel: +30 210 772 1636
kgianna@central.ntua.gr

35. Multipoint Turbulence Structure and Modelling

Cambon, C.
ECL Ecully, France.
Tel: +33 472 186 161
claude.cambon@ec-lyon.fr

36. Swirling Flows

Braza, M.
IMFT, France
Tel: +33 (0) 561 285 839
braza@imft.fr

37. Bio-Fluid Mechanics

Nicoud, F.
Université de Montpellier, France
franck.nicoud@umontpellier.fr

39. Aeroacoustics

Bailly, C.
Ecole Centrale de Lyon, France
Tel: +33 472 186 014
christophe.bailly@ec-lyon.fr

40. Smoothed Particle Hydrodynamics

Rogers, B. D.
University of Manchester, UK
Tel: +44 (0) 161 306 6000
Benedict.Rogers@manchester.ac.uk

41. Fluid Structure Interaction

Braza, M.
IMFT, France
Tel: +33 (0) 561 285 839
marianna.braza@imft.fr
Lacazedieu, E.
EDF R&D, France
Tel: +33 (1) 30 87 80 87
elisabeth.lacazedieu@edf.fr

42. Synthetic Models in Turbulence

Nowakowski, A.
University of Sheffield, England
Tel: +44 114 222 7812
a.f.nowakowski@sheffield.ac.uk

43. Fibre Suspension Flows

Lundell, F.
The Royal Institute of Technology,
Sweden
Tel: +46 87 906 875
fredrik@mech.kth.se

44. Multiscale-generated Turbulent Flows

Fortune, V.
Université Pierre et Marie Curie, France
Tel: +33 549 454 044
veronique.fortune
@lea.univ-poitiers.fr

45. Uncertainty Quantification in Industrial Analysis and Design

Lucor, D.
d'Alembert Institute, France
Tel: +33 (0) 144 275 472
didier.lucor@upmc.fr

46. Oil, Gas and Petroleum

Sommerfeld, M.
Otto von Guericke-Universität
Germany
martin.sommerfeld@ovgu.de
Khanna, S.
BP Global, USA

47. 3D Wakes

Morrison, J.F.
Imperial College, London
Tel: +44 (0) 20 7594 5067
j.morrison@imperial.ac.uk
Cadot, O.
ENSTA Paris Tech,
Université Paris-Saclay
Tel: +33 (0) 16 931 9756
cadot@ensta.fr

48. Respiratory Aerosols

Kassinis, S.
University of Cyprus
kassinis@ucy.ac.cy
Sznitman, J.
Biofluids Laboratory, Israel
sznitman@bm.technion.ac.il

49. Non-Ideal Comp. Fluid Dynamics

Guardone, A.
Politecnico di Milano, Italy
alberto.guardone@polimi.it
Pini, M.
Delft University of Technology,
The Netherlands
M.Pini@tudelft.nl

50. GeoAstro

Marino, R.
CNRS/École Centrale de Lyon,
France
raffaele.marino@ec-lyon.fr

51. High-Pressure & Compressible Combustion

di Mare, F.
University Bochum, Germany
Francesca.dimare@rub.de

ERCOFTAC Pilot Centres

Alpe - Danube - Adria

Steiner, H.
Inst. Strömungslehre and
Wärmeübertragung
TU Graz, Austria
kristof@ara.bme.hu

Belgium

Hillewaert, K.
Bâtiment Eole,
6041 Gosselies,
Belgium.
Tel: +32 71 910 942
Fax: +32 495 385 030
koen.hillewaert@cenaero.be

Brasil

Rodriguez, O.
Department of Mechanical Engineering,
Sao Carlos School of Mechanical
Engineering,
Universidade de Sao Paulo,
Brasil.
oscarmhr@sc.usp.br

Czech Republic

Bodnar, T.
Institute of Thermomechanics AS CR,
5 Dolejskova,
CZ-18200 Praha 8,
Czech Republic.
Tel: +420 224 357 548
Fax: +420 224 920 677
bodnar@marian.fsik.cvut.cz

Iberia

Onate, E.
Universitat Politenica de Catalunya,
Valero, E.
Universidad Politécnica de Madrid,
Spain.
onate@cimne.upc.edu
eusebio.valero@upm.es

France South

Braza, M.
IMF Toulouse,
CNRS UMR - 5502,
Allée du Prof. Camille Soula 1,
F-31400 Toulouse Cedex, France.
Tel: +33 534 322 839
Fax: +33 534 322 992
Braza@imft.fr

France West

Hadjadj, A.
Tel: +33 232 959 794
hadjadj@coria.fr
CORIA, France
Lucor, D.
Tel: +33 (0)169 157 226
didier.lucor@limsi.fr
LIMSI-CNRS, France

Germany North

Sommerfeld, M.
University of Magdeburg,
Germany
Tel: +49 345 552 3680
martin.sommerfeld@ovgu.de

Germany South

Becker, S.
Universität Erlangen, IPAT
Cauerstr. 4
91058 Erlangen
Germany
Tel: +49 9131 85 29451
Fax: +49 9131 85 29449
sb@ipat.uni-erlangen.de

Greece

M. Founti.
National Tech. University Of Athens,
School of Mechanical Engineering,
Lab. of Steam Boilers and
Thermal Plants,
Heron Polytechniou 9,
15780 Zografou, Athens, Greece
Tel: +30 210 772 3605
Fax: +30 210 772 3663
mfou@central.ntua.gr

Italy

Rispoli, F.
Tel: +39 064 458 5233
franco.rispoli@uniroma1.it
Borello, D.
Tel: +39 064 458 5263
domenico.borello@uniroma1.it
Sapienza University of Rome,
Via Eudossiana, 18
00184 Roma, Italy

Italy

Rispoli, F.
Tel: +39 064 458 5233
franco.rispoli@uniroma1.it
Borello, D.
Tel: +39 064 458 5263
domenico.borello@uniroma1.it
Sapienza University of Rome,
Via Eudossiana, 18
00184 Roma, Italy

Netherlands

Van Heijst, G.J.
J.M. Burgerscentrum,
National Research School for Fluid
Mechanics, Mekelweg 2,
NL-2628 CD Delft, Netherlands.
Tel: +31 15 278 1176
Fax: +31 15 278 2979
g.j.f.vanheijst@tudelft.nl

Nordic

Wallin, S.
KTH, Dept. of Mechanics,
SE-100 44 Stockholm,
Sweden
Tel: +46 733 303 453
stefanw@mech.kth.se

Poland

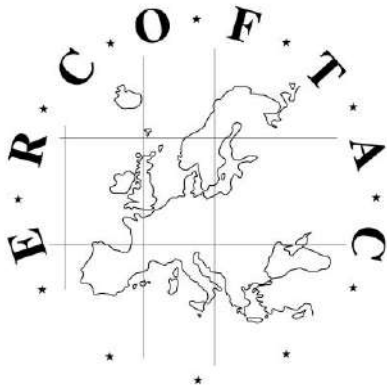
Szumbarski J.
Warsaw University of Technology,
Inst. of Aero. & App. Mechanics,
ul. Nowowiejska 24,
PL-00665 Warsaw, Poland.
Tel: +48 22 234 7444
Fax: +48 22 622 0901
jasz@meil.pw.edu.pl

France - Henri Bénard

Godefert, F.S.
Ecole Centrale de Lyon.
Fluid Mechanics and Acoustics Lab.,
F-69134 Ecully Cedex,
France.
Tel: +33 4 72 18 6155
Fax: +33 4 78 64 7145
fabien.godefert@ec-lyon.fr

United Kingdom

Juniper, M.
Department of Engineering,
Trumpington Street,
Cambridge, CB2 1PZ
United Kingdom.
Tel: +44 (0) 1223 332 585
mpj1001@cam.ac.uk



Best Practice Guidelines for Computational Fluid Dynamics of Dispersed Multi-Phase Flows

Editors

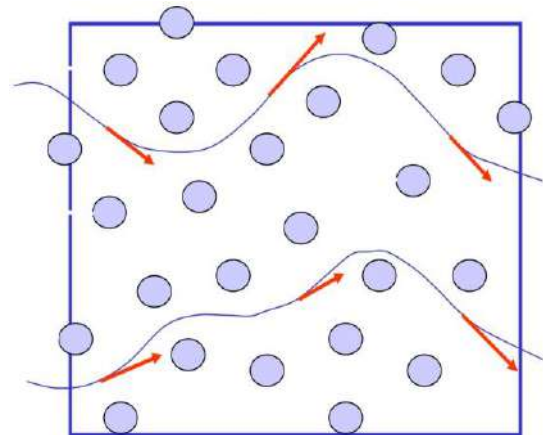
Martin Sommerfeld, Berend van Wachem
&
René Oliemans

The simultaneous presence of several different phases in external or internal flows such as gas, liquid and solid is found in daily life, environment and numerous industrial processes. These types of flows are termed multiphase flows, which may exist in different forms depending on the phase distribution. Examples are gas-liquid transportation, crude oil recovery, circulating fluidized beds, sediment transport in rivers, pollutant transport in the atmosphere, cloud formation, fuel injection in engines, bubble column reactors and spray driers for food processing, to name only a few. As a result of the interaction between the different phases such flows are rather complicated and very difficult to describe theoretically. For the design and optimisation of such multiphase systems a detailed understanding of the interfacial transport phenomena is essential. For single-phase flows Computational Fluid Dynamics (CFD) has already a long history and it is nowadays standard in the development of air-planes and cars using different commercially available CFD-tools.

Due to the complex physics involved in multiphase flow the application of CFD in this area is rather young. These guidelines give a survey of the different methods being used for the numerical calculation of turbulent dispersed multiphase flows. The Best Practice Guideline (BPG) on Computational Dispersed Multiphase Flows is a follow-up of the previous ERCOFTAC BPG for Industrial CFD and should be used in combination with it. The potential users are researchers and engineers involved in projects requiring CFD of (wall-bounded) turbulent dispersed multiphase flows with bubbles, drops or particles.

Table of Contents

1. Introduction
2. Fundamentals
3. Forces acting on particles, droplets and bubbles
4. Computational multiphase fluid dynamics of dispersed flows
5. Specific phenomena and modelling approaches
6. Sources of errors
7. Industrial examples for multiphase flows
8. Checklist of 'Best Practice Advice'
9. Suggestions for future developments



Copies of the Best Practice Guidelines can be acquired electronically from the ERCOFTAC website:

www.ercoftac.org

Or from:

ERCOFTAC (CADO)
PO Box 1212
Bushey, WD23 9HT
United Kingdom

Tel: +44 208 117 6170
Email: admin@cado-ercoftac.org

The price per copy (not including postage) is:

ERCOFTAC members		
First copy		<i>Free</i>
Subsequent copies		75 Euros
Students		75 Euros
Non-ERCOFTAC academics		140 Euros
Non-ERCOFTAC industrial		230 Euros
EU/Non EU postage fee		10/17 Euros